10.45 mm

240 mm

Organotin Photoresists for Extreme Ultraviolet Lithography Yu Zhang 2019

Organotin Photoresists for Extreme Ultraviolet Lithography

Yu Zhang

170 mm

170 mm

Invitation

You are cordially invited to the public defense of my PhD thesis entitled:

Organotin Photoresists for Extreme Ultraviolet Lithography

On Thursday, 11 April 2019 at 14:00 in the Agnietenkapel, Oudezijds Voorburgwal 231, 1012 EZ, Amsterdam

Yu Zhang
y.zhang@uva.nl
y.zhang@arcnl.nl

Paranymphs

Lianjia Wu
l.wu@arcnl.nl

Jarich Haitjema
j.haitjema@arcnl.nl

Organotin Photoresists for Extreme Ultraviolet Lithography

Cover design by Yu Zhang

ISBN: 978-94-028-1416-3

Full color version of the thesis and the electronic supplementary information are available at http://dare.uva.nl/en

Printed by Ipskamp Printing, Amsterdam

Organotin Photoresists for Extreme Ultraviolet Lithography

ACADEMISCH PROEFSCHRIFT

ter verkrijging van de graad van doctor

aan de Universiteit van Amsterdam

op gezag van de Rector Magnificus

prof. dr. ir. K.I.J. Maex

ten overstaan van een door het College voor Promoties ingestelde commissie,

in het openbaar te verdedigen in de Agnietenkapel

op donderdag 11 april 2019, te 14:00 uur

door

Yu Zhang

geboren te Heilongjiang

Promotiecommissie:

Promotor:	prof. dr. A.M. Brouwer	Universiteit van Amsterdam
Copromotores:	prof. dr. P.C.M. Planken	Universiteit van Amsterdam
	dr. S. Castellanos Ortega	Advanced Research Center for Nanolithography
Overige leden:	prof. dr. B. de Bruin	Universiteit van Amsterdam
	prof. dr. M. Tromp	Rijksuniversiteit Groningen
	dr. S. Grecea	Universiteit van Amsterdam
	prof. dr. W.J. Buma	Universiteit van Amsterdam
	dr. Y. Ekinci	Paul Scherrer Institute

Faculteit der Natuurwetenschappen, Wiskunde en Informatica

The research described in this thesis was carried out at the Advanced Research Center for Nanolithography (ARCNL), a public-private partnership of University of Amsterdam (UvA), the VU university Amsterdam (VU), the Netherlands Organization for Scientific Research (NWO) and the semiconductor equipment manufacturer ASML.

Contents

1 INTRODUCTION 1

1.1 PHOTOLITHOGRAPHY 1

1.2 EUV PHOTOLITHOGRAPHY 3

1.3 EUV PHOTORESISTS 4

1.3.1 Chemically amplified photoresists 6

1.3.2 Metal containing photoresists 7

1.3.3 Tin-containing photoresists 9

1.4 AIMS AND OUTLINE OF THIS THESIS 11

1.5 REFERENCES 12

2 EXPERIMENTAL METHODS 19

2.1 SPIN COATER 20

2.2 AFM 21

2.3 E-BEAM LITHOGRAPHY 23

2.4 EUV INTERFERENCE LITHOGRAPHY 24

2.5 DUV EXPOSURE 25

2.6 SCANNING ELECTRON MICROSCOPY 26

2.7 X-RAY PHOTOELECTRON SPECTROSCOPY 27

2.8 LOW DOSE PHOTOELECTRON SPECTROSCOPY 30

2.9 HARD X-RAY PHOTOELECTRON SPECTROSCOPY 31

2.10 REFERENCES 33

3 PHOTOCHEMICAL CONVERSION OF TIN-OXO CAGE COMPOUNDS STUDIED USING HARD X-RAY PHOTOELECTRON SPECTROSCOPY 37

3.1 INTRODUCTION 38

3.2 MATERIALS AND METHODS 39

3.2.1 Materials 39

3.2.2 Photoresists film preparation 39

3.2.3 Photoresists exposure 40

3.2.4 Characterization 40

3.3 RESULT AND DISCUSSION 40

3.3.1 Atomic concentration of different samples 40

3.3.2 Analysis of Sn, O and C chemical shifts 42

3.4 CONCLUSIONS 47

3.5 REFERENCES 48

4 INFLUENCE OF THERMAL PROCESS ON THE CHEMICAL REACTION AND REACTION YIELD IN A MODEL ORGANOTIN EUV PHOTORESIST 51

4.1 INTRODUCTION ... 52
4.2 MATERIALS AND METHODS ... 53
4.3 RESULT AND DISCUSSION ... 54
4.3.1 Overview XPS spectra ... 54
4.3.2 High-resolution XPS spectra ... 55
4.3.3 UV-Vis spectroscopy ... 60
4.3.4 Proposed mechanism ... 60
4.4 CONCLUSIONS ... 62
4.5 REFERENCES ... 62

5 THE RELATIONSHIP BETWEEN PHOTON ABSORPTION OF TIN-NANOCAGES AND THE EFFICIENCY OF PHOTOCHEMICAL REACTION ... 67

5.1 INTRODUCTION ... 68
5.2 EXPERIMENT ... 69
5.2.1 Sample preparation ... 69
5.2.2 Exposure ... 69
5.2.3 Characterization ... 69
5.3 RESULT AND DISCUSSION ... 70
5.3.1 UV-Vis spectra ... 70
5.3.2 Overview XPS spectra ... 71
5.3.3 High-resolution XPS spectra ... 72
5.3.4 Dose contrast curve ... 76
5.4 CONCLUSIONS ... 77
5.5 REFERENCES ... 78

6 EXTREME ULTRAVIOLET PATTERNING OF TIN-OXO CAGES ... 81

6.1 INTRODUCTION ... 82
6.2 MATERIALS AND METHODS ... 83
6.2.1 Materials ... 83
6.2.2 EUV exposure ... 84
6.2.3 Post-exposure analysis ... 84
6.3 RESULT AND DISCUSSION ... 85
6.3.1 Open-frame experiments: contrast curves ... 85
6.3.2 Interference lithography experiments: patterning ... 91
6.4 CONCLUSIONS ... 94
6.5 REFERENCES ... 94

7 THE PHOTOREACTION MECHANISM OF TIN OXO CAGES UNDER EUV EXPOSURE ... 97

7.1 INTRODUCTION ... 98
7.2 EXPERIMENT ... 100
7.2.1 Sample preparation ... 100

7.2.2 Exposure *100*
7.2.3 Photoelectron spectroscopy *100*
7.2.4 TOF-SIMS mass spectrometry *101*
7.2.5 Outgassing measurement *101*
7.3 RESULT AND DISCUSSION 101
7.3.1 In-situ XPS *101*
7.3.2 In-situ EUV exposure with detection of outgassing products *105*
7.3.3 Ex-situ EUV and XPS *106*
7.3.4 Ex-situ TOF-SIMS *110*
7.3.5 Chemical changes upon EUV irradiation *112*
7.3.6 Chemical changes in ex-situ measurement. *113*
7.4 CONCLUSIONS 115
7.5 REFERENCES 116

8 DUAL-TONE APPLICATION OF A TIN OXO CAGE PHOTORESIST UNDER E-BEAM AND EUV EXPOSURE 121
8.1 INTRODUCTION 122
8.2 MATERIALS AND METHODS 123
8.2.1 Materials *123*
8.2.2 Exposure *123*
8.2.3 Characterization *123*
8.3 RESULT AND DISCUSSION 123
8.3.1 Topography characterization *123*
8.3.2 XPS characterization *128*
8.4 CONCLUSIONS 131
8.5 REFERENCES 131

9 LOW-VALENT TIN CARBOXYLATES AS PHOTORESISTS 135
9.1 INTRODUCTION 136
9.2 EXPERIMENTAL DETAILS 137
9.3 RESULT AND DISCUSSION 138
9.3.1 Sensitivity of SnE and SnA *138*
9.3.2 IR spectroscopy of SnA and SnE *143*
9.3.3 X-ray Photoelectron Spectra of SnA and SnE *147*
9.4 CONCLUSIONS 150
9.5 REFERENCES 150

SUMMARY 153

SAMENVATTING 157

PUBLICATION LIST 161

ACKNOWLEDGEMENT..163

Chapter 1

Introduction

1.1 Photolithography

Photolithography is a key technology that has enabled the rapid development of semiconductor industry during the past 60 years. It is a technique that enables geometric features to be transferred from a mask to a photo-responsive material (photoresists) deposited on a substrate.[1] The typical photolithography process is illustrated in Scheme 1.1. The standard procedure is started with spin-coating a photoresist as a thin layer on the silicon substrate, and then exposing the photoresist thin film with an irradiation source, commonly ultraviolet light. The solubility of the photoresist is changed as a result of chemical reactions induced by the local exposure. In a development step, either the exposed part or the unexposed part can be removed by washing with a suitable solvent, generating positive tone or negative tone patterns, respectively. Using the protection by the photoresist, the pattern from the mask is transferred to the silicon substrate via an etching step.

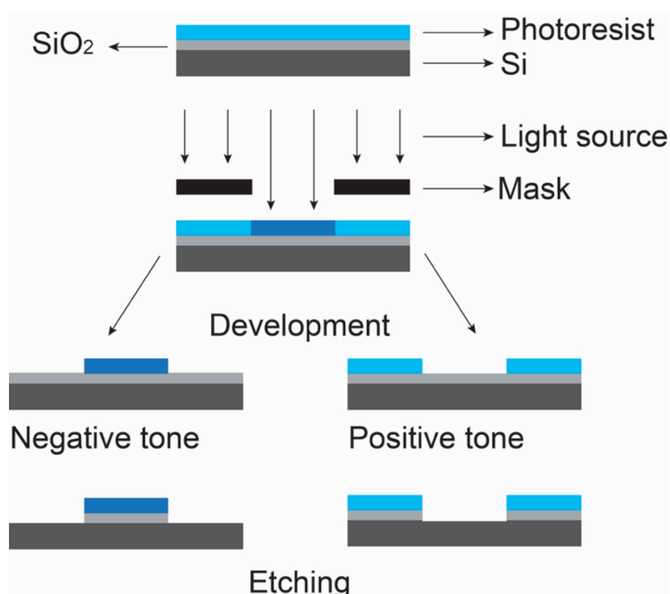

Scheme 1.1. *Fundamental photolithography procedure.*

Optical lithography has been the dominant pattern transfer technology in the semiconductor industry for more than 5 decades because it can fulfill the requirement of high volume production of microelectronic components.[2-4] In addition to the improvement of the throughput and decrease of the cost, another significant challenge in the semiconductor industry is the increasing transistor density per unit area, which implies that the feature size should become smaller and smaller. Until now, the shrinkage of the critical dimension (CD) of the device features has been able to match the International Technology Roadmap for Semiconductor (ITRS) and the famous Moore's law.[5-7] The number of transistors on a chip has been doubled on the average every 18 months. The minimum feature size that a projection system can print is given approximately by the Rayleigh equation:[8]

$$CD = k\lambda / NA \tag{1.1}$$

In equation 1.1, CD is the critical dimension, k is a coefficient that incorporates process-related factors, NA is the numerical aperture of the optical system, and λ is the wavelength of the projection light. During the past decades, the resolution (CD) has been systematically improved (CD became smaller) by optimizing the process factor k, which has reached its practical limit at k = 0.25, and by reducing the wavelength of the incident light.[8] In the past decades, the wavelength used in optical lithography was continuously scaled down from 436 nm, 365 nm, 248 nm until 193 nm.[3, 8, 9] The shorter wavelengths are dictated by the available light sources, which in practice are excimer lasers, KrF for 248 nm and ArF for 193 nm. A natural next choice would have been to turn to the F_2 laser at 157 nm, but this turned out to be problematic (the birefringence of the CaF_2 crystal lens, vacuum exposure, etc.).[10] Instead, the 193 nm wavelength scanners where improved by using immersion lithography, which allowed to increase the numerical aperture from NA = 0.93 to NA = 1.35.[11-14] With these improvements, the lower limit of the critical dimension is now CD = 0.25 × 193 / 1.35 = 36 nm. To create smaller features, multiple patterning techniques are required. To avoid the added costs of these processes and to open a new path to smaller CD's a significant step was needed. Extreme ultraviolet photolithography (EUVL), which uses 13.5 nm radiation, was developed to meet these challenges.[9, 15, 16]

To achieve high quality patterns, the variation of the pattern feature is one of the most significant problems.[17, 18] The variation of the line boundary of the resist pattern is called line edge roughness (LER).[18] Kozawa et al. have investigated the reason for the LER.[19] Almost all of the resists and process factors can affect the LER.[19] At the beginning, the molecular size was considered to be the main reason for LER since it was considered the minimum dissolution unit.[20] Later, Kozawa et al. found that the chemical inhomogeneity generated at the edge of the pattern

between the unexposed and exposed areas (or soluble and insoluble molecules) was the main concern.[21, 22] Since the photon induced chemical reaction is a stochastic process, the inhomogeneity in the distribution of the soluble and insoluble molecules at the boundary leads to LER generation.[21, 23] As the pattern resolution is aiming at approaching the atomic scale in EUV photolithography, the stochastic effects are becoming a more and more serious concern. The photon shot noise in particular is a fundamental physical limitation.[22, 24] The difficulty to improve the resolution, LER and the sensitivity simultaneously is also known as the RLS trade-off, illustrated in Fig. 1.1.[25, 26]

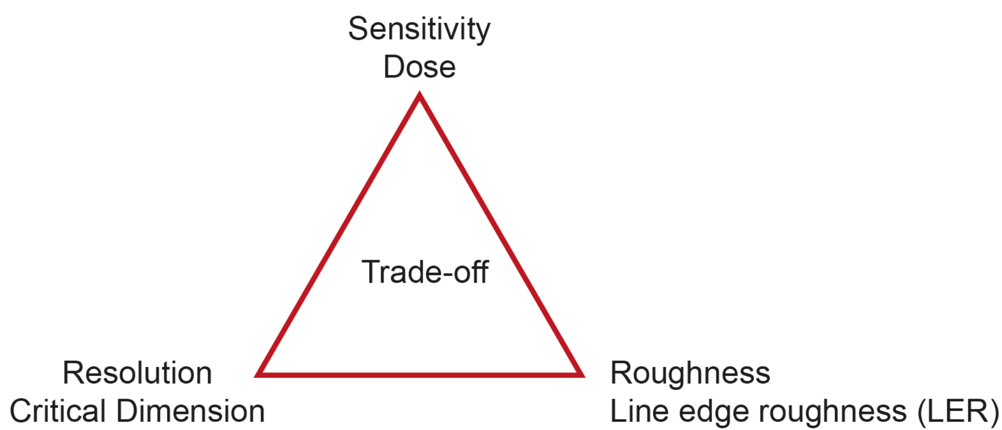

Figure 1.1. *The resolution: LER: Sensitivity or RLS trade-off.*

1.2 EUV photolithography

EUVL development has been initiated in the 1980s, and it was suggested to viably extend Moore's law.[27, 28] EUVL has many similarities with the previous generations of optical lithography technologies. The pattern resolution in EUVL still follows the Rayleigh equation. Since the wavelength used in EUVL is 13.5 nm it potentially supports the resolution of the pattern down to sub-10 nm in a single process step.[16] It enables the feature size on the semiconductor chips to become smaller and smaller.[29-31]

Yet, there are some important differences between the ultraviolet lithography technologies and EUVL, which are mainly due to the extremely short wavelength of 13.5 nm used in EUVL. One of the most significant differences is the EUV optics, which rely on reflection instead of traditional transmission optics. The schematic of current optical train in an ASML EUV photolithography machine is shown in Scheme 1.2.

In order to make EUVL a high-volume manufacturing tool for electronic devices, big efforts have been put in the EUV light source, optics, metrology, contamination control, masks and mask handling, and resists. Among these components, the photoresist is considered as one of the most critical issues in realizing EUVL in industry. In this thesis, we focus on the EUV photoresists.

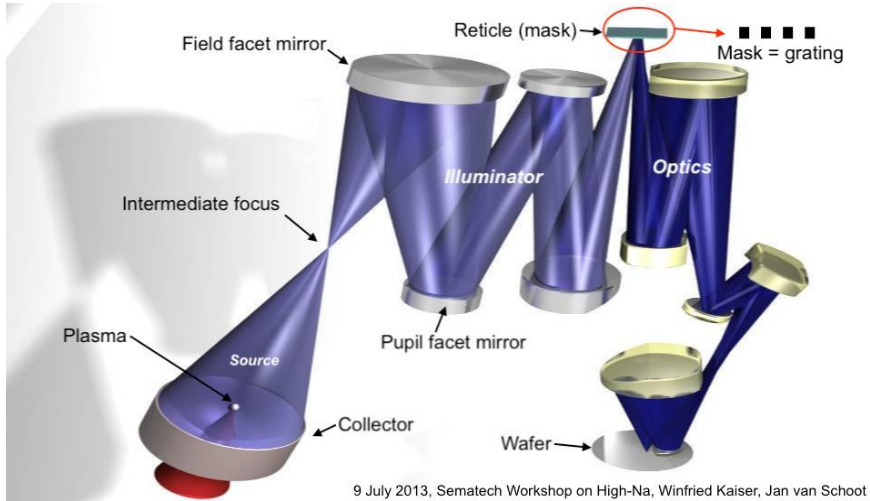

Scheme 1.2. *Current optical train in ASML EUV photolithography machine (NXE: 3300/3350/3400).*

1.3 EUV photoresists

A photoresist is a photo-responsive material of which the solubility can be switched by irradiation-induced chemical conversion, in many cases followed by a heat treatment. In the development of photolithography, each wavelength reduction has required the preparation of novel photoresists that are not only sensitive at the new wavelength, but also meet all of the requirements of an effective resist material. A good resist that is acceptable for high-volume manufacture must give good resolution, high solubility contrast, good etch resistance, high sensitivity and low outgassing. In order to continuously push the critical feature size down in EUV lithography, considerable efforts have been put in developing photoresists for the next generation EUV lithography.[32]

EUV photoresists with high sensitivity are preferable, because the EUV exposure tools are currently photon limited. Thus the sensitivity of the photoresist plays an important role in EUVL. The shrinkage of the CD also places restrictions on the thickness of the photoresist. The aspect ratio is defined as the height divided by the width of the features being patterned. The aspect ratio of 2.5 or smaller has been acceptable. Higher aspect ratio starts to incur larger potential for pattern collapse.[33]

For 15 nm features fabrication, a film thickness around 30 nm is routinely used. As a result, a high absorbance of the thin photoresist at 13.5 nm becomes the key factor for the sensitivity of the EUV photoresist. Ultra-high absorbance on the other hand should also be avoided because it leads to an insufficient penetration depth of the light so that the film cannot be completely exposed down to the substrate. It has been identified by Kunz et al. that ideal imaging is typically achieved for a film transmittance of 50 – 80%.[34] Kozawa et al. reported that a minimum transmittance of 70% is required for vertical sidewalls.[35, 36] Based on the Lambert-Beer law, when a 30 nm film is used and the transmittance is 70%, the needed absorption coefficient of the photoresist is around 12 μm^{-1}. Because the source power of the current generation of EUVL machines is limited, and overall reflectivity of the EUV optics is relatively low, a resist sensitivity on the order of 10 – 15 mJ cm^{-2} has been mentioned as a requirement to achieve the wafer throughput that would make EUV economical.[24] But it may generate high LER under this low dose due to the photon stochastics. To search for proper materials with required absorption, the absorption cross section of different elements has been calculated from tabulated data[37], as shown in Fig. 1.2.

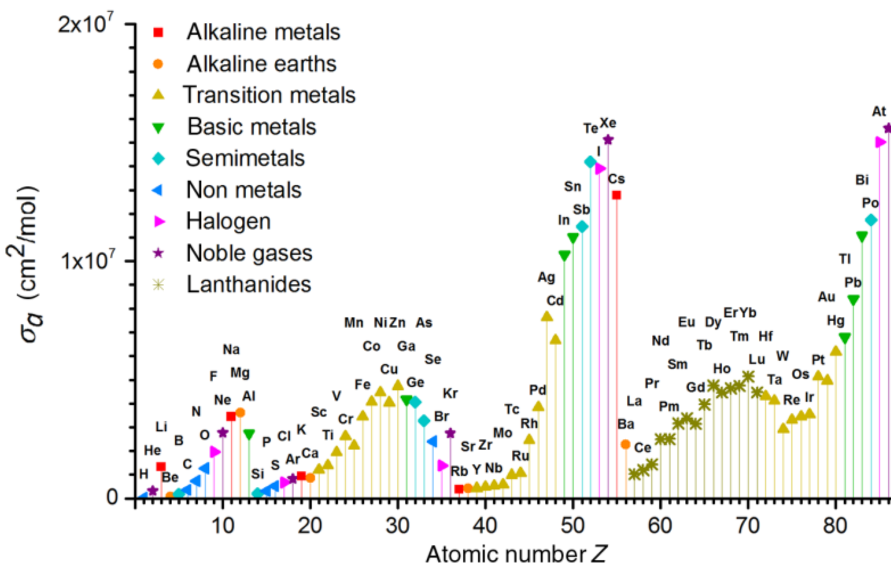

Figure 1.2. *Atomic absorption cross-section at EUV (13.5 nm) of elements with atomic number Z from 1 to 86, from tabulated data.*[37, 38] *Figure from ref. 38.*

Traditionally, the photoresists are polymer molecules, mainly containing carbon and oxygen atoms.[39-41] After considering the EUV absorption cross-sections of the different elements illustrated in Fig. 1.2, metal-containing materials were investigated as photoresist for EUVL instead of traditional organic polymer type photoresist.

1.3.1 Chemically amplified photoresists

The current standard type of photoresists is the so-called chemically amplified photoresist (CAR), in which chemical amplification is accomplished by employing acid catalyzed deblocking of dissolution inhibiting groups. The strong acid required is generated by a local photochemical reaction of a compound called the photo-acid generator.[41] Two of the common deprotection pathways are the conversion of carbonates or esters to phenolic or carboxylic OH. The typical photo-induced acid catalyzed deprotection chemistry (photoresist for 248 nm as an example) is shown in Fig. 1.3. The chemical reaction increases the fraction of free OH groups in the exposed part of the photoresist, which increases the solubility of the exposed part in aqueous base. The chemically amplified photoresists are widely used in 193 nm high-volume manufacturing lithography. For EUV lithography, researchers try to further adapt the CAR concept to develop EUV photoresists.[42-44]

Since the absorptions of carbon and oxygen atoms are quite low at the EUV wavelength, in order to increase the sensitivity, it is important to improve the acid generation efficiency and catalysis as much as possible.[45] The migration of the catalyst is an essential aspect of the chemical amplification mechanism, but the spreading of catalyst also leads to the decrease of resolution and increase of LER.[46] To prevent the acid diffusion and improve the LER, base quencher was added into the photoresists thin film to react with the residual acid.[47, 48]

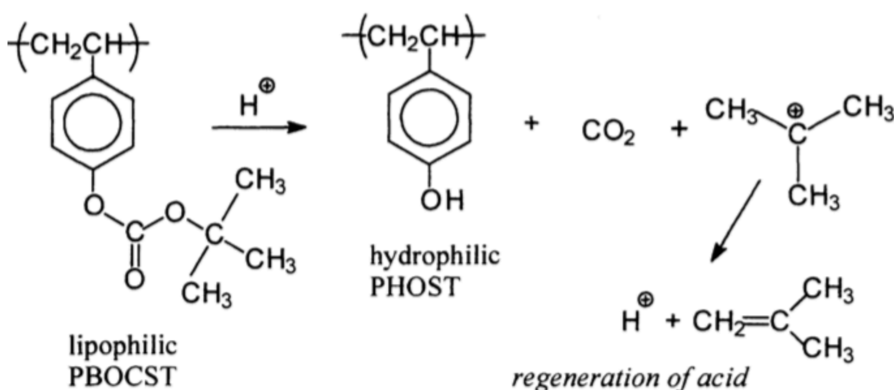

Figure 1.3. *Acid catalyzed deprotection chemistry (photoresist for 248 nm as an example). Figure from ref. 41.*

The photoreaction mechanism of the CAR under EUV exposure was investigated by several groups.[49-51] The main difference is that the photons give rise to molecular photochemistry during photolysis at 193 nm or even longer wavelength exposure. Under EUV (92 eV) exposure, primary photoelectrons are emitted from the valence band and the semi-core levels. These primary electrons have sufficient energy to

further ionize the photoresist molecules, generating secondary electrons, as shown in Fig. 1.4. Not only the photon-induced chemical reaction, but also the photoelectrons generated after the EUV photon absorption contribute to chemical conversion.[52] The photoelectron generating mechanism under EUV is the same regardless of the type of photoresist. Because the photoelectrons diffuse within the photoresist, they induce the so-called secondary electron blur, which decreases the resolution and increases the line edge roughness of the EUV generated pattern.[53]

Effort also needs to be put to improve the etching resistance of the organic polymer type photoresists. The final goal of the photoresist is to protect the underlying substrate from the etching. But with the resolution increasing, the film thickness of the resist has to be decreased to prevent pattern collapse. The thinner the organic photoresist film, the harder for the film thickness to protect the under-layer substrate from the etch process.[54] To avoid these problems of organic polymer type photoresist, molecular organometallic photoresists started to be introduced.

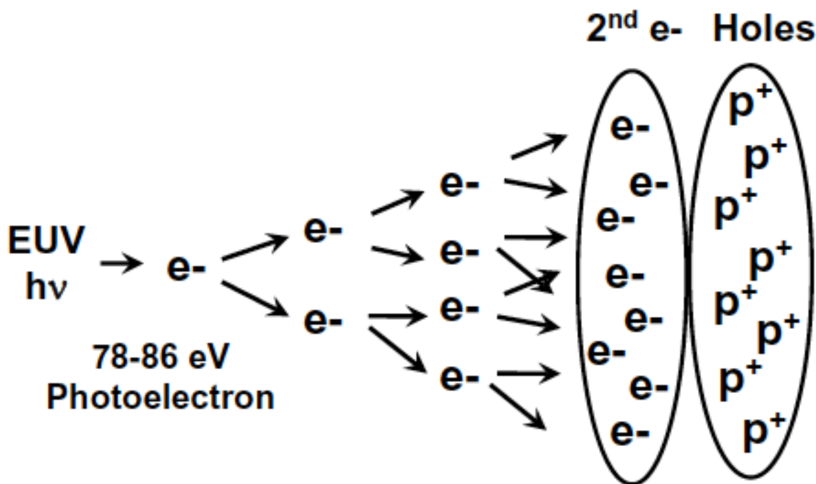

Figure 1.4. *Qualitative scheme depicting multiple electrons being created after the absorption of an EUV photon. Figure from ref. 52.*

1.3.2 Metal containing photoresists

As an alternative to the traditional organic polymer type photoresist, which is mainly composed from carbon and oxygen atoms, the metal containing photoresist were introduced to EUVL. Based on the absorption cross sections at the EUV energy of 92 eV, shown in Fig. 1.2, metals can be expected to have much higher absorption than most of the organic photoresist under EUV exposure. Additionally, the metal containing photoresists also have higher mass density than the organic photoresist, which potentially decreases the secondary electron blur.[55] Since this

type of photoresists are not blended with photoacid generators, acid diffusion is not a problem any more when the molecular metal containing photoresist is used.

The metal containing resist started to attract interest due to their high EUV absorption cross section, which can fulfill the absorption coefficient requirement of EUV photolithography. The hybrid metal containing type photoresists were introduced, firstly by Ober's group at Cornell introduced the Hf- and Zr-containing type nanoparticles mixed with a photo-acid generator were tested as EUV photoresists.[56-58] The properties of hybrid photoresist, their EUV patterning performance, and the chemical reaction mechanism were introduced with this work. Based on photolysis of the carboxylic group and surface charge change of the nanoparticles, the hydrodynamic size of the nanoparticles can be changed, therefore switching the solubility of the photoresist.[59, 60] It was shown that the Zr-/Hf-type nanoparticles give 25 times higher etching resistance than polymer type photoresists.[61] Additionally, the sensitivity of these Zr- and Hf-type photoresists was demonstrated with high-resolution patterns with EUV doses as low as 4.2 mJ cm^{-2}.[58] Hf-, Zr- and Ti-methacrylate clusters were introduced by Castellanos's group as EUV photoresists.[62] HfSOx cluster photoresist was introduced and the mechanism was studied by Herman and coworkers.[63] They also use a sodium template butyltin cluster with β-Keggin,[64] and butyltin oxo hydroxo,[65] as model photoresists to investigate the patterning mechanism. Other molecular hybrid compounds inspired in metal organic frameworks comprising Zn-based dimers were introduced as EUV photoresist by Ober and coworkers.[66] Brainard's group explored a wide range of metal containing molecular type photoresists such as palladium and platinum containing molecules as positive tone photoresist,[67] antimony molecule photoresist,[68] tin molecule photoresists (negative tone).[69, 70] All the photoresist introduced above show good resolution and sensitivity performance. The US company Inpria was the first to develop inorganic photoresists for industrial application.[71-73] The actual molecular structure was not disclosed, but it it known to be tin-based, and both patent descriptions[73, 74] and a publication[75] suggest that it is like the tin cages discussed below. Several chemical structures of the metal containing photoresist mentioned above are shown in Fig. 1.5.

The absorption coefficients of different metal containing photoresists at the EUV energy were measured by Fallica et al.[38, 76] The advantage of the metal containing photoresist is a clear superiority over the organic type photoresist when we consider the EUV absorption ability, especially for the tin containing photoresists.

To improve the sensitivity of the EUV photoresist, except improving the EUV absorption, the photoresists also need to efficiently undergo photolytic conversion.[77] The photolysis of the carboxylic group upon UV irradiation has been reported.[60, 78]

This mechanism has been observed in several EUV photoresist systems, such as Hf-, Zr- based nanoparticles, and Zr-, Hf- cluster, and $L_2M(C_2O_4)$ type resist.[60, 62, 67, 68, 79, 80] Their performance under EUV exposure shows that the design based on the reaction mechanism is a good approach to create new EUV photoresist.

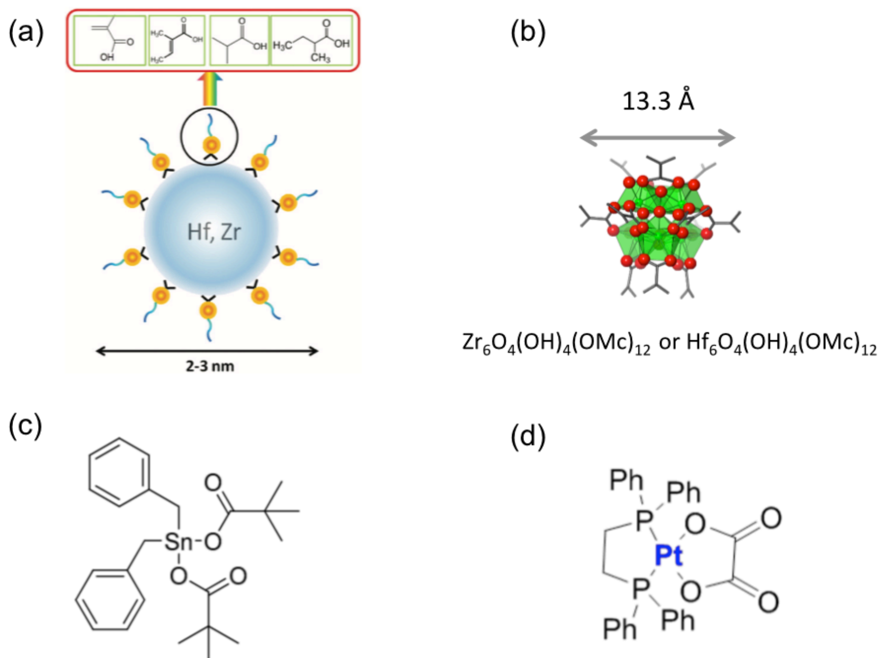

Figure 1.5. *(a) Hf-, Zr- based nanoparticles from Ober's group.*[59] *(b) Hf-, or Zr cluster from Castellanos' group.*[62] *(c) Tin carboxylate molecule from Brainard's group.*[79] *(d) Pt based photoresist from Brainard's group.*[67]

Above all, various metal containing photoresists were investigated as EUV photoresists. Not only the pattern performance under EUV lithography, most of the works also introduce the chemical reaction mechanism of the photoresist under EUV exposure. In addition to searching for the best pattern performance, we also would like to understand the reason behind. In this way, we might find a more efficient way to build more efficient EUV photoresists.

1.3.3 Tin-containing photoresists

Among all the metal containing molecules or complexes, the tin-containing molecules are probably the most attractive due to their potentially high EUV absorbances. The tin containing organic molecules are called organotin compounds if they contain at least one bond between tin and carbon. The organotin molecular complexes have been developed for decades.[81-83] Their diversity of structures and

their suitability for construction of frameworks have attracted the attention of many research groups throughout the world. Various applications make use of organotin compounds, such as biocides, oil production, fracturing thickening agent, and green corrosion inhibitor.[84-86] They also start to set their foot into the EUV photoresist field. Based on the expectation mentioned above, the metal carboxylate complexes can be good EUV photoresists, those tin oxo cages also can be used as EUV photoresist. Among all the organotin compounds, the tin containing cages as shown in Fig. 1.6, have attracted the attention from Brainard et al.[70] The cages contain 12 tin atoms and twelve organic groups connected to the tin atoms, and also 20 oxygen atoms in the framework connecting the tin atoms. This tin oxo cage (with isopropyl R-groups) was first reported by Puff and Reuter.[87] The synthesis method and the molecular structure were introduced and characterized carefully. This structure is stable and soluble in many media, it can be crystallized and its structure has been well characterized. But there was no specific property or potential application described for this interesting molecule until Brainard's group introduced it as a metal-organic EUV photoresist.[70] They used the 12-Sn and oxygen as the main framework, the counterion and the outer shell organic chain were exchanged. The conditions used to prepare this compound into EUV photoresists were tested and optimized. Clear patterns were achieved under EUV interference lithography and the lithographic performance of tin oxo cages with different organic groups and counterions was also tested and compared. They successfully employed the tin oxo cages as EUV photoresists. But the photochemical reaction mechanism upon EUV exposure was not clear.

Another kind of organotin molecule introduced by Brainard's group into EUV photoresists are single tin atom containing organotin carboxylates.[79] Twenty one compounds of the type $R_2Sn(O_2CR')_2$ were tested under EUV exposure.[79] The photoreaction mechanism is clearer than in the case of the tin cages. Here it is mainly the decomposition reaction of the carboxylate and the Sn-C bond cleavage. They also found out the relationship between the hydrocarbon group size and the dose to gel value. Their results indicated that the sensitivity of photoresists showed strong correlation with the R groups, while the carboxylate groups were unlikely involved in the reaction upon EUV exposure. But when the R group is fixed, the higher the molecule weight of the R' group, the lower the sensitivity of the photoresist, except the acrylate and methacrylate compound. Their sensitivity and high-resolution pattern ability under EUV exposure have been proven.

In this thesis, we study two kinds of tin compounds. The main subject is the organotin oxo cage as shown in Fig. 1.6. In addition we briefly explored low valent tin(II) carboxylates. The tin oxo cages were chosen due to their well-defined molecular structure, high EUV sensitivity, their easy synthesis and good pattern

ability which made them good to use as a model system to investigate the chemical reaction mechanism upon irradiation. In addition to EUV, we also use DUV as irradiation source to trace the photoreaction in the model EUV resist. In the last chapter we also explore tin(II) 2-ethylhexanoate and tin(II)acetate, which are formally not organotin compounds, and can be expected to react via different pathways. Tin(II) 2-ethylhexanoate has been applied for UV-assisted imprinting lithography.[78] The photoreaction mechanism upon UV exposure has been described.[78]

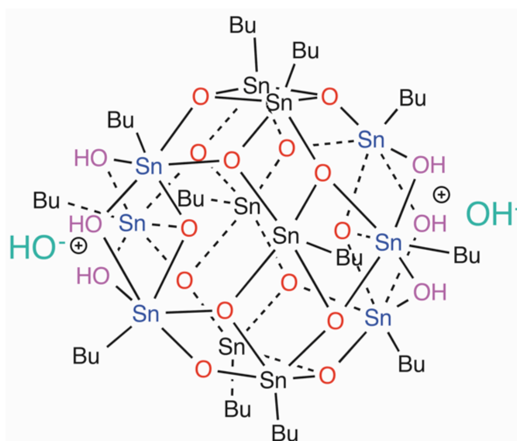

Figure 1.6. *Chemical structure diagram of the tin oxo cage* $[(BuSn)_{12}O_{14}(OH)_6](OH)_2$ *with hydroxide as counterion.*

1.4 Aims and outline of this thesis

This thesis is the result of a research project in the Nanophotochemistry group at the Advanced Research Center of Nanolithography. In our group, we are aiming at investigating the photoreaction mechanism inside the photoresist for next generation photolithography. In this thesis, we used the tin oxo cages as a model compound and investigated the reaction mechanism of the photon-induced reaction. The possibility of using a small tin containing molecule as photoresist was also investigated.

In Chapter 2, we discuss the details of the experimental methods we used throughout this thesis. The chapter starts with sample preparation method and the way we used to characterize the pattern performance. It then shows the methods we used for characterizing the photon-induced chemical changes in the photoresist.

In Chapter 3, the photoreactions of the tin oxo cages with hydroxide group upon deep UV (225 nm) exposure under dry N_2 and air atmosphere are studied and compared by using hard X-ray Photoelectron Spectroscopy (HAXPES). The

photoreaction mechanism in the tin oxo cages is proposed. XPS is demonstrated to be a valuable technique for investigating the chemical changes in the photoresist thin films. This work serves as a motivation for the following studies on the photoreaction mechanism in the photoresist thin films upon exposure.

In Chapter 4, the effect of thermal processing on the chemical reactions and reaction yield in the tin oxo cages are investigated, again using HAXPES. In addition to the photon-induced reaction, we prove that the chemical reactions in the bake processes also act as significant roles in the final performance of the photoresist.

In Chapter 5, we used three kinds of tin oxo cages, which have the same cage structure but three different conterions (hydroxide, acetate, trifluoroactate), to investigate the relationship between photon absorption, chemical reaction and the solubility changes in the photoresist.

In Chapter 6, we study the pattern performance of the tin oxo cages under EUV exposure. Different process conditions are tested. Our results indicate that sensitivity and resolution are only meaningful for photoresist when the process conditions are optimized.

In Chapter 7, we investigate the photoreaction mechanism of tin oxo cages under EUV (13.5 nm) and DUV (225 nm) exposure. Different X-ray photoelectron spectroscopies combined with mass spectrometry methods are used to investigate the photon-induced chemistry in the photoresist films. To study primary reactions between photons and the tin oxo cage, the photoelectron spectrum with photon energy 92 eV was measured.

In Chapter 8, we describe the discovery of a dual-tone property of the tin oxo cages photoresist upon EUV and E-beam exposure. Additionally, we study the chemical reactions in the TinOH thin films under different conditions.

In Chapter 9, we study possibility of using the tin(II) carboxylate molecules as EUV photoresist. The patterning performance and the chemical reaction of the thin films upon EUV are studied.

1.5 References

1. C. A. Mack, in Fundamental Principles of Optical Lithography: The Science of Microfabrication, Wiley Publishing, 2007, 1-28.
2. D. G. Flagello, T. Matsuyama, Y. Ohmura and D. M. Williamson, "The lithographic lens: its history and evolution", *Proc. SPIE* 2006, **6154**, 61540301-61540314.

3. K. Ronse, "Optical lithography-a historical perspective", *C. R. Phys.*, 2006, **7**, 844-857.
4. C. Ngô and C. Rosilio, "Lithography for semiconductor technology", *Nucl. Instrum. Methods Phys. Res., Sect. B*, 1997, **131**, 22-29.
5. M. H. Bennett and G. E. Moore, "Lithography and the future of Moore's law", *Proc. SPIE*, 1995, **2439**, 243901-17.
6. D. R. Holmes, Jr. and M. J. Mack, "Moore's Law: Apples and Oranges", *JACC Cardiovasc. Interv.*, 2015, **8**, 1667-1669.
7. C. A. Mack, "Fifty Years of Moore's Law", *IEEE T. Semiconduct. M.*, 2011, **24**, 202-207.
8. B. W. Smith, in *Nanolithography*, ed. M. Feldman, Woodhead Publishing, 2014, **1**, 1-41.
9. G. Marsh, "Moore's law at the extremes", *Materials Today*, 2003, **6**, 28-33.
10. G. Sun, S. Cho, C. Clark, S. V. Verkhoturov, M. J. Eller, A. Li, A. Pavia-Jimenez, E. A. Schweikert, J. W. Thackeray, P. Trefonas and K. L. Wooley, "Nanoscopic cylindrical dual concentric and lengthwise block brush terpolymers as covalent preassembled high-resolution and high-sensitivity negative-tone photoresist materials", *J. Am. Chem. Soc.*, 2013, **135**, 4203-4206.
11. A. Yen, B. W. Smith, H. Kang, A. Bourov, F. Cropanese and Y. Fan, "Water immersion optical lithography for 45-nm node", *Proc. SPIE*, 2003, **5040**, 679-689.
12. H. Sewell, *US6980277*, 2005, 7.
13. Y.-C. Yeo, B.-J. Lin and C. Hu, *US7700267*, 2010, 12.
14. D. Flagello and J. Doering, *US6954256*, 2005, 13.
15. C. Wagner and N. Harned, "Lithography gets extreme", *Nat. Photonics*, 2010, **4**, 24-26.
16. K. Kemp and S. Wurm, "EUV lithography", *C. R. Phys.*, 2006, **7**, 875-886.
17. C. A. Mack, "Reducing roughness in extreme ultraviolet lithography", *Proc. SPIE*, 2017, **10450**, 104500P.
18. E. Gogolides, V. Constantoudis, G. P. Patsis and A. Tserepi, "A review of line edge roughness and surface nanotexture resulting from patterning processes", *Microelectron. Eng.*, 2006, **83**, 1067-1072.
19. T. Kozawa, S. Tagawa, J. J. Santillan, M. Toriumi and T. Itani, "Image contrast slope and line edge roughness of chemically amplified resists for postoptical lithography", *J. Vac. Sci. Technol., B: Microelectron. Nanometer Struct.--Process., Meas., Phenom.*, 2007, **25**, 2295-2300.
20. O. Hiroaki, T. Katsutomo, K. Kiminori and I. Toshiro, "Development of New Positive-Tone Molecular Resists Based on Fullerene Derivatives for Extreme Ultraviolet Lithography", *Jpn. J. Appl. Phys.*, 2010, **49**, 06GF0401-06.
21. K. Takahiro, O. Hiroaki, I. Toshiro and T. Seiichi, "Relationship between Chemical Gradient and Line Edge Roughness of Chemically Amplified Extreme Ultraviolet Resist", *Appl. Phys. Express*, 2010, **3**, 036501-036503.
22. K. Takahiro, "Relationship between Stochastic Effect and Line Edge Roughness in Chemically Amplified Resists for Extreme Ultraviolet Lithography Studied by Monte Carlo Simulation", *Jpn. J. Appl. Phys.*, 2012, **51**, 08650401-06.

23. P. De Bisschop, J. Van de Kerkhove, J. Mailfert, A. V. Pret and J. Biafore, "Impact of stochastic effects on EUV printability limits", *Proc. SPIE*, 2014, **9048**, 90480901-90480915.
24. P. Naulleau, in *Frontiers of Nanoscience*, eds. A. Robinson and R. Lawson, Elsevier, 2016, **11**, 177-192.
25. S. Nagahara, M. Carcasi, H. Nakagawa, E. Buitrago, O. Yildirim, G. Shiraishi, Y. Terashita, Y. Minekawa, K. Yoshihara, M. Tomono, H. Mizoguchi, J. Estrella, T. Nagai, T. Naruoka, S. Dei, M. Hori, A. Oshima, M. Vockenhuber, Y. Ekinci, M. Meeuwissen, C. Verspaget, R. Hoefnagels, G. Rispens, R. Maas, H. Nakashima and S. Tagawa, "Challenge toward breakage of RLS trade-off for EUV lithography by Photosensitized Chemically Amplified Resist (PSCAR) with flood exposure", *Proc. SPIE*, 2016, **9776**, 97760701-18.
26. K. Matsuzawa, T. Fujii, S. Matsumaru, T. Yamada, Y. Komuro, D. Kawana and K. Ohmori, "Challenges to overcome trade off between high resolution and high sensitivity in EUV lithography", *J. Photopolym. Sci. Technol.*, 2016, **29**, 489-493.
27. H. Kinoshita, "History of extreme ultraviolet lithography", *J. Vac. Sci. Technol., B: Microelectron. Nanometer Struct.--Process., Meas., Phenom.*, 2005, **23**, 2584-2588.
28. W. T. Silfvast and O. R. Wood, "Tenth micron lithography with a 10 Hz 37.2 nm sodium laser", *Microelectron. Eng.*, 1988, **8**, 3-11.
29. B. J. Rice, in *Nanolithography*, ed. M. Feldman, Woodhead Publishing, 2014, **2**, 42-79.
30. E. Buitrago, T. S. Kulmala, R. Fallica and Y. Ekinci, in *Frontiers of Nanoscience*, eds. A. Robinson and R. Lawson, Elsevier, 2016, **11**, 135-176.
31. A. Tullo, "IBM breakthrough leads to first 5-nm chip", *C&EN Global Enterprise*, 2017, **95**, 11-11.
32. R. L. Brainard, G. G. Barclay, E. H. Anderson and L. E. Ocola, "Resists for next generation lithography", *Microelectron. Eng.*, 2002, **61-62**, 707-715.
33. B. Paivanranta, A. Langner, E. Kirk, C. David and Y. Ekinci, "Sub-10 nm patterning using EUV interference lithography", *Nanotechnology*, 2011, **22**, 37530201-37530207.
34. R. R. Kunz, T. M. Bloomstein, D. E. Hardy, R. B. Goodman, D. K. Downs and J. E. Curtin, "Outlook for 157 nm resist design", *J. Vac. Sci. Technol., B: Microelectron. Nanometer Struct.--Process., Meas., Phenom.*, 1999, **17**, 3267-3272.
35. T. Kozawa and S. Tagawa, "High-Absorption Resist Process for Extreme Ultraviolet Lithography", *Jpn. J. Appl. Phys.*, 2008, **47**, 8354-8359.
36. A. P. G. Robinson and R. A. Lawson, in *Frontiers of Nanoscience*, eds. A. Robinson and R. Lawson, Elsevier, 2016, **11**, 447-478.
37. B. L. Henke, E. M. Gullikson and J. C. Davis, "X-Ray Interactions: Photoabsorption, Scattering, Transmission, and Reflection at E = 50-30,000 eV, Z = 1-92", *Atomic Data and Nuclear Data Tables*, 1993, **54**, 181-342.

38. R. Fallica, J. Haitjema, L. Wu, S. C. Ortega, A. M. Brouwer and Y. Ekinci, "Absorption coefficient of metal-containing photoresists in the extreme ultraviolet", *J. Micro/Nanolitho. MEMS MOEMS*, 2018, **17**, 7.
39. E. Reichmanis, O. Nalamasu and F. M. Houlihan, "Organic Materials Challenges for 193 nm Imaging", *Acc. Chem. Res.*, 1999, **32**, 659-667.
40. S.-Y. Moon and J.-M. Kim, "Chemistry of photolithographic imaging materials based on the chemical amplification concept", *J. Photochem. Photobiol., C*, 2007, **8**, 16.
41. W. Conley and H. Ito, "Chemically amplified resists: past, present, and future", *Proc. SPIE*, 1999, **3678**, 3678-3672.
42. S. Kruger, S. Revuru, C. Higgins, S. Gibbons, D. A. Freedman, W. Yueh, T. R. Younkin and R. L. Brainard, "Fluorinated Acid Amplifiers for EUV Lithography", *J. Am. Chem. Soc.*, 2009, **131**, 9862-9863.
43. S. A. Kruger, C. Higgins, B. Cardineau, T. R. Younkin and R. L. Brainard, "Catalytic and Autocatalytic Mechanisms of Acid Amplifiers for Use in EUV Photoresists", *Chem. Mater.*, 2010, **22**, 5609-5616.
44. E. Hassanein, C. Higgins, P. Naulleau, R. Matyi, G. Gallatin, G. Denbeaux, A. Antohe, J. Thackeray, K. Spear, C. Szmanda, C. N. Anderson, D. Niakoula, M. Malloy, A. Khurshid, C. Montgomery, E. C. Piscani, A. Rudack, J. Byers, A. Ma, K. Dean and R. Brainard, "Film quantum yields of ultrahigh PAG EUV photoresists", *Proc. SPIE*, 2008, **6921**, 69211I01-13.
45. T. Fujii, S. Matsumaru, T. Yamada, Y. Komuro, D. Kawana and K. Ohmori, "Patterning performance of chemically amplified resist in EUV lithography", *Proc. SPIE*, 2016, **9776**, 97760Y01-06.
46. J. L. Sturtevant, G. M. Schmid, M. D. Stewart, C.-Y. Wang, B. D. Vogt, V. M. Prabhu, E. K. Lin and C. G. Willson, "Resolution limitations in chemically amplified photoresist systems", *Proc. SPIE*, 2004, **5376**, 333-342.
47. B. D. Vogt, S. Kang, V. M. Prabhu, A. Rao, E. K. Lin, W.-l. Wu, S. K. Satija and K. Turnquest, "Influence of base additives on the reaction-diffusion front of model chemically amplified photoresists", *J. Vac. Sci. Technol., B: Microelectron. Nanometer Struct.--Process., Meas., Phenom.*, 2007, **25**, 175-182.
48. S. Nagahara, L. Yuan, W. J. Poppe, A. Neureuther, Y. Kono, A. Sekiguchi, K. Fujiwara, T. Watanabe, K. Taira, S. Kusumoto, T. Nakano and T. Shimokawa, "Understanding quencher mechanisms by considering photoacid-dissociation equilibrium in chemically amplified resists", *Microlithography*, 2005, **5753**, 338-349.
49. Y. Komuro, H. Yamamoto, K. Kobayashi, Y. Utsumi, K. Ohomori and T. Kozawa, "Acid generation mechanism in anion-bound chemically amplified resists used for extreme ultraviolet lithography", *Jpn. J. Appl. Phys.*, 2014, **53**, 11650301-11650308.
50. R. Hirose, T. Kozawa, S. Tagawa, D. Shimizu, T. Kai and T. Shimokawa, "Difference between Acid Generation Mechanisms in Poly(hydroxystyrene)- and Polyacrylate-Based Chemically Amplified Resists upon Exposure to Extreme Ultraviolet Radiation", *Jpn. J. Appl. Phys.*, 2008, **47**, 7125-7127.

51. H. Yamamoto, H. Kudo and T. Kozawa, "Study on resist performance of chemically amplified molecular resists based on cyclic oligomers", *Microelectron. Eng.*, 2015, **133**, 16-22.
52. J. Torok, R. Del Re, H. Herbol, S. Das, I. Bocharova, A. Paolucci, L. E. Ocola, C. Ventrice Jr, E. Lifshin, G. Denbeaux and R. L. Brainard, "Secondary Electrons in EUV Lithography", *J. Photopolym. Sci. Technol.*, 2013, **26**, 625-634.
53. R. Gronheid, T. R. Younkin, M. J. Leeson, C. Fonseca, J. S. Hooge, K. Nafus, J. J. Biafore and M. D. Smith, "EUV secondary electron blur at the 22nm half pitch node", *Proc. SPIE*, 2011, **7969**, 79690401-11.
54. J. Paula, M. Rudolpha, S. Riedela, S. Wegeb, C. Hohlec and V. Beyerc, "Advanced Dual Hard Mask Patterning Scheme to Enable High Resolution Lithography for sub 30 nm Technology Nodes", *ECS Meet. Abstr.*, 2012, **MA2012-02**, 2928.
55. D. De Simone, A.-M. Goethals, F. V. Roey, T. Zhang, P. Foubert, E. Hendrickx, G. Vandenberghe and K. Ronse, "Progresses and Challenges of EUV Lithography Materials", *J. Photopolym. Sci. Technol.*, 2014, **27**, 601-610.
56. S. Chakrabarty, C. Ouyang, M. Krysak, M. Trikeriotis, K. Cho, E. P. Giannelis and C. K. Ober, "Oxide nanoparticle EUV resists: toward understanding the mechanism of positive and negative tone patterning", *Proc. SPIE*, 2013, **8679**, 86790601-08.
57. S. Chakrabarty, C. Sarma, L. Li, E. P. Giannelis and C. K. Ober, "Increasing sensitivity of oxide nanoparticle photoresists", *Proc. SPIE*, 2014, **9048**, 90481C01-05.
58. J. Jiang, S. Chakrabarty, M. Yu and C. K. Ober, "Metal Oxide Nanoparticle Photoresists for EUV patterning", *J. Photopolym. Sci. Technol.*, 2014, **27**, 4.
59. L. Li, S. Chakrabarty, J. Jiang, B. Zhang, C. Ober and E. P. Giannelis, "Solubility studies of inorganic-organic hybrid nanoparticle photoresists with different surface functional groups", *Nanoscale*, 2016, **8**, 1338-1343.
60. L. Li, S. Chakrabarty, K. Spyrou, C. K. Ober and E. P. Giannelis, "Studying the Mechanism of Hybrid Nanoparticle Photoresists: Effect of Particle Size on Photopatterning", *Chem. Mater.*, 2015, **27**, 5027-5031.
61. M. Trikeriotis, M. Krysak, Y. S. Chung, C. Ouyang, B. Cardineau, R. Brainard, C. K. Ober, E. P. Giannelis and K. Cho, "A new inorganic EUV resist with high-etch resistance", *Proc. SPIE*, 2012, **8322**, 83220U.
62. S. Castellanos, L. Wu, M. Baljozovic, G. Portale, D. Kazazis, M. Vockenhuber, Y. Ekinci and T. Jung, "Ti, Zr, and Hf-based molecular hybrid materials as EUV photoresists", *Proc. SPIE*, 2018, **10583**, 105830A.
63. R. T. Frederick, J. M. Amador, S. Goberna-Ferrón, M. Nyman, D. A. Keszler and G. S. Herman, "Mechanistic Study of HafSOx Extreme Ultraviolet Inorganic Resists", *J. Phys. Chem. C*, 2018, **122**, 16100-16112.
64. R. Frederick, T. Diulus, D. Hutchison, M. Nyman and G. S. Herman, "Effect of Oxygen on Thermal and Radiation Induced Chemistries in a Model Organotin Photoresist", *ACS Appl. Mater. Interfaces*, 2019, DOI: 10.1021/acsami.8b16048.

65. R. T. Frederick, S. Saha, J. Trey Diulus, F. Luo, J. M. Amador, M. Li, D.-H. Park, E. L. Garfunkel, D. A. Keszler and G. S. Herman, "Thermal and radiation chemistry of butyltin oxo hydroxo: A model inorganic photoresist", *Microelectron. Eng.*, 2019, **205**, 26-31.
66. H. Xu, K. Sakai, K. Kasahara, V. Kosma, K. Yang, H. C. Herbol, J. Odent, P. Clancy, E. P. Giannelis and C. K. Ober, "Metal–Organic Framework-Inspired Metal-Containing Clusters for High-Resolution Patterning", *Chem. Mater.*, 2018, **30**, 4124-4133.
67. M. Sortland, R. Del Re, J. Passarelli, J. Hotalen, M. Vockenhuber, Y. Ekinci, M. Neisser, D. Freedman and R. L. Brainard, "Positive-tone EUV resists: complexes of platinum and palladium", *Proc. SPIE*, 2015, **9422**, 9422-9427.
68. J. Passarelli, M. Murphy, R. Del Re, M. Sortland, J. Hotalen, L. Dousharm, R. Fallica, Y. Ekinci, M. Neisser, D. A. Freedman and R. L. Brainard, "Organometallic carboxylate resists for extreme ultraviolet with high sensitivity", *J. Micro/Nanolitho. MEMS MOEMS*, 2015, **14**, 043503.
69. R. Del Re, J. Passarelli, M. Sortland, B. Cardineau, Y. Ekinci, E. Buitrago, M. Neisser, D. A. Freedman and R. L. Brainard, "Low-line edge roughness extreme ultraviolet photoresists of organotin carboxylates", *J. Micro/Nanolitho. MEMS MOEMS*, 2015, **14**, 043506.
70. B. Cardineau, R. Del Re, M. Marnell, H. Al-Mashat, M. Vockenhuber, Y. Ekinci, C. Sarma, D. A. Freedman and R. L. Brainard, "Photolithographic properties of tin oxo clusters using extreme ultraviolet light (13.5nm)", *Microelectron. Eng.*, 2014, **127**, 44-50.
71. E. Buitrago, R. Fallica, D. Fan, T. S. Kulmala, M. Vockenhuber and Y. Ekinci, "SnOx high-efficiency EUV interference lithography gratings towards the ultimate resolution in photolithography", *Microelectron. Eng.*, 2016, **155**, 44-49.
72. E. Buitrago, M. Meeuwissen, O. Yildirim, R. Custers, R. Hoefnagels, G. Rispens, M. Vockenhuber, I. Mochi, R. Fallica, Z. Tasdemir and Y. Ekinci, "State-of-the-art EUV materials and processes for the 7 nm node and beyond", *Proc. SPIE*, 2017, **10143**, 10143-10148.
73. S. T. Meyers, J. T. Anderson, J. B. Edson, K. Jiang, D. A. Keszler, M. K. Kocsis, A. J. Telecky and B. Cardineau, *US patent US 9310684B2*, 2016.
74. S. T. Meyers, J. T. Anderson, J. B. Edson, K. Jiang, D. A. Keszler, M. K. Kocsis, A. J. Telecky and B. Cardineau, *US 2016/0116839 A1*, 2015.
75. W. D. Hinsberg and S. Meyers, "A numeric model for the imaging mechanism of metal oxide EUV resists", *Proc. SPIE*, 2017, **10146**, 101460401-11.
76. R. Fallica, J. K. Stowers, A. Grenville, A. Frommhold, A. P. G. Robinson and Y. Ekinci, "Dynamic absorption coefficients of chemically amplified resists and nonchemically amplified resists at extreme ultraviolet", *J. Micro/Nanolitho. MEMS MOEMS*, 2016, **15**, 03350601-07.
77. B. Cardineau, in *Frontiers of Nanoscience*, eds. A. Robinson and R. Lawson, Elsevier, 2016, **11**, 377-420.
78. H. H. Park, W. L. Law, X. Zhang, S. Y. Hwang, S. H. Jung, H. B. Shin, H. K. Kang, H. H. Park, R. H. Hill and C. K. Ko, "Facile size-tunable fabrication of

functional tin dioxide nanostructures by multiple size reduction lithography", *ACS Appl. Mater. Interfaces*, 2012, **4**, 2507-2514.

79. R. Del Re, M. Sortland, J. Passarelli, B. Cardineau, Y. Ekinci, M. Vockenhuber, M. Neisser, D. A. Freedman and R. L. Brainard, "Low-LER tin carboxylate photoresists using EUV", *Proc. SPIE*, 2015, **9422**, 94222101-10.
80. E. C. Mattson, Y. Cabrera, S. M. Rupich, Y. Wang, K. A. Oyekan, T. J. Mustard, M. D. Halls, H. A. Bechtel, M. C. Martin and Y. J. Chabal, "Chemical Modification Mechanisms in Hybrid Hafnium Oxo-methacrylate Nanocluster Photoresists for Extreme Ultraviolet Patterning", *Chem. Mater.*, 2018, **30**, 6192-6206.
81. N. Hollingsworth, G. A. Horley, M. Mazhar, M. F. Mahon, K. C. Molloy, P. W. Haycock, C. P. Myers and G. W. Critchlow, " Tin(II) aminoalkoxides and heterobimetallic derivatives: the structures of $Sn_6(O)_4(dmae)_4$, $Sn_6(O)_4(OEt)_4$ and $[Sn(dmae)_2Cd(acac)_2]_2$", *Appl. Organomet. Chem.*, 2006, **20**, 687-695.
82. J. Jiang, J. Liang, S. Zhao, Y. Wang, J. Qi, Y. Huang, T. Xiong and D. Zhu, "Syntheses, Crystal Structures and Luminescent Properties of Drum and Ladder-Like Organooxotin Clusters with Carbazole Ligand", *J. Cluster Sci.*, 2016, **28**, 971-982.
83. S. Kundu, R. K. Metre, R. Yadav, P. Sen and V. Chandrasekhar, "Multi-pyrene assemblies supported on stannoxane frameworks: synthesis, structure and photophysical studies", *Chem. Asian. J.*, 2014, **9**, 1403-1412.
84. L. C. Dias, G. M. de Lima, J. A. Takahashi and J. D. Ardisson, "New di- and triorganotin(IV) carboxylates derived from a Schiff base: synthesis, characterization andin vitroantimicrobial activities", *Appl. Organomet. Chem.*, 2015, **29**, 305-313.
85. C. J. M. van der Kerk, in Organotin Compounds: New Chemistry and Applications, ACS publishing, 1976, 1-25.
86. M. A. Champ, "A review of organotin regulatory strategies, pending actions, related costs and benefits", *Sci. Total Environ.*, 2000, **258**, 21-71.
87. H. Puff, H. Reuter, "Zur hydrolyse von Monoorganylzinn-trihalogeniden III. Isolierung und Röntgenstrukturanalyse von Verbindungen mit dem neuartigen Käfig-ion $[(i\text{-}PrSn)_{12}O_{14}(OH)_6]^{2+}$", *J. Organomet. Chem.,* 1989, ***373***, 173-184.

Chapter 2

Experimental methods

This chapter describes the experimental methods used in the research described in this thesis. This includes preparation of photoresist thin film samples, their exposure to electron beams and to deep ultraviolet (DUV) and extreme ultraviolet (EUV) light, and characterization of the films before and after exposure. In most of the work, we focus on tin-oxo cage molecules as photoresist models, as discussed in Chapter 1. These compounds were synthesized in our laboratory by Jarich Haitjema. In Chapter 9, commercial tin(II)carboxylates are explored.

Photoresist samples are prepared as thin films on flat and smooth substrates by means of spin coating. Different substrates are used depending on the application or the analysis method to be used: quartz substrates, which are UV-transparent, are used for UV-vis absorption spectroscopy; double side polished Si wafers and CaF_2 substrates, which are IR-transparent, are used for FTIR spectroscopy; bare Si wafers or Si wafers coated with HMDS are used as substrate for patterning; Si wafers coated with Cr (2 nm) and Au (18 nm) as conductive substrate are used for X-ray photoelectron spectroscopy. The topography and the surface roughness of the sample are characterized using atomic force microscopy (AFM). After the thin film is prepared, various exposure methods are used to investigate the response of the photoresist. For 225 nm deep ultra violet (DUV) exposure a laser was used, or Laser Driven Light Source System with a monochromator. Extreme ultraviolet (EUV) radiation (13.5 nm; 92 eV) was obtained from the EUV interference lithography tool at the Swiss Light Source XIL-II beamline (Paul Scherrer institute, PSI, Villigen, Switzerland). For electron beam exposure (E-beam) an e-beam lithography tool was used. After development and other follow-up processes such as rinse, post exposure bake (PEB), and hard bake (HB), the patterns of the photoresists were characterized by using AFM and scanning electron microscopy. In order to gain information on the photochemical conversion in the photoresist, UV-vis spectroscopy, IR spectroscopy, mass spectrometry, and photoelectron spectroscopy were used to characterize the chemical properties of the photoresist both before and after EUV/DUV exposure. Combining the above characterization methods, the properties and the chemical changes of the photoresist were evaluated. In this chapter, we briefly introduce the working principles and implementations of the most important tools and techniques used in this research.

2.1 Spin coater

As it was explained in Chapter 1, photoresists materials are applied as thin films on a substrate by spin coating. Typically, the film thickness required is several tens of nanometers. Ideally, the surface roughness (R_q) of the photoresist thin film should be below 0.5 nm, due to the requirement to write high-resolution patterns on it. In order to meet this requirement, different spin coating parameters need to be optimized, such as the spin coating speed, acceleration, spinning time, solvent, and surface tension of the substrate.

Spin coating has been widely used in the semiconductor industry as a method to prepare uniform thin films on flat substrates. The photoresist material is dissolved in an organic solvent and a certain amount of the solution is applied on the substrate. The spin coater accelerates the substrate to a high rotation speed, and the majority of the solution will be flung off the substrate. At the same time, the high-speed airflow above the substrate can remove the remaining solvent from the thin film and leave the photoresist layer. Using this simple and easy method, a homogeneous, uniform thin film of photoresist can be deposited on the substrate. The spin coating process is illustrated in Scheme. 2.1.[1]

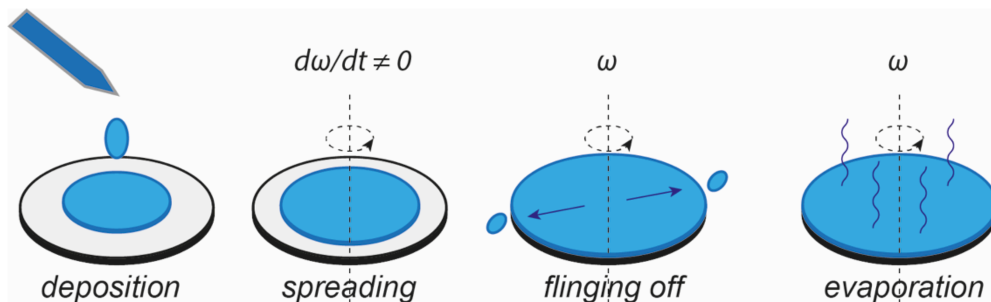

Scheme 2.1. *Spin coating process.*

The film thickness (l) is proportional to the concentration of the solution (c) and to the inverse square root of the spinning speed (angular velocity) ($1/\sqrt{\omega}$). Compared with the spinning speed, the concentration of the solution plays a more important role in determining the film thickness obtained. The spin speeds chosen determine the range of the film thickness that can be realized from a certain solution. The film thickness will also depend on the solvent viscosity, vapor pressure, local temperature and humidity. Therefore, the film thickness curve of a certain material is determined empirically. At low concentrations, the film thickness depends approximately linearly on the solution concentration. In this thesis, we prepared the tin-oxo cages into thin films for different purposes; we mainly controlled the concentration of the solution. Here, we use the tin-oxo cages with hydroxide

counterion (TinOH) as an example. The compound is a powder that was dissolved in toluene at different concentrations and spin coated with the same spin coating parameters (acceleration 700 rpm s^{-1}, final speed 2500 rpm for 35 s) on the Si substrate. The relationship between the film thickness and the solution concentration as determined using AFM (section 2.2), is shown in Fig. 2.1. Importantly, we find that the spin coating procedure is well reproducible, also on different spin coaters in different laboratories.

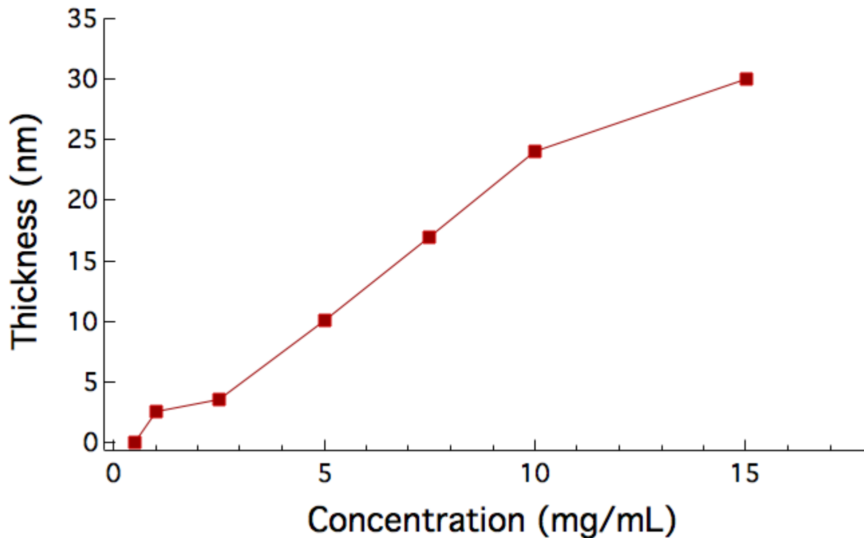

Figure 2.1. *Thickness of TinOH films vs. concentration (in toluene) for a fixed set of spin coating parameters.*

2.2 AFM

The topography and the surface roughness of the sample are usually characterized by means of atomic force microscopy (AFM). AFM is a high-resolution imaging technique with a small probe (tip) scanning back and forth in a controlled manner across a sample to measure the surface topography at up to atomic resolution. A laser beam deflection system is equipped in AFM, where a laser is reflected from the back of the reflective AFM cantilever onto a position-sensitive detector. AFM relies on the forces between the tip and the sample surface, by measuring the deflection of the cantilever. The force (F) can be calculated by using Hooke's law (eq. 2.1) where z indicates the bending, and k the stiffness of the cantilever.[2]

$$F = -kz \quad (2.1)$$

There is a feedback loop using the laser deflection to control the force and tip position. As the tip interacts with the sample surface, either controlling the force F

(corresponding to contact mode) or the position *z* (corresponding to tapping mode), the laser position on the detector can be used in the feedback loop to trace the surface topography and generate images. The working principle of AFM is shown in Scheme 2.2.

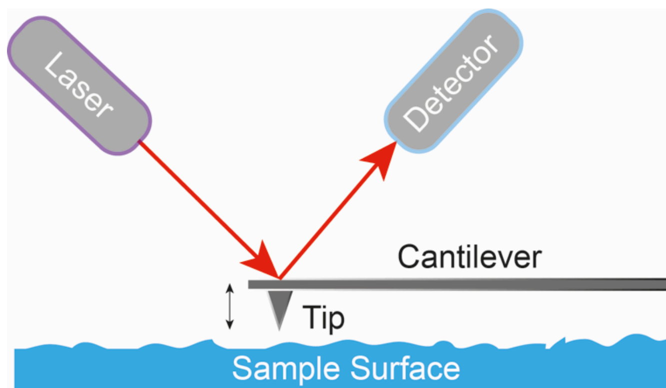

Scheme 2.2. *Schematic for Atomic Force Microscopy.*

In our experiments we used the ScanAsyst-Air mode with a silicon tip on a Nitride cantilever in Bruker Dimension Icon AFM. The ScanAsyst mode is developed based on the Peakforce tapping mechanism, which decouples cantilever response from resonance dynamics, to adjust all critical imaging parameters automatically.

The film prepared from spin coating can be characterized by AFM. To measure the film thickness, a scratch is made through the thin film, and AFM is used to scan across the edge of the scratch. The surface roughness of the thin film, which is characterized as the root-mean square roughness (R_q), also needs to be controlled in the thin film preparation procedure and can be derived from AFM measurement. The chemical compatibility of the substrate and the solution is important for the formation of a smooth spin-coated film. When the solvent and the substrate are both hydrophobic or hydrophilic, the solution will spread across the surface.[1] To illustrate this, solutions of TinOH in different solvents (isopropanol, 2-butanol and toluene) were spin-coated on silicon with a native oxide layer (hydrophilic) and on a silicon/silicon oxide substrate that was previously allowed to react with hexamethyldisilazane (HMDS) to make it hydrophobic. The surface topography of the different samples was imaged with AFM as shown in Fig. 2.2.

As is shown in Fig. 2.2, the topographies of the TinOH thin films under different preparation conditions are quite different. Comparing the three samples in a), b) and c), in polar solvent as IPA and 2-butanol, the topography of the thin film looked really rough and seems to form crystallized structures in a), and holes in b). In c) the surface also shows some larger structures, but the surface roughness and height

difference are smaller than in a) and b). Based on the condition in c), we tried to optimize the process again. Firstly, a post apply bake step (PAB) was added and afterwards the topography is shown in d). The height difference becomes smaller, but the large structure was still observed. A further optimization was done on the substrate. By modifying the substrate to make it very hydrophilic using oxygen plasma treatment or hydrophobic using HMDS, the final surface roughness of the sample was improved significantly to $R_q < 0.5$ nm as shown in e) and f). The possible reason could be that the tin-oxo cages contain hydrophobic components (butyl chains) and hydrophilic groups, which help it deposit on hydrophobic/hydrophilic surface homogeneously. Since the HDMS treatment is easier to apply, we used this method to prepare thin films for all further experiments, such as to test the tin-oxo cages performance under EUV/DUV/E-beam lithography.

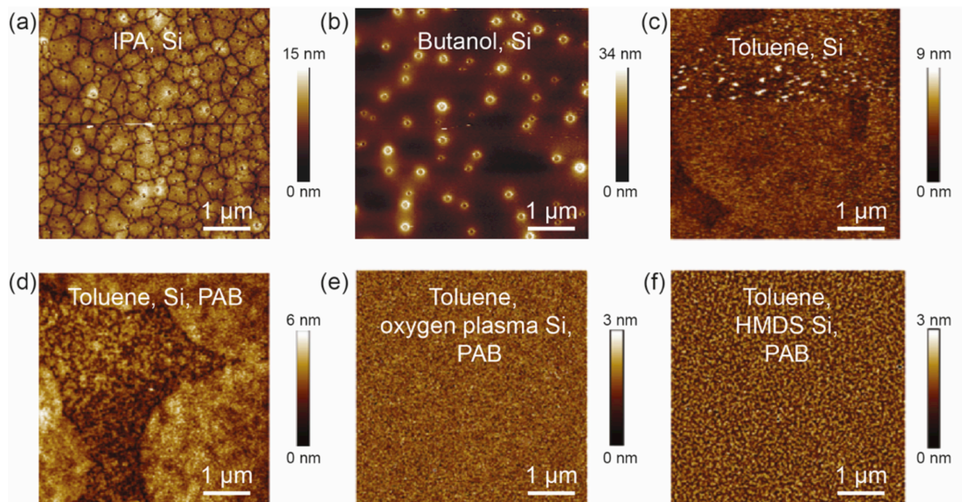

Figure 2.2. *Topography of TinOH films (a-d) on a non-treated Si substrate prepared from solutions (a) in isopropanol (IPA), (b) in butanol, (c) in toluene, (d) in toluene followed by a post application bake (PAB) step; (e) on oxygen plasma treated Si wafer in toluene and followed by a PAB step, (f) on HMDS surface treated Si wafer in toluene with PAB.*

2.3 E-beam lithography

Electron-beams are often used as a surrogate for other high-energy radiation patterning, because when using high energy photons the chemical changes are caused mostly by secondary electrons, as discussed in Chapter 1, which are also the main chemical agents arising from electron beam irradiation. In this work, E-beam lithography was performed using the Raith Voyager at the Amsterdam Nanocenter (AMOLF). The beam energy was up to 50 keV and the current range was from 50

pA to 40 nA. The beam size can be less than 2.5 nm. E-beam lithography was used to test the dual-tone pattern performance of the tin-oxo cages resist in Chapter 8.

2.4 EUV interference lithography

As mentioned above, we use extreme ultra violet interference lithography as a patterning method to test the performance of the tin-oxo cages as EUV photoresists. After preparing the photoresist amorphous thin film, the photoresist layer can be exposed to the interference pattern of coherent beams that form a parallel wave and hence an optical pattern featuring intensity peaks and valleys. In this research, we used the EUV interference lithography tool at the Swiss Light Source XIL-II beamline (Paul Scherrer institute, PSI, Villigen, Switzerland).[3-5] The working principle of EUV interference lithography is described in references [3, 4]. The incident beam from the synchrotron source passes through two diffracting gratings (Cr/Mo based) on the Si_3N_4 membrane, generating the interference pattern from the two first-order diffracted beams on the photoresist layer. The dose on the mask and the dose on the sample can be measured and controlled. The scheme of the two-beam EUV transmission-diffraction interference lithography method for patterning line-space structure is shown in Scheme 2.3.

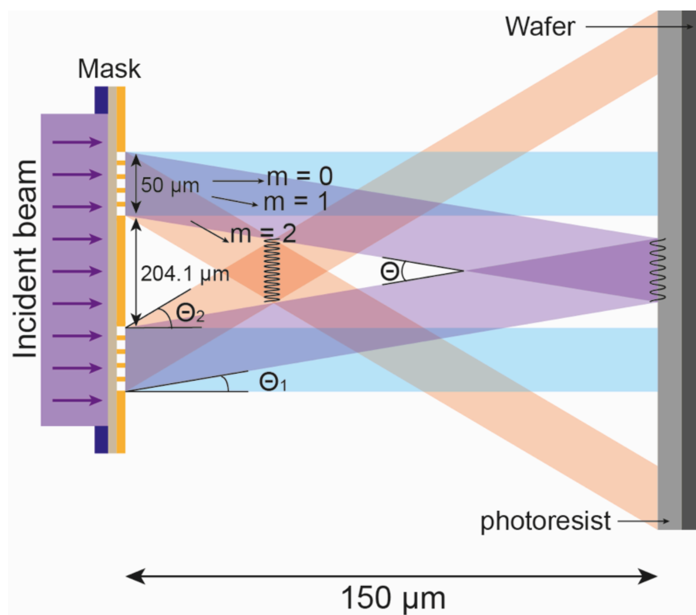

Scheme 2.3. *EUV interference lithography. Only the 1st and 2nd order diffractions interfering beams at angles Θ_1 and Θ_2 are illustrated. The diffracted beams that diverge are omitted here.[3] The physical dimension is depending on the specific mask; here we use an example from reference 6.*

As explained in reference 5, when the incident beam arrives at the mask and passes through the grating, it is diffracted by each grating in certain angles Θ_m given by:

$$sin\Theta_m = m\lambda/P_g \quad (2.2)$$

In eq. 2.2 m is the diffraction order and P_g is the grating periodicity. When the two gratings are illuminated with the same intensity, in the area where the diffracted beams interfere the periodicity (pitch) P of the aerial image is given by eq. 2.3.

$$P = \frac{\lambda}{2\sin\left(\frac{\Theta}{2}\right)} \quad (2.3)$$

Since λ = 13.5 nm, the pitch can be as small as ~7 nm, which is half of the wavelength. In equation 2.3, Θ is the angle between the two diffracted beams and in the case of two beams as in Fig. 4, $\Theta = 2\Theta_m$, and therefore, combining equations 2.2 and 2.3, we arrive at equation 2.4.

$$P = P_g/2m \quad (2.4)$$

The size and shape of the exposed pattern is the same as the size and shape of the gratings, but the line pattern of the grating is demagnified. It is common practice to describe the resolution of a lithography method by the half pitch (*HP*) of the pattern it generates. In the interference lithography with $m = 1$, the resolution of the pattern will be $HP = P_g/4$. For example: $P_g = 72$ nm gratings on mask can make a $HP = 18$ nm structure on wafer. Thus, in addition to the incident beam wavelength, which is determined by the light source, the line spacing of the grating is another essential component for high-resolution interference lithography.

The photon flux of the beam is between 20 and 50 mW cm^{-2}. By controlling the exposure time, the dose on the sample can be controlled. The exposure is done in the end station chamber with 10^{-7} mbar vacuum. High resolution patterns with 6 nm half pitch have been demonstrated in this set up.[6]

2.5 DUV exposure

A YAG-pumped OPA laser (Ekspla NT342B, University of Amsterdam), delivering nanosecond pulses at 225 nm at 10 Hz (2.5 mJ/pulse) was used as the irradiation source. The irradiated spot was approximately round, with an area of around 0.2 cm^{-2}. Alternatively, a continuous light source was used consisting of an Energetiqs EQ-99X Laser Driven Light Source System with a TRIAX190 monochromator. Using a band pass of 10 nm, this delivers 0.2 mW cm^{-2} at the sample.

2.6 Scanning Electron Microscopy

After development and other subsequent processes (such as rinse, post exposure bake, and hard bake), the patterns' quality on the different photoresists was evaluated by means of scanning electron microscopy (SEM). The SEM generates images by scanning the sample with a high-energy beam of electrons. As the electrons interact with the sample they produce secondary electrons, backscattered electrons, Auger electrons, characteristic X-rays and cathodoluminescence. Usually, the secondary electrons or the backscattered electrons are collected by detectors and the resulting signals are converted into images. The SEM schematic is shown in Scheme 2.4.

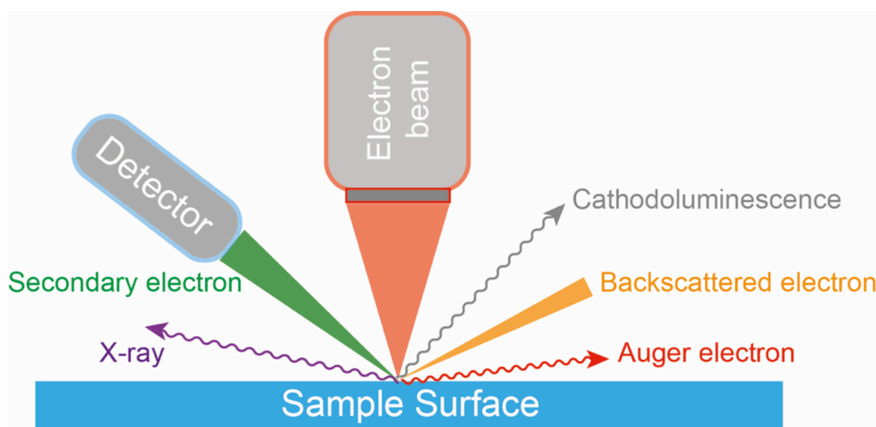

Scheme 2.4. *Schematic of a SEM.*

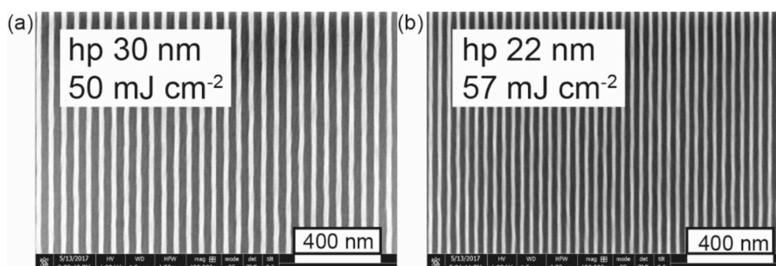

Figure 2.3. *SEM images of TinOH photoresist patterned by means of EUV interference lithography.*

In this work, SEM was performed on a FEI Verios 460 at Amsterdam nanocenter (AMOLF). In addition to AFM, which is mainly the tip diameter that limits the measurement accuracy,[7] SEM was used to characterize the line patterns of the photoresist. A significant issue of SEM is the sensitivity of photoresist to beam damage.[8, 9] To decrease the damage caused by the electrons on the photoresist

pattern while scanning, all the SEM in this thesis is taken at a relatively low acceleration potential of 1 kV and a moderate current of 50 nA. The SEM is used to characterize the pattern generated from the EUV interference lithography, and an example is shown in Fig. 2.3.

2.7 X-ray Photoelectron Spectroscopy

In order to obtain information on the chemical conversion in the photoresists thin film upon irradiation, extremely sensitive analysis techniques are required. X-ray photoelectron spectroscopy (XPS) is a widely used surface-sensitive technique and it plays a key role in the research described in this thesis.[10] It can be applied to a broad range of materials and can provide quantitative chemical state data of the samples.

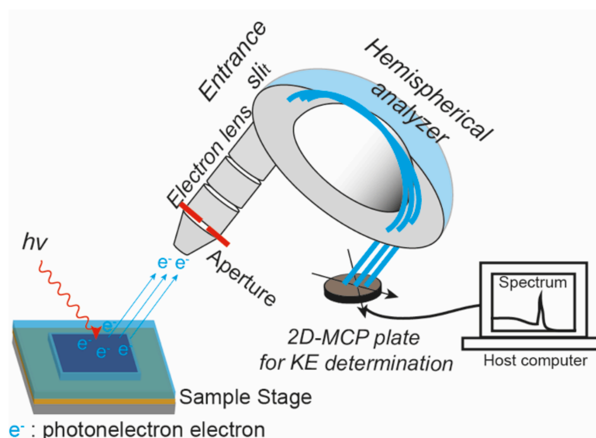

Scheme 2.5. *The basic components of an XPS instrument.*

The components of an XPS instrument are shown in Scheme 2.5. An XPS instrument essentially is composed of an X-ray source, electron extraction optics and energy filter (bandpass filter), and a detection system. The X-ray source used should have sufficient photon energy to access a proper number of core level electrons. The commonly used X-ray sources are Al Kα and Mg Kα emission sources, and synchrotron radiation. When X-rays hit the sample, photoelectrons are ejected with a series of energies and directions. The electron optics consisting of a set of electrostatic and/or magnetic lens units can collect a portion of these emitted electrons, and those electrons are transferred through the apertures. Electrostatic fields are set within the hemispherical analyzer to only allow electrons of a certain energy (pass energy) to reach the detector slits and onto the microchannel plate which is for E_{kin} determination. In order to increase the energy resolution, it is common that electrons are already decelerated with a band pass filter before they are directed to the hemispherical analyzer. The signals are transferred as spectra on

the host computer.[11] In this thesis, to characterize chemical changes in the photoresists upon EUV/DUV exposure we used two XPS instruments with a monochromatic Al Kα X-ray source (1.5 keV photon energy) at PSI (Surface Science Lab) and at ARCNL/AMOLF. Both instruments used a hemispherical energy analyzer: a SPECS Analyzer Phoibos 150 in the PSI Surface Science Lab, and a SCIENTA HIPP-3 at ARCNL/AMOLF.

When the X-ray beam is directed onto the sample, the X-ray photon energy can be absorbed by the core level electrons in the atoms. When the core-level electrons get enough energy from the photon, they will escape from the atoms. Most of the photo-emitted electrons can undergo inelastic collisions, recombination, recapture or trapping in different excited states within the sample, which can reduce the number of escaping photoelectrons. Only a small fraction of the electrons can escape from the sample surface with a certain kinetic energy E_{kin}, which can be measured by the electron spectrometer (detector). The binding energy E_{bind} of the emitted electrons can be determined by using the Einstein relationship, equation 2.5:

$$E_{bind} = E_{photon} - (E_{kin} + \psi) \tag{2.5}$$

In eq. 2.5 E_{bind} is the binding energy of the electron, E_{photon} is the energy of the X-ray photon, E_{kin} is the kinetic energy of the electron, which is measured by the instrument, and ψ is the combined work function of the spectrometer and the sample. The work function of the spectrometer is constant for a given spectrometer and can be quantified by a specific calibration by using a clean gold foil as a reference. The gold is used as reference because it is a conducting material and the measured values do not need to have an added charge correction to the reported values.[12] Contrarily, for non-conductive samples, photoelectron emission leads to surface charging, which can affect the sample work function. As the photoelectrons are ejected, positive charge can build up at the sample surface and shift the E_{kin} values. When the surface charge is stable and uniform, one practical way is to use the binding energy of C 1s from carbon species involved in C-C or C-H (285.0 eV) bonds or the binding energy of Au 4f from a gold coating (84.0 eV) as an internal standard to correct all the measured E_{bind}.[13]

Since each core-level electron has its unique binding energy, all the elements except hydrogen and helium can be identified by this technique through the binding energy measurement. The binding energy of the core-level electron is sensitive to the chemical environment. In this thesis, the XPS spectra were calibrated according to the Au $4f_{7/2}$ peak from a gold foil or the C 1s peak from hydrocarbon bonds as mentioned above before the different spectra were compared to each other to measure relative peak shifts. The schematic of XPS is shown in Scheme 2.6.

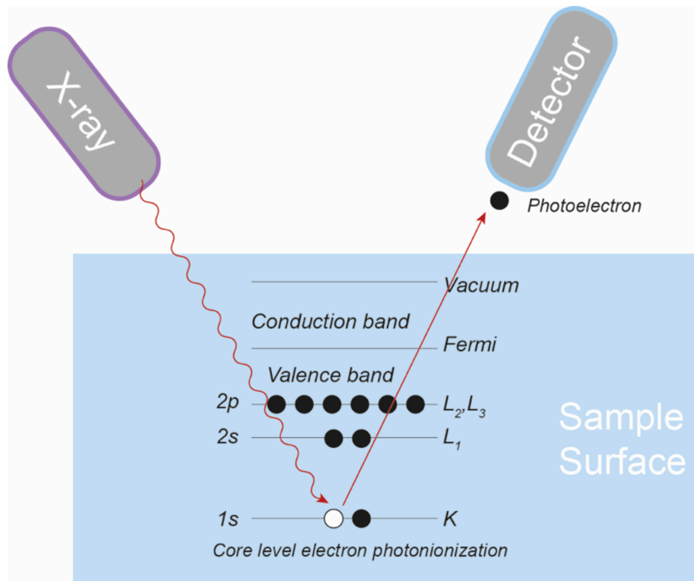

Scheme 2.6. *Mechanism of X-ray photoelectron spectroscopy.*

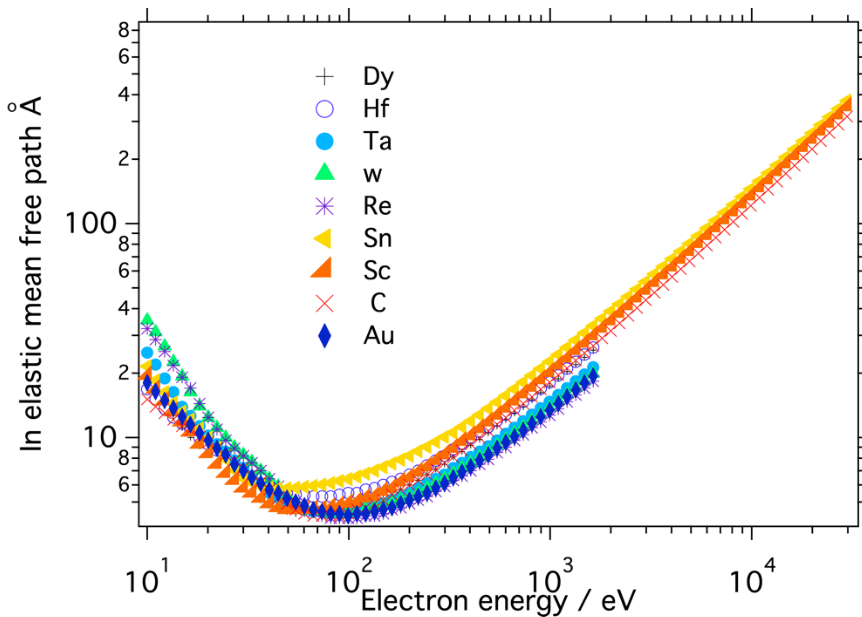

Figure 2.4. *Inelastic mean free path of electrons as a function of the electron kinetic energy in different solids.*[14-17]

The photoelectrons generated in the sample during XPS experiments with a certain kinetic energy can only travel a limited distance, which means that only the electrons emitted and escaped from near the surface of the sample can be detected. The characteristic depth *d* from which the emitted photoelectrons reach the detector

is called escape depth.[14, 15] When the effect from elastic electron scattering are negligible, the escape depth (ED) can be simplified as the product of the inelastic mean free path (IMFP) and cosine of electron emission angle.[17, 18] Since the emission angle is fixed for each measurement, the ED is proportional to the IMFP. The IMFP of electrons as a function of the E_{kin} in different solids is shown in Fig. 2.4.[16, 17] Based on the relationship in Fig. 2.4 and equation 2.5, with the photon energy increasing, E_{bind} is constant, and E_{kin} is increased in the same way as the photon energy. When E_{kin} increased, the mean free path of the electrons and, accordingly, the escape depth are also increased significantly.[19, 20]

When 1.5 keV X-ray condition is used, the maximum escape depth is around 5 nm from the sample surface, and thus only electrons within this depth can escape into the vacuum and be detected by the electron spectrometer. All the samples for XPS are prepared as thin films of ca. 20 nm thickness on 1 × 1 cm^2 substrate. To fulfill the conductivity requirement, all the substrates are pre-coated with 2 nm Cr and 18 nm Au. At PSI, the X-ray beam size is around 2 × 2 mm^2, which is a large area and allows to collect photoelectrons from almost the whole sample surface. At AMOLF, the X-ray beam size is around 100 μm^2. All the spectra were recorded in the transmission mode of the hemispherical analyzer. In order to compare the data with different photon energies and different equipment, the relative sensitivity factors are considered during data analysis as described below in section **2.9**.

2.8 Low dose photoelectron spectroscopy

The synchrotron based low dose photoelectron spectroscopy (Low dose PES) at the PM4 beam line (BESSY-II, Helmholtz-Zentrum-Berlin) is used for recording photoelectron spectra with excitation at relatively low photon energies.[21] It also allows us to expose the sample to EUV radiation and measure the XPS *in situ*. We made use of an angle-resolved time of flight (ArTOF) detector, which due to its high transmission (around 13%) allows for ~1000 times faster acquisition times and reduced dose rates compared to a traditional hemispherical analyzer, without losing the energy resolution.[22] In ArTOF, the full acceptance cone of the electron lens is used and a time resolved 2D detector is placed at the end of the lens where the angular pattern is projected. This design allows the simultaneous measurement of two coordinates x and y and the arrival time of the electron. When all the parameters are known with high precision, the trajectory and the corresponding velocity distribution along it, can be calculated with high precision. The kinetic energy of the emitted electrons and the emission angle also can be accurately determined.[22] By using the ArTOF, the sample change over time also can be monitored, because the spectra for each individual event are stored.[22]

Three plane gratings (150, 360 and 1228 l/mm) covering the photon energy ranges 7 – 1000, 18 – 2000 and 75 – 2000 eV are available in the PM4 beamline.[22] The photon energy range can be varied from 7 to 2000 eV by interchanging the gratings. A lower photon flux is used in this beamline for probing the samples in order to reduce radiation induced sample damage. In addition, it also reduces the sample charging problems of the non-conductive samples. Fig. 2.5 shows the photon flux as a function of photon energy for the three different gratings.

In the experiments at this beam line, due to technical difficulties we could only use the 360 l/mm grating, c_{ff} 1.7. Since the range of the photon energy is wider as from 17 to 2000 eV, both the EUV exposure (at 92 eV) and recording the full range photoelectron spectra (binding energy between 380 and 800 eV) can be realized directly at the same time without breaking the vacuum at this end station. By moving a slit out of the photon beam, the sample can be exposed to a higher dose of 92 eV photons, followed by high resolution XPS measurements at higher energies to trace the chemical changes in the samples without any contamination from the atmosphere.

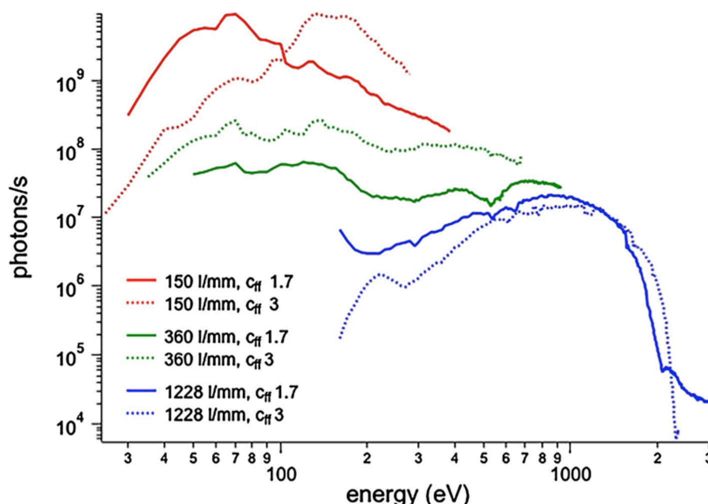

Figure 2.5. *Photon flux as a function of photon energy for the three gratings (red, green and blue colors), c_{ff} is the constant focus distance. This figure is adapted from reference 21.*

2.9 Hard X-ray photoelectron spectroscopy

The synchrotron based hard x-ray photoelectron spectroscopy (HAXPES) established at the KMC-1 beamline at the BESSY II synchrotron was also used to characterize the photoresist films. Comparing with the other XPS experiments, it provides a high photon energy from 2 to 12 keV with high photon flux of 10^{11}-10^{12}

photon s^{-1}, combined with a special electron spectrometer, the SCIENTA R-4000 hemispherical analyzer. This special electron spectrometer was designed and developed for the HAXPES and it can detect electron kinetic energies up to 15 keV and meet the high requirement of stability and resolution during the measurement. Based on Fig. 2.4, when the photon energy is around 2 - 12 keV, the probing depth could be 2 – 20 nm, it even could reach to 80 – 100 nm with porous soft materials, which means this technique with high photon energy can detect the electron from the bulk of the materials.[23] Variation of the photon energy was done to unambiguously assign spectral features to direct photoionization lines, since for the latter the electron kinetic energy increases with the incident photon energy, whereas lines arising from Auger transitions have a constant kinetic energy. The total energy resolution of the experiment, with the main contributions coming from the photon bandwidth and the electron analyzer resolution, was estimated to approx. 250 meV. The X-ray beam size is down to 100 × 100 μm^2 with power ~10 $\mu W\ cm^{-2}$, which allowed the recording of the spectrum in a few minutes without significant damage to the sample.[24] These special properties of the HAXPES open up the possibilities for the study of properties of the photoresist as thin film.[23, 25] The pressure in the experimental chamber was in the low 10^{-9} mbar range, and the samples were introduced via a load-lock chamber.

In this thesis, we mainly used 2005 eV as photon energy for HAXPES experiments. All the spectra were recorded in the transmission mode of the analyzer. The sample requirement for this measurement is the same as what has been mentioned in the XPS measurement.

For quantitative analysis of the XPS spectra, sensitivity factors (S) need to be considered, which convert the relative peak areas (I) to relative numbers of atoms (n) in the detected volume as shown in equation (2.6).[26, 27]

$$n = I/S \tag{2.6}$$

The number of photoelectrons detected per second from an orbital of constituent atoms is measured as peak area:

$$I = nf\sigma\phi yAT\beta \tag{2.7}$$

Where f is the X-ray photon flux, σ is the photoelectric cross-section, ϕ is an angular correction factor for the instrument arrangement (angle between photon path and emitted photoelectron that is detected), y is a photoelectric ground state efficiency factor, A is the area from which photoelectrons are detected, and T is the efficiency of the detection of emitted photoelectrons of that energy by the analyzer, β is the mean free path of the photoelectrons in the samples.[26, 27]

The sensitivity factor is given by:

$$S = f\sigma\phi yAT\beta \tag{2.8}$$

Seah et al. mentioned that there are three options to get the relative sensitivity factors for XPS data quantification:[27] (i) developing an own database, which is time consuming, (ii) using theoretical calculation such as the one of Seah et al.,[27] (iii) using a database such as the one based on the data from Wagner et al.[26, 28, 29] We choose the easier approach which is using the database. When the Al Kα X-ray source is used, the sensitivity factors relative to C 1s can be found from database base on Wagner et al.'s data, where they measured the data from two setups and there was a good consistency between the data from the two setups on the same compound.[26, 28, 29] When the synchrotron X-ray sources were used, regardless of the difference from the transmission function, the main difference is from the photon energy where 2005 eV is used instead of 1487 eV. We need consider the mean free path change. As shown in Fig. 2.4, the escape depths of photon electrons with different kinetic energies are different and proportional to the inelastic mean free path. At the same equipment, the electron emission angle is fixed, the larger the inelastic mean free path, the more electrons can escape to the vacuum and be detected by the analyzer. To correct the relative sensitivity factor S' with the escape depth β':

$$S' = \beta' S/\beta \tag{2.9}$$

Using the inelastic mean free path (from Fig. 2.4) of carbon and tin as example, the ratio between the inelastic mean free path of electron from carbon and Sn is around 1.19 when Al Kα X-ray source is used. The ratio is changed to 1.18 when the 2005 eV is used. Thus, in this case, there is no significant effect from the photon energy.

In this way, the XPS spectra at different photon energies can be analyzed quantitatively.

2.10 References

1. M. D. Tyona, "A theoritical study on spin coating technique", *Adv. Mater. Res.*, 2013, **2**, 195-208.
2. B. Cappela and G. Dietler, "Force-distance curves by atomic force microscopy", *Surf. Sci. Rep.*, 1999, **34**, 1–104.
3. N. Mojarad, J. Gobrecht and Y. Ekinci, "Interference lithography at EUV and soft X-ray wavelengths: Principles, methods, and applications", *Microelectron. Eng.*, 2015, **143**, 55-63.
4. N. Mojarad, M. Hojeij, L. Wang, J. Gobrecht and Y. Ekinci, "Single-digit-resolution nanopatterning with extreme ultraviolet light for the 2.5 nm technology node and beyond", *Nanoscale*, 2015, **7**, 4031-4037.

5. V. Auzelyte, D. Grützmacher, L. J. Heyderman, F. Luo, S. Olliges, C. Padeste, P. K. Sahoo, T. Thomson, A. Turchanin, C. David and H. H. Solak, "Extreme ultraviolet interference lithography at the Paul Scherrer Institut", *J. Micro/Nanolitho. MEMS MOEMS*, 2009, **8**, 02120401-10.
6. D. Fan and Y. Ekinci, "Photolithography reaches 6 nm half-pitch using EUV light", *Proc. SPIE*, 2016, **9776**, 97761V.
7. L. Azarnouche, E. Pargon, K. Menguelti, M. Fouchier, D. Fuard, P. Gouraud, C. Verove and O. Joubert, "Unbiased line width roughness measurements with Critical dimension Scaning Electron Microscopy and Critical Dimension Atomic Force Microscopy", *J. Appl. Phys.*, 2012, **111**, 084318.
8. T. Ohashi, T. Sekiguchi, A. Yamaguchi, J. Tanaka and H. Kawada, "Photoresist cross-sectional shape change caused by scanning electron microscope-induced shrinkage", *Proc. SPIE*, 2015, **14**, 14-18.
9. G. F. Lorusso, V. Rutigliani, F. Van Roey and C. A. Mack, "Unbiased roughness measurements: Subtracting out SEM effects", *Microelectron. Eng.*, 2018, **190**, 33-37.
10. M. Aziz and A. F. Ismail, in *Membrane Characterization*, eds. N. Hilal, A. F. Ismail, T. Matsuura and D. Oatley-Radcliffe, Elsevier, 2017, Chapter 5, 81-93.
11. P. van der Heide, in *X‐Ray Photoelectron Spectroscopy*, Wiley, 2011, Chapter 3, 27-60.
12. B. D. Ratner and D. G. Castner, in *Surface Analysis – The Principal Techniques*, eds. J. C. Vickerman and I. S. Gilmore, Wiley, 2 edn., 2009, Chapter 3, 47-112.
13. M. Jacquemin, M. J. Genet, E. M. Gaigneaux and D. P. Debecker, "Calibration of the X-Ray Photoelectron Spectroscopy Binding Energy Scale for the Characterization of Heterogeneous Catalysts: Is Everything Really under Control?", *ChemPhysChem*, 2013, **14**, 3618-3626.
14. M. P. Seah and W. A. Dench, "Quantitative electron spectroscopy of surfaces: A standard data base for electron inelastic mean free paths in solids", *Surf. Interface Anal.*, 1979, **1**, 2-11.
15. T. Akari, in *High-Resolution Spin-Resolved Photoemission Spectrometer and the Rashba Effect in Bismuth Thin Films*, Spinger, 2015, Chapter 2, 15-30.
16. Tanuma, S., C. J. Powell and D. R. Penn, "Calculations of electron inelastic mean free paths. IX. Data for 41 elemental solids over the 50 eV to 30 keV range", *Surf. Interface Anal.*, 2011, **43**, 689-713.
17. C. J. Powell and A. Jablonski, *NIST Electron Inelastic-Mean-Free-Path Database* - Version 1.2 National Institute of Standards and Technology, Gaithersburg, MD, 2010
18. A. Jablonski and C. J. Powell, "Relationships between electron inelastic mean free paths, effective attenuation lengths, and mean escape depths", *J. Electron. Spectrosc. Relat. Phenom.*, 1999, **100**, 137-160.
19. S. Tanuma, C. J. Powell and D. R. Penn, "Calculations of electron inelastic mean free paths", *Surf. Interface Anal.*, 2005, **37**, 1-14.

20. S. Tanuma, C. J. Powell and D. R. Penn, "Calculations of electron inelastic mean free paths. V. Data for 14 organic compounds over the 50–2000 eV range", *Surf. Interface Anal.*, 1994, **21**, 165-176.
21. E. Giangrisostomi, R. Ovsyannikov, F. Sorgenfrei, T. Zhang, A. Lindblad, Y. Sassa, U. B. Cappel, T. Leitner, R. Mitzner, S. Svensson, N. Mårtensson and A. Föhlisch, "Low Dose Photoelectron Spectroscopy at BESSY II: Electronic structure of matter in its native state", *J. Electron. Spectrosc. Relat. Phenom.*, 2018, **224**, 68-78.
22. R. Ovsyannikov, P. Karlsson, M. Lundqvist, C. Lupulescu, W. Eberhardt, A. Föhlisch, S. Svensson and N. Mårtensson, "Principles and operation of a new type of electron spectrometer – ArTOF", *J. Electron. Spectrosc. Relat. Phenom.*, 2013, **191**, 92-103.
23. M. Gorgoi, S. Svensson, F. Schäfers, G. Öhrwall, M. Mertin, P. Bressler, O. Karis, H. Siegbahn, A. Sandell, H. Rensmo, W. Doherty, C. Jung, W. Braun and W. Eberhardt, "The high kinetic energy photoelectron spectroscopy facility at BESSY progress and first results", *Nucl. Instrum. Methods Phys. Res., Sect. A*, 2009, **601**, 48-53.
24. Y. Zhang, J. Haitjema, X. Liu, F. Johansson, A. Lindblad, S. Castellanos, N. Ottosson and A. M. Brouwer, "Photochemical conversion of tin-oxo cage compounds studied using hard x-ray photoelectron spectroscopy", *J. Micro/Nanolitho. MEMS MOEMS*, 2017, **16**, 023510.
25. F. Schaefers, M. Mertin and M. Gorgoi, "KMC-1: a high resolution and high flux soft x-ray beamline at BESSY", *Rev. Sci. Instrum.*, 2007, **78**, 123102.
26. C. D. Wagner, L. E. Davis, M. V. Zeller, J. A. Taylor, R. H. Raymond and L. H. Gale, "Empirical atomic sensitivity factors for quantitative analysis by electron spectroscopy for chemical analysis", *Surf. Interface Anal.*, 1981, **3**, 211-225.
27. M. P. Seah, I. S. Gilmore and S. J. Spencer, "Quantitative XPS: I. Analysis of X-ray photoelectron intensities from elemental data in a digital photoelectron database", *J. Electron. Spectrosc. Relat. Phenom.*, 2001, **120**, 93-111.
28. C. D. Wagner, "Sensitivity factors for XPS analysis of surface atoms", *J. Electron. Spectrosc. Relat. Phenom.*, 1983, **32**, 99-102.
29. J. F. Moulder and J. Chastain, Handbook of X-ray Photoelectron Spectroscopy: A Reference Book of Standard Spectra for Identification and Interpretation of XPS Data, Physical Electronics Division, Perkin-Elmer Corporation, 1992.

Chapter 3

Photochemical conversion of tin-oxo cage compounds studied using hard x-ray photoelectron spectroscopy*

Molecular inorganic materials are currently considered as photoresists for extreme ultraviolet lithography (EUVL). Their high EUV absorption cross section and small building block size potentially render high sensitivity and resolution as well as low line-edge roughness. The photochemical reaction mechanisms that allow these kinds of materials to function as photoresists, however, are still poorly understood. We discuss photochemical reactions upon deep UV (DUV) irradiation of a model negative-tone EUV photoresist material, namely the well-defined molecular tin-oxo cage compound $[(SnBu)_{12}O_{14}(OH)_6](OH)_2$, which is spin-coated to thin layers of 20 nm. The core electronic structures (Sn 3d, O 1s and C 1s) of unexposed and DUV exposed films were then investigated using synchrotron radiation-based hard X-ray photoelectron spectroscopy. Different chemical oxidation states and concentrations of atoms and atom types in the unexposed and exposed films were found. We observed that the exposure in a nitrogen atmosphere prevented oxidation but still led to carbon loss, albeit with a smaller conversion. Finally, a mechanistic hypothesis for the basic DUV photoreactions in molecular tin-oxo cages is proposed.

* This chapter was published in slightly modified form in: Y. Zhang, J. Haitjema, X. Liu, F. Johansson, A. Lindblad, S. Castellanos, N. Ottosson, A. M. Brouwer, *J. Micro/Nanolith. MEMS MOEMS*, 2017, **16**, 023510; and in: Y. Zhang, J. Haitjema, X. Liu, F. Johansson, A. Lindblad, S. Castellanos, N. Ottosson, A. M. Brouwer, *Proc. SPIE,* 2017, **10146**, 1014606.

3.1 Introduction

Metal-containing hybrid inorganic materials are considered promising candidates as photoresists in high volume semiconductor manufacturing using extreme ultraviolet lithography (EUVL), ever since these materials were introduced in the past years.[1-5] Photoresists based on HfO_2 and ZrO_2 nanoparticles were synthesized and shown to form patterns in EUVL by Ober's group.[1-3] Tin-oxo cages[6], palladium complexes[7], organotin compounds,[8] and other molecular compounds have further been explored as EUV photoresist by Brainard's group. Recently, Inpria introduced Sn-based hybrid photoresists.[5] Compared with traditional organic chemically amplified photoresists (CARs), some of these inorganic photoresists show higher sensitivity,[2, 4, 9, 10] can be employed as thinner layers due to their higher EUV absorptivity, have higher etching resistance,[9] and potentially yield both lower line-edge roughness and higher resolution due to their smaller building blocks.[11-13] Such findings have shown the great potential for inorganic materials to be used as EUV photoresist. CARs have now been used and optimized for many years, first for deep UV (DUV) and more recently for EUV, and their critical photochemical reactions are generally well understood.[14] In contrast, the photoreaction mechanisms in the inorganic photoresist have not been thoroughly investigated yet. To further improve the performance of the inorganic photoresists, systematic studies of the key photoreaction mechanisms in the photoresist are necessary.

In this contribution, we study the structure and photochemistry in spin-coated layers of the tin-oxo cage compound $[(SnBu)_{12}O_{14}(OH)_6](OH)_2$, which can be seen as an ideal model system of inorganic nanoscale photoresists, given its well-defined metal-oxo core structure with surrounding n-butyl organic ligands and hydroxide counterions; see Fig. 3.1. To synthesize the compound, we followed the route in Ref. 15. The molecule contains Sn atoms with high EUV photon absorption,[10, 16, 17] and it has been demonstrated to work as an EUV photoresist.[6, 8] Despite the relatively simple structure of this molecular system, few spectroscopic methods are suitable to study the details of the photochemical reactions occurring in thin films, both due to limited sensitivity and limited chemical contrast. For example, UV-absorption spectra contain little structural information, while vibrational spectra (Raman or IR absorption) of thin films are close to their sensitivity limits, and in the case of the tin cages, give limited information due to the absence of characteristic vibrational marker bands. Here, we apply hard X-ray photoelectron spectroscopy (HAXPES) with tunable high photon energies from synchrotron sources, typically ranging from 1.7 keV to 10 keV. The detection limit is extremely low, and core-level photoemission naturally gives rise to elemental sensitivity because each element emits electrons from core levels in completely separated and well-defined energy ranges. The known relative emission efficiencies for different core levels

allow quantitative analysis of chemical composition. The chemical shifts in the binding energies of atoms in chemically different bonding environments make the method sensitive to chemical structure.[18]

Finally, the high photon energy in HAXPES gives the photoemitted electrons high kinetic energy and thus long inelastic mean free paths that allow the probing of molecular layers far below the surface. Thus, the bulk properties of the spin-coated photoresist layer can be accessed before and after exposure.[19]

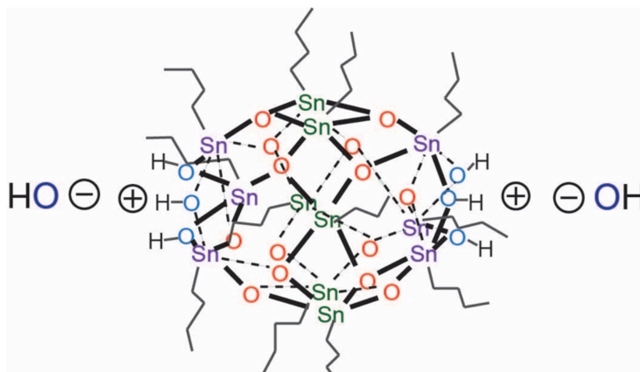

Figure 3.1. *Molecular structure of the* $[(SnBu)_{12}O_{14}(OH)_6](OH)_2$ *tin-oxo cage compound.*

3.2 Materials and Methods

3.2.1 Materials

The tin-oxo cage with tosylates as counterions (TinS) was synthesized from butylstannoic acid hydrate and *p*-toluene sulfonic acid monohydrate.[15] Tin-oxo cages with hydroxide as counterions (TinOH) were obtained by mixing a solution of aqueous tetramethylammonium hydroxide (TMAH) with a solution of TinS in isopropanol. TinOH precipitated, and the product was filtered directly. Results of a more extensive series of tin cage compounds will be published elsewhere. Glass coverslips were purchased from Menzel Gläser and cut into 1 × 1 cm^2.

3.2.2 Photoresists film preparation

For photoelectron spectroscopy experiments, it is essential that the substrates are conducting. These were prepared by coating piranha base-cleaned glass coverslips with 2 nm Cr and 18 nm Au layers using a sputter coater (Leica EM ACE 600 Double sputter coater). The tin oxo-cage material was dissolved in toluene to a concentration of 7.5 mg mL^{-1}. Solutions were filtered through a 0.25 µm PTFE filter right before spin coating. Thin layers [~20 nm, determined by atomic force microscopy (AFM)] were obtained by spin coating under 2000 rpm for 45 s with a

speed of 750 rpm s^{-1} on the Cr/Au coated glass coverslips. The samples were subjected to post-application bake at 90 °C for 1 min.

3.2.3 Photoresists exposure

A YAG-pumped OPA laser (Ekspla NT342B), delivering nanosecond pulses at 225 nm at 10 Hz (2.5 mJ $pulse^{-1}$) was used as the irradiation source. Some samples were exposed under ambient conditions with a dose of 1.3 J cm^{-2}. The dose was chosen to ensure a substantial chemical conversion in this first study of product formation. The other samples were exposed in an enclosed sample chamber, containing dry N_2, to the same dose (i.e. the exposure time was corrected for the losses due to window reflectivity).

3.2.4 Characterization

All samples were characterized using HAXPES at the HIKE end station[20]. The photon energy used for measurement was 2005 eV. The total energy resolution of the experiment was estimated to approx. 250 meV. Two types of spectra were recorded; (i) overview spectra taken from 0-800 eV binding energy (BE) in which all relevant lines were included, and (ii) detailed core-level spectra of the Sn 3d, C 1s and O 1s regions. The overview spectra were used to extract atomic number ratios, whereas the detailed spectra were used to resolve the chemical shifts in the respective elemental region. The X-ray power was ~10 μW cm^{-2}, which allowed the recording of a spectrum in a few minutes. Radiation damage to the materials was apparent only after ca. 2 hours.

3.3 Result and Discussion

3.3.1 Atomic concentration of different samples

Overview HAXPES spectra of unexposed TinOH thin films, as well as samples exposed to DUV in air and in N_2, are shown in Fig. 3.2. All the peaks are marked with the electronic state from which the electrons originate. Au 4f peaks, originating from the layer underneath the tin cage layer, are present in the spectra and were used for binding energy calibration; the Au $4f_{7/2}$ binding energy was set to 84.00 eV.[21] The tin cage gives rise to clear Sn 3d peaks at ~487 and ~498 eV (5/2 and 3/2 spin-orbit components, respectively), an O 1s peak at ~531 eV, and a C 1s peak at ~285 eV. The peak positions correspond well with those in the literature.[19, 22-24]

The atomic ratios of Sn, O and C atoms inside the three samples are proportional to the area ratios of the peaks in the spectrum, and can be extracted with knowledge of the photoionization cross sections.[25] For the unexposed sample, the extracted atomic ratios correspond well within the error bar to the expected chemical composition. For the exposed samples, since the number of Sn atoms is unlikely to change due to

exposure, the O1s and C1s peak areas are normalized to the Sn peak area, and the atom ratios for these samples are given in Table 3.1.

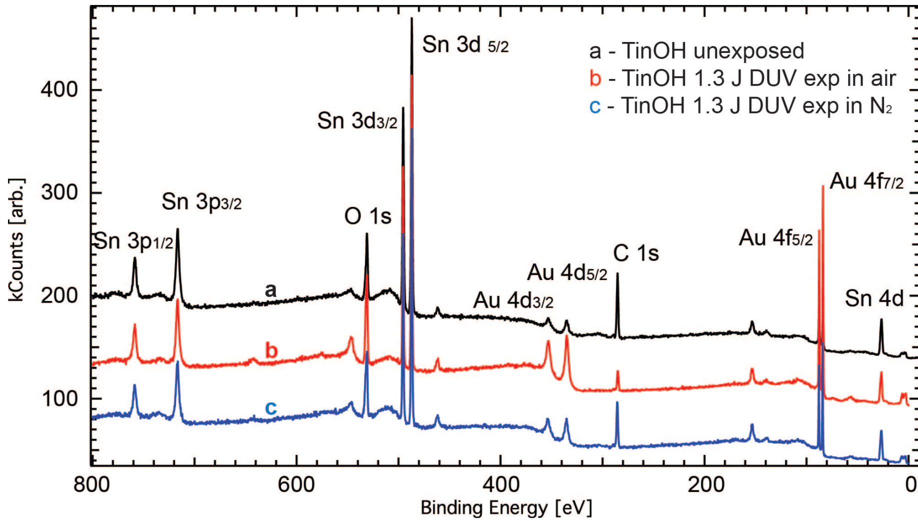

Figure 3.2. *Overview HAXPES spectrum of TinOH unexposed sample (a, black), TinOH DUV-exposed in air (b, red) and TinOH DUV-exposed in* N_2 *(c, blue). (The spectra are displaced vertically to avoid overlapping of the peaks.)*

Table 3.1. *Atomic ratios of TinOH unexposed sample, TinOH DUV-exposed in air, and TinOH DUV-exposed in* N_2.

Atom no.	Sn	O	C
Expected	12	22	48
TinOH_unexposed	12	22±1	48±1
DUV exp air	12	32±1	18±1
DUV exp N_2	12	22±1	36±1

As can be seen from Table 3.1, after the TinOH sample was exposed to DUV in air, the oxygen content was significantly increased while the carbon content was drastically decreased. This suggests that oxidation happens during the exposure, together with Sn-C bond or C-C bond cleavage, causing a loss of volatile carbon-containing species. When the sample was exposed in dry N_2, however, the O content stayed the same; this is because when no oxygen-containing gas-phase species is present, no further oxidation is possible and the photo-induced outgassing apparently does not cause any further loss of oxygen either. Compared with the carbon loss when TinOH was exposed in air, less C was lost under the same DUV dose.

For the TinOH sample exposed to DUV in air, we can make a crude estimate of the average photochemical quantum yield for breaking of Sn-C bonds based on the loss of carbon of ~63%. Using the measured UV absorbance of the thin film at 225 nm we find that the absorbed dose is ~0.40 J cm^{-2}. This corresponds to 4.5×10^{17} photons cm^{-2}. These lead to the breaking of 6.7×10^{15} Sn-C bonds per cm^2. The average quantum yield for loss of a butyl group is thus ~1.5 %. More accurate quantitative characterization of the photochemical process is needed, but we can already conclude that the carbon loss reaction is not very efficient.

3.3.2 Analysis of Sn, O and C chemical shifts

The high-resolution Sn $3d_{5/2}$ photoelectron spectra of the samples are shown in Fig. 3.3(a). Small, well-reproducible shifts can be clearly observed, which we interpret as a result of a change of the Sn oxidation state. The dependency of the Sn 3d binding energy on the Sn oxidation state has been well established in the literature.[19] The center of the Sn $3d_{5/2}$ peak after DUV exposure in air is shifted to higher binding energy, indicating that the oxidation state of the Sn atoms has increased. In contrast, the center energy position after DUV exposure in N_2 is shifted to a lower binding energy, indicating a net reduction of Sn atoms.

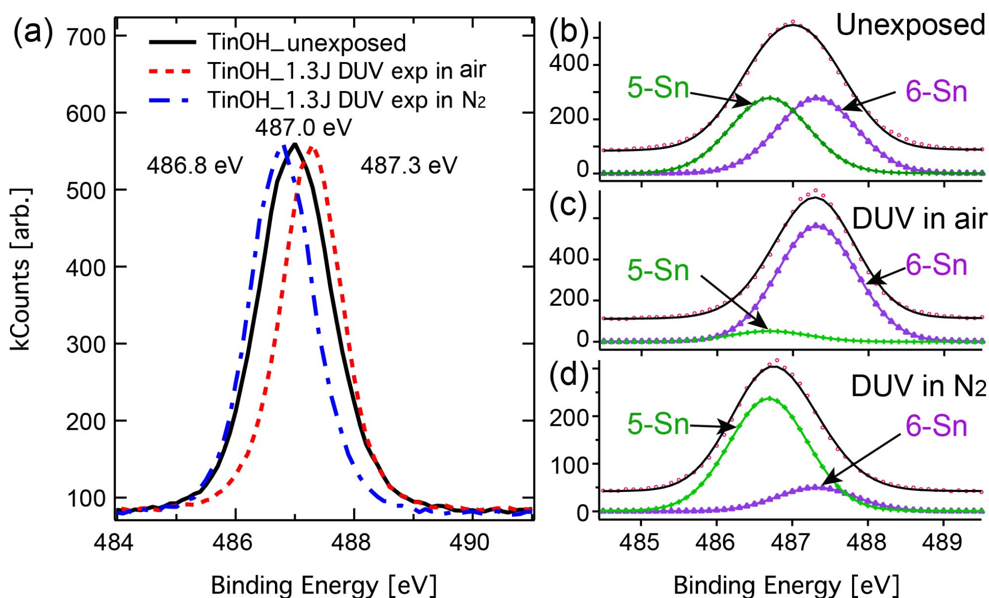

Figure 3.3. *Sn $3d_{5/2}$ core-level spectra for TinOH unexposed sample, TinOH DUV-exposed in air, and TinOH DUV-exposed in N_2. (a) Core-level spectra sharing the same scale on the ordinate axis, (b)-(d) Fits for each sample using the two-component model described in the text.*

In Fig. 3.3(b)-(d), we show least squares fits to the data using two Voigt line-shapes, i.e. each component is a Gaussian convoluted with a Lorentzian function (10%) that accounts for the finite lifetime of the core ionized state. Because there are two kinds of Sn atoms inside the tin oxo cages (5-coordinated Sn atoms in the center part of molecule, 6-coordinated Sn atoms in the side parts of the molecule facing the counter-ion), two sub-peaks were used to model the spectrum of the unexposed sample. Although the photolysis products are probably more complex, we take these peaks to be representative for tin in lower and higher oxidation states, respectively, and use the same peak positions and bandwidths to model the Sn peaks in the exposed samples – leaving only the amplitude as the free parameters. Under these constraints, the spectra in Fig. 3.3(b)-(d) were simultaneously fitted for the best global fit describing the full data set.

The results are presented as solid lines in Figs. 3.3(b)-(d), together with the data as circles. The peak at 486.7 eV (green) corresponds to the 5-coordinated Sn (low oxidation state, low BE) and the peak at 487.3 eV (purple) to the 6-coordinated Sn (higher oxidation state, high BE). In Fig. 3.3(b), the intensity of the two peaks is constrained to the 1:1 ratio corresponding to the equal abundance of the two types of tin. After DUV exposure in air, the intensity of the component corresponding to the low oxidation state decreases and the intensity is transferred to the peak of the more highly oxidized Sn component. In contrast, the fitting results from the sample exposed in N_2 indicated that some of the higher oxidation state Sn atoms were converted to a lower oxidation state. The FWHM of the three spectra were 1.58 eV, 1.22 eV and 1.27 eV, respectively; see Fig. 3.3(a). The peaks became narrower after exposure because one type of Sn atom became more dominant, but the FWHM values of the underlying components were constant at 1.17 eV.

The O 1s photoelectron spectra are shown in Fig. 3.4. O 1s peaks from all samples were normalized based on the O atoms ratio obtained from the overview spectra. Similar to the Sn 3d data, Fig. 3.4(a) shows the O 1s spectra with a common scale on the ordinate axis, whereas Fig. 3.4(b)-(d) show least squares fits to the data. As seen in Fig. 3.4(a), after DUV exposure in air, the O 1s peak shifted to higher binding energy and a considerably higher intensity, whereas the O 1s peak of the sample exposed under N_2 atmosphere shifted slightly to lower binding energies without change of the intensity.[22]

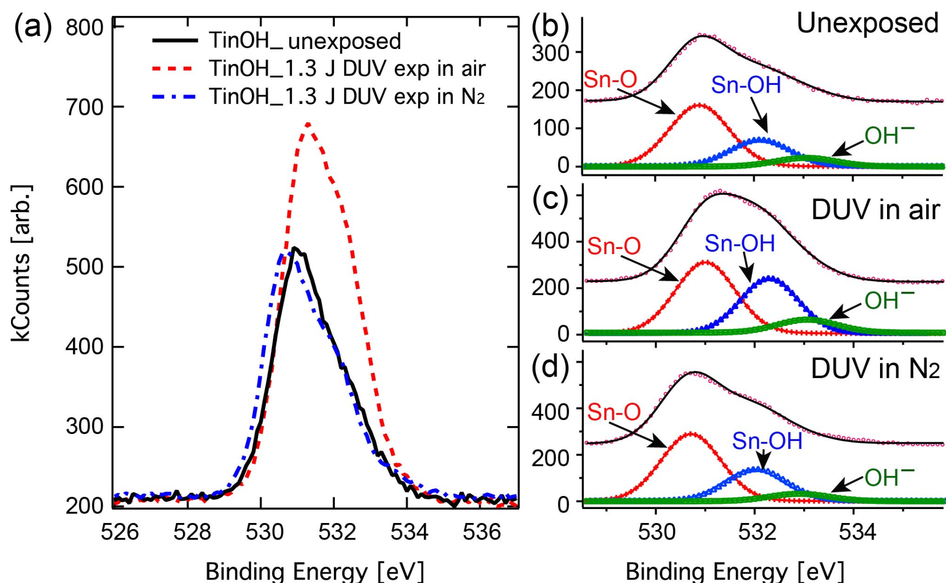

Figure 3.4. *The O 1s core level spectra for TinOH unexposed sample, sample exposed in air and sample exposed in N_2. (a) Core-level spectra sharing the same scale on the ordinate axis, (b)-(d) Least squares fits for each sample using the three-component model described in the text.*

Table 3.2. *Relative numbers of three types of O atoms derived from O 1s spectra as well as extracted binding energies of the respective features (see Fig. 3.4).*

Atom no.	Sn-O	Sn-OH	OH/CO	Total number
BE (eV)	530.7	532.1	533.0	
Expected	14	6	2	22
TinOH_unexposed	14	6	2	22
DUV exp air	16	13	3	32
DUV exp N_2	14	6	2	22

There are three kinds of O atoms in the TinOH cage, as can be seen in Fig. 3.1. Three Voigt peaks are assumed in the modeling of the unexposed sample, each shown in Fig. 3.4(b). We assign the low-BE peak (red) to the oxygen atoms bridging three Sn atoms, the intermediate one (dark blue) to the oxygen in the OH groups bridging two Sn atoms, and the high-BE (light blue) to the O in the OH^- counterions. Similar to the Sn $3d_{5/2}$ fitting, we assume that the underlying spectral features in the spectra of the DUV-exposed samples are the same, *i.e.* their binding energy positions and linewidth parameters, whereas the intensities might be altered

due to chemical conversion. Under these assumptions, the three spectra were fitted simultaneously to get a global optimum fit. The result is shown in Fig. 3.4(b)-(d).

After the sample was exposed to DUV in air, the peaks of all three kinds of O increased in intensity. Because extensive oxidation has obviously taken place here, most probably resulting in a mixture of oxidation products, the simple approximation with three types of O is probably not fully valid, but again they do likely represent chemical environments close to those of the unexposed material. It is also possible that O_2^-, O^-, O_2^{2-} would be chemisorbed on top of the photoresist.[25] For the sample exposed to DUV in N_2, on the other hand, no oxidation can take place, and the intensity of the three components almost stayed the same. The intensities of the peaks were converted into the number of oxygen atoms per molecule in the corresponding chemical state; the values are listed in Table 3.2, along with the extracted binding energy of the respective peak.

The C 1s photoelectron spectra were analyzed in the same way as their Sn 3d and O 1s counterparts. Figure 3.5(a) shows the data, normalized by the calculation from the overview spectra of the three samples. There is no clear energy shift observed in the main low-BE peak of the spectra after exposure, but the intensities and peak shape change significantly. In the unexposed sample, only two kinds of C atoms inside the tin-oxo cage can be distinguished from the spectra, attributed to Sn-C and C-C bonding configurations. After exposure, however, there is a shoulder observed near 286.1 eV and a new feature around 289.2 eV. These features likely arise from C 1s electron emission from C atoms with C-O and C=O bonds, respectively, as the increased BE indicates higher oxidation of some of the C atoms.[26] Thus, four Voigt peaks are used to describe the spectra of the DUV-exposed samples, the results of which are shown in Fig. 5(c)-(d). The extracted concentration of the respective atomic type per molecule and the corresponding binding energies are listed in Table 3.3. The unexposed sample gives the ratio expected from the chemical structure. Furthermore, the C atom number in the in C-C and Sn-C configurations from both samples exposed to DUV was decreased. At the same time C in C-O and C=O binding motifs were increased slightly, which further demonstrated the oxidation during the DUV exposure. For the sample exposed in air, the C-O and C=O can be taken as a sign of oxidation on the carbon chain part, in agreement with the increasing of the O content. However, as we concluded from the overview spectra and Sn 3d, and O 1s spectra, there was no oxidation or O gain in the sample exposed to DUV in N_2. The increase of the C=O feature at 289.2 eV from the sample exposed in N_2 must, therefore, be because of a light-induced rearrangement within the tin-oxo cages. Although there is no extra O gained, the carbon chain might be cleaved at the Sn-C bond or C-C bond after which the product could further react with an oxygen atom in the cage to form C-O or C=O bonds.

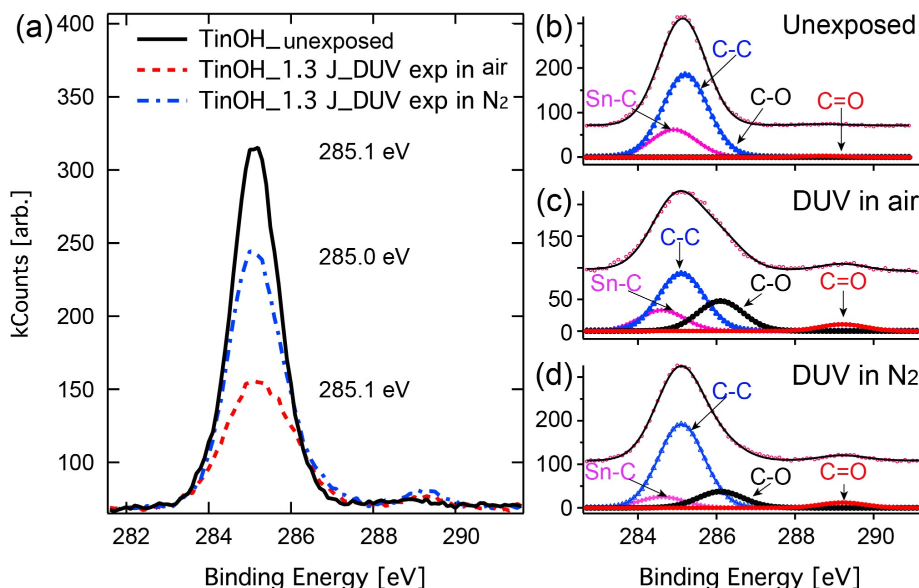

Figure 3.5. *(a) C 1s core level spectra for TinOH unexposed sample, TinOH DUV-exposed in air and TinOH DUV-exposed in N_2. (b)-(d) Fits for each sample using the four-component model described in the text.*

Based on the analysis of the HAXPES data presented above, we propose reaction pathways of the DUV induced reaction, schematically shown in Fig. 3.6. According to quantum-chemical calculations using density functional theory (DFT), the lowest electronically excited triplet state is of a $\sigma \rightarrow d$ type.[27] In this state, the Sn-C bond is easily broken to form two radicals. If present, oxygen and H_2O can directly react with the Sn radicals and increase the oxidation states of Sn atoms, which corresponds to the results shown in Fig. 3.3. The butyl radical could further donate a hydrogen atom or abstract one from neighbor cages to form butene or butane, volatile stable molecules that are readily released into vacuum. A hydrogen atom could be abstracted from a butyl group and form a C-centered radical, which could further react and form side chain oxygenation products that may account for the 289.2 eV band in Fig. 3.5. For the sample exposed in N_2, the chance for the radicals to recombine is greater after the Sn-C bond cleavage occurs, since there is no active molecule like O_2 or H_2O. That would explain why more C is lost in the sample exposed in air than in the sample exposed in N_2. The cleaved butyl radical could also react with the O inside the cage forming a C-O bond, corresponding to the C-O peaks in Fig. 3.5(c) and (d). Another possible reaction is the transfer of a hydrogen atom from the butyl radical to the Sn radical to form butene and a tin hydride. The formation of such an oxidation-sensitive but otherwise stable reaction product could be the explanation of our finding that the formation of insoluble material after exposure to EUV is enhanced by post-exposure baking.[28]

Table 3.3. *Relative numbers of four types of C atoms derived from C 1s spectra (Fig.5).*

Atom no.	Sn-C	C-C	C-O	C=O	Total number
BE (eV)	284.9	285.2	286.1	289.2	
Expected	12	36	0	0	48
TinOH unexposed	12	36	0	0	48
DUV exp air	3	9	5	1	18
DUV exp N_2	8	22	4	2	36

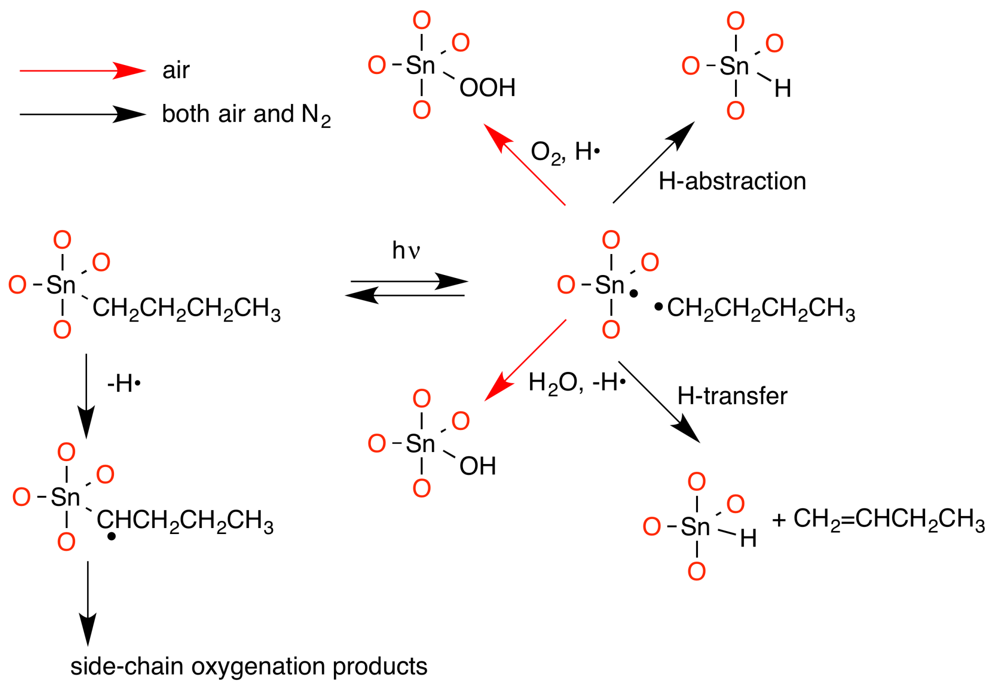

Figure 3.6. *Proposed photochemical reactions for TinOH exposed to DUV in air and N_2.*

3.4 Conclusions

HAXPES is demonstrated to be a powerful tool for analyzing the chemical changes upon DUV exposure in air and under N_2 in thin films of tin-oxo cages. Based on the detailed analysis of the presented HAXPES spectra, a mechanism of the photoreactions of TinOH films exposed to DUV in air or under N_2 could be proposed.

While the exposure conditions are very different from those in an EUV lithography tool, the present study highlights the relevance of gas-phase/film interactions for the final photochemical product formation. In ongoing experiments, we further compare these results with the changes induced in solution-phase photochemistry of the tin cages, in which products can be isolated and subjected to a wide range of chemical analysis techniques and with the results of EUV exposures of thin films at 13.5 nm.

3.5 References

1. L. Li, S. Chakrabart, K. Spyrou, C. K. Ober, E. P. Giannelis, "Studying the Mechanism of Hybrid Nanoparticle Photoresists: Effect of Particle Size on Photopatterning", *Chem. Mater.,* 2015, **27**, 5027-5031.
2. S. Chakrabarty, C. Ouyang, M. Krysak, M. Trikeriotis, K. Cho, E. P. Giannelis, C. K. Ober, "Oxide nanoparticle EUV resists: toward understanding the mechanism of positive and negative tone patterning", *Proc. SPIE,* 2013, **8679**, 1-8.
3. S. Chakrabarty, C. Sarma, L. Li, E. P. Giannelis, C. K. Ober, "Increasing sensitivity of oxide nanoparticle photoresists," *Proc. SPIE,* 2014, **9048**, 90481C-1.
4. J. Stowers, D. A. Keszler, "High resolution, high sensitivity inorganic resists," *Microelectron. Eng.,* 2009, **86**, 730-733.
5. T. S. Meyers, T. J. Anderson, B. J. Edson, K. Jiang, A. D. Keszler, K. M. Kocsis, J. A. Telecky, J. B. Cardineau, *US 2016/0116839 A1*, 2015.
6. B. Cardineau, R. Del Re, M. Marnell, H. Al-Mashat, M. Vockenhuber, Y. Ekinci, C. Sarma, D. A. Freedman, R. L. Brainard, "Photolithographic properties of tin-oxo clusters using extreme ultraviolet light (13.5 nm)". *Microelectron. Eng.,* 2014, **127,** 44-50.
7. M. Sortland, R. Del Re, J. Passarelli, J. Hotalen, M. Vockenhuber, Y. Ekinci, M. Neisser, D. Freedman, R.L. Brainard, "Positive-tone EUV resists: complexes of platinum and palladium", *Proc. SPIE,* 2015, **9422**, 94222701-9.
8. R. Del Re, M. Sortland, J. Pasarelli, B. Cardineau, Y. Ekinci, M. Vockenhuber, M. Neisser, D. Freedman, R. L. Brainard, "Low-LER tin carboxylate photoresists using EUV", *Proc. SPIE,* 2015, **9422**, 94222101-10.
9. M. Trikeriotis, M. Krysak, Y. S. Chung, C. Ouyang, B. Cardineau, R. Brainard, C. K. Ober, E. P. Giannelis, K. Cho, "A new inorganic EUV resist with high etch resistance", *Proc. SPIE,* 2012, **8322**, 83220U-1.
10. R. Fallica, J. K. Stowers, A. Grenville, A. Frommhold, A. P. G. Robinson, Y. Ekinci, "Dynamic absorption coefficients of chemically amplified resists and nonchemically amplified resists at extreme ultraviolet", *J. Micro/Nanolith. MEMS MOEMS,* 2016, **15**, 033506, 1-7.
11. T. Kozawa, "Lower Limit of Line Edge Roughness in High-Dose Exposure of Chemically Amplified Extreme Ultraviolet Resists", *Jpn. J. Appl. Phys.,* 2012, **51**, 06FC1.

12. F. Luo, V. Manichev, M. Li, G. Mitchson, B. Yakshinskiy, T. Gustafsson, D. Johnson, E. Garfunkel, "Helium ion beam lithography(HIBL)using HafSOx as resist," *Proc. SPIE,* 2016, **9779**, 977928-1.
13. D. Fan and Y. Ekinci, "Photolithography reaches 6 nm half-pitch using EUV light", *Proc. SPIE,* 2016, **9776,** 97761V-1.
14. E. Hassanein, C. Higgins, P. Naulleau, R. Matyi, G. Gallatin, G. Denbeaux, A. Antohe, J. Thackeray, K. Spear, C. Szmanda, C.N. Anderson, D. Niakoula, M. Malloy, A. Khurshid, C. Montgomery, E. C. Piscani, A. Rudack, J. Byers, A. Ma, K. Dean, R. L. Brainard, "Film quantum yields of ultrahigh PAG EUV photoresists", *Proc. SPIE,* 2008, **69211**, 69211I-1.
15. F. Banse, F. Ribot, P. Toladeno, J. Maquet, C. Sanchez, "Hydrolysis of Monobutyltin Trialkoxides: Synthesis and Characterizations of $\{(BuSn)_{12}O_{14}(OH)_6\}(OH)_2$", *Inorg. Chem.,* 1995, **34**, 9.
16. R. Fallica, J. Haitjema, L. Wu, S. Castellanos, A. M. Brouwer, Y. Ekinci, "Absorption and Exposure Kinetics of Photoresists at EUV", *Proc. SPIE,* 2017, **10143**, 101430A–11.
17. B. L. Henke, E. M. Gullikson, J. C. Davis, "X-Ray Interactions: Photoabsorption, Scattering, Transmission, and Reflection at E = 50-30,000 eV, Z = 1-92", *Atomic Data and Nuclear Data Tables,* 1993, **54**,181-342.
18. N. Mårtensson, E. Sokolowski, S. Svensson, "50 years anniversary of the discovery of the core level chemical shifts. The early years of photoelectron spectroscopy", *J. Electron. Spectrosc. Relat. Phenom.,* 2014, **193**, 27-33.
19. M. Fondell, M. Gorgoi, M. Boman, A. Lindblad, "An HAXPES study of Sn, SnS, SnO and SnO_2", *J. Electron. Spectrosc. Relat. Phenom.,* 2014, **195**, 195-199.
20. F. Schaefers, M. Mertin, M. Gorgoi, "KMC-1: A high resolution and high flux soft x-ray beamline at BESSY", *Rev. Sci. Instrum.,* 2007, **78**, 123102.
21. M. P. Seah, "Post-1989 calibration energies for X-ray photoelectron spectrometers and the 1990 Josephson constant", *Surf. Interface Anal.,* 1989, **14**, 488-488.
22. X. Xiao, B. Han, D. Deng, X. Cai, and Y. Wang, "Enhanced formaldehyde sensing properties of SnO_2 nanorods coupled with Zn_2SnO_4", *RSC Advances,* 2015, **5**, 42628-42636.
23. C. Liu, H. Huang, G. Cao, F. Xue, R. A. Paredes Camacho, X. Dong, "Enhanced Electrochemical Stability of Sn-Carbon Nanotube Nanocapsules as Lithium-Ion Battery Anode", *Electrochim. Acta,* 2014, **144**, 376-382.
24. T. Kawabe, K. Tabata, E. Suzuki, Y. Yamaguchi, Y. Nagasawa, "Electronic States of Chemisorbed Oxygen Species and Their Mutually Related Studies on SnO_2 Thin Film", *J. Phys. Chem. B*, 2011, **105**, 4239-4244.
25. M. B. Trzhaskovskaya, V. I. Nefedov, V. G. Yarzhemsky "Photoelectron Angular distribution parameters for Elements Z=1 to Z=54 in the photoelectron energy range 100–5000 eV", *Atomic Data and Nuclear Data Tables,* 2001, **77**, 97-159.
26. C. M. Preuss, T. Tischer, C. Rodriguez-Emmenegger, M. M. Zieger, M. Bruns, A. S. Goldmann, C. Barner-Kowollik, "A bioinspired light induced avenue for the design of patterned functional interfaces", *J. Mater. Chem. B*, 2014, **2**, 36-40.

27. J. Haitjema, Y. Zhang, N. Ottosson, A. M. Brouwer, "Photoreactions of tin oxo cages, model EUV photoresists", *J. Photopolym. Sci. Technol.*, 2017, **30**, 99-102.
28. J. Haitjema, Y. Zhang, M. Vockenhuber, D. Kazazis, Y. Ekinci, A. M. Brouwer, "Extreme ultraviolet patterning of tin-oxo cages", *Proc. SPIE,* 2017, **10143**, 1014325.

Chapter 4

Influence of thermal process on the chemical reaction and reaction yield in a model organotin EUV photoresist*

Tin oxo cages ($[(RSn)_{12}O_{14}(OH)_6]OH_2$) are considered as sensitive negative tone photoresists for extreme ultraviolet lithography. In addition to the photochemical process, subsequent processing steps (post exposure baking, developing, rinsing and hard baking) also play important roles in the final performance of the photoresist. Especially, the thermal effect in different bake processes can result in significant chemical changes in the photoresist. Here ultraviolet light (225 nm) was used as the irradiation source. Synchrotron radiation-based hard X-ray photoelectron spectroscopy (HAXPES) was used to monitor the chemical changes of the photoresist. The reaction yields in exposure, post-exposure bake and hard bake steps were calculated and compared. Higher reaction yield generated from the resist can be achieved by adding thermal processes.

---

* Y. Zhang, J. Haitjema, X. Liu, F. Johansson, A. Lindblad, N. Ottosson, S. Castellanos, A. M. Brouwer, "Influence of thermal process on the chemical reaction and the reaction yield in a model organotin EUV photoresist", *Manuscript in preparation.*

4.1 Introduction

In the semiconductor industry, in order to achieve the smallest possible feature sizes, the wavelength of irradiation in photolithography has recently been decreased from 193 nm to 13.5 nm (extreme ultraviolet, EUV). In order to achieve high-resolution structures of the required quality, suitable photoresists are needed. While the traditional organic chemically amplified photoresists (CARs) can be adapted for EUV application,[1, 2] metal containing photoresist such as zirconium and hafnium nanoparticles and clusters, tin oxo cages, and platinum and palladium complexes have attracted attention in recent years because of the potential for stronger absorption of EUV photons and higher etch resistance.[3-10]

When CARs are used, a post exposure baking step (PEB) is included in the process to allow spreading of the photogenerated acid and catalytic cleavage of dissolution inhibiting groups. In this way, the sensitivity of the photoresists is enhanced, albeit at the expense of resolution.[11-14] When the organometallic photoresists are used, in some cases a post exposure bake (PEB) step is also added, and the performance of the pattern and the sensitivity of the photoresists can be improved.[15, 16] Although the PEB step has been used in the processing of organometallic photoresists, the reason why it can promote the reaction and improve the performance of the pattern generated from the photoresists thin film was not explained.[16-18]

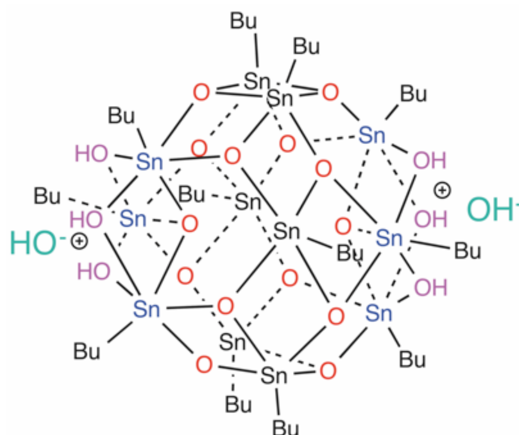

Figure 4.1. *The chemical structure of the tin oxo cage with hydroxides as counterions (TinOH). The Sn atoms colored black (in the center of the structure) are 5-coordinated, the ones in blue (at the sides, bridged by OH groups) are 6-coordinated.*

Tin containing molecular inorganic compounds have a potential advantage as photoresists for EUV lithography due to their high EUV absorption cross section.[19, 20] In this work, we choose a tin oxo cage, $[(BuSn)_{12}O_{14}(OH)_6](OH)_2$, as a model photoresist, and used hard x-ray photoelectron spectroscopy (HAXPES) to analyse

the changes in the photoresist thin film after exposing to deep UV light and processing with a post-exposure bake step at 100 ^oC for 2 min, and a final hard bake (HAB) step at 150 ^oC for 1 min. We found that the PEB process can promote the chemical conversion in the photoresist thin film, further oxidizing the exposed tin oxo cages. The HAB process (after development of the pattern) can even further improve the reaction yield. As shown in Chapter 6, thermal processes in the lithography procedure can increase the sensitivity in the pattern formation of tin oxo cages photoresist.[15] This sensitivity increase is essentially promoted by the chemical reaction in the tin oxo cages photoresist thin films during baking.

4.2 Materials and methods

The tin oxo cage with hydroxide as counterion ($[(BuSn)_{12}O_{14}(OH)_6](OH)_2$, TinOH, see Fig.1), was synthesized according to the literature.[21, 22] Solutions in toluene (7.5 mg mL^{-1}) were filtered with a 0.2 μm PTFE filter and spin coated[23] on different substrates (20 nm Au coated glass and quartz) with an acceleration of 700 rpm/s, followed by 35 s at 2500 rpm. A post application bake (PAB; 90 °C, 60 s) was used to remove residual solvent. The thickness of the films was 20 ± 3 nm, as determined by Atomic Force Microscopy (AFM).

Thin films of tin oxo cages on different substrates (20 nm Au coated glass and quartz) were exposed under dry N_2 atmosphere to 225 nm ultraviolet light from an Ekspla NT342b laser running at 10 Hz (2.5 mJ/pulse) up to a total dose of 1.3 J cm^{-2}. Post exposure bake (PEB, 100 °C, 2 min) and hard bake (HAB, 150 °C, 1 min), were done on a hotplate in air atmosphere.

Hard X-ray photoelectron spectroscopy (HAXPES), was conducted on the HIKE end station at BESSY-II, Helmholtz-Zentrum-Berlin[24] with a photon energy of 2005 eV, as in our previous work.[23] All XPS spectra were calibrated using the Au $4f_{7/2}$ line with a binding energy of 84.0 eV.[25] The resolution of the survey spectra is 0.25 eV, and the resolution of the high-resolution spectra is 0.1 eV. The band shapes were fitted with a sum of Voigt functions, i.e. a Gaussian convolved with a Lorentzian function (10%) that accounts for the finite lifetime of the core ionized state.

UV-Vis absorption spectra of the thin films of TinOH on quartz substrates were measured in transmission mode using a Shimadzu UV-2600 spectrometer.

4.3 Result and Discussion

4.3.1 Overview XPS spectra

Overview spectra XPS survey scans of unexposed, 1.3 J cm^{-2} DUV exposed, and further baked samples (PEB and HAB) are presented in Fig. 4.2. The atomic orbitals from which the electrons originate are marked in the spectra. All the relevant peaks of the elements (Sn M edge around 487 eV ($3d_{5/2}$) and 496 eV ($3d_{3/2}$), C K edge (1s) around 285 eV and O K-edge (1s) around 531 eV, Au $4f_{7/2}$ at 84.0 eV) are observed as expected.[23, 26] The Au 4f peaks are from the substrate underneath the photoresist thin film, indicating that the detection sensitivity of the measurement, due to the relatively high electron energies, is not limited to the sample surface. All the spectra are presented with the Sn $3d_{5/2}$ peaks normalized to the same intensity.

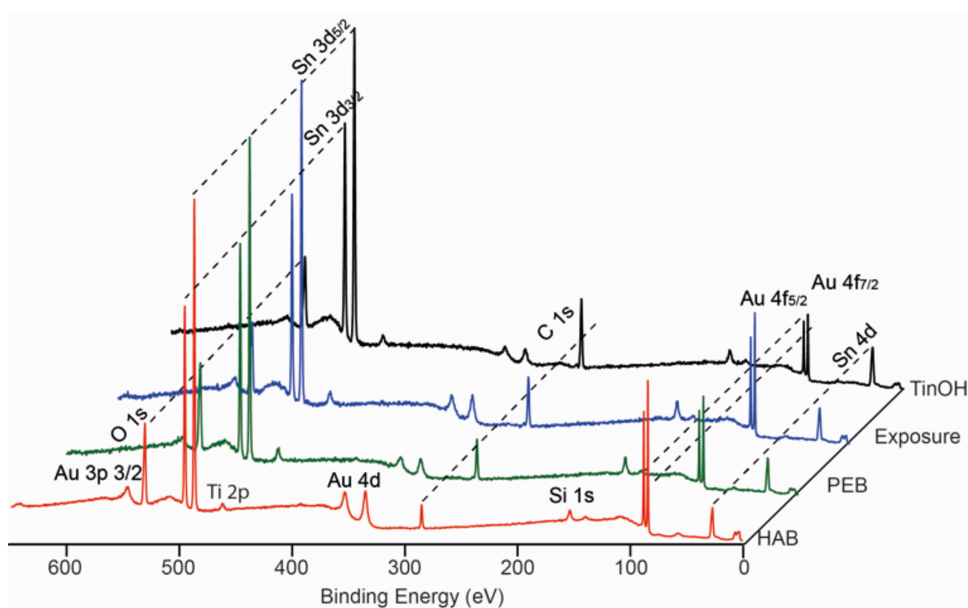

Figure 4.2. *HAXPES spectra of thin films of TinOH: unexposed sample, sample exposed to 1.3 J cm^{-2} DUV under dry N_2, sample exposed to 1.3 J cm^{-2} DUV under dry N_2 and further PEB (100 ℃, 2 min) and sample exposed to 1.3 J cm^{-2} DUV under dry N_2, PEB (100 ℃, 2 min in air) and HAB (150 ℃, 1 min in air). The spectra are scaled to equal intensities of the Sn 3d peaks.*

The relative number of atoms of each element in the sample can be derived from the peak area ratios of Sn 3d, O 1s and C 1s. The peak areas were calculated after subtracting the linear background at each peak position in the survey spectra, and the atom ratios (Table 4.1) were calculated using known sensitivity factors.[27] We assumed that no Sn atoms are lost during the exposure and further processes. Thus,

the O 1s and C 1s peak areas are normalized to the Sn 3d peak areas which correspond to 12 tin atoms.

Table 4.1. *Atomic ratio of unexposed TinOH sample, sample exposed to 1.3 J cm^{-2} DUV under dry N_2, sample exposed to 1.3 J cm^{-2} DUV under dry N_2 and PEB (100°C, 2 min in air), and sample exposed to 1.3 J cm^{-2} DUV under dry N_2, PEB, and HAB (150 ^{o}C, 1 min in air).*

	Sn	O	C
Theoretical	12	22	48
Unexposed	12	22 ± 1	48 ± 1
1.3 J cm^{-2} (N_2)	12	22 ± 1	36 ± 1
PEB in air	12	29 ± 1	32 ± 1
HAB in air	12	25 ± 1	18 ± 1

As we can see from the data in Table 4.1, the atomic ratio in the unexposed sample corresponds well with the theoretical composition of the TinOH molecule free of solvents. After exposing the photoresist thin film in dry N_2 atmosphere to 1.3 J cm^{-2} of 225 nm light, the carbon content decreased by about 25%. This indicates Sn-C or C-C bond cleavage with generation of carbon-containing volatile species, as we stated in our previous work.[23] With a further PEB step at 100 ^{o}C for 2 min in air, another 8% more carbon was lost and about 32% extra oxygen was gained, likely due to oxidation reactions of photoproducts in the thin film. After a further HAB step at 150 ^{o}C for 1 min, ~63% of the initial carbon atoms were lost, and ~14% of oxygen was lost comparing with the sample after the PEB step. In our previous study, we found the unexposed part to be stable in air at 100 ^{o}C without mass loss. Upon baking at 150 ^{o}C water was lost, probably due to deprotonation of the bridging OH groups by the hydroxide counter ions.[28] A further reason for oxygen loss could be the formation of unstable oxygen containing species that were detached from the thin film, or condensation reactions between cages that lead to elimination of water. In any case, it is clear that the PEB and HAB processes increase the chemical conversion of the photoresists significantly.

4.3.2 High-resolution XPS spectra

High-resolution XPS spectra were recorded around the Sn 3d, O 1s and C 1s peak positions of the four different samples. In Fig. 4.3, the high-resolution Sn $3d_{5/2}$ spectra of unexposed, 1.3 J cm^{-2} exposed and further PEB and HAB treated samples are shown with the respective fits of the band with a sum of two Voigt functions. The Sn $3d_{5/2}$ peak from the unexposed sample is centered at 487.0 eV. After 1.3 J cm^{-2}, 225 nm DUV exposure in N_2, the peak shifts to 486.8 eV. With a further PEB

step in air, the Sn $3d_{5/2}$ peak shifts to higher binding energy (487.2 eV). After a final HAB step, the peak maximum is found at 487.1 eV. Two kinds of Sn atoms are present in the tin oxo cage: 5-coordinated (in the central part of the cage) and 6-coordinated (at the sides of the cage), as shown in Fig. 4.1. The differences in the binding energies of these two types of Sn are small, but in order to fit the spectra from the unexposed sample (Fig. 4.3a) we use two Voigt line shapes centered at 486.7 and 487.3 eV, respectively. We previously assigned the peak with higher binding energy to the 6-coordinated Sn, but recent DFT calculations[29] indicate that the assignment should be reversed. After DUV exposure and the following thermal processes, there are probably more than two kinds of environment of the Sn atoms, but to simplify the analysis, we only use the two types of Sn atoms to model the band of the Sn 3d electrons. We used the same peak position and bandwidths from the spectrum of the unexposed sample to fit the spectra of the exposed and baked samples, leaving only the intensity of the two components as the free parameter. Under these constraints, the spectra of the exposed and PEB, and HAB treated samples are fitted as shown in Fig. 4.3b-d. In Fig. 4.3a, the intensities of the two peaks were constrained to a 1:1 ratio, representing the equal numbers of the two types of Sn in the unexposed cages. After exposure and further thermal processes, the ratios between the two types of Sn atoms were changed. Since the areas of the spectra are proportional to the atomic concentration in the thin film, the ratio change between the low and high binding energy Sn atoms were calculated based on the fitting result and listed in Table 4.2.

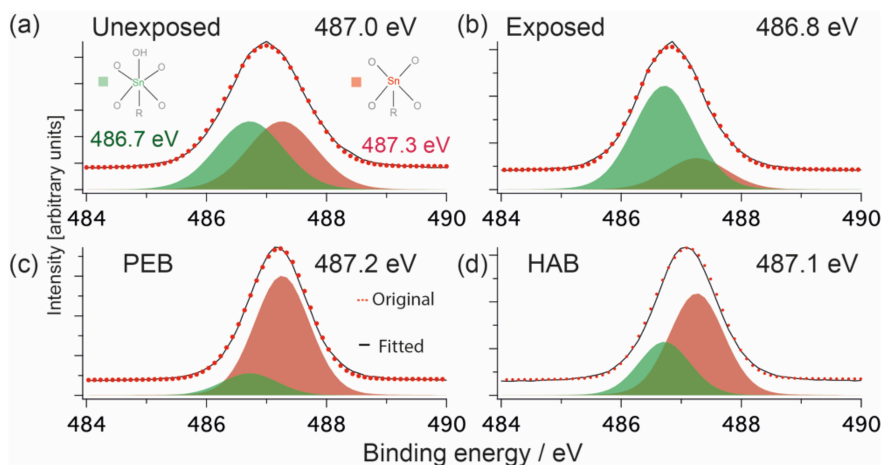

Figure 4.3: *High-resolution Sn $3d_{5/2}$ HAXPES spectra of thin film of TinOH; (a) unexposed sample, (b) sample exposed to 1.3 J cm^{-2} DUV under dry N_2, (c) sample exposed to DUV and PEB (100 ^oC, 2 min, in air), and (d) sample exposed to DUV, PEB and HAB (150 ^oC, 1 min in air).*

As shown in Table 4.2, after DUV exposure under N_2, the fraction of Sn atoms with lower BE increased. After PEB in air, the higher-binding-energy component dominates. Finally, after a HAB step, the ratio of the two types of Sn is again closer to 1.

Table 4.2. *Relative contributions of two types of Sn atoms derived from Sn $3d_{5/2}$ spectra as well as extracted binding energies (BE) of the respective features (see Fig. 4.3).*

	Sn_{low}	Sn_{high}
BE / eV	486.7	487.3
Theoretical number	6	6
Unexposed	6	6
1.3 J cm^{-2} (N_2)	9.2	2.8
PEB in air	1.9	10.1
HAB in air	4.0	8.0

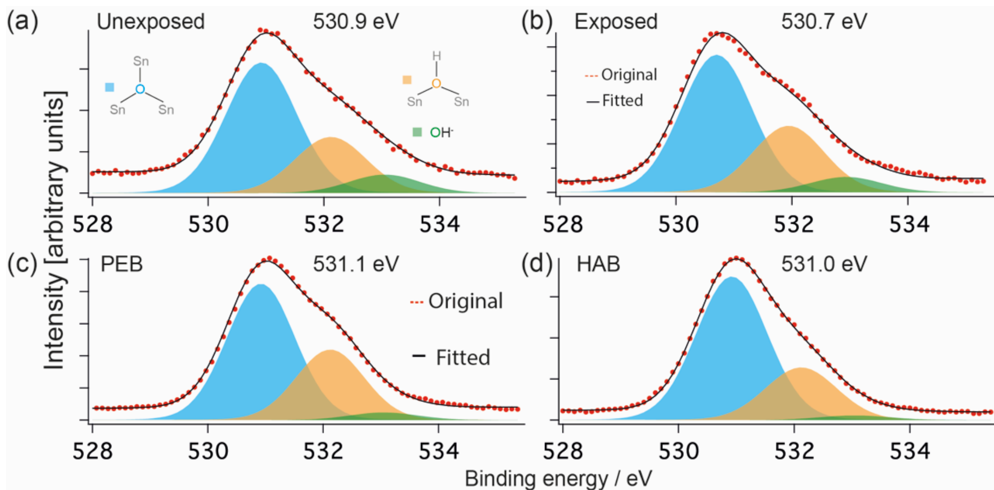

Figure 4.4. *High-resolution O 1s HAXPES spectra of thin film of TinOH (a) unexposed sample, (b) sample exposed to 1.3 J cm^{-2} DUV under dry N_2, (c) sample exposed to 1.3 J cm^{-2} DUV under dry N_2 further PEB (100 ^oC, 2 min) and (d) sample exposed to 1.3 J cm^{-2} DUV under dry N_2, PEB (100 ^oC, 2 min in air) and HAB (150 ^oC, 1 min in air).*

The high-resolution O 1s spectra of the four samples are shown in Fig. 4.4. We distinguish three kinds of oxygen atoms in the TinOH cages: 14 O atoms connected to 3 Sn atoms, 6 bridging OH groups, and two O atoms in the hydroxide

counterions. Applying the same analysis method as for the Sn 3d peaks, three Voigt peaks representing the three kinds of oxygen atoms were fitted into each spectrum. Based on the stoichiometry, the lowest binding energy peak must represent the oxygen atoms shared by the three Sn atoms. The middle peak is assigned to the oxygen atoms at the side part of the cages in the OH groups shared by two Sn atoms, and the highest binding energy peak represents the oxygen atom in the OH^- counterions.

Table 4.3. *Binding energies (BE, in eV) and relative numbers of three types of O atoms derived from O 1s spectra (see Fig. 4.4).*

	Sn-O	SnOH	OH^-	Total number
BE / eV	530.9	532.1	533.1	
Theoretical	14	6	2	22
Unexposed	14	6	2	22
1.3 J cm^{-2} (N_2)	14	6.7	1.5	22
PEB in air	18	9.5	1.0	29
HAB in air	18	6.6	0.6	25

We use the same restrictions from the spectrum of unexposed sample to fit the exposed sample and PEB/HAB treated samples. After fitting, the ratios of the three peaks in different samples were calculated and listed in Table 4.3. After exposure, the ratio between the three kinds of oxygen atoms changed slightly. There is a small decrease in the intensity at the OH- peak position, which could be because of the detachment of the counterion and generation of water. With a further PEB in air, the ratio of the SnO and SnOH peaks was increased, indicating the oxygen from the air could oxidize the Sn atoms. After the HAB step, the ratio of SnOH and the highest OH^- peaks were decreased. This could be a result of loss of water due to the deprotonation by the OH^- groups or condensation reactions.

In Fig. 4.5 we show the high-resolution C1s spectra of the four samples with the fits with up to four components. The main C 1s peaks of the four spectra were almost at the same position. There are only two kinds of carbon atom distinguishable in the unexposed tin oxo cages, the C in the Sn-C and the C-C. The quantum-chemical calculations predict that the 6 C-atoms that are bound to the 6-coordinated Sn-atoms have a lower binding energy than the others.[27] After exposure and further processes, a shoulder at ~286 eV and a new peak at ~289 eV are evident, which are likely carbon atoms in C-O and C=O bonds, respectively.[30] The atomic ratios of the four kinds of carbon atoms are listed in Table 4.4. After exposure, the amount of Sn-C

and C-C decreased and the signal of C-O and C=O increased. After a PEB step, both the C-O and C=O shoulders were decreased slightly, indicating that C-O and C=O containing species are not stable under PEB conditions and detached from the thin film. After HAB, all kinds of carbon atoms decreased, indicating that the Sn-C bonds and C-O bonds in the film were not stable under HAB condition, and easily detached from the thin film further diffused into the atmosphere.

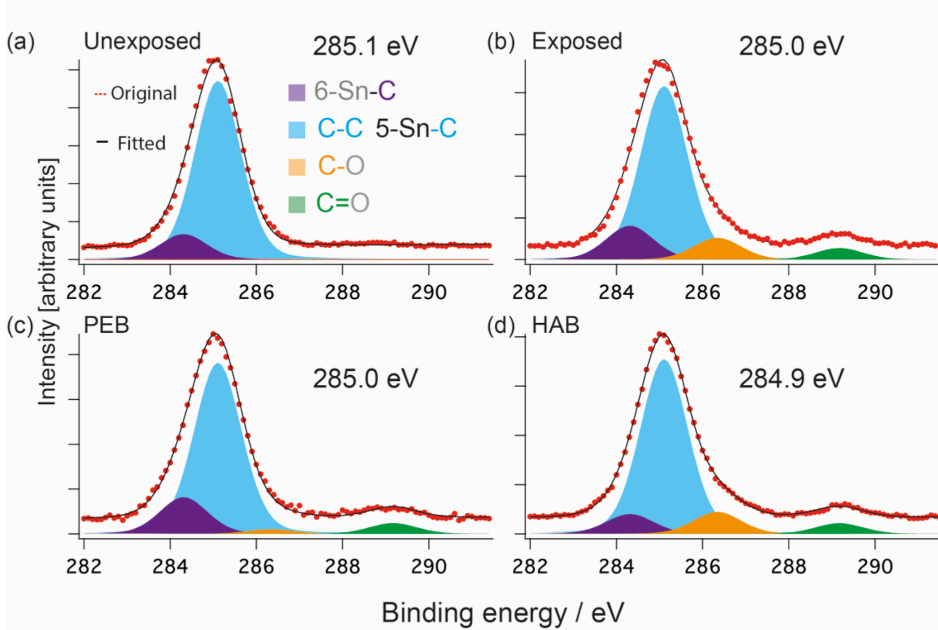

Figure 4.5. *High-resolution C 1s HAXPES spectra of thin films of TinOH; (a) unexposed sample, (b) sample exposed to 1.3 J cm^{-2} DUV under dry N_2, (c) sample exposed to 1.3 J cm^{-2} DUV under dry N_2 further PEB (100°C, 2 min) and (d) sample exposed to 1.3 J cm^{-2} DUV under dry N_2 further PEB (100°C, 2 min in air) and HAB (150°C, 1 min in air).*

Table 4.4. *Relative numbers of four types of C atoms derived from C 1s spectra as well as extracted binding energies of the respective features (see Fig. 4.5).*

Atom type	Sn-C	C-C	CO	C=O	Total number
BE / eV	284.4	285.2	286.4	289.3	0
Theoretical	6	42	0	0	48
Unexposed	6	42	<0.1	<0.3	48
1.3 J cm^{-2} (N_2)	5.1	26	3.3	1.7	36
PEB in air	5.3	25	0.7	1.5	32
HAB in air	1.6	16	1.7	0.8	18

4.3.3 UV-Vis spectroscopy

UV-Vis spectroscopy was also used to follow the chemical change in the TinOH thin film as shown in Fig. 4.6. Two samples were prepared with the same thickness on the quartz substrate for UV-Vis measurement. The first sample was exposed to DUV with doses of 60, 120 and 200 mJ cm^{-2} (Fig. 4.6a). The second sample was exposed to 60 mJ cm^{-2} DUV, and then treated with the thermal process (PEB, and HAB). The UV-vis spectra were recorded after each process step as shown in Fig. 4.6b.

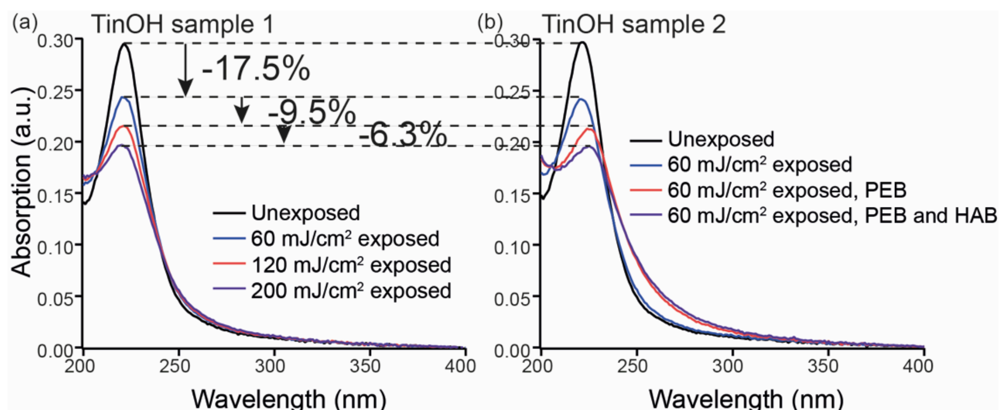

Figure 4.6. *(a) UV-vis spectra of TinOH thin film exposed to DUV with 60, 120 and 200 mJ cm^{-2}. (b) UV-vis spectra of 200 mJ cm^{-2} DUV exposed TinOH thin film, followed by PEB and HAB processes.*

As it can be observed in Fig. 4.6a, the absorption peak of the unexposed material is at around 225 nm. In this first sample, with increasing DUV exposure dose, the absorption decreases. Thermal processes were applied after exposure on the second sample. The decrease of the absorption peak after PEB in the second sample is comparable with the decrease when additional 60 mJ cm^{-2} DUV dose was applied on the first sample. The decrease of the absorption peak after HAB process applied on the second sample is comparable with the decrease when additional 80 mJ cm^{-2} DUV dose was applied in the first sample. A clear difference between the two sets of spectra appears on the absorption maxima position and the long-wavelength side of the band. As we have shown previously, the appearance of red-shifted absorption is consistent with conversion of Sn-C to Sn-O bonds.[31]

4.3.4 Proposed mechanism

After analysing the HAXPES spectra, we can propose possible reaction mechanisms in the tin oxo cages as shown in Fig. 4.7. The chemical reactions that occurred during exposure under N_2 are indicated with blue arrow. According to our previous work, we expect a Sn-C bond cleavage upon DUV exposure.[23, 32] Since

there is no other reactive species present during the sample exposure in N_2, the two radicals may recombine again or the butyl radical could escape. It could form a stable molecule by donating or abstracting a hydrogen atom, forming butene or butane, respectively. These products have been independently detected as outgassing products in EUV irradiation (Chapter 7). The carbon chain could also re-attach to the oxygen atoms forming a structure with μ_2-OBu bridging units. This would account for the C-O peaks in the C1s spectrum (Fig. 4.5b). Such bridging OR groups are known as a structural motif, e.g. resulting from methanolysis of TinOH,[27] or as a building block of the recently discovered Na^+ containing tin oxo cage.[33, 34] Moreover, in recent solution-phase DUV photolysis experiments, butanol was detected as a reaction product, in addition to butene and butyraldehyde.[35] The latter could account for the C=O species detected by XPS.

When a butyl radical donates a hydrogen atom, a tin hydride can be formed. While trialkyl tin hydrides are well known, and fairly stable molecules, the type of hydride formed here may well be oxidation sensitive and give rise to products containing Sn-O bonds upon contact with air. Another oxidation sensitive product would arise from the direct elimination of butanol (Fig. 4.7).

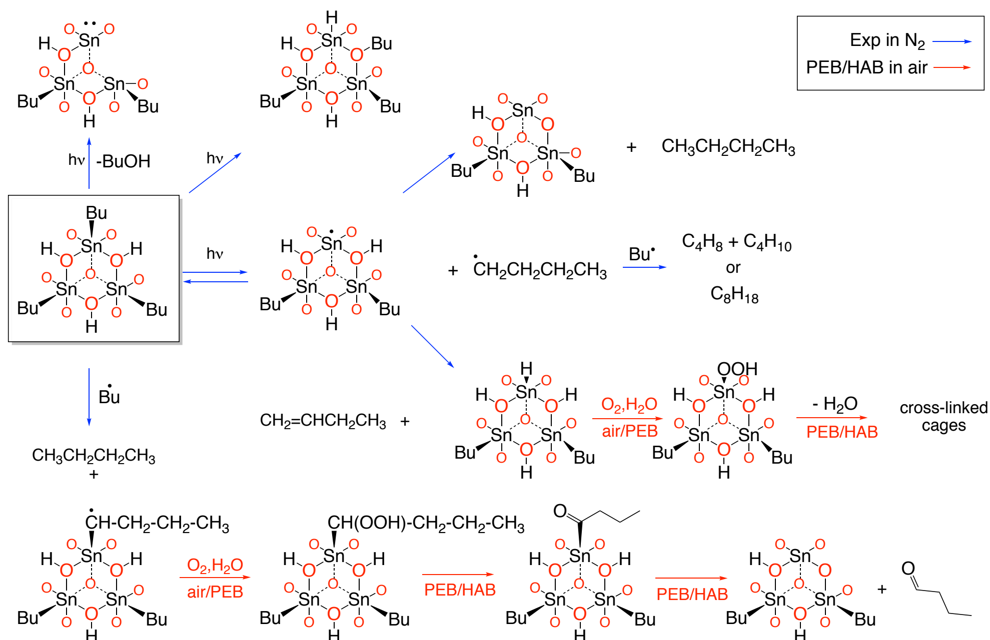

Figure 4.7. *Proposed photochemical reactions for TinOH exposed to DUV in N_2 and further PEB and HAB. For the purpose of illustration, reactions are depicted at the 6-coordinated tin sites in the "cap" on one side of the cage. The O-atoms drawn with only single bonds to the Sn atoms are part of the central "belt" of the cage.*

The initially formed butyl radical can form butane by abstracting a hydrogen from the same molecule from which it originated, or from a neighboring molecule. One possibility is that a hydrogen atom is picked up from a bridging OH-group. Abstraction of hydrogen atoms from a butyl group could lead to radicals that can survive under nitrogen but react with oxygen as soon as the sample is exposed to air, if only briefly.

While we have no other direct evidence for the proposed intermediates, they do agree with the observed changes in the XPS spectra after photolysis. The loss of unsaturated or oxygen containing molecules leads to a net reduction of the tin cage, which explains the shift of the Sn 3d binding energy to slightly lower values.

During the PEB step in air at 100 °C, the active species left over from the exposure get the chance to react with oxygen or H_2O. The Sn atoms site were further oxidized as shown in Fig. 4.3c. The oxygen ratio increased significantly, as shown in Table 4.1. Further reactions occur in the HAB step at 150 °C. More carbon is lost, but also the oxygen content becomes smaller, indicating the loss of organic compounds containing oxygen and/or water resulting from condensation reactions. The intact tin oxo cage film, in contrast, is stable at this temperature (Chapter 6), apart from some loss of solvent and water. The chemical reactions during baking are indicated with red arrows in Fig. 4.7.

4.4 Conclusions

The thermal effects from PEB and HAB on the photoresist thin film after DUV exposure were investigated by means of HAXPES and UV-vis absorption measurements. Based on the analysis of the HAXPES spectra, chemical reactions in the tin oxo cages were proposed. Both the PEB and HAB can promote further chemical reaction after DUV exposure in the tin oxo cages. The PEB process leads to oxidation of intermediates produced in the exposed tin oxo cages, enhancing the chemical differences between the unexposed and exposed parts and further increasing the solubility differences in the development process. The HAB further reduces the amount of organic components in the pattern, and makes the pattern more robust.

4.5 References

1. Y. Vesters, J. Jiang, H. Yamamoto, D. De Simone, T. Kozawa, S. D. Gendt and G. Vandenberghe, "Sensitizers in EUV chemically amplified resist: mechanism of sensitivity improvement", *Proc. SPIE*, 2018, **10583**, 1058307.
2. T. Manouras, D. Kazazis, E. Koufakis, Y. Ekinci, M. Vamvakaki and P. Argitis, "Ultra-sensitive EUV resists based on acid-catalyzed polymer backbone breaking", *Proc. SPIE*, 2018, **10583**, 105831R.

3. J. Stowers and D. A. Keszler, "High resolution, high sensitivity inorganic resists", *Microelectron. Eng.*, 2009, **86**, 730-733.
4. M. E. Krysak, J. M. Blackwell, S. E. Putna, M. J. Leeson, T. R. Younkin, S. Harlson, K. Frasure and F. Gstrein, "Investigation of novel inorganic resist materials for EUV lithography", *Proc. SPIE*, 2014, **9048**, 904805.
5. A. E. Grigorescu and C. W. Hagen, "Resists for sub-20-nm electron beam lithography with a focus on HSQ: state of the art", *Nanotechnology*, 2009, **20**, 292001.
6. L. Li, S. Chakrabarty, J. Jiang, B. Zhang, C. Ober and E. P. Giannelis, "Solubility studies of inorganic-organic hybrid nanoparticle photoresists with different surface functional groups", *Nanoscale*, 2016, **8**, 1338-1343.
7. L. Li, S. Chakrabarty, K. Spyrou, C. K. Ober and E. P. Giannelis, "Studying the Mechanism of Hybrid Nanoparticle Photoresists: Effect of Particle Size on Photopatterning", *Chem. Mater.*, 2015, **27**, 5027-5031.
8. B. Cardineau, in *Frontiers of Nanoscience*, eds. A. Robinson and R. Lawson, Elsevier, 2016, **11**, 377-420.
9. S. Castellanos, L. Wu, M. Baljozovic, G. Portale, D. Kazazis, M. Vockenhuber, Y. Ekinci and T. Jung, "Ti, Zr, and Hf-based molecular hybrid materials as EUV photoresists", *Proc. SPIE*, 2018, **10583**, 105830A.
10. M. Trikeriotis, M. Krysak, Y. S. Chung, C. Ouyang, B. Cardineau, R. Brainard, C. K. Ober, E. P. Giannelis and K. Cho, "A new inorganic EUV resist with high-etch resistance", *Proc. SPIE*, 2012, **8322**, 83220U.
11. W. D. Hinsberg, F. A. Houle, M. I. Sanchez and G. M. Wallraff, "Chemical and physical aspects of the post-exposure baking process used for positive-tone chemically amplified resists", *IBM J. Res. Dev.*, 2001, **45**, 667-682.
12. F. H. Dill and J. M. Shaw, "Thermal Effects on the Photoresist AZ1350J", *IBM J. Res. Dev.*, 1977, **21**, 210-218.
13. M. T. Postek, J. L. Sturtevant, S. J. Holmes, T. G. Van Kessel, P. C. D. Hobbs, J. C. Shaw and R. R. Jackson, "Postexposure bake as a process-control parameter for chemically amplified photoresist", *Proc. SPIE*, 1993, **1926**, 106.
14. M. H. Somervell, J. Jiang, B. Jung, M. O. Thompson and C. K. Ober, "Line edge roughness of high deprotection activation energy photoresist by using sub-millisecond post exposure bake", *Proc. SPIE*, 2013, **8682**, 86821N.
15. J. Haitjema, Y. Zhang, M. Vockenhuber, D. Kazazis, Y. Ekinci and A. M. Brouwer, "Extreme ultraviolet patterning of tin-oxo cages", *J. Micro/Nanolitho. MEMS MOEMS*, 2017, **16**, 033510.
16. Y. Ekinci, H. H. Solak, C. Padeste, J. Gobrecht, M. P. Stoykovich and P. F. Nealey, "20 nm Line/space patterns in HSQ fabricated by EUV interference lithography", *Microelectron. Eng.*, 2007, **84**, 700-704.
17. S. T. Meyers, J. T. Anderson, J. B. Edson, K. Jiang, D. A. Keszler, M. K. Kocsis, A. J. Telecky and B. Cardineau, *US patent 20160116839A1*, 2016.
18. Y. Ekinci, M. Vockenhuber, B. Terhalle, M. Hojeij, L. Wang and T. R. Younkin, "Evaluation of resist performance with EUV interference lithography for sub-22 nm patterning", *Proc. SPIE*, 2012, **8322**, 83220W.

19. R. Fallica, J. Haitjema, L. Wu, S. Castellanos, A. M. Brouwer and Y. Ekinci, "Absorption coefficient and exposure kinetics of photoresists at EUV", *Proc. SPIE*, 2017, **10143**, 101430A.
20. B. Cardineau, R. Del Re, M. Marnell, H. Al-Mashat, M. Vockenhuber, Y. Ekinci, C. Sarma, D. A. Freedman and R. L. Brainard, "Photolithographic properties of tin-oxo clusters using extreme ultraviolet light (13.5 nm)", *Microelectron. Eng.*, 2014, **127**, 44-50.
21. C. Eychenne-Baron, F. Ribot and C. Sanchez, "New synthesis of the nanobuilding block $\{(BuSn)_{12}O_{14}(OH)_6\}^{2+}$and exchange properties of $\{(BuSn)_{12}O_{14}(OH)_6\}(O_3SC_6H_4CH_3)_2$", *J. Organomet. Chem.*, 1998, **567**, 137-142.
22. F. R. Frederic Banse, P. Toladeno, J. Maquet, C. Sanchez, "Hydrolysis of Monobutyltin Trialkoxides: Synthesis and Characterizations of $\{(BuSn)_{12}O_{14}(OH)_6\}(OH)_2$", *Inorg. Chem.*, 1995, **34**, 9.
23. Y. Zhang, J. Haitjema, X. Liu, F. Johansson, A. Lindblad, S. Castellanos, N. Ottosson and A. M. Brouwer, "Photochemical conversion of tin-oxo cage compounds studied using hard x-ray photoelectron spectroscopy", *J. Micro/Nanolitho. MEMS MOEMS*, 2017, **16**, 023510.
24. F. Schaefers, M. Mertin and M. Gorgoi, "KMC-1: a high resolution and high flux soft x-ray beamline at BESSY", *Rev. Sci. Instrum.*, 2007, **78**, 123102.
25. M. P. Seah, "Post-1989 calibration energies for X-ray photoelectron spectrometers and the 1990 Josephson constant", *Surf. Interface Anal.*, 1989, **14**, 488-488.
26. M. Fondell, M. Gorgoi, M. Boman and A. Lindblad, "An HAXPES study of Sn, SnS, SnO and SnO_2", *J. Electron. Spectrosc. Relat. Phenom.*, 2014, **195**, 195-199.
27. G. Sun, S. Cho, C. Clark, S. V. Verkhoturov, M. J. Eller, A. Li, A. Pavia-Jimenez, E. A. Schweikert, J. W. Thackeray, P. Trefonas and K. L. Wooley, "Nanoscopic cylindrical dual concentric and lengthwise block brush terpolymers as covalent preassembled high-resolution and high-sensitivity negative-tone photoresist materials", *J. Am. Chem. Soc.*, 2013, **135**, 4203-4206.
28. Y. Zhang, J. Haitjema, M. Baljozovic, M. Vockenhuber, D. Kazazis, T. A. Jung, Y. Ekinci and A. M. Brouwer, "Dual-tone Application of a Tin-Oxo Cage Photoresist Under E-beam and EUV Exposure", *J. Photopolym. Sci. Technol.*, 2018, **31**, 249-255.
29. A. M. Brouwer, unpublished results.
30. C. M. Preuss, T. Tischer, C. Rodriguez-Emmenegger, M. M. Zieger, M. Bruns, A. S. Goldmann and C. Barner-Kowollik, "A bioinspired light induced avenue for the design of patterned functional interfaces", *J. Mater. Chem. B*, 2014, **2**, 36-40.
31. J. Haitjema, L. Wu, A. Giuliani, L. Nahon, S. Castellanos and A. M. Brouwer, "Photo-induced Fragmentation of a Tin-oxo Cage Compound", *J. Photopolym. Sci. Technol.*, 2018, **31**, 243-247.
32. J. Haitjema, Y. Zhang, N. Ottosson and A. M. Brouwer, "Photoreactions of Tin Oxo Cages, Model EUV Photoresists", *J. Photopolym. Sci. Technol.*, 2017, **30**, 99-102.

33. S. Saha, D.-H. Park, D. C. Hutchison, M. R. Olsen, L. N. Zakharov, D. Marsh, S. Goberna-Ferrón, R. T. Frederick, J. T. Diulus, N. Kenane, G. S. Herman, D. W. Johnson, D. A. Keszler and M. Nyman, "Alkyltin Keggin Clusters Templated by Sodium", *Angew. Chem., Int. Ed.*. 2017, **56**, 10140-10144.
34. R. T. Frederick, J. T. Diulus, I. Lyubinetsky, D. C. Hutchison, M. R. Olsen, M. Nyman and G. S. Herman, "Surface characterization of tin-based inorganic EUV resists", *Proc. SPIE*, 2018, **10586**, 1058607.
35. J. H. Y. Boeije, unpublished result.

Chapter 5

The relationship between photon absorption of tin-nanocages and the efficiency of photochemical reaction*

In this chapter we investigate the UV-photoresponse of tin oxo cages with three different counterions (hydroxide (TinOH), acetate (TinA), trifluoroacetate (TinF)). The tin oxo cages were prepared as thin films and exposed to UV light (225 nm) in a dry N_2 atmosphere. The changes in the UV-vis absorption with exposure dose showed that TinOH and TinA react faster than TinF. This is also reflected in the sensitivity of the films as negative tone photoresists. Synchrotron-based hard x-ray photoelectron spectroscopy (HAXPES) showed that after exposure to a high photon dose more carbon was lost in TinF than in the other two compounds.

---

* Y. Zhang, J. Haitjema, X. Liu, F. Johansson, A. Lindblad, S. Castellanos, N. Ottosson, A. M. Brouwer, "The relationship between photon absorption of tin-nanocages and the efficiency of photochemical reaction", *Manuscript in preparation.*

5.1 Introduction

The photoresist plays an important role in the development of the photolithography industry. Comparing with traditional organic chemically amplified photoresists (CARs), molecular inorganic materials are attractive because they can easily be used as thinner film, because of their stronger etching resistance and high sensitivity to ultraviolet and extreme ultraviolet (EUV) light.[1] Various molecular inorganic materials as well as nanoclusters and nanoparticles have been investigated.[2-8] Among those molecular inorganic materials, tin-based molecules are most attractive, due to the high absorption cross section of tin atoms in the EUV spectral range.[9, 10, 11] Good patterning performance has been achieved by Inpria with tin based photoresist,[12-15] and Brainard and coworkers studied several Sn-containing molecular materials that showed application potential.[1, 16, 17] Although the Sn containing molecules have been shown to work as photoresists, how photon absorption and the further chemical reaction in the inorganic photoresist leads to solubility change and pattern formation is still unclear.

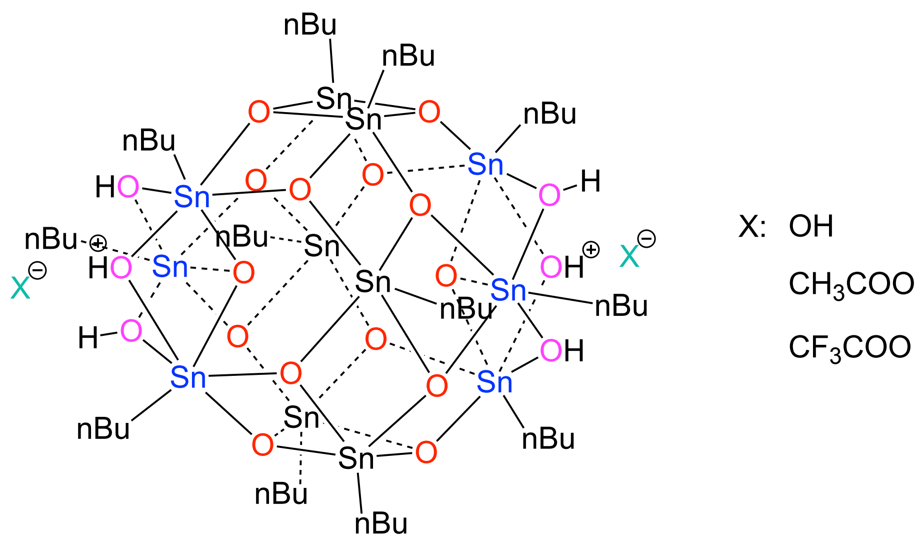

Figure 5.1. *Tin oxo cages with same cage structure but three different counterions: hydroxide (OH), acetate (A), trifluoroacetate (F).*

In this study, we investigated three kinds of tin oxo cages with the same cage structure but three different counterions (hydroxide, acetate, trifluoroacetate) ($[(RSn)_{12}O_{14}(OH)_6]X_2$, TinOH, TinA and TinF as shown in Fig. 5.1) as model photoresists, to investigate the relationship between photon absorption, the chemical reaction and the solubility change of the photoresist. A 225 nm DUV laser was used as irradiation source. In order to measure the photon absorption of the photoresist in the DUV range, the resists were prepared as thin films on quartz substrates. UV-vis

absorption changes during the DUV exposure were monitored. Additionally, the chemical changes of the photoresist before and after exposure were investigated by synchrotron-based hard X-ray photoelectron spectroscopy. To minimize the effect of oxygen and water, all the exposures were done in dry N_2 atmosphere. By comparing the UV absorption coefficient and the chemical reaction efficiency, the relationship between the photon absorption of the photoresist and the chemical reaction yield of the tin oxo cage photoresists become clearer.

5.2 Experiment

5.2.1 Sample preparation

As in our previous work, tin oxo cages with hydroxide, acetate, and trifluoroacetate as counterions (TinOH, TinA and TinF) were obtained according to the synthesis method described in the literature.[18, 19, 20] A structure diagram of the tin oxo cages is shown in Fig. 5.1. UV transparent quartz substrate with thickness 500 ± 20 μm where purchased from SIEGERT WAFER and cut into 1 × 1 cm^2 squares for the UV-vis absorption measurement. It was cleaned with piranha-base before thin film preparation. Glass coverslips from Menzel Gläser were cut into 1 × 1 cm^2 squares coated with 2 nm Cr and 18 nm Au layers using a sputter coater (Leica EM ACE 600 Double sputter coater) and used as substrates for X-ray photoelectron spectroscopy measurement. 2-inch Si wafer was purchased from SIEGERT WAFER and it was pretreated with HMDS for photoresist dose contrast curve measurement. The tin oxo-cage materials were dissolved in toluene individually to a concentration of ~7.5 mg mL^{-1}. Solutions were filtered through a 0.25 μm PTFE filter before spin coating on different substrates. Around 20 nm thin films were achieved by spin-coating the solutions with 2500 rpm for 45 s. The spin coated samples were prebaked at 90 ^{o}C for 1 min.

5.2.2 Exposure

Exposures were done with a YAG-pumped OPA laser (Ekspla NT342B) which provided nanosecond pulses at 225 nm at 10 Hz (2.5 mJ/pulse). Samples for UV-vis spectroscopy and for dose contrast curves were exposed to 225 nm DUV with a sequence of doses. Samples for HAXPES were exposed to 1.3 J cm^{-2}. All the exposures were done in a sample chamber with continuously flushing with dry N_2.

5.2.3 Characterization

UV-vis spectra were measured using a Shimazu UV-2600 spectrometer. A Bruker Dimension Icon Atomic Force Microscope (AFM) was used to characterize the thin film thickness. Hard X-ray photoelectron spectroscopy (HAXPES) located at the HIKE end station, BESSY-II, Helmholtz-Zentrum-Berlin was used to record X-ray photoelectron spectra.[21] In this work, 2005 eV was used as the photon energy. Both

the overview spectra including all relevant lines, and high-resolution spectra of Sn 3d, C 1s, O 1s and F 1s were recorded. All the spectral positions were corrected with the Au $4f_{7/2}$ reference at 84.0 eV and the spectra were further analyzed using Igor Pro software.

5.3 Result and Discussion

5.3.1 UV-Vis spectra

The UV-vis spectra of the TinOH, TinA and TinF are shown in Fig. 5.2. All the three tin oxo cages give strong absorption at ~225 nm. The samples were exposed to 225 nm laser with a series of doses (from 0 to 3 J cm^{-2}), and the UV-vis spectrum was recorded immediately after each exposure. The intensity of the main peak at 225 nm continuously decreased with increasing dose. To compare the spectral changes of the three cages, the peak absorbances normalized to the original unexposed sample are plotted in Fig. 5.2d. The intensity decreases of TinOH spectra and TinA are similar, and faster than that of TinF.

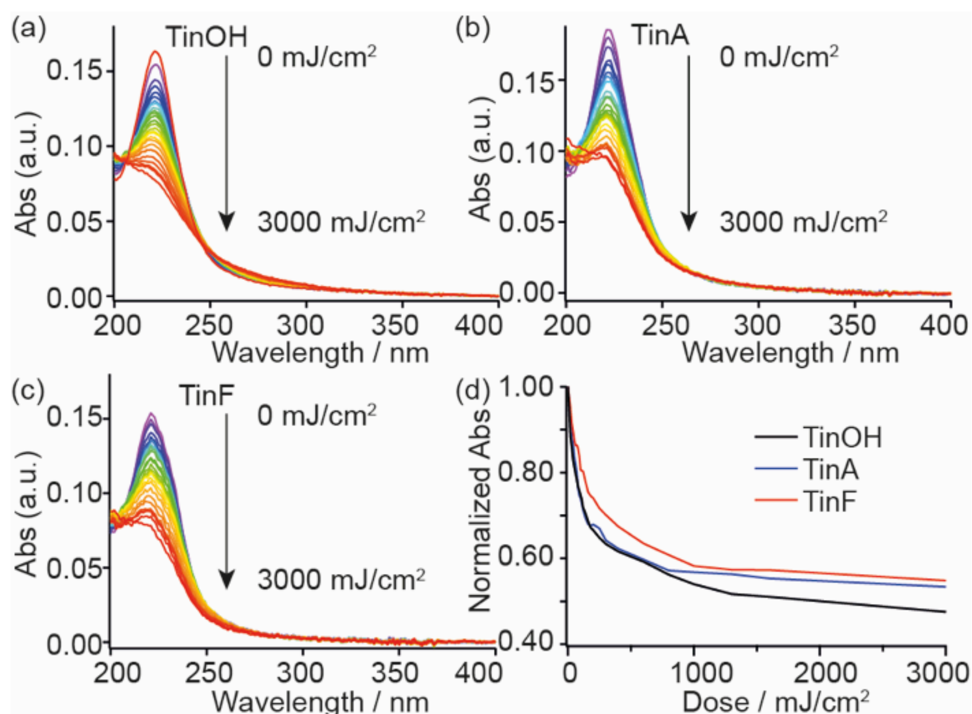

Figure 5.2. *UV-Vis spectra of thin films of (a) TinOH. (b) TinA. (c) TinF. (d) peak intensities vs. dose.*

The films thicknesses of the cages on quartz were measured as 20 ± 2 nm. The densities of the thin films were assumed to be the same as the TinOH crystal density

(1.84 g cm^{-3}).[22] The absorption coefficients of the three unexposed tin oxo cages can be calculated from the spectra based on Lambert-Beer's Law. We find that the linear absorption coefficient of TinOH, TinA, and TinF to be 18.8 μm^{-1}, 20.5 μm^{-1} and 17.8 μm^{-1} respectively, which are the same within experimental error. When 1.3 J cm^{-2} DUV dose (equal to 1.5×10^{18} photons) is used to expose the sample. TinOH, TinA and TinF can absorb ~550 photons/molecule. The decrease of the UV-vis absorption at 225 nm was 48 % for TinOH, 46 % for TinA and 43 % for TinF.

5.3.2 Overview XPS spectra

Thin films prepared from TinOH, TinA and TinF were further characterized by means of HAXPES. The overview spectra of TinOH, TinA and TinF are shown in Fig. 5.3. As expected, the Sn 3d $_{5/2}$ at ~487 eV, O 1s at ~531 eV, C 1s at ~285 eV and F 1s at 688 eV peaks from the photoresist thin films and Au $4f_{7/2}$ at 84 eV from the Au layer underneath are clearly observed in the spectra. The elemental composition of the three tin oxo cages thin films was verified using the overview spectra, because the peak areas are proportional to the amount of each element present in the sample. We assume the tin atoms do not escape from the thin films during the exposure, so all the other element peaks in the exposed samples were normalized to Sn 3d (equal to 12 Tin atoms). The calculated elemental ratios of the samples are listed in the Table 5.1, where we can see that the atomic composition of the unexposed sample agrees well with the theoretical elemental ratio from the molecules. We also compare the atomic ratio after exposure to a very high dose of UV. In all the three kinds of tin oxo cages the carbon fraction decreased, by 25 % in TinOH, 27 % in TinA and 50 % in TinF. The oxygen number almost stayed the same for all the tin oxo cages. In the TinF, the fluorine atom number decreased from 6 to 3, indicating -CF_3 group cleaved and diffused into the N_2. If we calculate the chemical reaction efficiency by calculating the carbon atomic ratio change in the tin oxo cages, the chemical reaction yield of the TinF is apparently higher than TinOH and TinA. It didn't show clear connection between the photon absorption and chemical reaction yield. Since the only difference among the three tin oxo cages is at the counterion part, we can propose the counterion part can affect the chemical reaction yield.

Table 5.1. *Atomic ratio of tin oxo cage before and after exposure.*

	TinOH			TinA			TinF			
Atom	Sn	O	C	Sn	O	C	Sn	O	C	F
Theory	12	22	48	12	22	52	12	22	52	6
Unexposed	12	22	48	12	24	51	12	24	50	6
Exposed	12	22	36	12	24	38	12	24	26	3

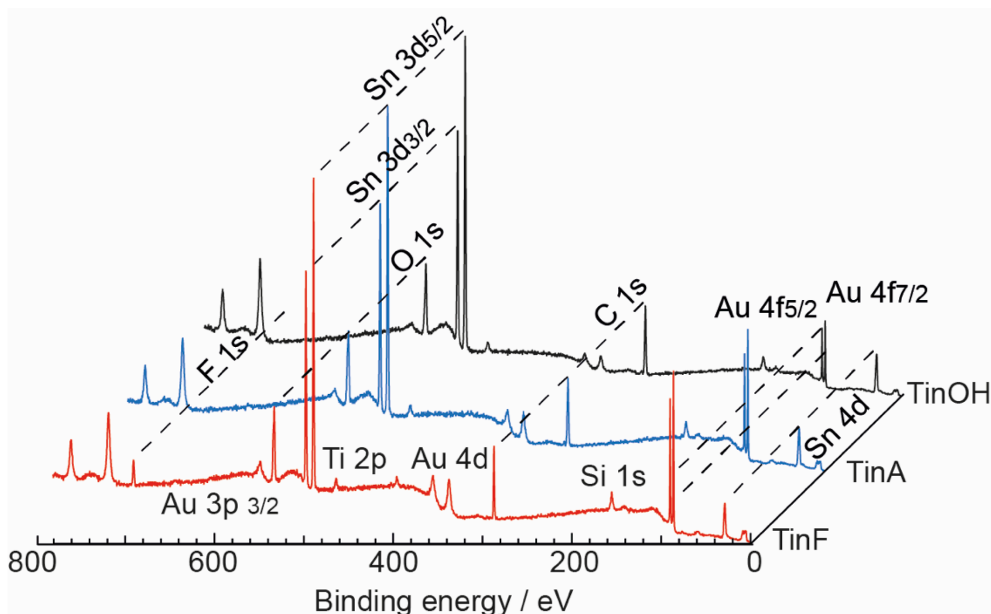

Figure 5.3. *The survey overview spectra of unexposed TinOH, TinA and TinF thin films.*

5.3.3 High-resolution XPS spectra

High-resolution Sn 3d spectra of the three tin oxo cages are shown in Fig. 5.4. All the binding energies were calibrated with respect to Au $4f_{5/2}$ (84.0 eV). For all the tin oxo cages samples, the $Sn3d_{5/2}$ peak positions are at ~487 eV. For unexposed samples, the Sn $3d_{5/2}$ peak positions are at 487.0 eV (TinOH), 486.9 eV (TinA) and 486.8 eV (TinF). Since all the tin atoms are from the core cage part, which is the same for the three tin oxo cages, the Sn $3d_{5/2}$ peaks are almost at the same position. But the full widths at half maximum (FWHM) of the Sn $3d_{5/2}$ band are different: 1.36 eV, 1.29 eV and 1.14 eV, for TinOH, TinA and TinF, respectively. Apparently, the counterions affect the electron distribution in the tin cage via their hydrogen bonding to the bridging OH groups. The difference in the binding energies of the 6-coordinated and 5-coordinated Sn atoms are increased when the hydrogen bond donor is stronger (OH^- > ^-OAc > $^-O_2CCF_3$). After the tin oxo cages are exposed to DUV, only the Sn 3d $_{5/2}$ peak position of TinOH slightly shifted to lower binding energy (486.8 eV). The Sn $3d_{5/2}$ peaks of TinA and TinF stay at the same position. The FWHM of the Sn $3d_{5/2}$ from three tin oxo cages became narrower, TinOH is 1.27 eV; TinA is 1.17 eV; TinF is 1.13 eV.

By using the same method as in our previous work,23 the green sub-peak in Fig. 5.4 represents the 6-coordinated tin atoms in the side part of the cages, and the pink sub-peak represents the 5-coordinated tin atoms in the middle part of the cage. We

assumed there are only the two kinds of tin atoms in both the unexposed and exposed samples. After exposure, the ratio between the two sub-peaks was changed as calculated in the Table 5.2.

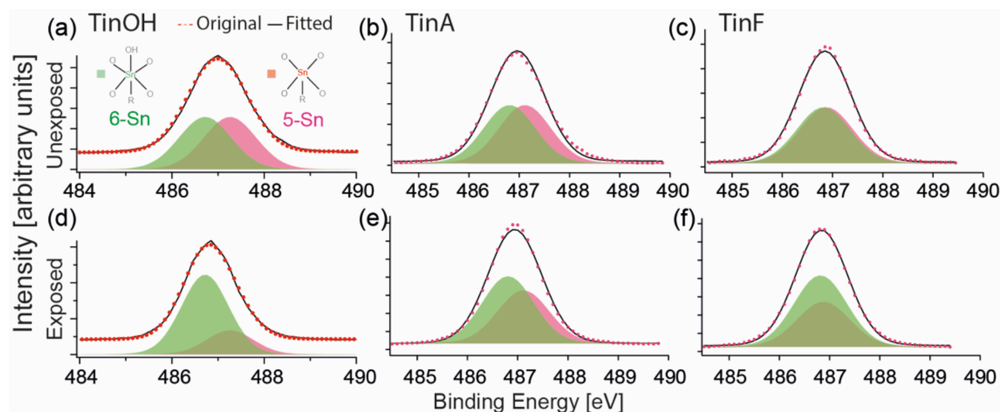

Figure 5.4. *Sn3d $_{5/2}$ spectra of TinOH (a,d), TinA (b,e) and TinF (c,f) before and after exposure in dry N_2.*

Table 5.2. *Relative numbers of two types of tin atoms derived from Sn 3d$_{5/2}$ spectra as well as extracted binding energies of the respective features (see Fig.5.4).*

	atom no.	6-Sn	5-Sn
TinOH	BE (eV)	486.7	487.3
	Unexp	6	6
	exposed	9.2	2.8
TinA	BE (eV)	486.8	487.1
	Unexp	6	6
	exposed	6.7	5.3
TinF	BE (eV)	486.8	486.9
	Unexp	6	6
	exposed	7.4	4.6

By using the same method, high-resolution O 1s spectra of the three cages are analyzed as shown in Fig. 5.5. As shown in the spectra, there is no obvious shifting after exposure. Similarly, three sub-peaks representing the oxygen atoms in Sn-O, Sn-OH and connected counterions (OH^- in TinOH, CH_3COO^- in TinA and CF_3COO^- in TinF) were fitted in the spectra. In the spectra of the unexposed sample, the three sub-peaks were fitted according to the ratio 14: 6: 2 for TinOH and 14: 6: 4 for TinA and TinF. After exposure, the number of oxygen atoms in all three cages is barely changed. But the shapes of the O 1s spectra are changed,

indicating the chemical environment of the oxygen atoms in the film are changed. As before, we model the spectra with only three kinds of oxygen atoms in the cages after exposure. The contributions of the three sub-peaks are calculated and listed in Table 5.3 together with the binding energy. As shown in Table 5.3, the total oxygen number in the TinOH didn't change, but the Sn-OH shoulder increased slightly which could due to the hydroxide counterion attach to the cage part further change the chemical environment of oxygen in hydroxide slightly. For TinA and TinF, both the COO- and Sn-OH sub-peaks increased. Since the total oxygen atom number did not change, some rearrangements at the oxygen atoms must have occurred.

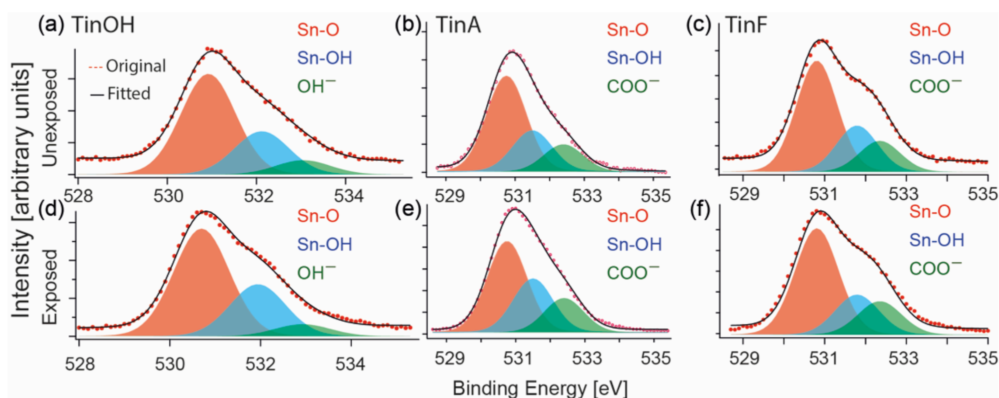

Figure 5.5. *O 1s spectra of TinOH (a,d), TinA (b,e) and Tin F(c,f) before and after exposure in dry* N_2*.*

Table 5.3. *Relative numbers of three types of oxygen atoms derived from O 1s spectra as well as extracted binding energies of the respective features (see Fig.5.5).*

atom no.		Sn-O	Sn-OH	COO/OH
TinOH	BE (eV)	530.7	532.1	533.0
	Unexp	14	6	2
	exp	14	6.7	1.5
TinA	BE (eV)	530.8	531.5	532.5
	Unexp	14	6	4
	exp	11	8.5	5.0
TinF	BE (eV)	530.8	531.9	532.4
	Unexp	14	6	4
	exp	14	5.7	3.9

High-resolution C 1s spectra of the three tin oxo cages are shown in Fig. 5.6. Sub-peaks were fitted to the C 1s spectra according to the different chemical environments in the cages. We assumed the main C 1s peak (~285 eV) originates from CH_2 and CH_3 of the butyl groups and stays at the same position for all the samples, regardless of unexposed or exposed samples. The changes are mainly at the 286.4 eV shoulder from C-O and the peak at around 289.3 eV from C=O. The carbon atoms connected with F have a specific peak around 293 eV. According to our previous work, sub-peaks representing six carbon types 6-Sn-C, 5-Sn-C, C-C, CO, COO and $–CF_3$ were fitted into the spectra. As shown in Fig. 5.6, the ratio between different C atoms are changed significantly after exposure. In the TinOH spectra, there is a clear peak rising at ~289 eV, and a shoulder growing up at ~286 eV. For TinA the shoulder at ~286 eV becomes much stronger. For TinF, similar with TinA, the shoulder at ~286 eV becomes more obvious. But the contribution of carbon from the $–CF_3$ group at ~293 eV is decreased relative the COO sub-peak. The ratios between the different carbon atoms were calculated and are listed in Table. 5.4.

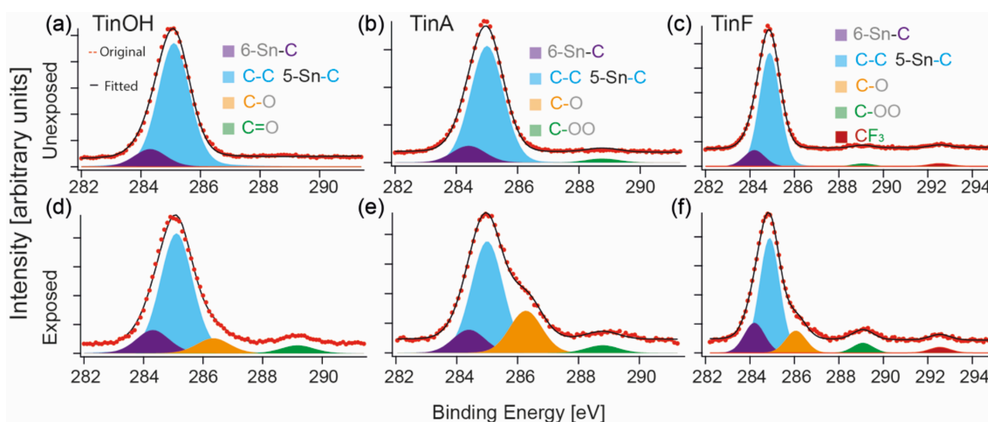

Figure 5.6. *C 1s spectra of TinOH (a,d), TinA (b,e) and TinF (c,f) before and after exposure in dry N_2.*

As shown in Table 5.4, similar with our previous work,[23] apparently, the Sn-C bond cleaved and the generated butyl radical could abstract a hydrogen atom to form butane, or donate a hydrogen atom to form butene. Also, products can be formed with the butyl group attached to O atoms, as shown by the *in situ* exposure experiments in Chapter 7. In the present experiments, however, some oxygen-containing products could arise from reaction of photoproducts that are sensitive to oxidation during transfer between instruments, in which brief contact with the ambient air could not be fully avoided. These two processes can explain why the oxygen number did not change to a measurable extent, but the C 1s peak shape

changed and the shoulder increased at 286.4 eV. The atomic ratio of carbon from C-O is higher in TinA than TinOH and TinF. We assumed that the counterion could change the electron distribution in the cage part, and the oxygen in the TinA can react with the cleaved butyl radical forming C-O bond easier than in the TinOH. The $-CF_3$ ratio decrease also indicate the counterion could participate in the chemical reaction during the exposure.

Table 5.4. *Relative numbers of two types of carbon atoms derived from C 1s spectra as well as extracted binding energies of the respective features (see Fig. 5.6).*

		Sn-C	C-C	C-O	C=O/COO	$-CF_3$
TinOH	BE (eV)	284.4	285.2	286.4	289.3	--
	Unexp	6.0	42.0	0	0	--
	exp	5.1	26	3.3	1.7	--
TinA	BE (eV)	284.4	285.0	286.3	288.8	--
	Unexp	6.0	43	0	2	--
	exp	4.8	23	8.7	1.6	--
TinF	BE (eV)	284.2	284.9	286.1	289.1	292.5
	Unexp	6.0	40	0	2.0	2.0
	exp	4.3	16	3.2	1.4	0.8

There is no obvious shifting in the F 1s peak from the TinF. The possible reason could be the $-CF_3$ is directly cleaved without any further reaction with the cage and then diffused out into the atmosphere, which is in agreement with what has been observed from the C 1s peak at $-CF_3$ position.

5.3.4 Dose contrast curve

Solubility changes of the tin oxo cages were tested by the dose contrast curves. The thin films were exposed with a sequence of doses, and developed using a 2:1 IPA/H_2O mixture for 30 s. After development, the film thicknesses were measured with AFM. The dose contrast curves are shown in Fig. 5.7 as plots of the remaining film thickness vs the input dose.

The minimum dose needed to convert the photoresists into fully insoluble are 34 mJ cm^{-2} (TinOH), 40 mJ cm^{-2} (TinA) and 110 mJ cm^{-2} (TinF). The contrast of the three photoresist can be calculated by using the following equation[24, 25]:

$$\gamma = \left[\log\left(\frac{D_f}{D_i}\right)\right]^{-1}$$

Where D_i is the dose induced a negative tone photoresist first to become insoluble and D_f is the dose induced the negative tone photoresist into fully insoluble. The contrasts of the three photoresists calculated from the equation are 2.11 ± 0.03 (TinOH), 1.66 ± 0.01 (TinA) and 0.96 ± 0.08 (TinF). This observation is in line with the UV absorption experiments. The higher carbon loss in TinF after the high exposure dose of 1.3 J cm^{-2} is perhaps not that relevant for the photoresist performance, which in all cases requires < 100 mJ cm^{-2}.

The three anions used differ in basicity, nucleophilicity, and hydrogen bond acceptor strength, all increasing in the series CF_3COO^- < CH_3COO^- < OH^-. Since there is a clear difference in the reactivity we conclude that at some stage of the photoinduced chain of reactions the anion does play a role. It could abstract protons, or bond directly to tin atoms.

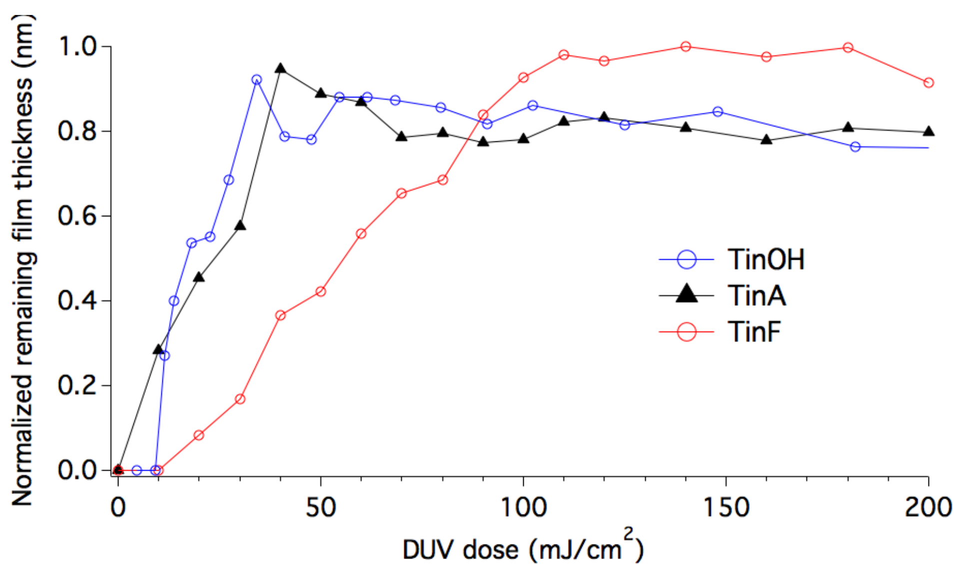

Figure 5.7. *Dose contrast curves of TinOH, TinA and TinF under 225 nm DUV exposure.*

5.4 Conclusions

In this work, the UV photoresponses of three tin oxo cages photoresists with different counterions were compared. The absorption coefficient of the three cages, the chemical reaction yield and the solubility changes in the resist layer were characterized. The UV sensitivity of TinOH and TinA was clearly higher than that of TinF. Since the anions in the former two compounds are more basic and nucleophilic than the trifluoroacetate anion, this suggests that the anions are involved in the chemical process that leads to solubility switching.

5.5 References

1. J. Passarelli, M. Murphy, R. Del Re, M. Sortland, J. Hotalen, L. Dousharm, R. Fallica, Y. Ekinci, M. Neisser, D. A. Freedman and R. L. Brainard, "Organometallic carboxylate resists for extreme ultraviolet with high sensitivity", *J. Micro/Nanolitho. MEMS MOEMS*, 2015, **14**, 043503.
2. B. Cardineau, R. Del Re, M. Marnell, H. Al-Mashat, M. Vockenhuber, Y. Ekinci, C. Sarma, D. A. Freedman and R. L. Brainard, "Photolithographic properties of tin-oxo clusters using extreme ultraviolet light (13.5 nm)", *Microelectron. Eng.*, 2014, **127**, 44-50.
3. L. Li, S. Chakrabarty, K. Spyrou, C. K. Ober and E. P. Giannelis, "Studying the Mechanism of Hybrid Nanoparticle Photoresists: Effect of Particle Size on Photopatterning", *Chem. Mater.*, 2015, **27**, 5027-5031.
4. S. Chakrabarty, C. Ouyang, M. Krysak, M. Trikeriotis, K. Cho, E. P. Giannelis and C. K. Ober, "Oxide nanoparticle EUV resists: toward understanding the mechanism of positive and negative tone patterning", *Proc. SPIE*, 2013, **8679**, 86790601-08.
5. S. Chakrabarty, C. Sarma, L. Li, E. P. Giannelis and C. K. Ober, "Increasing sensitivity of oxide nanoparticle photoresists", *Proc. SPIE*, 2014, **9048**, 90481C01.
6. C.-C. Yeh, H.-C. Liu, W. Heni, D. Berling, H.-W. Zan and O. Soppera, "Chemical and structural investigation of zinc-oxo cluster photoresists for DUV lithography", *J. Mater. Chem. C*, 2017, **5**, 2611-2619.
7. A. F. Demirors, P. P. Pillai, B. Kowalczyk and B. A. Grzybowski, "Colloidal assembly directed by virtual magnetic moulds", *Nature*, 2013, **503**, 99-103.
8. J. Bauer, L. R. Meza, T. A. Schaedler, R. Schwaiger, X. Zheng and L. Valdevit, "Nanolattices: An Emerging Class of Mechanical Metamaterials", *Adv. Mater.*, 2017, **29**, 1701850.
9. B. L. Henke, E. M. Gullikson and J. C. Davis, "X-Ray Interactions: Photoabsorption, Scattering, Transmission, and Reflection at E = 50-30,000 eV, Z = 1-92", *Atomic Data and Nuclear Data Tables*, 1993, **54**, 181-342.
10. R. Fallica, J. K. Stowers, A. Grenville, A. Frommhold, A. P. G. Robinson and Y. Ekinci, "Dynamic absorption coefficients of chemically amplified resists and nonchemically amplified resists at extreme ultraviolet", *J. Micro/Nanolitho. MEMS MOEMS*, 2016, **15**, 03350601-07.
11. R. Fallica, J. Haitjema, L. Wu, S. Castellanos, A. M. Brouwer and Y. Ekinci, "Absorption coefficient and exposure kinetics of photoresists at EUV", *Proc. SPIE*, 2017, **10143**, 101430A.
12. S. T. Meyers, J. T. Anderson, J. B. Edson, K. Jiang, D. A. Keszler, M. K. Kocsis, A. J. Telecky and B. Cardineau, *US 2016/0116839 A1*, 2015.
13. S. T. Meyers, J. T. Anderson, J. B. Edson, K. Jiang, D. A. Keszler, M. K. Kocsis, A. J. Telecky and B. Cardineau, *US 9310684B2*, 2016.
14. E. Buitrago, R. Fallica, D. Fan, T. S. Kulmala, M. Vockenhuber and Y. Ekinci, "SnOx high-efficiency EUV interference lithography gratings towards the ultimate resolution in photolithography", *Microelectron. Eng.*, 2016, **155**, 44-49.

15. A. Grenville, J. T. Anderson, B. L. Clark, P. D. Schepper, J. Edson, M. Greer, K. Jiang, M. Kocsis, S. T. Meyers, J. K. Stowers, A. J. Telecky, D. De Simone and G. Vandenberghe, "Integrated fab process for metal oxide EUV photoresist", *Proc. SPIE*, 2015, **9425**, 94250S01.
16. R. Del Re, J. Passarelli, M. Sortland, B. Cardineau, Y. Ekinci, E. Buitrago, M. Neisser, D. A. Freedman and R. L. Brainard, "Low-line edge roughness extreme ultraviolet photoresists of organotin carboxylates", *J. Micro/Nanolitho. MEMS MOEMS*, 2015, **14**, 043506.
17. A. Narasimhan, S. Greskowiak, B. Srivats, H. Herbol, L. Wisehart, J. Schad, C. Kelly, W. Earley, L. E. Ocola, M. Neisser, G. Denbeaux and R. L. Brainard, "Studying thickness loss in extreme ultraviolate resists due to electron beam exposure using experiment and modeling", *J. Micro/Nanolitho. MEMS MOEMS*, 2015, **14**, 043502.
18. C. Eychenne-Baron, F. Ribot and C. Sanchez, "New synthesis of the nanobuilding block $\{(BuSn)_{12}O_{14}(OH)_6\}^{2+}$and exchange properties of $\{(BuSn)_{12}O_{14}(OH)_6\}(O_3SC_6H_4CH_3)_2$", *J. Organomet. Chem.*, 1998, **567**, 137-142.
19. J. Haitjema, Y. Zhang, M. Vockenhuber, D. Kazazis, Y. Ekinci and A. M. Brouwer, "Extreme ultraviolet patterning of tin-oxo cages", *J. Micro/Nanolitho. MEMS MOEMS*, 2017, **16**, 033510.
20. L. Van Lokeren, R. Willem, D. van der Beek, P. Davidson, G. A. Morris and F. Ribot, "Probing the Anions Mediated Associative Behavior of Tin-12 Oxo-Macrocations by Pulsed Field Gradient NMR Spectroscopy", *J. Phys. Chem. C*, 2010, **114**, 16087-16091.
21. F. Schaefers, M. Mertin, M. Gorgoi, "KMC-1: A high resolution and high flux soft x-ray beamline at BESSY", *Rev. Sci. Instrum.*, 2007, **78**, 123102.
22. F. R. Frederic Banse, P. Toladeno, J. Maquet, C. Sanchez, "Hydrolysis of Monobutyltin Trialkoxides: Synthesis and Characterizations of $\{(BuSn)_{12}O_{14}(OH)_6\}(OH)_2$", *Inorg. Chem.*, 1995, **34**, 9.
23. Y. Zhang, J. Haitjema, X. Liu, F. Johansson, A. Lindblad, S. Castellanos, N. Ottosson and A. M. Brouwer, "Photochemical conversion of tin-oxo cage compounds studied using hard x-ray photoelectron spectroscopy", *J. Micro/Nanolitho. MEMS MOEMS*, 2017, **16**, 023510.
24. Y. Ekinci, H. H. Solak, C. Padeste, J. Gobrecht, M. P. Stoykovich and P. F. Nealey, "20 nm Line/space patterns in HSQ fabricated by EUV interference lithography", *Microelectron. Eng.*, 2007, **84**, 700-704.
25. S. A. Campbell, in The Science and Engineering of Microelectronic Fabrication, *Oxford University Press,*, 2001, 188.

Chapter 6

Extreme ultraviolet patterning of tin-oxo cages*

We report on the extreme ultraviolet (EUV) patterning performance of tin-oxo cages. These cage molecules were already known to function as a negative tone photoresist for EUV radiation, but in this work, we significantly optimized their performance. Our results show that sensitivity and resolution are only meaningful photoresist parameters if the process conditions are optimized. We focus on contrast curves of the materials using large area EUV exposures and patterning of the cages using EUV interference lithography. It is shown that baking steps, such as post-exposure baking (PEB), can significantly affect both the sensitivity and contrast in the open-frame experiments as well as the patterning experiments. Thicker layers render lower EUV doses to induce a solubility change but decreased the patterning quality. The patterning experiments were affected by minor changes in processing conditions such as rinsing time. In addition, we show that the anions of the cage can influence the sensitivity and quality of the patterning, probably through their effect on physical properties of the materials.

* This chapter was published in modified form in J. Haitjema, Y. Zhang, M. Vockenhuber, D. Kazazis, Y. Ekinci and A. M. Brouwer, "Extreme ultraviolet patterning of tin-oxo cages", *J. Micro/Nanolitho. MEMS MOEMS*, 2017, **16**, 7.[1]

6.1 Introduction

Extreme ultraviolet lithography (EUVL) is a powerful technique, which can further improve the resolution of patterning in advanced semiconductor manufacturing. Nevertheless, there are still many challenges to be overcome for the introduction of EUVL into high volume manufacturing. One of these challenges is the photoresist performance. The high energy per photon means fewer photons for the same dose compared to previous optical lithography based on ultraviolet light, which exacerbates stochastic noise related to photon absorption events.[2] This leads to increased line edge roughness and puts limits on the achievable resolution for a given dose. One way to get more chemical conversion per absorbed photon is to use chemical amplification mechanisms such as in acid sensitive resists.[3] However, the photoacid generators and their quenchers are randomly distributed, causing further stochastic effects.[4] Quenchers, in particular, are known to have a large contribution to stochastic noise, as a result of their low concentration in the photosensitive layer.[5]

For these reasons, it is interesting to search for alternative materials with improved properties, such as metal-containing compounds. These have a larger absorption cross section for EUV photons, which contributes to an increase in sensitivity.[6] This may eliminate the need for chemical amplification, removing statistical uncertainties in the position of photoacid generators and quenchers. Metal-containing compounds also have an improved etch resistance compared to conventional chemically amplified resists (CARs).[7, 8]

Nanoparticles, introduced by Trikeriotis et al.[8] and organic-inorganic hybrid compounds have demonstrated photoresist performance.[9, 10] Since the latter materials are molecular, they are well defined with a single particle size, as opposed to the nanoparticle systems. Tin-oxo cages are the subject of the present work (see Fig. 6.1).[11] The cage has a 2+ charge and is therefore stabilized by one or two counterions.

The tin-oxo cage molecules can be regarded as the tin analog of the silicon-containing silsesquioxane class of compounds. Hydrogen silsesquioxane (HSQ) is the most prominent member of this family, and it has been used to achieve high resolution patterning with both e-beam and EUV lithography.[12] However, the sensitivity of HSQ is very low, mainly due to the low EUV absorption. EUV absorption can be increased significantly by incorporating metal atoms that strongly absorb EUV light. It is not possible to directly replace silicon with tin in HSQ due to the larger size of the tin atom. The tin-oxo cage material is a similar building block with a slightly different shape. The calculated linear absorption coefficient (α) for TinS is 13.3 μm^{-1} assuming a density of 1.9 g cm^{-3} taken from the crystal

structure,[13] and using atomic EUV absorption coefficients reported in the literature.[14] Recently, the absorption coefficients α for some of the tin cage materials were measured,[15] and found to be in good agreement with the predicted ones.

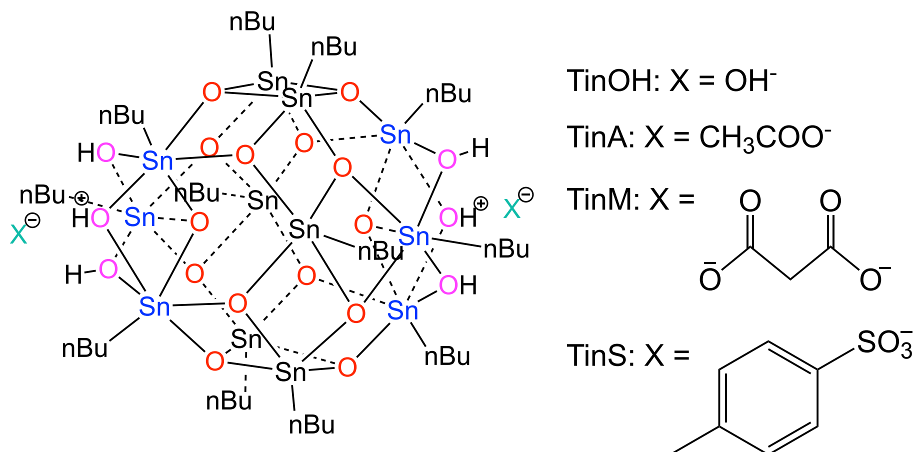

Figure 6.1. *Tin-oxo cages with four different anions: hydroxide (TinOH), acetate (TinA), malonate (TinM) and tosylate (TinS). For the malonate, the ratio of tin cages to malonate anions is 1:1.*

The absorption coefficient α of organic polymer-based resist is typically ~5 μm^{-1}, whereas tin-based materials from Inpria Corp. show higher absorption coefficients, even up to 20 μm^{-1}.[16] While a large absorption coefficient favors sensitivity, it is not known how efficiently absorbed photons induce a change in solubility of these materials, nor is it known what the maximum achievable efficiency is.

The tin-oxo cage system has the advantage that two structural features can be readily altered: the anions at the side of the cage (X^-) and the organic groups (n-butyl chains in Fig. 6.1). In this study, we focus on the EUV patterning of some selected materials of this class. The chemical changes upon exposure to short-wavelength UV light are discussed elsewhere.[17, 18]

6.2 Materials and methods

6.2.1 Materials

We synthesized the tin-oxo cage with two tosylates as the anions (TinTs) according to a procedure described by Eychenne-Baron et al.[19] The dihydroxide form of the tin cage (TinOH) was obtained using a procedure described by Eychenne-Baron et al.[19] A 20 wt.% solution of TinS in isopropanol (IPA) was mixed with a solution of aqueous tetramethylammonium hydroxide (TMAH) in IPA. The TMAH was used

in excess (2.3×). Precipitation occurred instantaneously. The resulting suspension was filtered to obtain a white powder. The diacetate (TinA) and malonate (TinM) analogues of the tin cluster were obtained using a procedure described by van Lokeren et al.[20] More details about synthesis can be found in the reference 1. NMR analysis was carried out using a Bruker AV-400 NMR spectrometer. The ^{1}H and ^{119}Sn NMR spectra were found to be in agreement with the literature.[11, 13, 19] The thermogravimetic analysis (TGA) of TinOH was performed using a NETZSCH thermogravimetric analyzer, using 22.2 mg of sample in an Al_2O_3 crucible. Heating was performed from 35 °C to 800 °C at 10 K min^{-1}. in an 80% / 20% N_2 / O_2 atmosphere.

For a typical thin film of ~40 nm thickness, a solution of the tin-oxo cage (with any of the counterions except malonate) of 15 mg mL^{-1} in toluene is made using sonication (30 s). The malonate form did not sufficiently dissolve in toluene and was therefore dissolved in methanol. Particulates were removed by filtering the solutions using an 0.2 µm syringe filter before spin coating. The solutions were spun on Si wafers (for interference lithography) and on 2 × 2 cm^2 Si chips (for open-frame experiments) with a spin speed of 2500 rpm for 45 s, with a subsequent soft bake of 30 s at 90 °C. Both wafers and chips were treated with hexamethyldisilazane (HMDS) before spin coating. After exposure, the samples were developed using a 2:1 IPA/H_2O mixture for 30 s and rinsed for 10 s with H_2O.

6.2.2 EUV exposure

EUV exposures were carried out at the XIL-II beamline of the Swiss Light Source (SLS) synchrotron at the Paul Scherrer Institut (PSI) with EUV light of λ = 13.5 nm.[21] For the open-frame experiments, 0.5 × 0.5 mm^2 areas were exposed to EUV light through a square aperture. For the patterning experiments, a transmission mask was used providing line/space patterns with pitches of 100, 80, 60 and 44 nm.

6.2.3 Post-exposure analysis

Atomic force microscopy (AFM) images were made using a Bruker Dimension Icon, using the PeakForce tapping (ScanAsysAir) mode. Perpendicular to the resist edge, fields of 40 × 5 µm^2 were scanned with 128 samples/line, using a scan speed of 0.5 Hz. The raw images were corrected for bowing using first- and Second-order corrections, and film thickness was measured by comparing the height of the film with the height of the substrate, as shown in Fig. 6.2. Scanning Electron Microscopy (SEM) imaging was performed using a Carl Zeiss SUPRA 55VP SEM with a voltage of 1 kV.

6.3 Result and Discussion

6.3.1 Open-frame experiments: contrast curves

Contrast curves (also known as H-D curves or characteristic curves) were obtained by measuring the remaining thickness after development as a function of EUV exposure dose using AFM imaging (see experimental section).

A typical AFM image of the material edge is shown in Fig. 6.2. Here, the left part of the image corresponds to the bare Si substrate that became uncoated after the unexposed material was removed by the developer. The right part of the image shows exposed and therefore insoluble material. It can be seen that the edge of the profile is partly covered by a wave pattern, caused by interference effects (knife-edge effect). To measure the remaining thickness correctly, the height of the resist was measured as far from the edge as possible and averaged over a certain distance window.

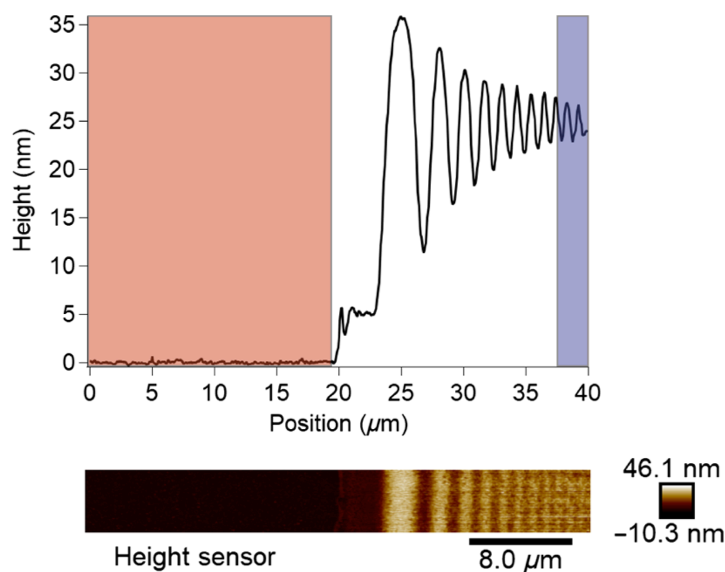

Figure 6.2. *AFM image of the material edge (top). Image height was corrected using a second-order flattening procedure. The height values of the image were then averaged along the y-axis to produce an edge cross section (top). The average substrate height (red) was compared with the average photoresist height far from the edge (blue).*

Contrast curves were first used to compare compounds with different counterions, TinOH and TinA. The anion of the tin cage can not only alter the reaction of the material to EUV excitation,[11] but also its physical properties such as solubility. For instance, doubly charged anions such as malonate combined with the cage

compound render the material more polymeric in nature because the tin cage can form elongated chains with the doubly charged counterion.[20]

TinOH and TinA were spin coated with a subsequent post-application bake (90°C) before exposure (see experimental). They did not differ significantly in their sensitivity judging from the contrast curves (Fig. 6.3). This could mean that the anions are not directly involved in the mechanism that leads to the solubility switch. They could act as nonreactive spacers, as was proposed by Cardineau et al.[11] We can observe the onset of gelation at ~10 mJ cm^{-2} and a maximum thickness at ~50 mJ cm^{-2}. At higher doses, the thickness decreases again. This is likely due to the further loss of butyl chains, in analogy to the results reported for deep UV exposures.[17]

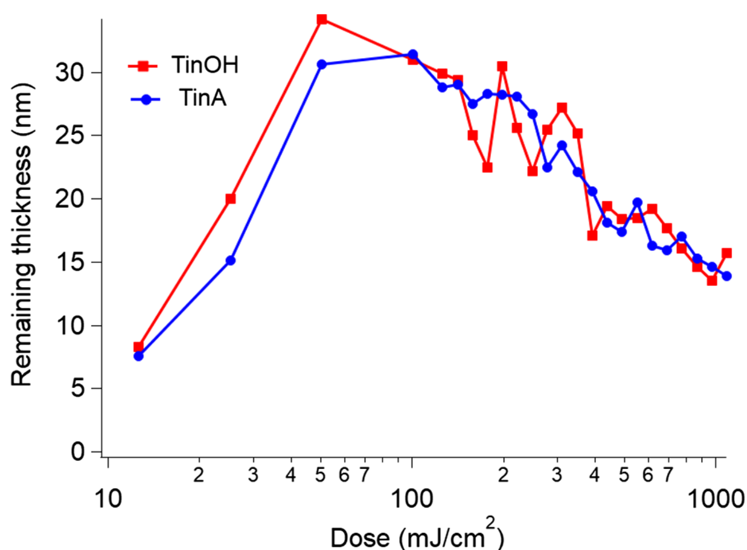

Figure 6.3. *Remaining layer thickness as a function of EUV dose for TinOH and TinA. Initial thickness was ~40 nm. No PEB was applied.*

In addition to the anion effect, improvements to the process can also alter the contrast curves. In fact, photoresist parameters such as sensitivity and resolution are only meaningful concepts if the process conditions are optimized. Parameters that were optimized in this work were: developer, development time, PAB, and PEB. Firstly, the use of a different developer may improve resist performance by providing a larger difference in the solubility rates of the exposed and unexposed areas (solubility contrast). A few other developers instead of the 2:1 IPA/H_2O mixture[11] were tested, such as 2-heptanone.[22] None of them, however, seemed to significantly improve resist performance. For this reason, only the results obtained with the 2:1 IPA/H_2O developer are shown.

Another important processing step is post-exposure baking (PEB). This is well-known for CARs: heating the resist after exposure allows diffusion of the photoacids, and induces the removal of the dissolution inhibiting protecting groups.[23] For non-CARs, the chemical effect of heating is less clear. Although photoacid diffusion does not apply here, the heating could still induce additional chemical reactions of species that were formed during the exposure step. This seem a likely mechanism, since EUV exposures take place in vacuum whereas the photoresist material is baked under ambient atmosphere, enabling reactions of reactive species with oxygen and moisture.

However, the conditions of the PEB should be carefully tuned, since the unexposed material may also change solubility. This can lead to loss of contrast. In the case of a negative tone resist, it is essential that the unexposed part can still be fully cleared by the developer.

The baking effect was studied for two different anions: the hydroxide and the malonate. The malonate form is more polymeric in nature and may, therefore, have a different response to heating. The effect of baking at 100°C for the hydroxide form is shown in Fig. 6.4.

PEB (100 °C, 2 min.) has a significant effect on the sensitivity of the tin-oxo cage material. A lower dose is required to reach the onset of gelation (7 mJ cm^{-2} PEB, 8 mJ cm^{-2} non PEB) and to achieve a remaining thickness of 20 nm, the dose needed is 2× smaller than without PEB. Additionally, the contrast seems to increase, as the initial increase of remaining thickness with dose is ~4 × larger for the baked samples. However, we note that the contrast measured in this way can be different from the theoretical contrast, which is defined as the difference in solubility rate between the exposed and non-exposed parts of the resist.[24] Measuring this more directly, for instance using a quartz crystal microbalance (QCM) would be needed to get an accurate value for the contrast.

The effect of baking was also investigated for a layer with higher initial thickness (60 nm instead of 40 nm). The baking effect was consistent here (see Fig. 6.5). However, we also note a large increase in the sensitivity for a thicker layer of TinOH. Only 2 mJ cm^{-2} was needed for a reasonable remaining thickness (26 nm). Calculations by others show that a reasonable dose at the bottom of the resist layer is required for this type of materials, in order to make the converted material attach to the substrate.[25] However, these results contradict this. Apparently, converted material attaches easily even if it is not in direct connection with the substrate. A thicker layer leads to a larger amount of converted material, which apparently leads to a higher remaining thickness as well. The effect of resist thickness was investigated earlier for CARs in previous work,[26] which also showed dependence of

lithographic performance on layer thickness. For CARs, pattern collapse occurred more often upon increasing layer thickness (25 to 30 nm), though on the other hand, LER decreased. Pattern quality also worsened for tin cage material upon increasing layer thickness (results not shown).

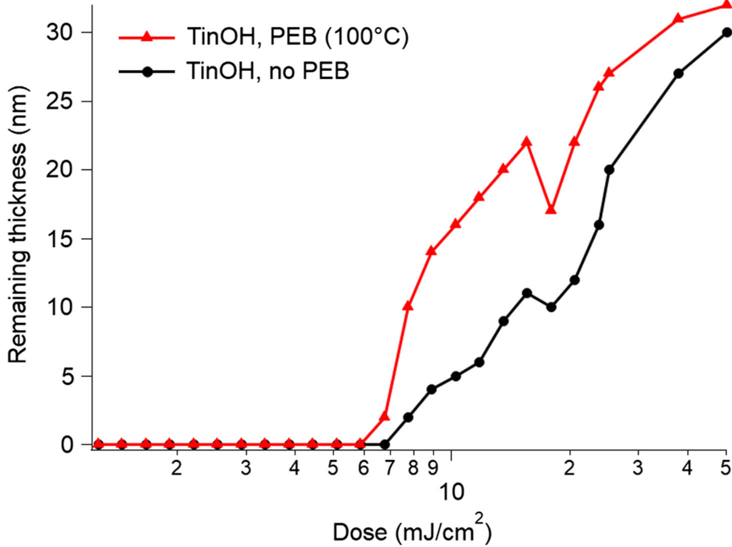

Figure 6.4. *Contrast curves of TinOH, measured without PEB (black) and with PEB at 100 °C (red). Initial thickness was ~40 nm.*

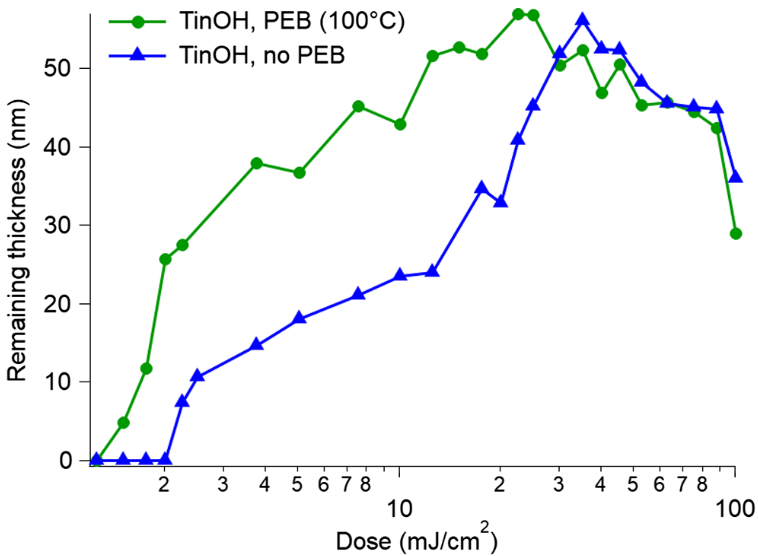

Figure 6.5. *The post-exposure baking effect for TinOH with a higher initial layer thickness (60 nm).*

The films were also baked after exposure at two higher temperatures: 120 °C and 150 °C. The unexposed parts of the film became partly insoluble. In the case of 120 °C, the unexposed resist layer was still lower in height than the exposed material, except at very low doses (< 5 mJ cm^{-2}). We suspect that, at these low doses, the shrinkage of the material was a larger factor than the solubility change. In the case of a 150 °C PEB, the unexposed layer was barely soluble, leading to a decrease in height of the exposed parts for all used doses (2-50 mJ cm^{-2}). PEB at these higher temperatures is probably not suitable for negative patterning. An extensive study on this 150 °C PEB condition applied on TinOH will be discussed in Chapter 8.

The effect of temperature on the materials was investigated by means of TGA, with which mass loss as a function of temperature can be measured. This can give additional information about the temperature stability of the unexposed material. A TGA curve of TinOH is shown in Fig. 6.6.

It can be seen that the remaining mass of TinOH first has a slight drop at the onset of the curve (< 100 °C). This can be attributed to the loss of some loosely attached IPA, the solvent that was used in the conversion step from TinS to TinOH (see experimental). The remaining mass reaches a first plateau around 100 °C, but drops suddenly above 150 °C, at which temperature we observe a change in solubility. Banse et al.[27] reported that the crystal structure of TinOH contains four molecules of IPA, but they observed that powders are easily obtained that contain less IPA. The weight loss at ~ 150 °C could be due to the loss of the most tightly bound solvent. It is also conceivable that water is eliminated, accompanied by deprotonation of the bridging OH-groups. Above ~200 °C, a gradual loss of ~22% of the original weight occurs that can be attributed to the loss of organic content (cleavage of the butyl groups). The final remaining mass is 72%, which is close to the theoretical remaining mass of 73% assuming complete conversion to SnO_2. The slightly lower remaining mass can be attributed to the presence of IPA or H_2O in the initial sample.

The temperature response can be different for different tin cage materials. The malonate form (TinM) was also baked at 120 °C. Surprisingly, the non-exposed TinM was still completely soluble even at this temperature. In addition, the sensitivity of the material seems to be high (see Fig. 6.7), although the high initial layer thickness also plays a role. If we compare the results to TinOH (Fig. 6.5), we see that in both cases a higher initial thickness leads to a higher remaining thickness. However, the measured contrast of TinM under these conditions appears to be lower than that of TinOH (PEB at 100 °C, Fig. 6.5), which could explain why the patterning results of TinM were not significantly better.

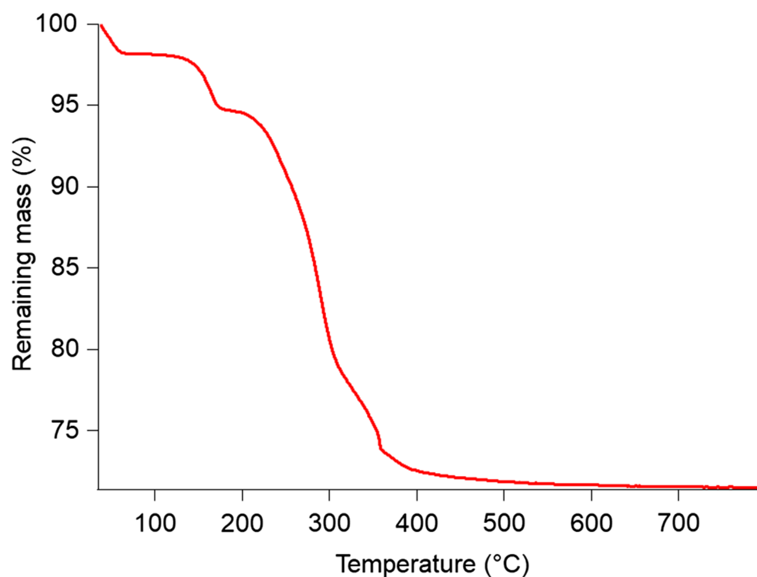

Figure 6.6. *TGA analysis for TinOH powder, in an 80%/20% N_2/O_2 atmosphere.*

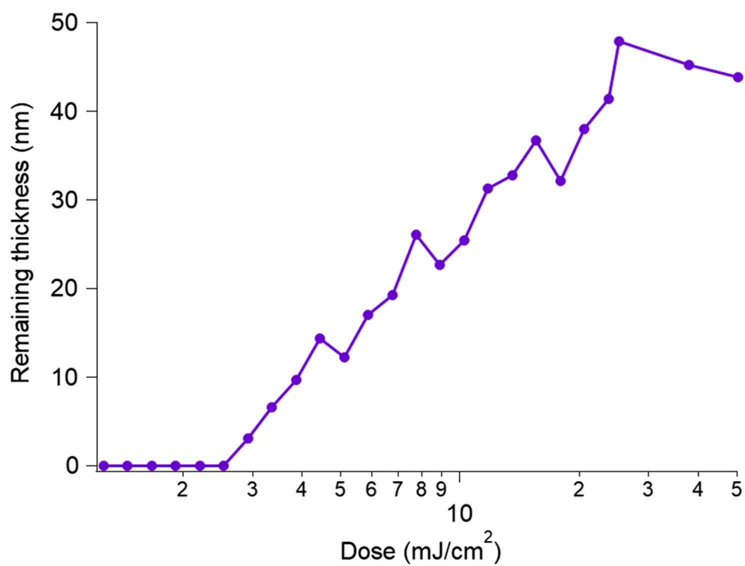

Figure 6.7. *Contrast curve of TinM, using a PEB of 120 °C. Initial thickness was ~50 nm.*

6.3.2 Interference lithography experiments: patterning

Line patterns were printed in ~30 nm thick films of the tin cage materials using EUV interference lithography. Transmission diffraction gratings on a Si_3N_4 membrane were used (mask) to create mutually coherent beams, which in turn interfere to form the desired interference pattern. In our case, by utilizing two gratings we obtained line/space patterns with half the periodicity of the gratings on the mask.[27] Patterning experiments are important to demonstrate the potential of materials for photoresist applications: a performance is sought with the resolution and sensitivity being as high as possible, and the line edge roughness being minimized.

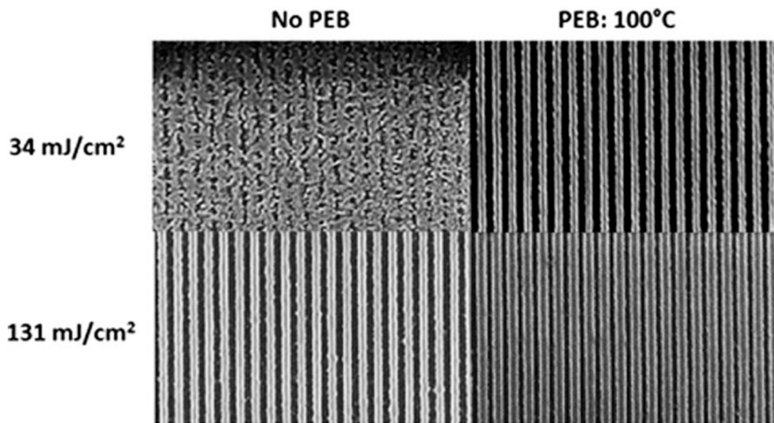

Figure 6.8. *The effect of PEB on TinOH measured at two different doses (34 and 131 mJ cm^{-2}) for 50 nm half-pitch lines.*

In Fig. 6.8 the effect of PEB can be seen. The pattern is almost invisible for the 34 mJ cm^{-2} dose when no post-exposure bake is applied, but clearly present when it is (100˚C, 30 s before development). In the case of the patterns written with 131 mJ cm^{-2} dose, the lines increase in width with respect to the spaces. The lines are around 50 nm for the non-PEB sample but increase in width to around 68 nm for the PEB sample. This must mean that kinetically stable reaction products are formed during the EUV exposure, which reacts further during the PEB step.

Other parameters that were investigated were rinsing time and hard baking (post-development baking, HAB). These parameters were investigated because they could have a favorable effect on microbridging, an undesirable phenomenon that was encountered during interference lithography experiments. The effect of rinsing and HAB on this phenomenon is shown in Fig. 6.9.

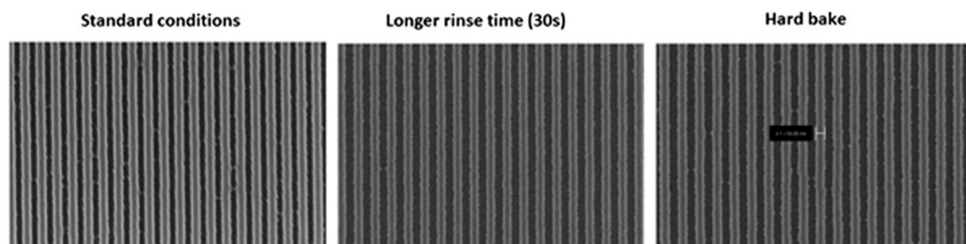

Figure 6.9. *Minimization of bridging effect, for TinOH using a dose of 110 mJ cm*$^{-2}$ *on 50 nm HP lines. The regular rinsing time was 10 s. PEB was performed at 100°C for 2 min for all three patterns. HAB (post-development baking) was performed at 200 °C for 1 min.*

The images show that the bridging effect is reduced if a longer rinsing time is used. Longer rinsing time also leads to smaller lines relative to the spaces. Under standard conditions the lines are around 60 nm, whereas longer rinsing decreases this to around 50 nm. This implies that the resist is still partially soluble in the rinser (H_2O) and that the rinsing time should be well adjusted. HAB (200 °C for 1 min) does not significantly change the pattern, although it slightly reduces the line width to around 55 nm.

The materials were also tested at higher resolution. Although 80 nm pitch lines could be printed, the 60 nm and 44 nm pitch lines were significantly more difficult to print. Significant bridging between lines was observed. Probably this has to do with a problem of the development or rinsing process. Pattern collapse does not seem very likely, however, since the aspect ratio of the pattern is close to 1:1. Rather, the lines seem to detach from the substrate, signaling poor adhesion of the resist film or pattern collapse. For none of the presently studied materials, patterns at 22 nm HP could be resolved. Further investigations and improvements are needed to reach high resolution, such as reducing the aspect ratio, changing and optimization of the rinsing solvent, and improving adhesion of the resist layer to the substrate using surface treatments or underlayers.

Similarly to the open-frame experiments, we also patterned thicker layers (30 nm instead of 20 nm). However, a higher sensitivity was not found here. A reason could be that adhesion of the lines is very important for patterning experiments. A thicker layer receives less light at the bottom, making this adhesion more difficult.

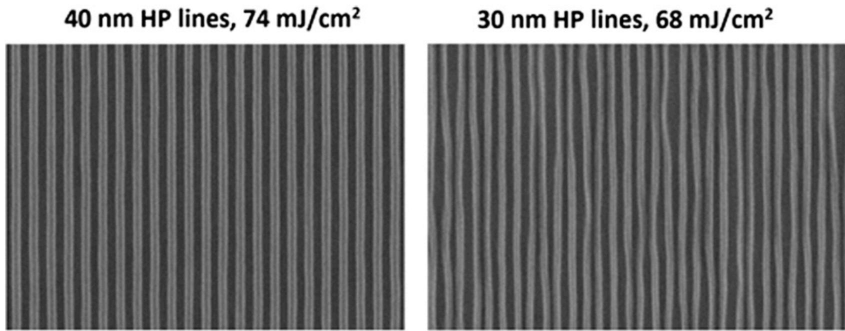

Figure 6.10. *Interference lithography on TinA. Processing conditions: PAB 90 °C (1 min), PEB 100 °C (1 min), HAB 200 °C (1 min).*

The best patterns were created for the tin cage with acetate (CH_3COO^-) anions. This material was significantly less prone to pattern collapse or bridging, perhaps owing to its better stability. Two patterns at half pitches of 40 nm and 30 nm for this anion can be seen in Fig. 6.10. As it is seen in the figure, patterning with high quality is obtained down to 30-nm HP and the resolution is limited by the pattern collapse due to the adhesion problems.

After publication of our work in reference 1, we further optimized the process conditions. The film thickness of new TinOH and TinA samples was around 30 nm. We obtained the best patterns for as shown in Fig. 6.11. The TinOH pattern at hp 22 nm (pitch 44 nm) can be seen in Fig. 6.11a. The TinA pattern at hp 30 nm can be seen in Fig. 6.11b. With lower aspect ratio, the pattern collapse or bridging was reduced. So far, however, we still failed to achieve higher resolution (hp 16 nm).

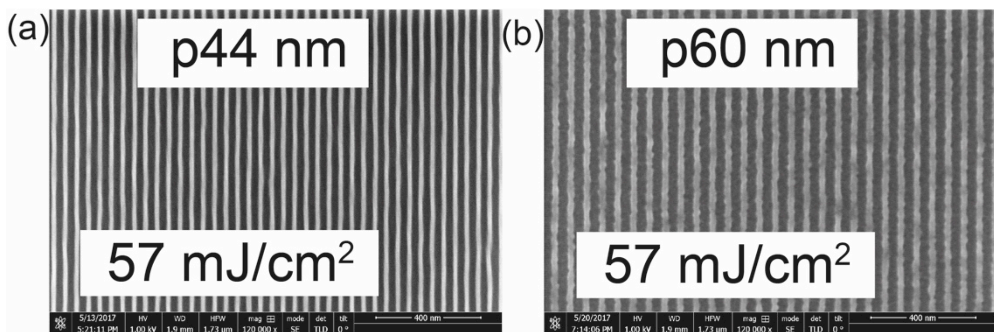

Figure 6.11. *Interference lithography on TinOH (a) and TinA (b). Process condition: (a) PAB 90 °C for 1 min, PEB 100 °C for 1 min, develop with 2:1 IPA: H_2O for 30s, rinse with H_2O for 20s, HAB 150 °C for 2 min. (b) PAB 90 °C for 1 min, PEB 100 °C for 1 min, 2:1 IPA: H_2O for 30s, rinse with H_2O for 10s HAB 100 °C for 1 min.*

6.4 Conclusions

We studied the EUV patterning of thin films of a small set of tin-oxo cage compounds. The relatively high packing density of Sn atoms provides a highly absorbing material,[15] since Sn is one of the most absorbing elements at 13.5 nm.[14] Optimization of the processing conditions provided a better sensitivity than was reported previously.[11] Large area exposure (contrast curve) experiments showed a dependence on initial layer thickness and PEB temperature. Post exposure baking also substantially improved the negative tone photoresist performance in patterning experiments. This suggests that EUV photoreaction products are formed that can further react during the baking step. Identification of such photoproducts is a target of our ongoing research. Loss of carbon, in any form, leaves the Sn atoms in a coordinately unsaturated state, making them potentially more reactive. While we have achieved progress, it is clear that further improvements are needed to make the materials competitive with the state of the art EUV resist. The process of improvement would benefit greatly from a better understanding of the photochemical processes at work. For instance, the relatively low sensitivity suggests that loss mechanisms may be at play in which EUV photons are not converted into the desired solubility change. Reduction of these loss mechanisms could pave the way towards more sensitive resist materials.

6.5 References

1. J. Haitjema, Y. Zhang, M. Vockenhuber, D. Kazazis, Y. Ekinci and A. M. Brouwer, "Extreme ultraviolet patterning of tin-oxo cages", *J. Micro/Nanolitho. MEMS MOEMS*, 2017, **16**, 7.
2. P. Naulleau, C. Anderson, W. Chao, S. Bhattarai, A. Neureuther, K. Cummins, S.-H. Jen, M. Neisser and B. Thomas, "EUV Resists: Pushing to the Extreme," *J. Photopolym. Sci. Technol.,* 2014, **27**, 725–730.
3. M. Shirai and M. Tsunooka, "Photoacid and photobase generators: chemistry and applications to polymeric materials," *Prog. Polym. Sci*., 1996, **21**, 1–45.
4. P. Naulleau, C. Anderson, W. Chao, S. Bhattarai and A. Neureuther, "Studying Resist Stochastics with the Multivariate Poisson Propagation Model," *J. Photopolym. Sci. Technol*., 2014, **27**, 747–750.
5. P. Naulleau, C. Anderson, W. Chao, S. Bhattarai and A. Neureuther, "Stochastics and EUV patterning in the 1x-nm Regime," *J. Photopolym. Sci. Technol*., 2016, **29**, 797-802.
6. D. De Simone, M. Mao, F. Lazzarino, G. Vandenberghe, "Metal Containing Resist Readiness for HVM EUV Lithography," J. *Photopolym. Sci. Technol*., 2016, **29**, 501–507.
7. K. Kasahara, V. Kosma, J. Odent, H. Xu, M. Yu, E.P. Giannelis and C.K. Ober, "Recent progress in nanoparticle photoresist development for EUV

lithography," *Proc. SPIE*, 2016, **9776**, 977604.

8. M. Trikeriotis, M. Krysak, Y.S. Chung, C. Ouyang, B. Cardineau, R. Brainard, C.K. Ober, E.P. Giannelis and K. Cho, "A new inorganic EUV resist with high-etch resistance," *Proc. SPIE*, 2012, **8322**, 83220U.
9. J.M. Amador, S.R. Decker, S. E. Lucchini, R.E. Ruther and D.A. Keszler, "*Patterning chemistry of HafSOx resist*," *Proc. SPIE*, 2014, **9051**, 90511A.
10. H. Nakagawa, T. Naruoka, and T. Nagai, "Recent EUV Resists toward High Volume Manufacturing," *J. Photopolym. Sci. Technol.,* 2014, **27**, 739–746.
11. B. Cardineau, R. Del Re, M. Marnell, H. Al-Mashat, M. Vockenhuber, Y. Ekinci, C. Sarma, D.A. Freedman and R.L. Brainard, "Photolithographic properties of tin-oxo clusters using extreme ultraviolet light (13.5 nm)," *Microelectron. Eng.,* 2014, **127**, 44–50.
12. N. Mojarad, J. Gobrecht and Y. Ekinci, "Beyond EUV lithography: a comparative study of efficient photoresists' performance," *Sci. Rep.,* 2015, **5**, 9235.
13. C. Eychenne-Baron, F. Ribot, N. Steunou, C. Sanchez, F. Fayon, M. Biesemans, J.C. Martins and R. Willem, "Reaction of Butyltin Hydroxide Oxide with *p*-Toluene sulfonic Acid: Synthesis, X-ray Crystal Analysis, and Multinuclear NMR Characterization of $\{(BuSn)_{12}O_{14}(OH)_6\}(4\text{-}CH_3C_6H_4SO_3)_2$," *Organometallics*, 2000, **19**, 1940–1949.
14. B. L. Henke, E. M. Gullikson and J. C. Davis, "X-Ray Interactions: Photoabsorption, Scattering, Transmission, and Reflection at E = 50-30,000 eV, Z = 1-92," *At. Data Nucl. Data Tables*, 1993, **54**, 181–342.
15. R. Fallica, J. Haitjema, L. Wu, S. C. Ortega, A. M. Brouwer and Y. Ekinci, "Absorption coefficient of metal-containing photoresists in the extreme ultraviolet", J. Micro/Nanolitho. MEMS MOEMS, 2018, **17**, 7.
16. R. Fallica, J. K. Stowers, A. Grenville, A. Frommhold, A. P. G. Robinson and Y. Ekinci, "Dynamic absorption coefficients of chemically amplified resists and nonchemically amplified resists at extreme ultraviolet wavelengths," *J. Micro/Nanolithogr. MEMS MOEMS,* 2016,**15**, 033506.
17. Y. Zhang, J. Haitjema, X. Liu, F. Johansson, A. Lindblad, S. Castellanos, N. Ottosson and A.M. Brouwer, "Photochemical conversion of a tin-oxo cage compound studied using hard x-ray photoelectron spectroscopy," *J. Micro/ Nanolithogr. MEMS MOEMS,* 2017, **16**, 023510.
18. J. Haitjema, Y. Zhang, N. Ottosson, A.M. Brouwer, "Photoreactions of Tin Oxo Cages, Model EUV Photoresists," *J. Photopolym. Sci. Technol.,* 2017, **30**, 99–102.
19. C. Eychenne-Baron, F. Ribot and C. Sanchez, "New synthesis of the nanobuilding block $[(BuSn)_{12}O_{14}(OH)_6]^{2+}$ and exchange properties of $[(BuSn)_{12}O_{14}(OH)_6](O_3SC_6H_4CH_3)_2$," *J. Organomet. Chem.,* 1998, **567**, 137–142.
20. L. van Lokeren, R. Willem, D. van der Beek, P. Davidson, G.A. Morris and

F. Ribot, "Probing the anions mediated associative behavior of tin-12 oxo-macrocations by pulsed field gradient NMR spectroscopy," *J. Phys. Chem. C*, 2010, **114**, 16087–16091.

21. N. Mojarad, M. Hojeij, L. Wang, J. Gobrecht and Y. Ekinci, "Single-digit-resolution nanopatterning with extreme ultraviolet light for the 2.5 nm technology node and beyond," ***Nanoscale*****,** 2015, **7**, 4031–4037.
22. S. Meyers, J.T. Anderson, J.B. Edson, K. Jiang, D.A. Keszler, M.K. Kocsis, A.J. Telecky and B.J. Cardineau, *U. S. Patent 2016/ 0116839 A1,* 2015.
23. W. D. Hinsberg, F.A. Houle, M.I. Sanchez and G.M. Wallraff, "Chemical and physical aspects of the postexposure baking process used for positive-tone chemically amplified resists," *IBM J. Res. Dev.,* 2001, **45**, 667–682.
24. C. A. Mack, "Lithographic Optimization Using Photoresist Contrast," *Microelectron. Man. Tech.,* 1991, **14**, 36–42.
25. W. D. Hinsberg and S. Meyers, "A numeric model for the imaging mechanism of metal oxide EUV resists," *Proc. SPIE*, 2017, **10146**, 1014604.
26. Y. Ekinci, M. Vockenhuber, N. Mojarad, D. Fan "EUV resists towards 11 nm half-pitch," *Proc. SPIE*, 2014, **9048**, 904804.
27. F. Banse, F. Ribot, P. Toledano, J. Maquet, C. Sanchez, "Hydrolysis of Monobutyltin Trialkoxides: Synthesis and Characterizations of $\{(BuSn)_{12}O_{14}(OH)_6\}(OH)_2$," *Inorg. Chem.,* 1995, **34**, 6371–6379.
28. N. Mojarad, J. Gobrecht and Y. Ekinci, "Interference lithography at EUV and soft X-ray wavelengths: Principles, methods, and applications," *Microelectron. Eng.,* 2015, **143**, 55–63.

Chapter 7

The photoreaction mechanism of tin oxo cages under EUV exposure*

In this work, we focus on tin oxo cages as model photoresists and investigate their photoreaction mechanism under EUV (13.5 nm) and DUV (225 nm) exposure. Sn-containing photoresists have attracted attention for EUV lithography because of their high photon absorption cross section at EUV (92 eV, 13.5 nm). We use different X-ray photoelectron spectroscopies combined with mass spectrometry methods to investigate the photon-induced chemistry in the photoresist films. To study primary reactions between EUV photons and the tin oxo cages, photoelectron spectrum with photon energies of 60, 92 120 and 150 eV were measured. This experimentally confirms the high contribution of tin atoms to the photoionization cross section of the tin oxo cages at 92 eV. Further chemical changes under EUV exposure were also investigated/identified by *in-situ and ex-situ* measurements such as XPS, time-of-flight secondary ionization mass spectrometry (TOF-SIMS) and resist outgassing measurements. The formation of carbonyl bonds was detected in both *in-situ* and *ex-situ* measurement. The EUV induced species were found to be very sensitive to a post-exposure bake step. The outgassing products butane, butene, octane and butanal are detected. Using these results, the chemical reaction mechanism that renders the solubility switch is proposed, making an additional comparison between EUV and DUV photochemistry and reaction yield. This work provides a model to understand the photon-photoresist interaction.

---

* Y. Zhang, J. Haitjema, M. Baljozovic, F. Johansson, N. Sadegh, M. Vockenhuber, D. Kazazis, I. Pollentier, J. D. Keelor, D. De Simone, A. Lindblad, T. A. Jung, Y. Ekinci, S. Castellanos, A. M. Brouwer, "The photoreaction mechanism of tin oxo cages under EUV exposure", *Manuscript in preparation.*

7.1 Introduction

With the progress of the semiconductor industry towards smaller, faster and more powerful next generation chips, EUV photolithography is a much-anticipated milestone because of the short wavelength of 13.5 nm, which enables to shift the frontiers imposed by the optical diffraction limit.[1-3] To make best use of this technique, not only the design of the photolithographic scanners needs attention, but also the photoresist material used.[4] Chemically amplified photoresists (CARs) based on photochemical acid generation and catalytic deprotection of dissolution inhibiting groups have been widely used in previous generations of photolithography that use 193 nm and 248 nm light sources.[5, 6] CARs, however, have low EUV photon absorption, and weak resistance to etching. Moreover, amplification has to be reduced in order to avoid pattern blur due to acid diffusion, which goes at the expense of sensitivity. As alternatives, inorganic or organometallic photoresists are considered for EUV lithography.[7, 8] The metal atoms in these compounds have a higher photon absorption cross section in the EUV range, possibly removing the need for chemical amplification, and contribute to a strong etch resistance.[9] A variety of metal containing photoresists has been studied, such as Hf-, Zr-, Ti-, and Sn-based materials.[10-16] Most of them have shown good sensitivity to EUV, and give high-resolution patterns. Among these metal-containing photoresists, Sn-containing materials are attractive owing to their high photon absorption cross section at the EUV wavelength.[17-19] Recently, Inpria has introduced Sn-based photoresists which are seriously considered for industrial application.[20, 21] Their large EUV absorption coefficient, chemical stability and good pattern performance make Sn-based materials attractive for next generation photolithography.[20, 22-24]

Different tin-containing photoresists were introduced as potential candidate EUV photoresists.[11, 18, 19, 21, 25] Tin oxo cage compounds can be used as a model to study the photoresist reaction mechanism under EUV exposure due to their easy preparation and well-defined molecular structures.[11, 19, 26] In the present work we focus on the tin oxo cage with n-butyl groups and hydroxide counterions, shown in Fig. 7.1. This class of compounds was first introduced as EUV photoresist by Brainard's group.[11] They showed that it could be used as a negative tone photoresist, with a resolution of 18 nm dense lines. They also proposed that the homolytic cleavage of the tin-carbon bond, forming a radical at a Sn atom and further cross-linking with the neighbor cage is the main reaction mechanism leading to the solubility switch. In our previous work, the facile cleavage of tin-carbon bonds in the tin oxo cages was supported by quantum-chemical calculations, in which one-electron oxidation or formation of a triplet excited state leads to spontaneous dissociation of the tin-carbon bond.[27] The chemical reaction in the solid thin film under DUV exposure was studied by means of X-ray Photoelectron Spectroscopy

(XPS), which confirmed the loss of carbon experimentally.[28] Photoexcitation of the bare tin cage dications in the gas phase also led to tin-carbon bond cleavage as the primary process.[28, 29] It was also discovered that the tin oxo cage can change tone from negative to positive under electron beam lithography and EUV lithography.[30]

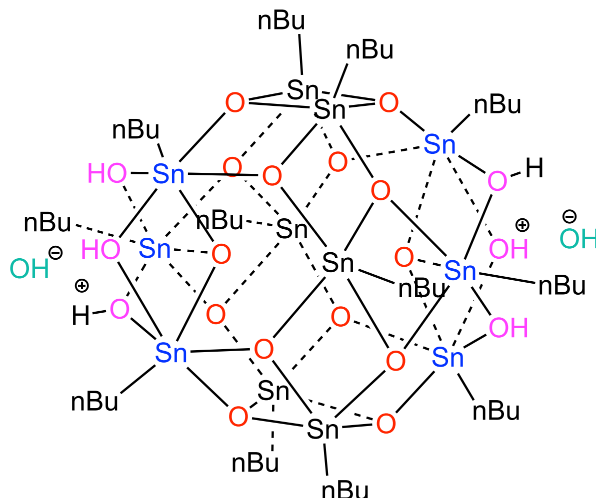

Figure 7.1. *Structure diagram of TinOH.*

In the present work, we study the chemical reactions in the tin oxo cage thin films induced by EUV radiation. We investigated the photoionization cross section of the tin oxo cages in the EUV wavelength range. The chemical reaction in the photoresist thin film as a function of EUV dose was studied using X-ray photoelectron spectroscopy (XPS) with in situ exposure. In other experiments, we performed EUV exposure with accurately known doses, and XPS analysis on a separate instrument.[31] Additionally, the reaction products upon DUV exposure were characterized for comparison. The exposed thin films were further characterized by Time-of-flight secondary ionization mass spectrometry (TOF-SIMS), to study the chemical composition of the final products. To detect low molecular weight reaction products directly, the tin oxo cage resist was exposed to EUV while volatile products were detected using an outgassing qualification tool at IMEC.[32] The products of the chemical reaction in the tin oxo cages upon EUV exposure were sufficiently evaluated based on all these different measurements. The chemical reaction pathway of tin oxo cages under different EUV exposure doses was quantified and this showed that the chemical reaction yield per photon is higher under EUV than under DUV exposure. The full analysis of this model photoresist's behavior under photon irradiation gives us the opportunity to find potential ways to build more efficient photoresists and push the EUV lithography toward success.

7.2 Experiment

7.2.1 Sample preparation

The synthesis of the tin oxo cages has been described in our previous publications.[31] In this work we focus on tin oxo cages with hydroxide as counterion (TinOH).[32] For XPS measurements, the substrate should be conductive. To prepare conductive substrates, 2 nm Cr and 18 nm Au were successively coated on 1 × 1 cm^2 Si substrates previously cleaned with base piranha (NH_4OH/H_2O_2 solution) using a Leica EM ACE 600 Double sputter coater. TinOH was dissolved in toluene (7.5 mg mL^{-1}) and filtered through a 0.25 μm PTFE filter right before spin coating on the prepared conductive substrate at 2500 rpm for 35 s after accelerating by 750 rpm s^{-1}. The resulting film thickness was characterized by means of AFM to be ~20 nm. Some samples were pre-exposed by EUV/DUV before measurements. Samples for mass spectrometry were prepared on HMDS pretreated Si and partially pre-exposed by EUV and DUV. Samples for the IMEC resist outgassing system were freshly introduced into the set-up without pre-exposure.

7.2.2 Exposure

In this work, EUV (13.5 nm, 92 eV) exposures were performed at the XIL-II beamline of the Swiss Light Source (SLS) synchrotron at the Paul Scherrer Institute. Deep UV light was produced by a nanosecond YAG-pumped OPA laser (Ekspla NT342B; 225 nm, 2.5 mJ $pulse^{-1}$, 10 Hz). For EUV, 8 × 8 mm^2 areas were exposed, while for DUV an area corresponding to the profile of the pulsed laser beam was exposed (diameter ~5 mm). The exposure dose was controlled by varying the exposure time. For the XPS samples, doses of 10, 50, and 250 mJ cm^{-2} were used for EUV exposed samples whereas we chose one dose (50 mJ cm^{-2}) to expose with DUV. For the ToF-SIMS analysis, the doses 20, 50 and 125 mJ cm^{-2} were chosen for both EUV and DUV exposures. Since the EUV exposure was done under high vacuum, to get rid of the oxygen and water effects from the atmosphere for DUV exposure, the samples were mounted in a chamber with 225 nm transparent quartz windows filled with dry N_2. However, the DUV exposure of the ToF-SIMS samples was performed in air.

7.2.3 Photoelectron spectroscopy

Low dose photoelectron spectroscopy (LowDose PES) was performed using the synchrotron light source (BESSY-II, Helmholtz-Zentrum-Berlin) at the PM4 beamline[33] using an angle-resolved time of flight (ArTOF) spectrometer.[34] A lower photon flux was used in this beamline for probing materials that are sensitive to radiation-induced sample damage. The sample change over time was monitored, and no significant charging or radiation damage was found in the spectra within 10 min. The ArTOF spectrometer makes it possible to record the spectra with high resolution. For our EUVL purpose, at this beamline, by moving a slit out of the

beam, the sample can be exposed to a higher flux of 92 eV photons and followed by the recording of high resolution XPS to trace the chemical changes in the samples without any contamination from the atmosphere. The sample was prepared on a conductive substrate as described above. In this work, we used a 360 l/mm grating, which gives access to the EUV at 92 eV and also allows to measure all the relevant atoms' chemical high resolution XPS spectra with photon energies up to 650 eV.

In addition to the in-situ measurement, ex-situ experiments were also performed to characterize the photon induced chemical changes. XPS with a SPECS analyzer Phoibos 150, and a monochromatic AlKα X-ray source (photon energy 1486.6 eV, power 200 W, at PSI) was used to investigate the chemical changes in the EUV exposed photoresist thin films. As a comparison, hard x-ray photon electron spectroscopy (HAXPES) was also used to study the DUV exposed photoresist thin films. The details of the HAXPES measurements can be found in our previous publication.[28] All peak positions of the core electrons are presented as binding energies and were corrected using the overview spectra, using the C 1s peak at 285.0 eV and the Au $4f_{7/2}$ lines at 84.0 eV from a clean Au-foil reference. Fits were performed using Gaussian peaks convoluted with a Lorentzian function (10%), which accounts for the finite lifetime of the core ionized state. Igor Pro software was used for spectra analysis. The element ratio in the sample is in proportion to the corresponded peak area ratio in the overview spectra. By using the software, each relevant peak was integrated individually. Using the relative sensitivity factor for each element from the literature[35] the elemental ratio in the thin films can be calculated from the corresponding peak area.

7.2.4 TOF-SIMS mass spectrometry

Time-of-flight secondary ionization mass spectrometry (TOF-SIMS) was conducted on a PHI nano TOF II instrument equipped with a 30 kV bismuth (Bi_3^+) source. The measured mass range was 0 – 3000 Da. EUV doses of 20, 50 and 125 mJ cm^{-2} were applied on 8.5 × 8.5 mm^2 areas on the samples to be measured.

7.2.5 Outgassing measurement

Unexposed TinOH thin film was prepared and introduced into an IMEC resist outgassing qualification system equipped with EUV light source for exposure, and a residual gas analyzer (RGA) for recording the mass spectrum of the outgassed products.

7.3 Result and Discussion

7.3.1 In-situ XPS

To characterize the photoelectron emission and the chemical changes of the photoresist, various X-ray photoelectron spectroscopy methods were used. As we

observed from the calculation of the photon absorption cross sections of different atoms,[17, 36] the Sn atom was calculated to have strong absorption at around 92 eV, mainly due to ionization of the 4d electrons.[36] To investigate the interaction between the low energy photon (at around EUV range) and the photoresist, low dose X-ray photoelectron spectroscopy was performed on the TinOH thin film. Photon energies 60, 92, 120 and 150 eV were applied and the photoelectron spectra were recorded as shown in Fig. 7.2. All the spectra were corrected for the photon flux, transmission function of the spectrometer and the inelastic mean free path of the electrons with different kinetic energies.[37] In the spectrum, we can observe a clear Sn 4d peak at ~26 eV and a valence band from ~4 to ~12 eV. The Sn 4d orbital is a rich source of primary electrons, which initiate the electron cascades mostly responsible for chemical changes in EUV resists. Comparing the intensity of the Sn 4d peaks at different photon energies, considerably more photoelectrons were generated from Sn 4d with 92 eV photon exposure.

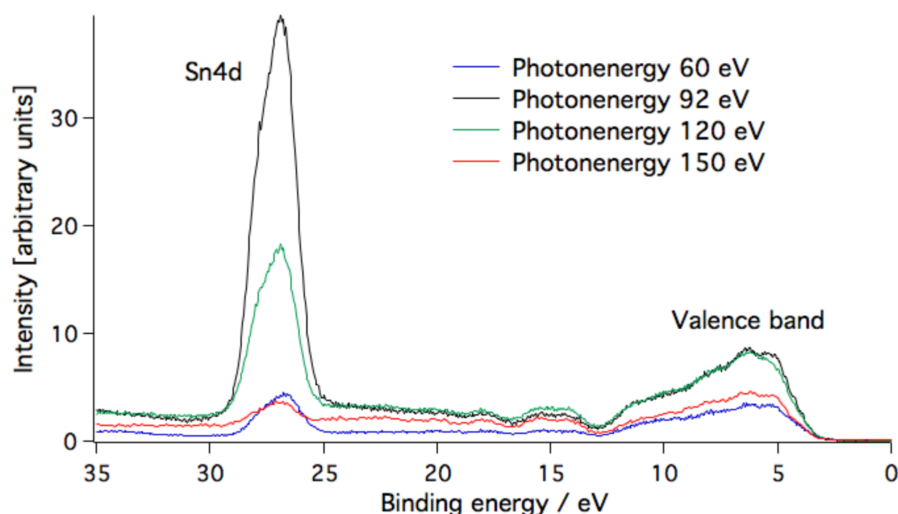

Figure 7.2. *PES of thin layer of tin oxo cage (OH^- counterions) with photon energies 60, 92, 120 and 150 eV, the intensity of the spectra has been corrected for the photon flux, electron inelastic mean free path and transmission function of the spectrometer.*

The chemical changes in the photoresists upon 92 eV irradiation can be monitored by recording XPS spectra at higher photon energies sequentially. We used 650 eV for overview spectra, 630 eV for high-resolution O 1s spectra, 580 eV for Sn 3d spectra and 380 eV for C 1s. Unfortunately, the photon flux in this set-up at the time of our experiments was not known. Therefore, we used the exposure time to indicate the dose increase, and further tracing the chemical changes.[33] The overview spectra of TinOH under different doses are shown in Fig. 7.3. In line with our

previous work, the relative concentrations of the elements in the thin film are consistent with the expected ratios of tin, oxygen and carbon of 12: 22: 48.[28] As we assumed in our previous work, Sn containing fragments are too heavy to escape from the thin film upon exposure; only fragments containing oxygen and carbon are expected to outgas from the film.[28] This assumption enables studying the change in concentration of O and C as a function of exposure dose, by comparing them to the Sn peaks, as shown in table 7.1. With increasing dose, the oxygen and carbon atom number continuously decreased. The carbon content decreased faster than the oxygen content, but the loss of oxygen is still pronounced. With 10 min exposure, ~2 carbon atoms and ~2 oxygen atoms were removed per tin oxo cage molecule. With 60 min exposure, around 6 oxygen atoms and 30 carbon atoms were removed.

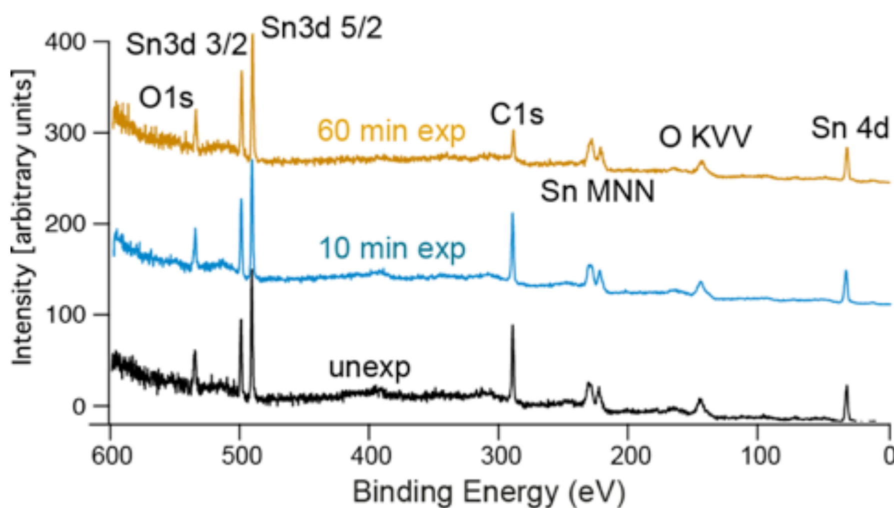

Figure 7.3. *XPS of TinOH thin layer, unexposed, 10 min and 60 min in-situ EUV exposed. Recorded with photon energy 650 eV.*

Table 7.1. *Relative amounts of Sn, O and C in TinOH films with increasing exposure time.*

TinOH	Sn	O	C
Theoretical	12	22	48
unexp	12	22 ± 2	48 ± 2
10 min exp	12	20 ± 2	46 ± 2
60 min exp	12	16 ± 2	18 ± 1

In addition to the XPS overview spectra, high-resolution XPS spectra were recorded to detect the intermediates or the final products in the thin films under EUV exposure. High-resolution XPS spectra provide detailed insight into chemical changes, by looking at differences in electron binding energy in the characteristic orbitals of the different elements in different chemical environments (chemical shift). This adds complementary information to overview spectra, where only the ratio between elements can be studied. The high-resolution spectra of the three

samples at Sn $3d_{5/2}$, O 1s, and C 1s positions were recorded using low dose XPS, as shown in Fig. 7.4. To properly interpret the high-resolution spectra, we need to consider the chemical composition of TinOH. As shown in Fig. 7.1, in the original TinOH structure, there are two types of tin atoms: six 5-coordinated tin atoms in the central belt of the cage and six 6-coordinated tin atoms at the caps of the cage. There are three types of oxygen atoms in the cages, 2 oxygen atoms from the hydroxide counterions (OH^-), 14 oxygen atoms bound to three Sn atoms (12 in the central belt of the cage and 2 on the inside) (Sn-O) and 6 oxygen atoms (Sn-OH) from the bridging hydroxides (μ_2-OH) at the caps of the cage. All carbon atoms are located in butyl chains, so that the carbon signal is mainly composed by the core level electrons from sp^3 orbitals. According to DFT calculations,[38] there are two kinds of carbon atoms in the tin oxo cages structure. The binding energies of the carbon atoms attached to the 6-coordinated tin atom are predicted to be clearly lower than those of all other carbons in the molecule, which have similar binding energies. Therefore, we assume that there are two types of carbon in TinOH in a ratio of 6: 42. Using this assumption, the XPS spectra can be fitted as shown in Fig. 7.4c.

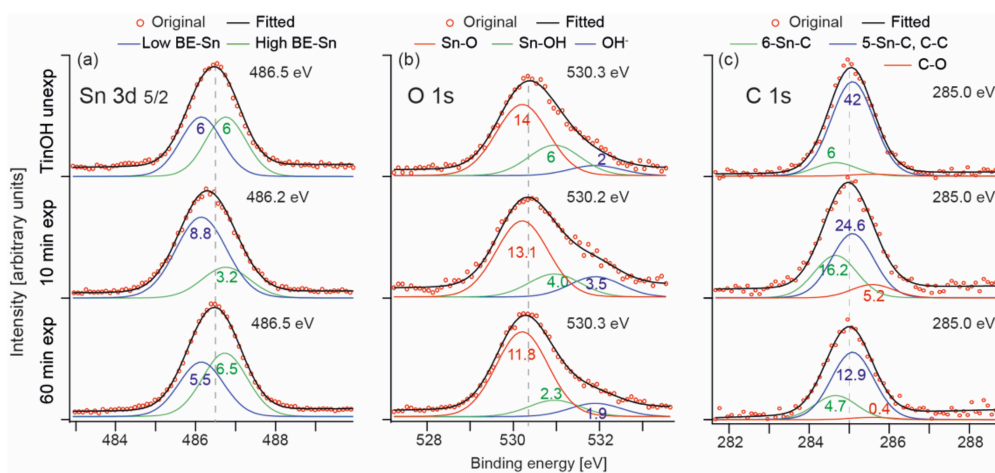

Figure 7.4. *Fitted Sn $3d_{5/2}$, O 1s, and C 1s spectra of unexposed TinOH (top) and TinOH exposed to 10 min (middle) and 60 min (bottom) of EUV.*

As shown in Fig. 7.4a, two sub-peaks contributing to the fitting represent two chemical environments of tin atoms (5-coordinated Sn with high binding energy, 6-coordinated with lower binding energy, according to DFT calculations).[38] Upon EUV exposure, the ratio of those components could change. However, we assume that these peaks are representative for the chemical changes occurring in the unexposed sample. Using this assumption, the spectra of the EUV exposed samples were fitted using a fixed peak position and bandwidth, so that the fitting was only

affecting the amplitudes. The spectral fits from all the samples were optimized simultaneously. As we see in Fig. 7.4a, the Sn $3d_{5/2}$ peak corresponding to the unexposed sample is centered at 486.5 eV. Upon increasing exposure time, the peak shifts to lower binding energy (486.2 eV after 10 min) and shifts back to 486.5 eV (after 60 min). The ratio of the two types of tin atoms changed, with the relative number of atoms (12 in total) marked on the sub-peaks in fig. 7.4a. After 10 min exposure, the higher binding energy sub-peak relatively decreased. After 60 min exposure, the ratio of the two peaks is again close to the original ratio.

For the chemical environment of the oxygen atoms, similarly to the Sn $3d_{5/2}$ spectra analysis, three sub-peaks are assigned to three chemical environments of oxygen atoms (Fig. 7.4b) (Sn-O, Sn-OH and OH^-) in the original TinOH structure. After exposure, there is no obvious shift in the position of the band maximum; the main O 1s peak is almost at the same position, centered at 530.3 eV. However, the shape of the spectrum changes significantly, especially the shoulder around 532.0 eV. Upon 10 min EUV exposure, the sub-peak at the hydroxide counterions position increases, while the Sn-OH sub-peak decreases. Upon increasing the exposure time to 60 min, the components on the high-binding-energy side decreased again.

For the C 1s spectra, the component ratio changes in the spectra are in agreement with the Sn $3d_{5/2}$ and O 1s spectra analysis. The sub-peaks shown represent the carbon atoms from carbon connected with 6 coordinated Sn (6-Sn-C, green) or carbon connected with 5 coordinated Sn (5-Sn-C) and C-C bonds (blue), respectively, while the red sub-peak represents the carbon atoms from C-O bonds. As shown in Fig. 7.4c, the C-O sub-peak appeared after 10 min of exposure and it decreased again with the higher EUV dose. The O 1s peak from C-O bonds also could be present at around 532.0 eV,[39] which is almost the same position as the OH^- sub-peak. The changes of the sub-peak at 532.0 eV could due to the change of C-O bond.

7.3.2 In-situ EUV exposure with detection of outgassing products

To further study which chemical species escape from the film upon exposure, outgassing products were detected with a residual gas analyzer (RGA) using a resist outgassing qualification system at IMEC. TinOH films were prepared on a 4-inch silicon wafer and continuously exposed to EUV with 40 mJ cm^{-2} while scanning a 5 $\times$ 5 cm^2 area under vacuum. A representative mass spectrum of outgassing products in the *m*/*z* range 0 - 300 is shown in Fig. 7.5.

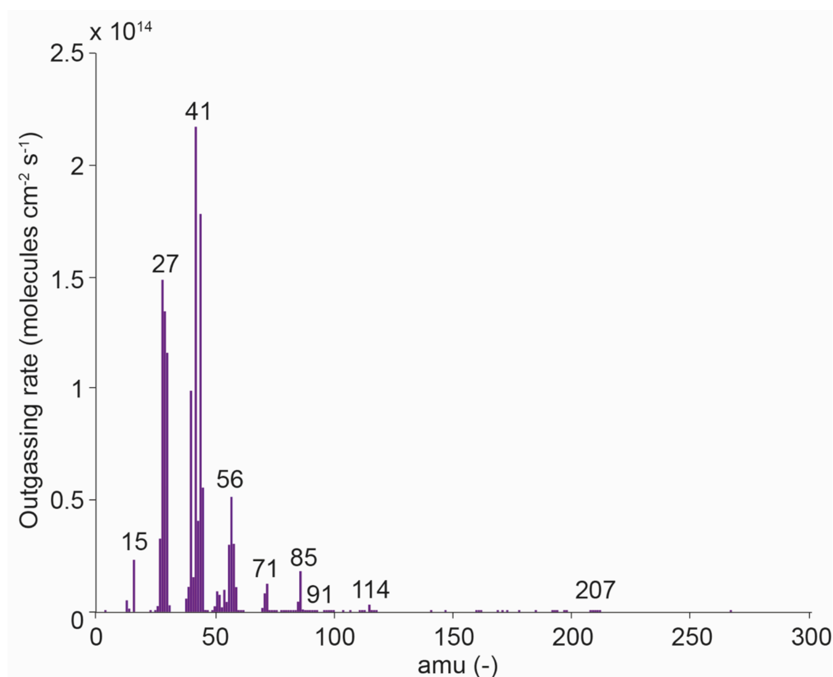

Figure 7.5. *Residual mass analyzer (RGA) mass spectrum of the TinOH thin film under EUV exposure.*

To analyze the spectra, we compare the peak with the model mass spectra from the NIST database[40] where it was found that the outgassing products are likely to be butane (58), butene (56), octane (114) and butanal (72). The mass peak at m/z = 207 could originate from the reagent BuSnOOH with molecule weight 208 from which the tin cages are synthesized. It is unclear whether this compound is already present in the fresh film as an impurity, or whether it is a product of decomposition of the tin oxo cage during exposure.

7.3.3 Ex-situ EUV and XPS

In the in-situ XPS measurement, a photon energy of 650 eV was used for the overview spectra, and the high-resolution spectra were measured with photon energies that give electron kinetic energies near 100 eV. For photoelectrons in this kinetic energy range the inelastic mean free path is around 1.5 nm.[37] Therefore, only the very surface of the thin film can be analyzed. Considering the dose contrast curve of TinOH under EUV in previous work (chapter 6),[31] we choose 10 mJ cm^{-2} (under exposed), 50 mJ cm^{-2} (near dose-to-gel) and 250 mJ cm^{-2} (overexposed) as the doses for further experiments. Differently from the low dose XPS experiment, where the sample was exposed and measured in the sample chamber under high vacuum (*in-situ*), we did the exposure and characterization separately (*ex-situ*). The sample was prepared and exposed at the XIL-II EUV lithography beamline and then

transferred under ambient atmosphere to the Al Kα XPS setup, both at PSI. This means that the sample had the chance to react with oxygen/water during transfer in the atmosphere. In previous work, it was already shown that by adding a post exposure bake step, the sensitivity of TinOH can be improved, probably by reaction of the products of irradiation with O_2 or H_2O in the atmosphere.[31] Here we also studied the effect of the PEB step, which supposedly accelerates the oxidation process of the thin film on the exposed part. For comparison, a 225 nm DUV, 50 mJ cm^{-2} exposed sample was also measured by means of HAXPES.

Similarly to the *in-situ* experiment, the overview spectra, high-resolution Sn $3d_{5/2}$, O 1s and C 1s spectra were measured. Since the X-ray source is fixed at the energy of Al Kα (1487 eV), all the spectra of the EUV exposed samples were recorded at this photon energy. The inelastic mean free path of the electrons generated with a photon energy of 1487 eV is around 3 nm. Therefore, electrons can be detected from deeper sub-surface layers compared to the measurement with 650 eV or lower photon energies. The DUV exposed sample was measured by means of HAXPES with photon energy 2005 eV. Using the previously made assumption that no tin atoms are lost during exposure, we calculated the area ratio of the different elements from the overview spectra as shown in Table 7.2. Since the samples were exposed to air, reaction with H_2O and O_2 or carbon contamination is possible.

Table 7.2. *The Sn, O and C atomic ratios calculated from the overview XPS spectra of different TinOH samples.*

TinOH	Sn	O	C
Theoretical	12	22	48
unexp	12	22±1	48±2
EUV 10 mJ cm^{-2}	12	22±2	52±3
EUV 50 mJ cm^{-2}	12	25±2	46±2
EUV 250 mJ cm^{-2}	12	21±2	33±2
EUV 50 mJ cm^{-2} PEB	12	20±2	42±3
DUV 50 mJ cm^{-2}	12	22±2	41±2

Upon 10 mJ cm^{-2} EUV exposure, the carbon ratio increased slightly, which could be due to the carbon contamination during the transfer. Upon 50 mJ cm^{-2} exposure, the amount of carbon decreased, while the oxygen content increased. This could be due to exposure to O_2. Upon 250 mJ cm^{-2} exposure, both the carbon and oxygen content decreased. When a post-exposure baking step was added (100 °C, 2 min) after 50 mJ cm^{-2} exposure, the oxygen number and carbon number slightly decreased. In the case of 50 mJ cm^{-2} DUV exposure, 3.5 × more carbon was lost than with 50 mJ cm^{-2} EUV exposure. This number, however, is not very reliable because of the inherent

errors in the numbers (see table 7.2) and the risk of some carbon contamination. The overview spectra of the samples are shown in Fig. 7.6.

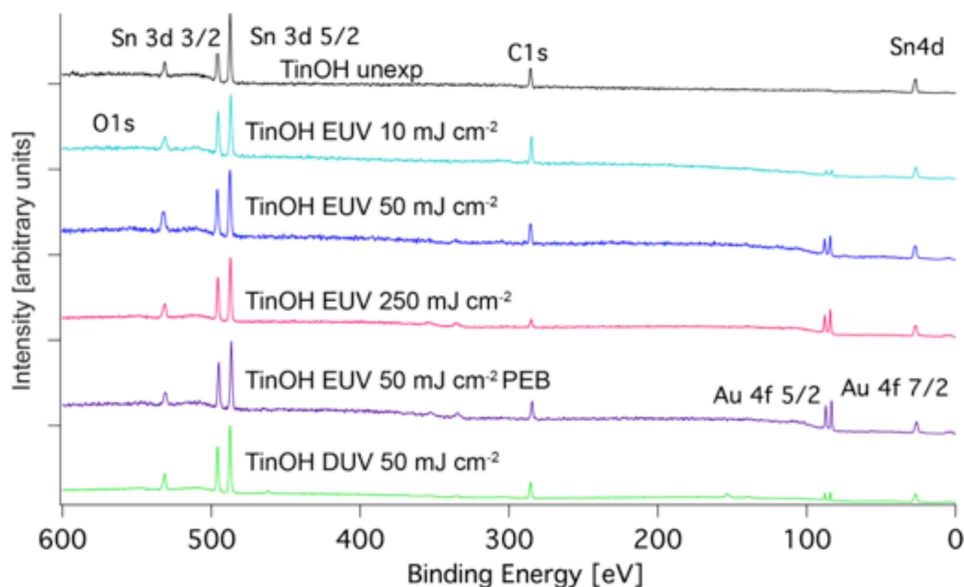

Figure 7.6. *PES of TinOH thin layer, unexposed, 10 mJ cm^{-2}, 50 mJ cm^{-2}, 250 mJ cm^{-2} EUV exposed, 50 mJ cm^{-2} EUV exposure with PEB, and 50 mJ cm^{-2}, DUV exposure. All the spectra from EUV exposures were recorded with photon energy 1487 eV, while the DUV exposed sample was measured with photon energy 2005 eV.*

High-resolution XPS spectra were also recorded for this *ex-situ* experiment, as shown in Fig. 7.7. Using the same assumptions, the high-resolution spectra of Sn $3d_{5/2}$, O 1s and C 1s were fitted by the same method we used for the *in-situ* XPS in Fig. 7.4. As shown in the Fig. 7.7a, the Sn $3d_{5/2}$ peak, instead of shifting to lower binding energy, shifts from 486.8 eV (in the unexposed sample) to higher binding energy, 487.0 eV (10 mJ cm^{-2}), 487.0 eV (50 mJ cm^{-2}) and 487.1 eV (250 mJ cm^{-2}). When a PEB step is added after the 50 mJ cm^{-2} EUV exposure, the peak shifts back to 487.9 eV. With 50 mJ cm^{-2} DUV exposure, the peak also shifts to the same direction to 486.9 eV. The two sub-peaks representing the 5-coordinated Sn (high binding energy), 6-coordinated Sn (low binding energy) atoms were fitted into each spectrum. The fitted ratio between the two types of Sn atoms is marked in Fig. 7.7a.

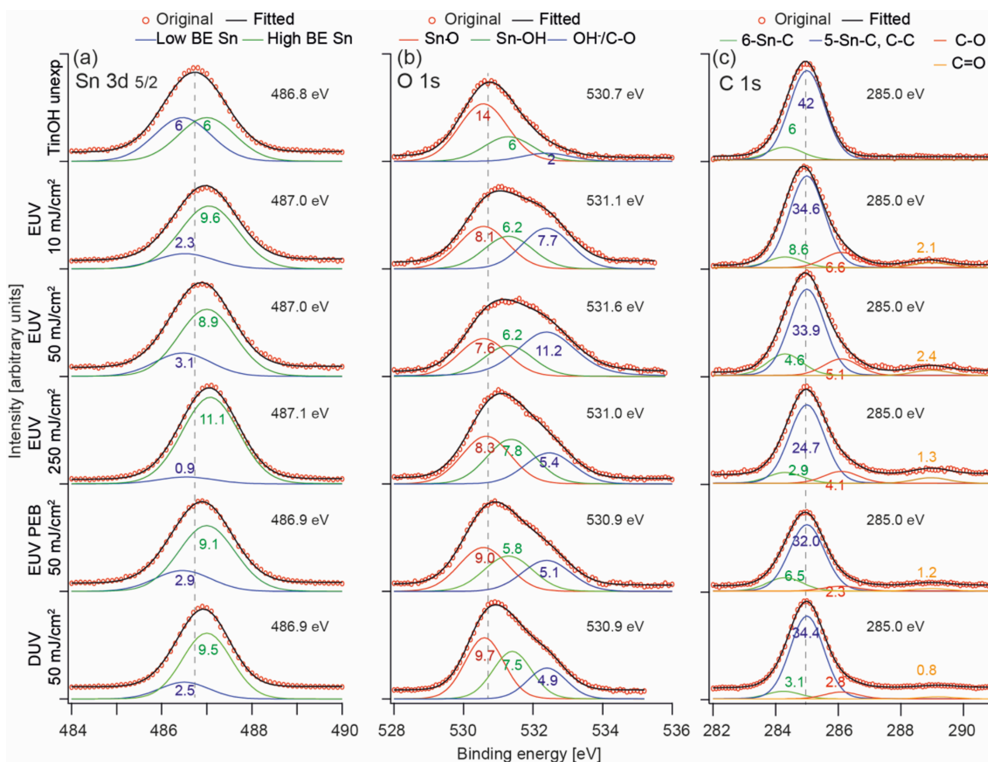

Figure 7.7. *Fitted Sn 3d$_{5/2}$, O 1s, and C 1s spectra of TinOH unexposed, 10, 50 and 250 mJ cm^{-2} EUV (92 eV) exposure, 50 mJ cm^{-2} EUV exposure with a PEB step, and 50 mJ cm^{-2} DUV exposure.*

Using the same assumptions as before, three sub-peaks representing the oxygen atom in Sn-O, Sn-OH and OH^- were fitted into the spectra. The atomic ratios calculated from the sub-peaks area ratio are marked on the spectra. Compared to the O 1s spectra in Fig. 7.4b, all spectra in the Fig. 7.7b show a large shoulder at the OH^- range, which could be due to the exposure to air during transfer of the sample. A clear shoulder shows up at the OH^- sub-peak position (532.4 eV) after a low dose exposure. The reason could be the same as what we observed from Fig. 7.4, where the butyl group connected on the neighboring oxygen atom, forming new C-O bonds, which are located at similar binding energies as OH^-.[39] When the dose was increased to 250 mJ cm^{-2}, the OH^- shoulder decreased a bit, but the Sn-OH sub-peak increased slightly. With an additional PEB step on the 50 mJ cm^{-2} exposed sample, the ratio of the OH^- peak also decreased.

The C 1s spectra were also analyzed after the EUV exposure at the XIL-II synchrotron station and transfer to the spectrometer. Compared to Fig. 7.4c, a larger range was recorded. We found that there is an additional peak at 289.0 eV, representing carbon from C=O. We also studied exposure to DUV (225 nm/5.5 eV,

pulsed laser) and compared this to EUV exposure. It was found that the relative amount of C=O is less under DUV than under EUV exposure.

7.3.4 Ex-situ TOF-SIMS

Additionally, time-of-flight secondary ionization mass spectrometry (TOF-SIMS) was used to characterize the EUV and DUV exposed films. This technique utilizes 30 kV ions (Bi_3^+) colliding with the film, upon which the ions that come off the surface are measured.[34] To compare the different chemical reaction mechanism of TinOH thin film under DUV and EUV, three doses (20, 50, 125 mJ cm^{-2}) were chosen to expose the TinOH thin film. As an example, the spectra from the unexposed, and 50 mJ cm^{-2} DUV and EUV exposed samples are shown in Fig. 7.8. For unexposed films, a tin cage ion having lost one butyl group, attached to a hydroxide anion, at *m*/*z*~2397 was observed in greatest abundance. A small amount of the intact parent ion ($[M]^+$) is detected at ~2436, while other fragmentation products are also present, such as a tin cage which lost 2 butyl groups ($[M\text{-}2Bu]^+$), and the cage without 3 butyl groups but with an extra hydroxide group ($[M\text{-}3Bu+OH]^+$). Low mass fragments of the tin-oxide comprising variable elemental formulas $[M_x+O_y+H_z]$ were also detected.

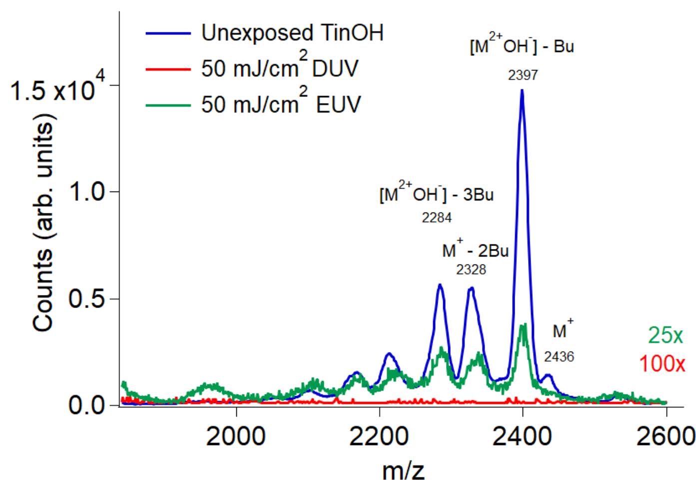

Figure 7.8. *ToF-SIMS spectra of fresh TinOH (blue) and TinOH exposed to 50 mJ/cm^2 DUV (225 nm) radiation and EUV radiation (13.5 nm). For comparison, the mass spectrum corresponding to EUV-exposed sample was amplified 25× while for DUV-exposure it was amplified 100×.*

By comparing the intensity decrease of the spectra at *m*/*z*~2394 (see Fig. 7.8), we can compare the reaction yield. Even though ToF-SIMS is generally not regarded as very quantitative[34], this can give a reasonable estimation. The intensity of the *m*/*z*~2394 in the unexposed sample is 1.5×10^4. It decreased upon exposure. The

intact and near-intact tin oxo cage was observed in far lower abundance for the exposed films relative to unexposed films. For EUV-exposed films, the near-intact tin oxo cage signal could still be detected, but a signal for these species was essentially absent in spectra of DUV-exposed films. Likely, these signals decreased because of cross-linking of different tin oxo cages, leading to large fragments that are outside the range of measurement of the ToF-SIMS instrument.

Weaker signals for bare tin or simple oxides (*m/z* 100-300) were found in all spectra (see Fig. 7.9). These signals correspond to Sn_xO_y fragments, which could be singly or multiply protonated. Since these fragments can already be found in unexposed films of TinOH, they are likely formed during the ToF-SIMS. Because the tin oxo cage has an elaborate Sn-O-Sn network at its core, it can be imagined that fragments from this network are extracted towards the detector.

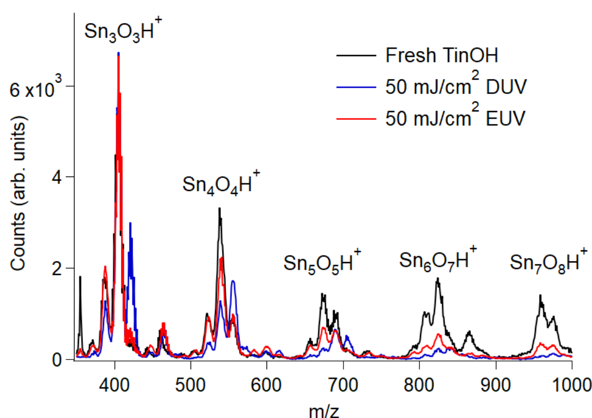

Figure 7.9. *ToF-SIMS spectra in the lower mass range, recorded on a fresh TinOH layer (black), a DUV-exposed layer (blue) and an EUV-exposed layer (red). The spectra were normalized to the first peak ($Sn_3O_3H^+$).*

For EUV exposed spectra, the peak position of these signals remained the same compared to the unexposed film, while for the DUV exposed film a clear change to higher *m/z* values was observed. This shift can be seen most clearly for $Sn_3O_3H^+$ and $Sn_4O_4H^+$. This shift equals an increase of about 16 *m/z* units. The most likely explanation for this is that some of the tin oxo cages were oxidized upon or after exposure in the open air. For example, the 5-coordinated Sn atom could oxidize, creating an additional Sn-O bond. If Sn_xO_y fragments are cleaved (as a result of incident Bi_3^+ ions) after this oxidation has taken place, they may contain an additional oxygen atom.

The ToF-SIMS results suggest that cross-linking occurs for films under both EUV and DUV exposure, and that the reaction to DUV is more efficient than for EUV

using the same energy dose. To quantify these changes, the remaining *m/z* 2200-2450 intensity was compared with the unexposed sample, and the remaining percentage was calculated and listed in Table 7.3. If we consider the converted tin oxo cages as the reaction yield, DUV is more effective than EUV exposure. For example, upon 20 mJ cm^{-2} exposure there is more intact tin oxo cage structure remaining in the EUV exposed sample. With 50 mJ cm^{-2} DUV exposure, the tin oxo cages seem already fully converted at the sample surface, while there is still around 2% of intact tin oxo cages remaining after EUV exposure.

Table 7.3. *Percentage of the remaining m/z 2200-2450 after DUV/EUV exposure.*

Exposure dose	EUV % left	DUV % left
0	100	100
20 mJ cm^{-2}	6.5	<0.13
50 mJ cm^{-2}	1.9	<0.05
125 mJ cm^{-2}	<0.07	<0.05

7.3.5 Chemical changes upon EUV irradiation

Upon EUV exposure, the primary electrons come mainly from the valence band ($E_{kin} > 80$ eV) or from the Sn 4d band ($E_{kin} > 60$ eV). The kinetic energies of more than 60 eV are high enough for these electrons to further promote chemical reactions in the thin film. In our previous work, using 225 nm DUV irradiation, only a decrease in the amount of carbon was observed, which originates from Sn-C bond cleavage (chapters 3 – 5).[28] When EUV is used, primary ionization occurs from atomic and molecular orbitals on Sn, O and C (Fig. 7.10). We may expect, however, that the initially formed ionized species thermalize rapidly, so that the reactions mainly occur from the most stable radical cation, that is, with an electron removed from the highest occupied molecular orbital. The secondary electrons can be expected to ionize mainly the valence manifold, not the Sn 4d orbitals which are shielded by the electron cloud of the molecule. Thus, the starting point is mostly the same for primary and secondary reactions. The emitted electrons will deposit energy in the film and thermalize. They will likely be trapped by tin cage molecules, which, being doubly positively charged, have a high electron affinity. Since the electron mean free path at the initial electron energies is small, the trapping will occur relatively close to the site of origin. Subsequent electron-hole recombination is a quite likely process, which reduces the overall efficiency of the photoreaction. This could explain why the overall quantum yield for the cleavage of butyl groups $\Phi \sim 0.55$ (see below) is not high, despite the generation of multiple electrons per photon.

Based on the results from the various experiments, we propose the reaction mechanism of TinOH under EUV as shown in Fig. 7.10. For the purpose of illustration we use a simplified structure representing a fragment of the tin-oxo cages. The primary reaction of the radical cation is the breaking of the Sn-C bond, because the highest occupied MO, from which an electron is removed, has a strong σ_{Sn-C} character. The butyl radical thus formed could transfer a hydrogen atom producing butene, or react with an active hydrogen atom forming butane, or react with another butyl radical to form octane or the disproportionation products butene and butane. These products were all detected in the outgassing experiment (Fig. 7.5).

Differently from the UV photochemistry, in which a tin-centered radical remains after homolytic cleavage of the Sn-C bond, the tin atom from which the butyl group was lost now has a positive charge. The fate of this tricationic species is not known. In any case it is not a stable molecule that would be detectable in the XPS spectra, because the higher positive charge would lead to a clear increase of the binding energies, which we do not observe. The trication could trap an electron, which would lead again to the same chemistry as in the homolytic photochemical cleavage. Another possible process is deprotonation from a μ_2-OH group, alleviating the high positive charge on the cage. In this reaction, the difference between the different counterions with different basicity, which was observed in chapter 5, could play a role. We observe the formation of C-O bonds in the in-situ experiment (Fig. 7.4b), which suggests a structural rearrangement in which a butyl group binds to an oxygen atom. The mechanism for this is not known. A possible structure is shown in Fig 4.7.

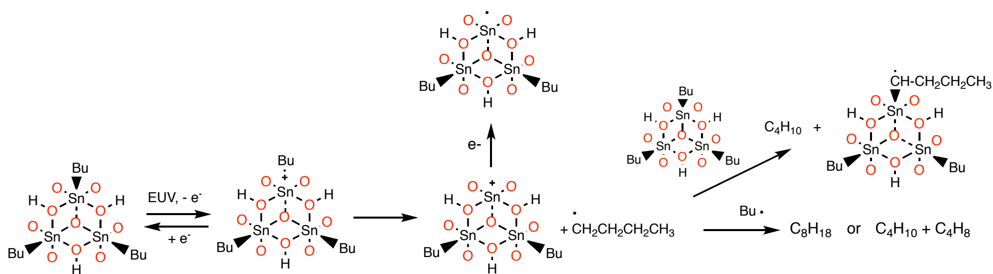

Figure 7.10. *Proposed reactions of TinOH thin film under EUV exposure.*

7.3.6 Chemical changes in *ex-situ* measurement.

The chemical reaction mechanism under EUV exposure should be the same, regardless of irradiation source. In the *ex-situ* experiment, the sample had the opportunity to react with water or oxygen in the atmosphere during transfer. The direct evidence can be found in Fig. 7.7b, where the O 1s sub-peaks at OH^-/C-O position from the exposed samples are increased significantly comparing with the

sub-peak from the *in-situ* measurement in Fig. 7.4b, which is due to oxygen or water absorbed in, or reacted with, the exposed thin films. As in DUV exposures, oxidation-sensitive low-valent tin compounds or hydrides are probably formed also after EUV irradiation. Upon increasing dose to 50 mJ cm^{-2}, the OH^-/C-O shoulder increased, as well as the total amount of oxygen in the film. With the EUV dose further increased to 250 mJ cm^{-2}, the exposed cages seem to form a more stable structure than under 50 mJ cm^{-2} exposure, which has less ability to react with or absorb water or oxygen. When a PEB step is added to the 50 mJ cm^{-2} EUV exposed sample, the unstable species such as the reacted absorbed oxygen, or water can detach from the thin film, which would explain that the oxygen atom number decreases as shown in Table 7.2 and that the OH^-/C-O sub-peak also decreases. With 50 mJ cm^{-2} DUV exposure, the ratio of the OH^-/C-O sub-peak is also much lower than for EUV exposure at the same dose. The clear C-O sub-peak at ~ 286 eV and C=O sub-peak at ~ 289 eV in 7.7c indicate that some carbon atoms were oxidized after exposure. It only showed up on exposed samples, and decreased with increasing dose. They decreased when a baking step (PEB) was applied, which indicates that this species is very sensitive to baking. Volatile products (e.g. butanal) could further outgas during PEB, causing this decrease in C and O content. Comparing with the Sn $3d_{5/2}$ peak from the unexposed sample, the spectra from all the rest of the samples are shifted to the higher binding energy range, which indicates that more electron withdrawing components are connected with the Sn atom in the cages.

From the element ratio and component ratio in the XPS, we can compare the reaction efficiency of tin oxo cages under EUV and DUV exposure at 50 mJ cm^{-2} exposure dose. The DUV linear absorption coefficient was measured in Chapter 5, and agrees well with the absorption coefficient in solution; the EUV linear absorption efficient has been measured in previous work.[31, 41] The same dose was applied on thin films with the same thickness. The absorbed number of photons and the chemical reaction yield are calculated and listed in Table 7.4. The photon energy of DUV is 5.5 eV (225 nm) while EUV has a photon energy of 92 eV, which is 17 times higher. The total absorbed number of DUV photons per molecule is almost 22 times higher than for EUV. The reaction quantum yield can be defined in different ways. In Chapter 3 we estimated the quantum yield for cleavage of butyl chains from the loss of carbon, averaged over a high-dose exposure in air, as $\Phi \sim 0.015$. If we apply the same definition here we note that 7 out of 48 carbon atoms are lost for 20 DUV photons per molecule absorbed on average. This corresponds to a photocleavage quantum yield of $\Phi \sim 0.09$ (Bu-group/photon). For EUV exposure with the same dose, only 2 carbon atoms are lost, but the absorbed number of photons is much smaller, resulting in $\Phi \sim 0.55$. When the PEB is added after the 50 mJ cm^{-2} EUV exposure, the quantum yield is increased to $\Phi \sim 1.7$. The DUV

photocleavage quantum yield found here is considerably higher than the value reported in chapter 3. There we made a crude estimate based on a high conversion, but in the present experiments we used a much smaller conversion, which is more representative of the reactivity of the tin cage. Apparently, the reactivity decreases as more and more butyl groups are lost.

Another way to define the quantum yield is in terms of the number of atoms that undergo a change, as detected in the XPS high-resolution spectra. Then we count the total change of the number of atoms in Sn-C and C-C bonds, and we find that around 0.54 carbon atoms reacted per absorbed DUV photon, about 10.5 carbon atoms reacted per absorbed EUV photon, and with a PEB step added after EUV exposure, this number didn't change. The photocleavage quantum yield is 0.09 for DUV, which corresponds to 0.36 carbon atoms per photon, so there are 0.18 other reactions per photon. Similarly, the butyl loss quantum yield is 0.55 for EUV, corresponding to 2.2 carbon atoms per photon. Because the total conversion is 10.5 carbons/photon the remaining 8.3 carbon atom/photon are changed but not lost. These are the carbon atoms forming C-O and C=O. When PEB is added, the butyl loss quantum yield is increased to $\Phi \sim 1.7$, corresponding to 6.8 carbon atoms per photon. The additional 4-carbon loss in the PEB step is mainly from the carbon atoms that were oxidized after EUV exposure.

Table 7.4. *With 50 mJ cm^{-2} DUV and EUV exposure, the absorbed photon number and the quantum yield of the TinOH thin film.*

TinOH	DUV	EUV	EUV + PEB
Abs coefficient (μm^{-1})	18.6	13.5	13.5
Abs photon/molecule	19.6	0.90	0.9
C change/abs photon	0.54	10.6	10.6
$\Phi_{photocleavage}$ (Bu-group/photon)	0.09	0.55	1.7

7.4 Conclusions

The photoelectron spectrum of TinOH was recorded with different photon energies. The Sn 4d electrons are a rich source of primary electrons in the Sn-containing photoresists under 92 eV excitation. Comparing with 60, 120 and 150 eV, more photoelectrons are generated at 92 eV photon energy.

High-resolution XPS spectra were measured for tin oxo cages which were exposed to high-energy photons: *in-situ* (vacuum conditions) and *ex-situ* (92 eV photon energy, followed by sample transfer under ambient atmosphere to the XPS instrument). For the *in-situ* measurements, the oxygen content in the sample decreased, while for the *ex-situ* measurements such decrease was not found. This

indicates that oxidation takes place upon bringing EUV-exposed tin oxo cage films under ambient atmosphere. In both the *in-situ* and *ex-situ* measurements, formation of carbon-oxygen bonds (C-O) was detected. In the *ex-situ* measurements, an additional formation of C=O was detected, as a result of reaction with water or oxygen. The C-O/C=O species were found to be very sensitive to a post-exposure bake step.

In an outgassing analysis using a residual gas analyzer (RGA), the outgassing of the carbonyl compound butanal was confirmed. Additional outgassing species included butane, butene, octane and butylstannoic acid. It is unclear whether butylstannoic acid was present in the film as an impurity, or whether it can be removed from the tin oxo cage. This could be relevant because outgassing of metal-containing compounds could lead to non-cleanable contamination on the optics of an EUV scanner.[36]

The chemical reaction quantum yields under DUV and EUV exposure were calculated and compared at a dose of 50 mJ cm^{-2}, which is close to the dose required for maximum remaining film thickness after exposure, baking and development. For UV excitation, ~0.09 butyl chains are cleaved per absorbed photon. In terms of quantum yield, EUV excitation is more efficient, giving a loss of ~0.55 butyl chains per photon, which can be increased to 1.7 when PEB is added. This increase is mainly from the cleavage of the EUV irradication induced species. Per unit energy dose, however, DUV is more efficient. Additional photoreactions are observed upon EUV exposure, however, which increase the total quantum efficiency. Chemical reaction mechanisms were proposed, in which Sn-C bond cleavage is an essential first step. Enabling easier Sn-C cleavage, for instance by using tin oxo cages with different attached organic groups, may improve the sensitivity and resolution of the tin oxo cages.

7.5 References

1. C. Wagner and N. Harned, "Lithography gets extreme", *Nat. Photonics*, 2010, **4**, 24-26.
2. R. van Es, M. van der Kerkhof, A. Minnaert, G. Fisser, J. de Klerk, J. Smits, R. Moors, E. Verhoeven, L. Levasier, R. Peeters, M. Pieters and H. Meiling, "EUV for HVM: towards an industrialized scanner for HVM NXE3400B performance update", *Proc. SPIE*, 2018, **10583**, 105830H.
3. J. van Schoot, K. Troost, F. Bornebroek, R. van Ballegoij, S. Lok, P. Krabbendam, J. Stoeldraijer, J. Benschop, J. Finders, H. Meiling, E. van Setten, B. Kneer, P. Kuerz, W. Kaiser, T. Heil and S. Migura, "The future of

EUV lithography: continuing Moore's Law into the next decade", *Proc. SPIE*, 2018, **10583**, 101430R.
4. C. K. Ober, V. Kosma, H. Xu, K. Sakai and E. P. Giannelis, "The Challenges of Highly Sensitive EUV Photoresists", *J. Photopolym. Sci. Technol.*, 2018, **31**, 261-265.
5. H. Ito, "Chemically amplified resists: past, present, and future", *Microlithography '99*, 1999, **3678**, 11.
6. H. Xu, V. Kosma, E. P. Giannelis and C. K. Ober, "In pursuit of Moore's Law: polymer chemistry in action", *Polym. J.*, 2017, **50**, 45-55.
7. K. Takahiro, S. Akinori and T. Seiichi, "Point Spread Function for the Calculation of Acid Distribution in Chemically Amplified Resists for Extreme Ultraviolet Lithography", *Appl. Phys. Express*, 2008, **1**, 027001.
8. J. L. Sturtevant, G. M. Schmid, M. D. Stewart, C.-Y. Wang, B. D. Vogt, V. M. Prabhu, E. K. Lin and C. G. Willson, "Resolution limitations in chemically amplified photoresist systems", *Proc. SPIE*, 2004, **5376**, 333-342.
9. M. Trikeriotis, M. Krysak, Y. S. Chung, C. Ouyang, B. Cardineau, R. Brainard, C. K. Ober, E. P. Giannelis and K. Cho, "A new inorganic EUV resist with high-etch resistance", *Proc. SPIE*, 2012, **8322**, 83220U.
10. E. C. Mattson, Y. Cabrera, S. M. Rupich, Y. Wang, K. A. Oyekan, T. J. Mustard, M. D. Halls, H. A. Bechtel, M. C. Martin and Y. J. Chabal, "Chemical Modification Mechanisms in Hybrid Hafnium Oxo-methacrylate Nanocluster Photoresists for Extreme Ultraviolet Patterning", *Chem. Mater.*, 2018, **30**, 6192-6206.
11. B. Cardineau, R. Del Re, M. Marnell, H. Al-Mashat, M. Vockenhuber, Y. Ekinci, C. Sarma, D. A. Freedman and R. L. Brainard, "Photolithographic properties of tin-oxo clusters using extreme ultraviolet light (13.5 nm)", *Microelectron. Eng.*, 2014, **127**, 44-50.
12. L. Li, X. Liu, S. Pal, S. Wang, C. K. Ober and E. P. Giannelis, "Extreme ultraviolet resist materials for sub-7 nm patterning", *Chem. Soc. Rev.*, 2017, **46**, 4855-4866.
13. L. Li, S. Chakrabarty, J. Jiang, B. Zhang, C. Ober and E. P. Giannelis, "Solubility studies of inorganic-organic hybrid nanoparticle photoresists with different surface functional groups", *Nanoscale*, 2016, **8**, 1338-1343.
14. L. Li, S. Chakrabarty, K. Spyrou, C. K. Ober and E. P. Giannelis, "Studying the Mechanism of Hybrid Nanoparticle Photoresists: Effect of Particle Size on Photopatterning", *Chem. Mater.*, 2015, **27**, 5027-5031.
15. S. Castellanos, L. Wu, M. Baljozovic, G. Portale, D. Kazazis, M. Vockenhuber, Y. Ekinci and T. Jung, "Ti, Zr, and Hf-based molecular hybrid materials as EUV photoresists", *Proc. SPIE*, 2018, **10583**, 105830A.
16. H. Xu, K. Sakai, K. Kasahara, V. Kosma, K. Yang, H. C. Herbol, J. Odent, P. Clancy, E. P. Giannelis and C. K. Ober, "Metal–Organic Framework-Inspired Metal-Containing Clusters for High-Resolution Patterning", *Chem. Mater.*, 2018, **30**, 4124-4133.
17. B. L. Henke, E. M. Gullikson and J. C. Davis, "X-Ray Interactions: Photoabsorption, Scattering, Transmission, and Reflection at E = 50-30,000 eV, Z = 1-92", *Atomic Data and Nuclear Data Tables*, 1993, **54**, 181-342.

18. R. T. Frederick, S. Saha, J. Trey Diulus, F. Luo, J. M. Amador, M. Li, D.-H. Park, E. L. Garfunkel, D. A. Keszler and G. S. Herman, "Thermal and radiation chemistry of butyltin oxo hydroxo: A model inorganic photoresist", *Microelectron. Eng.*, 2019, **205**, 26-31.
19. R. Frederick, T. Diulus, D. Hutchison, M. Nyman and G. S. Herman, "Effect of Oxygen on Thermal and Radiation Induced Chemistries in a Model Organotin Photoresist", *ACS Appl. Mater. Interfaces*, 2019, DOI: 10.1021/acsami.8b16048.
20. S. T. Meyers, J. T. Anderson, J. B. Edson, K. Jiang, D. A. Keszler, M. K. Kocsis, A. J. Telecky and B. Cardineau, *US 2016/0116839 A1*, 2015, 40.
21. S. T. Meyers, J. T. Anderson, J. B. Edson, K. Jiang, D. A. Keszler, M. K. Kocsis, A. J. Telecky and B. Cardineau, *US 9310684B2*, 2016.
22. R. Fallica, J. K. Stowers, A. Grenville, A. Frommhold, A. P. G. Robinson and Y. Ekinci, "Dynamic absorption coefficients of chemically amplified resists and nonchemically amplified resists at extreme ultraviolet", *J. Micro/Nanolitho. MEMS MOEMS*, 2016, **15**, 03350601-07.
23. E. Buitrago, M. Meeuwissen, O. Yildirim, R. Custers, R. Hoefnagels, G. Rispens, M. Vockenhuber, I. Mochi, R. Fallica, Z. Tasdemir and Y. Ekinci, "State-of-the-art EUV materials and processes for the 7nm node and beyond", *Proc. SPIE*, 2017, **10143**, 10143-10148.
24. C. K. Hohle, R. Gronheid, A. Vaglio Pret, T. Graves, D. Blankenship and J. J. Biafore, "Modeling and simulation of low-energy electron scattering in organic and inorganic EUV photoresists", 2017, **10146**, 1014609.
25. R. Del Re, M. Sortland, J. Passarelli, B. Cardineau, Y. Ekinci, M. Vockenhuber, M. Neisser, D. A. Freedman and R. L. Brainard, "Low-LER tin carboxylate photoresists using EUV", *Proc. SPIE*, 2015, **9422**, 94222101-10.
26. C. Eychenne-Baron, F. Ribot and C. Sanchez, "New synthesis of the nanobuilding block $\{(BuSn)_{12}O_{14}(OH)_6\}^{2+}$ and exchange properties of $\{(BuSn)_{12}O_{14}(OH)_6\}(O_3SC_6H_4CH_3)_2$", *J. Organomet. Chem.*, 1998, **567**, 137-142.
27. J. Haitjema, Y. Zhang, N. Ottosson and A. M. Brouwer, "Photoreactions of Tin Oxo Cages, Model EUV Photoresists", *J. Photopolym. Sci. Technol.*, 2017, **30**, 99-102.
28. Y. Zhang, J. Haitjema, X. Liu, F. Johansson, A. Lindblad, S. Castellanos, N. Ottosson and A. M. Brouwer, "Photochemical conversion of tin-oxo cage compounds studied using hard x-ray photoelectron spectroscopy", *J. Micro/Nanolitho. MEMS MOEMS*, 2017, **16**, 023510.
29. J. Haitjema, L. Wu, A. Giuliani, L. Nahon, S. Castellanos and A. M. Brouwer, "Photo-induced Fragmentation of a Tin-oxo Cage Compound", *J. Photopolym. Sci. Technol.*, 2018, **31**, 243-247.
30. Y. Zhang, J. Haitjema, M. Baljozovic, M. Vockenhuber, D. Kazazis, T. A. Jung, Y. Ekinci and A. M. Brouwer, "Dual-tone Application of a Tin-Oxo Cage Photoresist Under E-beam and EUV Exposure", *J. Photopolym. Sci. Technol.*, 2018, **31**, 249-255.

31. J. Haitjema, Y. Zhang, M. Vockenhuber, D. Kazazis, Y. Ekinci and A. M. Brouwer, "Extreme ultraviolet patterning of tin-oxo cages", *J. Micro/Nanolitho. MEMS MOEMS*, 2017, **16**, 033510.
32. G. Sun, S. Cho, C. Clark, S. V. Verkhoturov, M. J. Eller, A. Li, A. Pavia-Jimenez, E. A. Schweikert, J. W. Thackeray, P. Trefonas and K. L. Wooley, "Nanoscopic cylindrical dual concentric and lengthwise block brush terpolymers as covalent preassembled high-resolution and high-sensitivity negative-tone photoresist materials", *J. Am. Chem. Soc*, 2013, **135**, 4203-4206.
33. E. Giangrisostomi, R. Ovsyannikov, F. Sorgenfrei, T. Zhang, A. Lindblad, Y. Sassa, U. B. Cappel, T. Leitner, R. Mitzner, S. Svensson, N. Mårtensson and A. Föhlisch, "Low Dose Photoelectron Spectroscopy at BESSY II: Electronic structure of matter in its native state", *J. Electron. Spectrosc. Relat. Phenom.*, 2018, **224**, 68-78.
34. R. Ovsyannikov, P. Karlsson, M. Lundqvist, C. Lupulescu, W. Eberhardt, A. Föhlisch, S. Svensson and N. Mårtensson, "Principles and operation of a new type of electron spectrometer – ArTOF", *J. Electron. Spectrosc. Relat. Phenom.*, 2013, **191**, 92-103.
35. J. F. Moulder and J. Chastain, Handbook of X-ray Photoelectron Spectroscopy: A Reference Book of Standard Spectra for Identification and Interpretation of XPS Data, Physical Electronics Division, Perkin-Elmer Corporation, 1992.
36. J. J. Yeh and I. Lindau, "Atomic subshell photoionization cross sections and asymmetry parameters: $1 \leqslant Z \leqslant 103$", *Atomic Data and Nuclear Data Tables*, 1985, **32**, 1-155.
37. S. Tanuma, C. J. Powell and D. R. Penn, "Calculations of electron inelastic mean free paths", *Surf. Interface Anal.*, 2005, **37**, 1-14.
38. A. M. Brouwer, unpublished result.
39. A. Ganguly, S. Sharma, P. Papakonstantinou and J. Hamilton, "Probing the Thermal Deoxygenation of Graphene Oxide Using High-Resolution In Situ X-ray-Based Spectroscopies", *J. Phys. Chem. C*, 2011, **115**, 17009-17019.
40. NIST Chemistry WebBook, NIST Standard Reference Database Number 69, National Institute of Standards and Technology, 2005.
41. R. Fallica, J. Haitjema, L. Wu, S. Castellanos, A. M. Brouwer and Y. Ekinci, "Absorption coefficient and exposure kinetics of photoresists at EUV", *Proc. SPIE*, 2017, **10143**, 101430A.

Chapter 8

Dual-tone application of a tin oxo cage photoresist under e-beam and EUV exposure[*]

We report on the dual-tone property of the tin oxo cage $[(BuSn)_{12}O_{14}(OH)_6]OH_2$ photoresist. After exposing the resist film to a low dose extreme ultraviolet radiation or electron beam, applying a post exposure bake step and development with isopropanol/H_2O (2:1), a positive tone image is observed. The previously observed negative tone is found at higher doses. Atomic force microscopy and scanning electron microscopy were used to characterize the topography of the patterns. X-ray photoelectron spectroscopy was used to elucidate the chemical changes of the tin-oxo cages under different conditions. The photoresist, which has dual-tone property, paves the way to fabricate sophisticated structures in a single photoresist layer or may lead to metal containing resists with improved sensitivity.

* This chapter was published in: Y. Zhang, J. Haitjema, M. Baljozovic, M. Vockenhuber, D. Kazazis, T. A. Jung, Y. Ekinci and A. M. Brouwer, "Dual-tone Application of a Tin-Oxo Cage Photoresist Under E-beam and EUV Exposure", *J. Photopolym. Sci. Technol.*, 2018, **31**, 249-255.

8.1 Introduction

Photoresist performance plays a key role in high-resolution photolithography and must be adapted to the continuously decreased wavelength of the light source in lithography tools. Chemically-amplified photoresists are widely used in ultraviolet (UV) and deep wavelength ultraviolet (deep UV, DUV) technology.[1, 2] With the increasing requirements on photoresist performance, such as resolution, sensitivity and line edge roughness, inorganic molecular photoresists, especially metal containing photoresists, have attracted attention due to their small molecular size, strong etching resistance and high absorption cross-section at the extreme ultraviolet (EUV) wavelength of 13.5 nm.[3-7]

Tin-oxo cages are known to work as negative tone photoresists under EUV and DUV exposure and in electron beam lithography. They are highly sensitive and potentially give high resolution due to their high EUV absorption cross-section and small molecular size.[4, 8-10] To realize a negative tone pattern, a 30 mJ cm^{-2} EUV dose, a post exposure bake (PEB) step (~100°C for 2 min) and a development step (2:1 IPA/H_2O for 30 s) are needed.[4, 8]

Dual-tone properties of photoresists have been reported in recent years.[11-16] Switching between positive and negative tone patterns is usually achieved by changing developer.[3, 11, 13] In the present work, a dual-tone patterning is realized by performing the PEB step at an elevated temperature (150°C for 2 min) after EUV or e-beam exposure and before development (2:1 IPA/H_2O for 30 s). At low doses, a positive tone is achieved, while higher doses result in a negative tone pattern. The dual-tone property of the tin-oxo cage photoresist in principle gives the possibility to fabricate positive and negative tone structures in a single step.

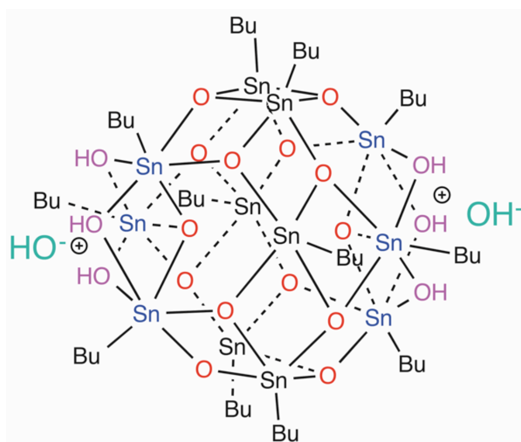

Figure 8.1. The chemical structure of the tin-oxo cage with hydroxides as counterions (TinOH).

8.2 Materials and Methods

8.2.1 Materials

The tin-oxo cages with hydroxide as counterion $[(BuSn)_{12}O_{14}(OH)_6]OH_2$ abbreviated here as TinOH was synthesized according to the literature.[8, 17] The compound was dissolved in toluene (~10 mg mL^{-1} for patterning and 2 mg mL^{-1} for XPS) and the solution was filtered through a 0.2 μm PTFE filter before spin-coating. The solutions were spin-coated (700 rpm s^{-1} acceleration, 2500 rpm for 35 s) on different substrates (pre-cleaned and HDMS-treated Si for patterning, 20 nm Au coated glass for XPS) to give 20 ± 2 nm thin films for patterning and 5 ± 2 nm thin films for XPS. Post application bake (PAB) (90 ^{o}C, 1 min) was applied to remove residual solvent. After exposure, the samples were baked at 150 ^{o}C for 2 min, developed in a 2:1 isopropanol/H_2O mixture for 30 s, rinsed with water for 30 s, blown dry with N_2, and finally baked (hard bake; HAB) at 150 ^{o}C for 1 min to further remove residual solvent.

8.2.2 Exposure

E-beam lithography was performed using a Raith e-line lithography system (30 keV, 32 pA). EUV (13.5 nm, 92 eV) interference lithography was performed at the XIL-II beamline of the Swiss Light Source, the synchrotron light source at the Paul Scherrer Institute (PSI).

8.2.3 Characterization

Atomic force microscopy (AFM, Bruker Dimension Icon) was used to check the film thickness and the topography of the exposed pattern. Scanning electron microscopy (SEM) images were recorded using the FEI Verios 460. X-ray photoelectron spectroscopy (XPS) using a SPECS analyzer Phoibos 150, with a monochromatic Al Kα source (1486.6 eV, power 200 W) was used to characterize the chemical changes of the resist thin film under different conditions. Thermogravimetric analysis (TGA) was performed with a NETZSCH STA 449 F3 Jupiter equipped with automatic sample changer.

8.3 Result and Discussion

8.3.1 Topography characterization

The tin-oxo cage with hydroxide counterions (TinOH, see Fig. 8.1) was used as a model photoresist. The photoresist solution was spin-coated on Si wafers and exposed to EUV or e-beam.

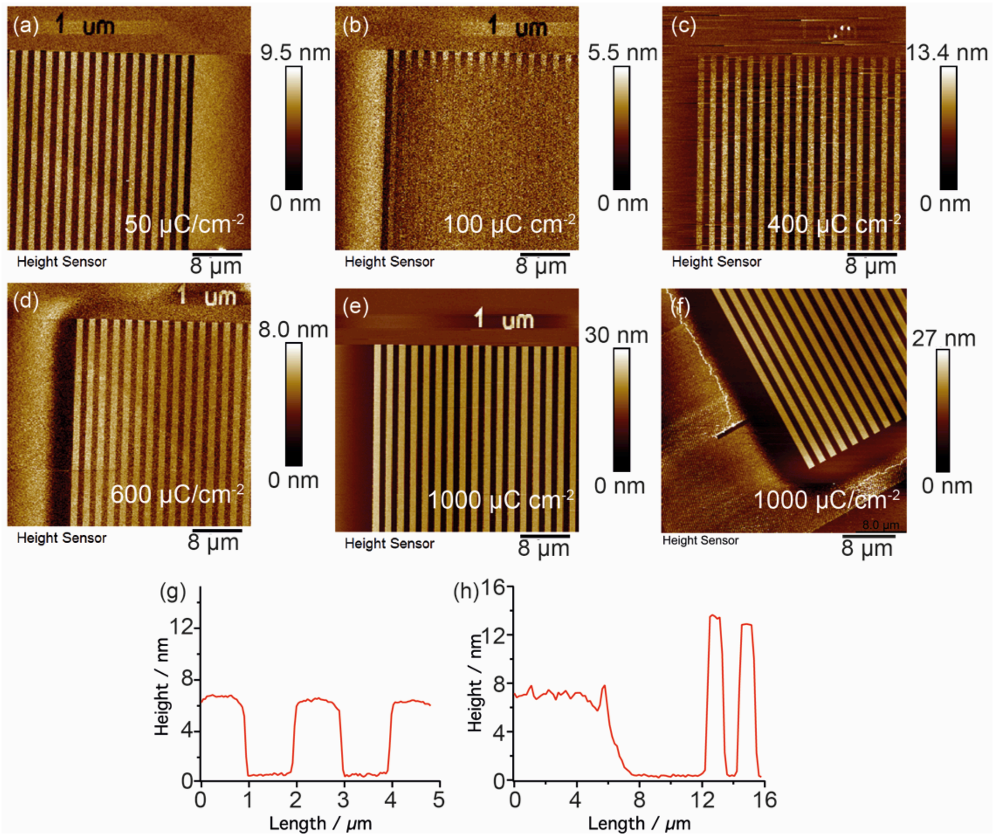

Figure 8.2. *AFM images of tin-oxo cage photoresist patterned using e-beam lithography performed with different doses, a) 50 μC cm^{-2}, b) 100 μC cm^{-2}, c) 400 μC cm^{-2}, d) 600 μC cm^{-2}, e) 1000 μC cm^{-2}, f) 1000 μC cm^{-2}, g) Cross section of positive tone pattern in a; h) Cross section of negative tone pattern in f.*

E-beam lithography was used to write 1 μm line/space patterns on the tin-oxo cage layer. After exposing the thin layer to different e-beam doses and applying PEB, development, rinse and HAB, the topography of the patterns was studied using AFM. Different tone patterns were observed on the same sample, as depicted in Fig. 8.2. The exposed part was removed in the first pattern in Fig. 8.2a, giving the positive tone pattern at a dose of 50 μC cm^{-2}. With 100 μC cm^{-2} (Fig. 8.2b), the exposed part was partly removed, making it difficult to distinguish the exposed and unexposed areas. When the dose was increased to 400 μC cm^{-2} (Fig. 8.2c) and 600 μC cm^{-2} (Fig. 8.2d), the negative tone pattern started to grow. At 1000 μC cm^{-2} (Fig. 8.2e and 8.2f), the exposed part is clearly negative tone. The edge of the high dose exposed part, however, was removed by the developer, and it thus shows a positive tone behavior. The spaces between the exposed lines were totally cleared. The phenomenon can be explained as a result of the proximity effect in e-beam lithography.[18] The high-energy primary electrons can interact with the resist layer or

further below at the interface of the resist and the substrate where low energy electrons are generated that diffuse to the unexposed areas. For this reason, the edge of the high dose exposed pattern behaves like the low dose exposed material, and gives rise to a positive tone. The higher the dose, the stronger the proximity effect will be. When the sample was exposed to 400 µC cm^{-2} and 600 µC cm^{-2} dose, respectively, the low energy electrons generated by the proximity effect are insufficient to convert the edge part. With a higher dose of 1000 µC cm^{-2}, the proximity effect is quite strong. Not only were the spaces between the exposed lines cleared, but also the area at the edge of the pattern was cleared. The different tones in the different images are clearly seen in the "1 um" marker at the top of each image.

Cross sections of the patterns in Figs. 8.2a and 8.2f are displayed in Figs. 8.2g and 8.2h. The original film thickness was 20 ± 2 nm. As we can observe from Fig. 8.2e, after all the processing the unexposed part left a ~7 nm thick film, and the 50 µC cm^{-2} exposed part was totally removed. In Fig. 8.2f, the film thickness of the 1000 µC cm^{-2} exposed part is 14 nm. The space between the exposed parts and the edge part of the pattern was cleaned. The area far away from the positive tone edge part of the pattern still exhibits a 7 nm thick film after the completed process. The width of the positive tone edge of the pattern (around 4.5 µm) could correspond to the diffusion length of the electron generated from proximity effect at the interface below the resist layer.[19]

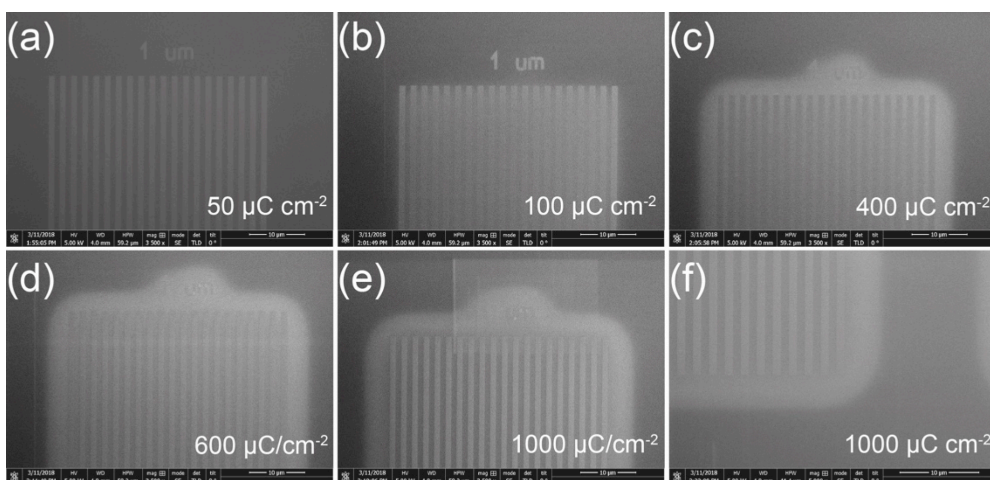

Figure 8.3. *SEM images of tin-oxo cage photoresist TinOH patterned using e-beam lithography with different doses, a) 50 µC cm^{-2}, b) 100 µC cm^{-2}, c) 400 µC cm^{-2}, d) 600 µC cm^{-2}, e) 1000 µC cm^{-2}, f) 1000 µC cm^{-2}, followed by PEB at 150°C for 2 min, development with 2:1 IPA/H_2O for 30 s, rinse with water for 10 s and HAB.*

SEM was also used to characterize the same e-beam exposed pattern. Since we observed (Fig. 8.2a) that the exposed part responds with a positive tone, the bright lines in Fig. 8.3a represent the positive tone pattern. With the dose increasing from 50 to 1000 μC cm^{-2}, the negative tone pattern starts and the edge effect also becomes obvious. The signal intensity cannot be used to distinguish the tone properties in these SEM images. AFM is a more appropriate technique to characterize the tone property.

The dual-tone phenomenon was also observed when the tin-oxo cage film was exposed to EUV. AFM and SEM were used to characterize the patterns from the EUV exposure. With the dose increasing from 3.6 to 53.5 mJ cm^{-2}, the positive tone first starts to show and then converts to negative tone pattern as shown in Figs. 8.4a to f.

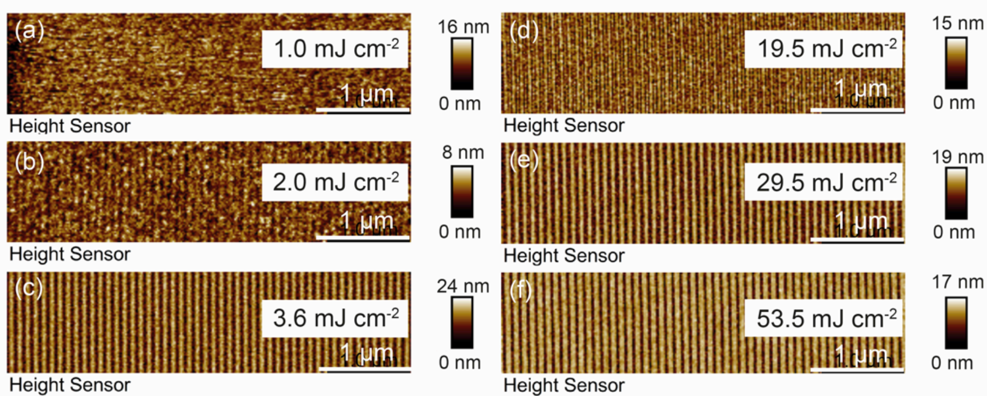

Figure 8.4. *AFM images of tin oxo cage photoresist patterned by EUV lithography (100 nm pitch) performed with different doses, a) 1 mJ cm^{-2}, b) 2 mJ cm^{-2}, c) 3.6 mJ cm^{-2}, d) 19.5 mJ cm^{-2}, e) 29.5 mJ cm^{-2}, f) 53.5 mJ cm^{-2}.*

We present the edges of the patterns from two exposure doses here (3.6 mJ cm^{-2}, 53.5 mJ cm^{-2}) in Fig. 8.5. The SEM images of 3.6 mJ cm^{-2} EUV exposed 100 nm pitch pattern is displayed in Fig. 8.5a, the AFM image is in Fig. 8.5b, and a cross section of Fig. 8.5b is displayed in Fig. 8.5c.

A clear positive tone pattern is observed in Fig. 8.5b. The depth of the positive tone pattern is around 7 nm, similarly to the result observed from the e-beam exposure. The remaining film thickness is also around 7 nm. Towards the edge of the pattern, the depth of the exposed line becomes lower because of the even lower dose of EUV at the edge part. The SEM and AFM results for a dose of 53.5 mJ cm^{-2} are presented in Figs. 8.5d, e and f. At this exposure the negative tone pattern starts to grow, while positive tone response was observed at the edge part of the pattern. The dose at the edge part is high enough to generate a positive tone, but the interference

line cannot be observed any more. The remaining thickness of the unexposed area is around 6 nm. Above all, the dual-tone property of the TinOH can be observed both under EUV and E-beam exposure.

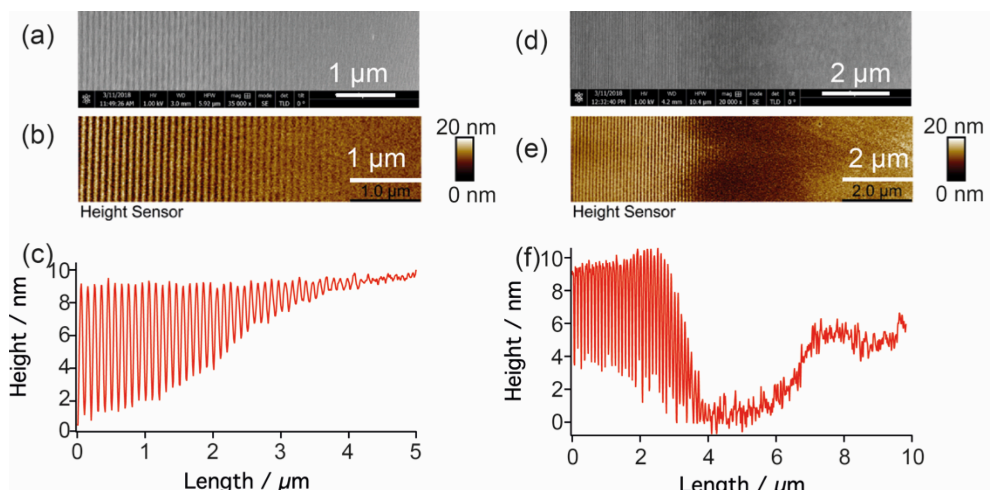

Figure 8.5. *a) SEM images of 3.6 mJ cm^{-2} EUV dose patterned tin oxo cage thin film, b) AFM images of 3.6 mJ cm^{-2} EUV dose patterned tin oxo cage thin film, c) Cross section of image in b; d) SEM images of 53.5 mJ cm^{-2} EUV dose patterned tin oxo cage thin film, e) AFM images of 53.5 mJ cm^{-2} EUV dose patterned tin oxo cage thin film, f) Cross section of image in e.*

The curves of remaining film thickness of TinOH as a function of EUV and e-beam dose are shown in Fig. 8.6. After performing PEB at 150°C for 2 min and development (2:1 IPA/H_2O for 30 s), the unexposed part has ~40% film thickness remaining. For the e-beam exposed sample, when the film was exposed to 50 - 200 μC cm^{-2} the film was totally cleaned. From 500 to 1300 μC cm^{-2}, there is a flat zone. With dose increasing from 1300 to 2000 μC cm^{-2}, the remaining film thickness increased. When the dose was increased above 2000 μC cm^{-2}, the film thickness decreased again due to the loss of more and more of the butyl groups, leading to densification of the materials. For the EUV exposed sample, the change of the film thickness shows a similar tendency. At the first stage (dose below 2 mJ cm^{-2}), the film thickness decreased with increase of the dose. As the dose was further increased, the remaining film thickness increased after overcoming a flat zone (dose 3 to 6 mJ cm^{-2}). The negative tone reaches a maximum when the dose reaches to 10 mJ cm^{-2}. The film thickness decreased slightly when higher dose was applied due to the densification of the materials similarly to the e-beam result. The plots of film thickness vs. dose again illustrate the dual-tone property of TinOH.

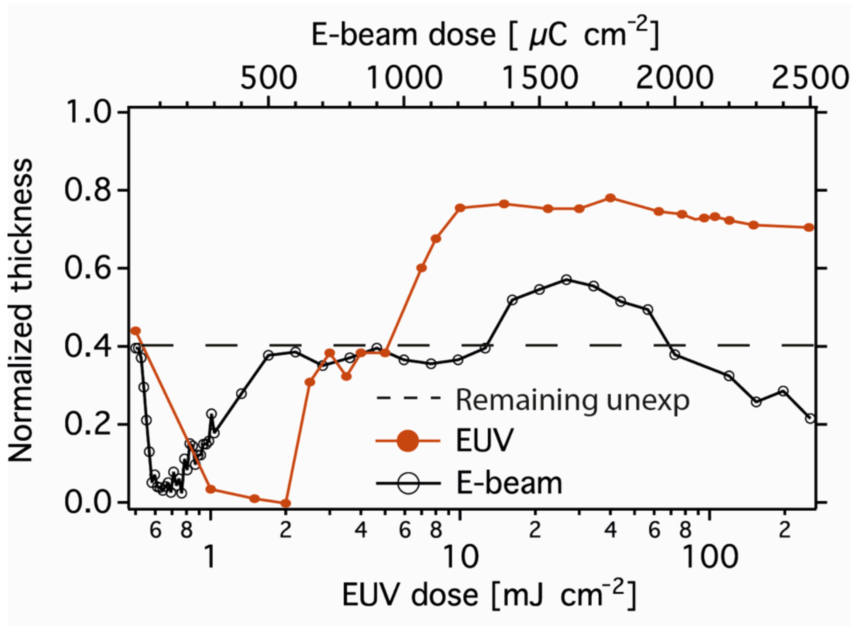

Figure 8.6. *Remaining layer thickness of TinOH films after EUV or e-beam exposure with post exposure bake (150°C for 2 min) and development in 2:1 IPA/H_2O for 30 s. Dashed line represents the thickness of remaining unexposed part. The initial layer thickness was ~20 nm.*

8.3.2 XPS characterization

The phenomenon of the dual tone pattern has been described above. The mechanism behind this phenomenon, however, is unknown. XPS was used in an attempt to characterize chemical changes in the EUV exposed tin-oxo cage thin films, and TGA was used to investigate the thermal stability of the material.

Several samples (Table 8.1) were produced with different exposure and baking conditions on Au coated glass substrates for XPS analysis. The overview spectra of the samples are shown in Fig. 8.7. All the relevant elements present in the composition of the material are observed in the spectra as Sn $3d_{3/2}$ and Sn $3d_{5/2}$, C 1s, and O 1s peaks.

Additionally, in some cases Au 4f peaks are visible, originating from the gold substrate below the thin photoresist layers. Since the area of each element's peaks is related to the atomic concentration of the element in the thin film, the relative atomic composition of the samples could be calculated, and the results are listed in Table 8.1.

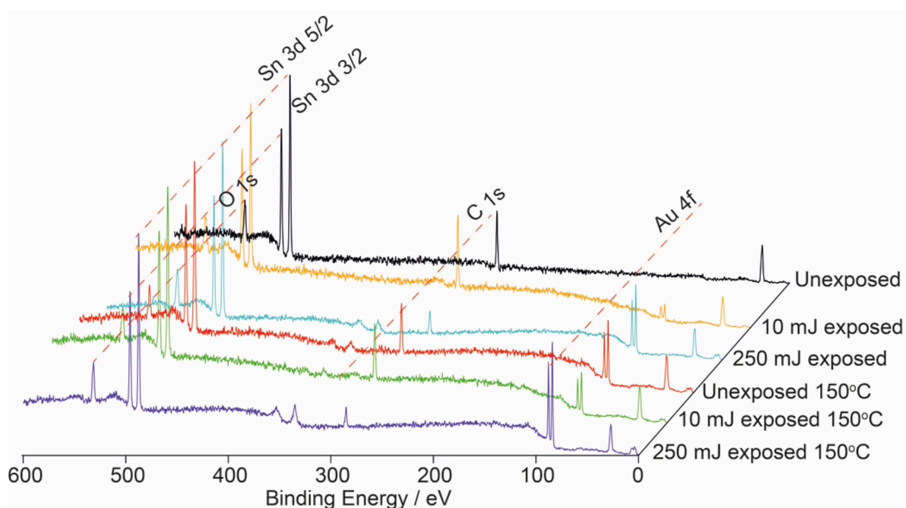

Figure 8.7. *Overview spectra of unexposed, 10 mJ cm^{-2}, and 250 mJ cm^{-2} exposed TinOH thin layer sample, and another set of samples that were prepared in the same way but were subjected to post exposure bake at 150°C for 2 min.*

Table 8.1. *Normalized relative atomic concentration of elements present in different tin-oxo cage samples calculated from spectra shown in Fig. 8.7.*

Atomic.	Sn	O	C
Theoretical	12	22	48
Unexposed	12	22±1	48±2
150 ^{o}C	12	18±1	50±2
10 mJ cm^{-2}	12	22±1	50±2
10 mJ cm^{-2} 150 ^{o}C	12	22±1	48±2
250 mJ cm^{-2}	12	22±1	33±2
250 mJ cm^{-2} 150 ^{o}C	12	24±1	34±2

In Table 8.1, all the elemental ratios are normalized to Sn. The elemental ratio of the unexposed sample agrees well with the theoretical ratio calculated from the molecular structure of the material. If there is no PEB at 150°C the unexposed layer can be removed by the 2:1 IPA/H_2O developer.[8] When the unexposed thin film was baked at 150°C for 2 min, a small loss of oxygen was observed. For the 10 mJ cm^{-2} EUV exposed samples, the element ratio stayed the same as in the original film irrespective of whether the baking step was performed. For the 250 mJ cm^{-2} EUV exposed thin films, a substantial fraction of carbon was lost while the oxygen content gained possibly by oxidation after baking at 150°C. The loss of carbon is caused by the breaking of Sn-C bonds upon photoactivation.[20] As observed before,

the film becomes insoluble in the developer at this stage of exposure and forms a negative tone pattern. PEB is not even needed although it helps to increase the sensitivity.[8]

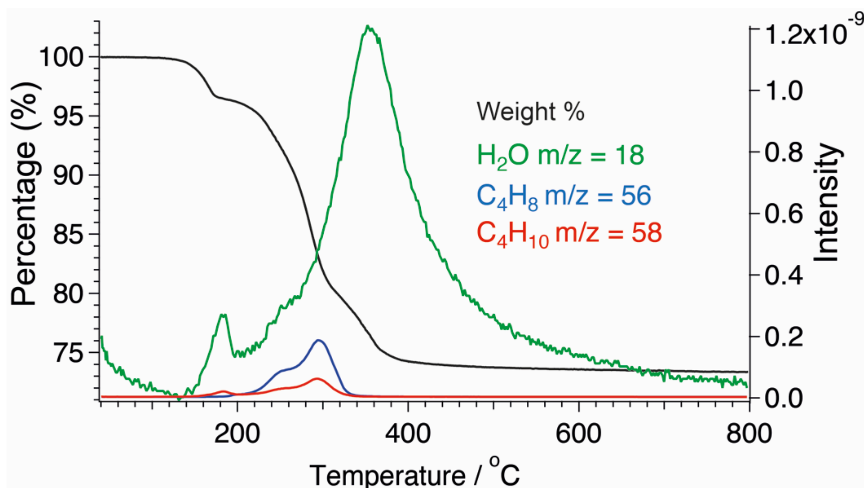

Figure 8.8. *TGA analysis of the TinOH powder. Weight vs. temperature (increase ca. 60 °C min^{-1}) (black), mass spectral traces corresponding to loss of water, butene and butane (green, blue and red).*

A thermogravimetric analysis (TGA) was performed on the original tin-oxo cage material in the powder form. Mass spectrometry was used to characterize the fragments lost during progressive heating. As shown in Fig. 8.8, there is no obvious mass loss below 130 °C. A loss of H_2O was observed between 130 to 200 °C. The theoretical decrease in mass for loss of two H_2O molecules would be 1.5%. In Fig. 8.8, the mass loss at 150 °C is 1%, indicating the materials could lose more than one H_2O molecule per molecule / unit $[(BuSn)_{12}O_{14}(OH)_6](OH)_2$, which is enough to lead to the solubility change. This result also corresponds well to the O loss observed in the XPS data of the unexposed sample after baking at 150 °C. Both these results indicate that the tin cage with the hydroxide counterion may be inherently unstable. In molecular quantum chemistry calculations we observed that the OH^- ion can easily attack the tin cage as a nucleophile, and it can also act as a base and deprotonate a bridging OH group.[21] Hydrogen bonding by a few water molecules can “tame” the reactive OH^- ion. We hypothesize that loss of such solvent-water molecules and the further loss of water due to deprotonation destabilize the cage structure, making it prone to undergo ring opening and condensation reactions with neighboring cages. We also observe loss of butane and butane in the TGA experiment, but this requires temperatures > 200°C. The results of our multi-technique analysis provide a tentative explanation for the reduced solubility of the unexposed materials after a PEB step at 150°C for 2 min. Low dose irradiation with EUV photons or electrons probably also leads to Sn-C bond

cleavage, but the chemical conversions are probably too small to be detectable in our XPS analysis. The small conversion, however, is sufficient to change the properties of the film. This makes it less sensitive to PEB, allowing the positive tone development. PMMA shows a similar tone switch in e-beam exposure, which is readily understood as a result of initial chain shortening (increasing solubility) followed by cross-linking (decreasing solubility).[16] In our materials, the explanation is still unknown. The molecular-level details of this conversion process remain to be investigated in future depth.

8.4 Conclusions

Dual-tone patterns can be realized by using tin-oxo cages as a photoresist for EUV and e-beam exposures. Upon baking the unexposed TinOH film at ~150°C, the solubility decreased. Considering the TGA results, we relate this to the water loss occurring at this temperature. In low-dose exposed regions of the same sample, however, the exposed part can still be dissolved after baking. Thus, the exposure changes the sensitivity of the material to heating. The chemical changes, which are decisive for this transition, are below or close to the limit of detection of our XPS analysis of a few percent. This indicates that the chemical modification of only a small number of the many atoms contained in the tin-oxo cages can already modify the development behavior of this resist material. Upon application of high doses of photons or electrons, in contrast, a substantial loss of carbon occurs, readily detectable by means of XPS, and the exposed part cannot be dissolved in the same developer. The unexposed part can still be dissolved, provided that the baking temperature is not too high. In this way, the same film can be used to generate a positive or negative tone photoresist with the same developer.

8.5 References

1. S. Matsumaru, T. Fujii, T. Kamizono, K. Suzuki, H. Yamazaki, M. Arai, Y. Komuro, A. Kawaue, D. Kawana, T. Hirayama and K. Ohmori, "Development of EUV chemically amplified resist which has novel protecting group", *Proc. SPIE*, 2015, **9425**, 94250U.
2. T. Fujii, S. Matsumaru, T. Yamada, Y. Komuro, D. Kawana and K. Ohmori, "Patterning performance of chemically amplified resist in EUV lithography", *Proc. SPIE*, 2016, **9776**, 97760Y.
3. L. Li, S. Chakrabarty, J. Jiang, B. Zhang, C. Ober and E. P. Giannelis, "Solubility studies of inorganic-organic hybrid nanoparticle photoresists with different surface functional groups", *Nanoscale*, 2016, **8**, 1338-1343.
4. B. Cardineau, R. Del Re, M. Marnell, H. Al-Mashat, M. Vockenhuber, Y. Ekinci, C. Sarma, D. A. Freedman and R. L. Brainard, "Photolithographic properties of tin-oxo clusters using extreme ultraviolet light (13.5 nm)", *Microelectron. Eng.*, 2014, **127**, 44-50.

5. R. Del Re, J. Passarelli, M. Sortland, B. Cardineau, Y. Ekinci, E. Buitrago, M. Neisser, D. A. Freedman and R. L. Brainard, "Low-line edge roughness extreme ultraviolet photoresists of organotin carboxylates", *J. Micro/Nanolitho. MEMS MOEMS*, 2015, **14**, 043506.
6. L. Li, S. Chakrabarty, K. Spyrou, C. K. Ober and E. P. Giannelis, "Studying the Mechanism of Hybrid Nanoparticle Photoresists: Effect of Particle Size on Photopatterning", *Chem. Mater.*, 2015, **27**, 5027-5031.
7. L. Li, X. Liu, S. Pal, S. Wang, C. K. Ober and E. P. Giannelis, "Extreme ultraviolet resist materials for sub-7 nm patterning", *Chem. Soc. Rev.*, 2017, **46**, 4855-4866.
8. J. Haitjema, Y. Zhang, M. Vockenhuber, D. Kazazis, Y. Ekinci and A. M. Brouwer, "Extreme ultraviolet patterning of tin-oxo cages", *J. Micro/Nanolitho. MEMS MOEMS*, 2017, **16**, 7.
9. Y. Zhang, J. Haitjema, X. Liu, F. Johansson, A. Lindblad, S. Castellanos, N. Ottosson and A. M. Brouwer, "Photochemical conversion of tin-oxo cage compounds studied using hard x-ray photoelectron spectroscopy", *J. Micro/Nanolitho. MEMS MOEMS*, 2017, **16**, 023510.
10. R. Fallica, J. Haitjema, L. Wu, S. Castellanos, F. Brouwer and Y. Ekinci, "Absorption coefficient and exposure kinetics of photoresists at EUV", *Proc. SPIE*, 2017, **10143**, 101430A.
11. X. Hu, J. A. Lawrence, J. Mullahoo, Z. C. Smith, D. J. Wilson, C. R. Mace and S. W. Thomas, "Directly Photopatternable Polythiophene as Dual-Tone Photoresist", *Macromolecules*, 2017, **50**, 7258-7267.
12. V. Canalejas-Tejero, S. Carrasco, F. Navarro-Villoslada, J. L. García Fierro, M. del C. Capel-Sánchez, M. C. Moreno-Bondi and C. A. Barrios, "Ultrasensitive non-chemically amplified low-contrast negative electron beam lithography resist with dual-tone behaviour", *J. Mater. Chem. C*, 2013, **1**, 1392.
13. A. Wolfberger, A. Petritz, A. Fian, J. Herka, V. Schmidt, B. Stadlober, R. Kargl, S. Spirk and T. Griesser, "Photolithographic patterning of cellulose: a versatile dual-tone photoresist for advanced applications", *Cellulose*, 2015, **22**, 717-727.
14. C. Xue, D. Y. Wong and A. M. Kasko, "Complex dynamic substrate control: dual-tone hydrogel photoresists allow double-dissociation of topography and modulus", *Adv. Mater.*, 2014, **26**, 1577-1583.
15. S. T. Meyers, J. T. Anderson, J. B. Edson, K. Jiang, D. A. Keszler, M. K. Kocsis, A. J. Telecky and B. Cardineau, *US 2016/0116839 A1*, 2015.
16. A. C. F. Hoole, M. E. Welland and A. N. Broers, "Negative PMMA as a high-resolution resist - the limits and possibilities", *Semicond. Sci. Technol.*, 1997, **12**, 1166.
17. C. Eychenne-Baron, F. Ribot and C. Sanchez, "New synthesis of the nanobuilding block $\{(BuSn)_{12}O_{14}(OH)_6\}^{2+}$ and exchange properties of $\{(BuSn)_{12}O_{14}(OH)_6\}(O_3SC_6H_4CH_3)_2$", *J. Organomet. Chem.*, 1998, **567**, 137-142.
18. T. H. P. Chang, "Proximity effect in electron-beam lithography", *J. Vac. Sci. Technol.*, 1975, **12**, 1271.

19. C. A. Mack, "Electron-beam lithography simulation for mask making: VI. Comparison of 10- and 50-kV GHOST proximity effect correction", *Proc. SPIE*, 2001, **4409**, 194-203.
20. J. Haitjema, Y. Zhang, N. Ottosson and A. M. Brouwer, "Photoreactions of Tin Oxo Cages, Model EUV Photoresists", *J. Photopolym. Sci. Technol.*, 2017, **30**, 99-102.
21. A. M. Brouwer, unpublished results.

Chapter 9

Low-valent Tin Carboxylates as Photoresists*

The interaction of two tin(II) carboxylate compounds, tin(II) 2-ethylhexanoate ($Sn[O_2CCH(C_2H_5)(C_4H_9)]_2$) and tin (II) acetate ($Sn(O_2CCH_3)_2$), with ultraviolet and extreme ultraviolet radiation was investigated. Both compounds are sensitive to these types of radiation, and can form insoluble films after light exposure. Resolved line patterns, however, could not be obtained. Investigation of the thin films using IR and XPS spectroscopies indicated that the materials undergo chemical changes during the spin coating process, which adversely affect the solubility. Further processing optimization will be needed before materials of this type can be useful as photoresists.

* We thank Maarten van der Geest and Zhichao Liu for their contributions to this work.

9.1 Introduction

Metal-containing photoresists have become a popular research subject for EUV photolithography due to their high EUV absorption cross-section and potentially high etch resistance.[1, 2] Among all the metal containing photoresists, the tin-containing photoresists have attracted the attention from Inpria, Brainard's group, Herman's group, and our own group.[3-11] The first organotin molecules introduced as photoresist by Brainard's group are the tin oxo cages.[6, 12] The patterning performance of these materials was well investigated by Brainard's group and our group.[6, 13, 14] In our previous work, we focused attention on the chemical changes inside the tin oxo cages molecules.[10, 11] Instead of these complex organotin molecules, we here consider the possibility to use smaller tin containing molecules as photoresist. Brainard's group also investigated dialkyltin(IV) dicarboxylates $R_2Sn(O_2CR')_2$, which are smaller than tin oxo cages.[12] The influences of the R' and R groups on the pattern performance were investigated. Their results indicated the sensitivity of the $R_2Sn(O_2CR')_2$ type of photoresists showed stronger correlation with the R groups than R' groups upon EUV exposure, especially the stability of the R radical. But when the R group is fixed, the higher the molecule weight of the R' group, the lower the sensitivity of the photoresist, except the alkene containing compounds.[5] Their sensitivity and high-resolution pattern ability under EUV exposure have been proven.[5]

Since it is known that ethylhexanoates of several low-valent metals (such as Sn, Zr, Hf, Ti and Sr, etc.) react under UV light,[15-20] we wondered if $Sn(OOCR)_2$ molecules would be suitable as EUV photoresists. The tin(II) 2-ethylhexanoate ($Sn[O_2CCH(C_2H_5)(C_4H_9)]_2$) (SnE) and tin (II) acetate ($Sn(O_2CCH_3)_2$) SnA molecules were chosen as our research items. The bond between the carboxylate group and the metal can break upon UV exposure. The 2-ethylhexanoate radical can decarboxylate and generate CO_2 and heptyl radical.[18, 20] From a mechanistic perspective, the chemistry is different from that of organotin compounds because there is no Sn-C bond to be broken. The acetate was considered because it contains a smaller organic fraction, so that photoconversion of the film will lead to smaller shrinkage.

The EUV linear absorption coefficient α can be calculated based on absorption cross sections in the literature[1] and the densities of the materials.[21] The calculated EUV linear absorption coefficient for SnE $\alpha = 6.9\ \mu m^{-1}$, and for SnA $\alpha = 17.5\ \mu m^{-1}$. For tin oxo cage with hydroxide as counterions $\alpha = 13.5\ \mu m^{-1}$.[21] Thus, SnA due to its small organic fraction could potentially give even higher EUV absorption than tin oxo cages.

The thin film preparation conditions, pattern performances, development conditions and the chemical changes upon exposure inside the thin film were investigated. We obtained the dose contrast curves of the two materials under DUV and EUV irradiation. IR and XPS were used to characterize the chemical changes in the two molecules upon exposure. These two molecules have potential to be used as EUV photoresists, but several questions concerning their stability and processing conditions need further attention.

9.2 Experimental details

Both tin (II) 2-ethylhexanoate (SnE) and tin (II) acetate (SnA) are commercially available from Sigma-Aldrich. SnE is a viscous liquid (melting point < 0°C), and SnA is a white powder. To make use of the two molecules as photoresist they need to be prepared as thin film on substrates. SnE (20 μL) was dissolved in 1 mL hexane and filtered through a 0.25 μm PTFE filter right before spin-coating. It was spin-coated with 2500 rpm for 30 s into 40-50 nm films on single side polished Si substrate (for lithography purpose), on double side polished Si (for FTIR), on Au coated single side polished Si substrate (for XPS), and on quartz substrate (for UV-vis spectroscopy). SnA (30 mg) was dissolved in 1 mL dry ethanol with sonication for 5 min and filtered through a 0.25 μm PTFE filter right before spin-coating. Similarly, the SnA solution is spin coated into 20-30 nm films on different substrates for different experiments as mentioned.

The thin films prepared on the Si wafer were exposed to 225 nm deep UV (DUV) and 13.5 nm extreme UV (EUV). The DUV exposure was performed at ARCNL using a deep UV light source (an Energetiqs EQ-99X Laser Driven Light Source System with a TRIAX190 monochromator). The EUV exposure was performed at the XIL-II beamline of Swiss Light Source (SLS).

UV-Vis absorption spectra of the thin films of SnA an SnE on quartz substrates were measured in transmission mode using a Shimadzu UV-2600 spectrometer. FTIR spectroscopy (Bruker Vertex 80v spectrometer) was used to measure the thin photoresist film prepared on the double side polished Si wafer in transmission mode under vacuum. Attenuated total reflectance (ATR) was measured on the Bruker ALPHA-P compact FTIR spectrometer. X-ray photoelectron spectroscopy (Al Kα based X-ray source) was used to characterize the photoresist film prepared on Au-Cr coated Si substrate. A Bruker Dimension Icon was used for Atomic force microscopy (AFM). The scanning electron microscopy (SEM) was performed using an FEI Verios 460 with a voltage of 1 kV. Thermal gravimetric analysis (TGA) and Differential Scanning Calorimeter (DSC) were performed with a NETZSCH STA 449 F3 Jupiter equipped with automatic sample changer.

9.3 Result and Discussion

9.3.1 Sensitivity of SnE and SnA

The UV-vis absorption spectra of SnE and SnA thin films are shown in Fig. 9.1. It is observed that both of the two compounds give their maximum absorption around 225 nm. Thus, 225 nm is a suitable wavelength to expose the two molecules. The film thicknesses were assumed to be the same regardless of the different substrates, and the linear absorption coefficients of SnE and SnA were estimated as 7.5 and 14.2 μm^{-1} at 225 nm.

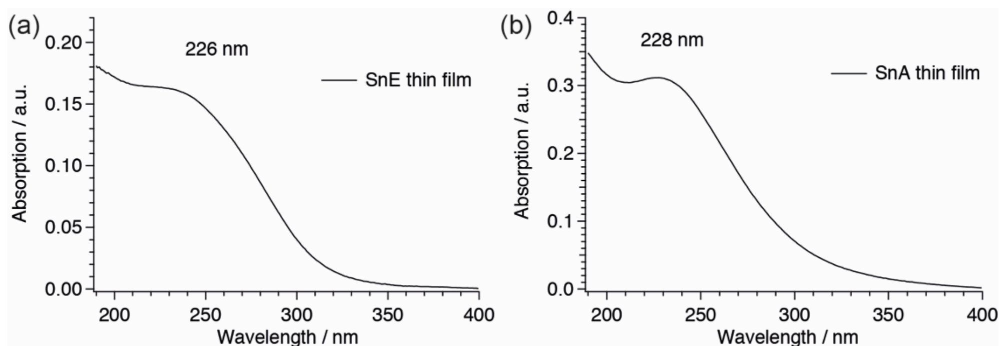

Figure 9.1. *UV absorption spectra of SnE thin film (a) and SnA thin film (b).*

After the two organotin molecules (SnA and SnE) were prepared into thin films on the Si wafers, we used 225 nm deep ultraviolet exposure and 13.5 nm (92 eV) extreme ultraviolet exposure to test their responses. The contrast curve of DUV exposed SnE gives a good indication of its sensitivity. A 50 nm film of SnE was prepared on a Si wafer and exposed to DUV with a series of doses (from 10 to 2000 mJ cm^{-2}) under ambient conditions. After exposure, different developing conditions were tested. At the beginning, the original solvent hexane used for spin-coating was tested as developer, which is a non-polar solvent, but the thin film could not be re-dissolved. In addition, we tried the polar solvents isopropanol and acetone, but neither of them can totally dissolve the unexposed/exposed part of the thin films. Finally, we found out the development condition as 0.0125% TMAH solution for 30 s followed by rinsing with water for 10 s. After development, the remaining film thickness was measured using AFM. The result is shown in Fig. 9.2.

Unexpectedly, there is still 14 nm film remaining at the unexposed part after development. From the dose contrast in Fig. 9.2, we can see there are three stages. At the first stage (below 100 mJ cm^{-2}), the remaining film thickness increases with the dose increasing but the film totally dissolved above 100 mJ cm^{-2}. It shows negative tone property at the first stage. At the second stage, from 100 to 600 mJ cm^{-2}, the thin film was totally removed and it showed as positive tone pattern. With

the dose continuously increasing to above 600 mJ cm^{-2}, it comes to the third stage in which the film thickness increased again and remained at the same thickness up to 2000 mJ cm^{-2}. The three stages could correspond to three kinds of products in the thin films, which have different solubility. With the ratio of those three products changing, the solubility of the thin films was changed as three stages. Comparing with the tone inversion controlled by playing with different PEB temperatures in chapter 8,[14] this work realizes dual tone pattern by using SnE in another way.

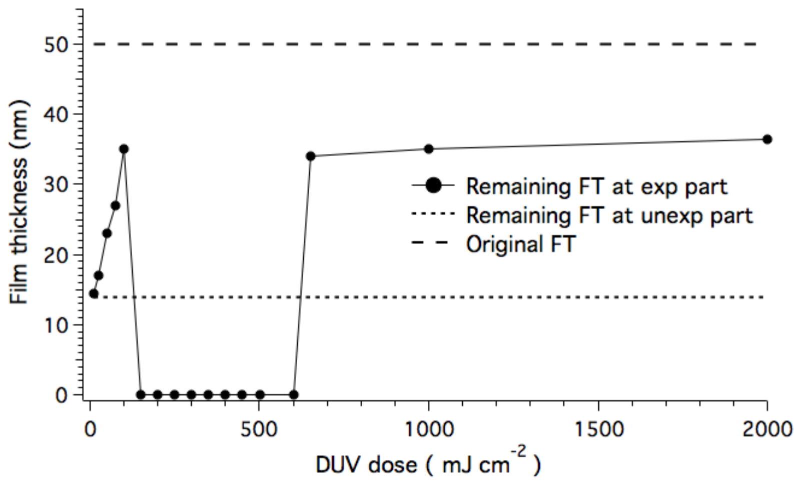

Figure 9.2. *Remaining film thickness of exposed areas on SnE after development as a function of doses. The initial film thickness (50 nm) and the film thickness of the unexposed part after development (14 nm) are marked in the figure.*

In addition to the DUV exposure, EUV exposure was also performed on the SnE photoresist. Since the EUV needs to be performed under high vacuum, a prebake step in the ambient atmosphere with 100 ^{o}C 2 min was applied to get rid of the residual solvent before they were transferred into the exposure chamber. After baking, the SnE thin film change from the original viscous oil into solid, which indicated a certain extent of chemical changes. After exposure, the thin film was developed at the same condition, where the sample was dipped in 0.0125% TMAH solution for 30 s and rinsed with water for 10 s. The developed sample was also characterized by AFM. As shown in Fig. 9.3, there was still around 80% of film thickness remaining at the unexposed part, which is around 40 nm. This thick remaining film at the unexposed part makes the whole pattern show as positive tone. Similar with the DUV dose contrast curve, this material seems to present three stages in the EUV dose contrast curve. But unfortunately, a layer of the material remains even for the dose giving the thinnest film after development at around 124 mJ cm^{-2}. The developing condition still needs to be optimized.

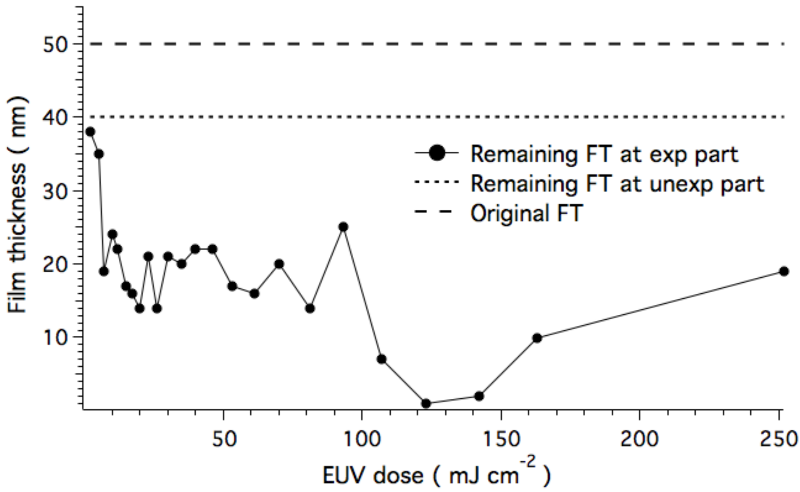

Figure 9.3. *Remaining film thickness of exposed areas of SnE after development as a function of doses. The initial film thickness (50 nm), and the remaining film thickness of the unexposed area after development (40 nm) are also marked in the figure.*

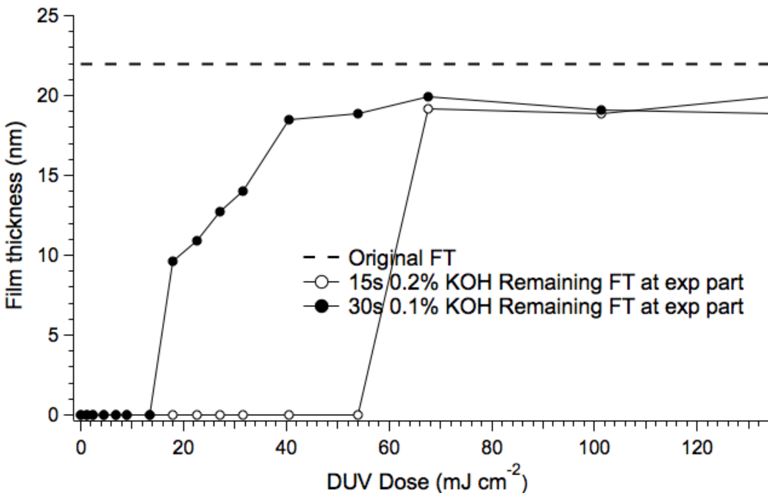

Figure 9.4. *Deep UV irradiation of SnA. Remaining film thickness of exposed areas after development as a function of doses. The initial film thickness (22 nm), and the two exposed samples developed with different KOH solutions are shown.*

Similarly, the performance of SnA was tested under DUV/EUV exposure. The carbon chain in the SnA is much smaller than that of SnE. For the DUV exposed sample, instead of TMAH solution, another alkaline solution was used as developer, which is KOH solution. By using different concentrations of KOH solution combining with different development time (15 s in 0.2% KOH solution or 30 s in

0.1% KOH solution), the dose contrast curve was achieved by measuring the remaining film thickness after developing as shown in Fig. 9.4. Clearly, a negative tone dose contrast curve is observed. At 30 s in 0.1% KOH solution developing condition, the thin film already converted to insoluble at ~14 mJ cm^{-2}. We can conclude that the dose contrast curve is very sensitive to the developing condition, suggesting that the sensitivity of the SnA can be further improved.

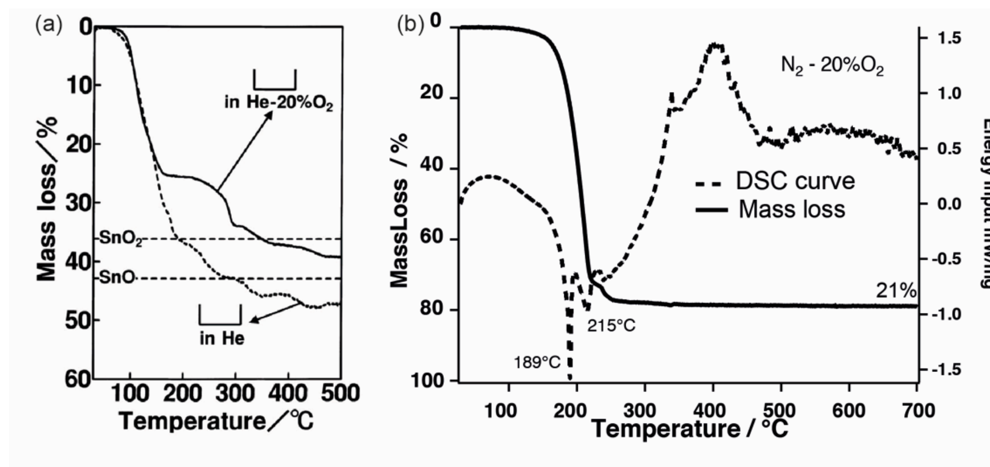

Figure 9.5. *Comparison between (a) the TGA of SnA as reported in reference* [22] *and (b) the TGA and DSC result of SnA powder from our measurement.*

A PAB step is also needed for SnA films to get rid of the residual solvent. The thermal stability of the SnA was tested. As it is shown in Fig. 9.5a, the TGA results of SnA from the literature,[22] mass loss of SnA powder starts at around 65 ^{o}C. A different TGA curve was obtained in N_2-20%O_2 atmosphere on the SnA powder by us as shown in Fig. 9.5b. In our curve the mass starts to drop at around 150 °C, which corresponds with the vaporizing temperature (140 – 160 °C) presented by Maruyama et al.[23] The mass loss is associated to an exothermic process, according to the DSC curve in Fig. 9.5b. At the end of the TGA, less material than expected remained (experimental, around 21%; calculated for total conversion to SnO, 57%; for total convertsion to SnO_2, 66%). It seems likely that the SnA is partly vaporized and partly decomposed above 150 °C.[24] The differences in the TGA curves could be explained by the different amounts of material used for each experiment (0.3 mg for the experiment in Fig 9.5a, 6.3 mg for the experiment in Fig. 9.5b). A similar phenomenon was observed by Seki et al.[22] on $(C_4H_9)_2Sn(CH_3COO)_2$, where the starting materials could affect the thermal behavior of the sample. The smaller the amount of starting materials was heated, the less mass loss was observed in the end of heating. The reason could be that the smaller amount of tin-containing materials

can be easier to fully oxidize into SnO/SnO_2. When larger amounts of materials were used, they can vaporize more before fully oxidizing.

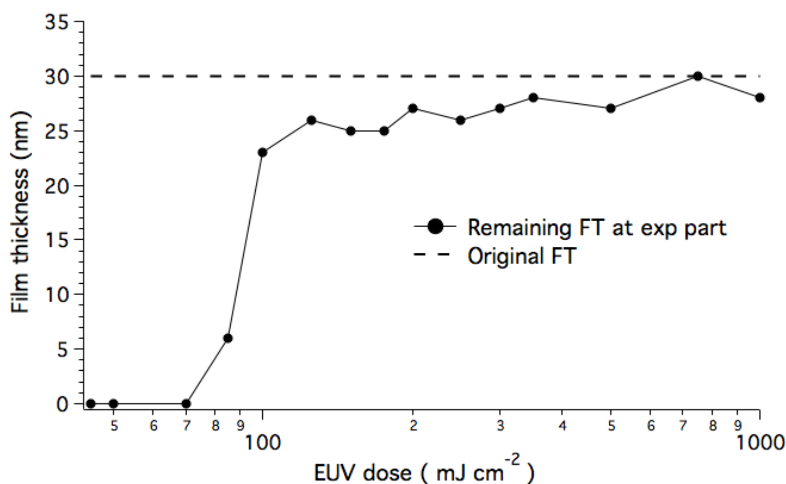

Figure 9.6. *EUV exposure of SnA. The initial film thickness (30 nm) and the remaining layer thickness of exposed areas after development as a function of dose.*

Then the SnA was exposed to EUV with a PAB step (100 ^{o}C, 2 min). After testing different developers, the EUV exposed sample was developed in 12% TMAH for 10 s and rinsed with water for 10 s. The remaining film thickness was characterized with AFM. The dose contrast curve is obtained as shown in Fig. 9.6. Apparently, it also shows negative tone property.

The results show that both SnA and SnE are sensitive to EUV. The two molecules were tested with EUV interference lithography to see if they can achieve high-resolution patterns. So far, unfortunately, neither of them gave the expected patterns. After development, the EUV interference lithography patterned SnE thin film under optical microscopy is shown in Fig. 9.7.

The bright parts are the 0th order exposed parts, and they were totally removed by the developer. The interference patterns are located as the darker area in the middle of the two 0th order exposed parts. But with the dose increasing, the interference-patterned part was either remained (20 mJ cm^{-2}) as a whole piece or removed (84 mJ cm^{-2}) as a whole piece after development. When the interference pattern part was characterized with AFM, there was no line structure at all.

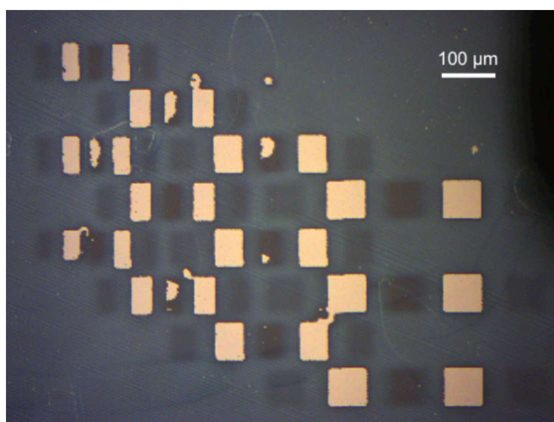

Figure 9.7. *The developed SnE pattern from EUV interference lithography observed under optical microscopy. The bright areas are the 0th order exposed parts (see Fig 2.3 in chapter 2), and in between each pair of bright areas is the location of the interference pattern. The grey part is the unexposed area.*

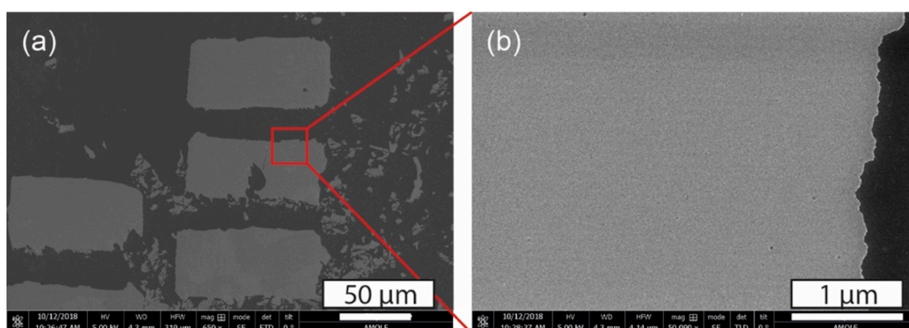

Figure 9.8. *SEM image of developed SnA sample with around 80 mJ cm^{-2}.*

Similarly, the SnA sample was exposed to EUV interference. After development, SEM was used to characterize the SnA sample as shown in Fig. 9.8. The whiter part is the exposed part, and the 50 nm half pitch interference pattern should locate at the middle rectangle exposed part. The red square part in Fig. 9.8a was zoomed into Fig. 9.8b, there are not any line structures. Definitely, both SnA and SnE are sensitive to DUV and EUV exposure, but the development conditions need to be optimized to emphasize the solubility difference between the exposed and unexposed parts and achieve high-resolution patterns. Also, the adhesion to the underlayer needs attention.

9.3.2 IR spectroscopy of SnA and SnE

The IR spectrum of the pristine SnE, which is a highly viscous liquid, was measured using ATR-FTIR and used as a reference spectrum for the rest of FTIR measurements. The samples were spin coated as thin films on double side polished

Si substrates and measured in transmittance mode. The IR spectra of different unexposed samples are shown in Fig. 9.9. There is free 2-ethyhexanoic acid as indicated by the COOH stretching at around 1707 cm^{-1} and the O-H stretching at around 3000 cm^{-1} in the spectrum (black) of the original liquid SnE, which is very similar to the one shown in reference[16]. The formation of the free acid could be a result of water adsorption causing hydrolysis:

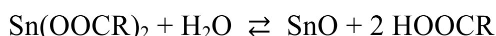

$$Sn(OOCR)_2 + H_2O \rightleftarrows SnO + 2\ HOOCR$$

When SnE was prepared as a thin film without any other additional process, the free acid is not present, as shown in the green spectrum in Fig. 9.9. The spectra were normalized to the peak intensity of the CH stretching (antisymmetric and symmetric stretching vibration of $–CH_3$ and $–CH_2$ at 2962, 2931 and 2869 cm^{-1}). With a bake step, the COO antisymmetric stretching at around 1562 and 1614 cm^{-1} disappeared, and shifted to around 1527 cm^{-1}, which could be due to a reorganization of acetate group from monodentate to bidentate chelating upon baking.[25] The baked sample prepared at PSI was also measured after one week aging under air atmosphere. As it shows in the blue spectrum in Fig. 9.9, the shape of the spectrum is quite similar with the spectrum from the freshly baked sample. The baked thin film is stable even exposed to the atmosphere for one week.

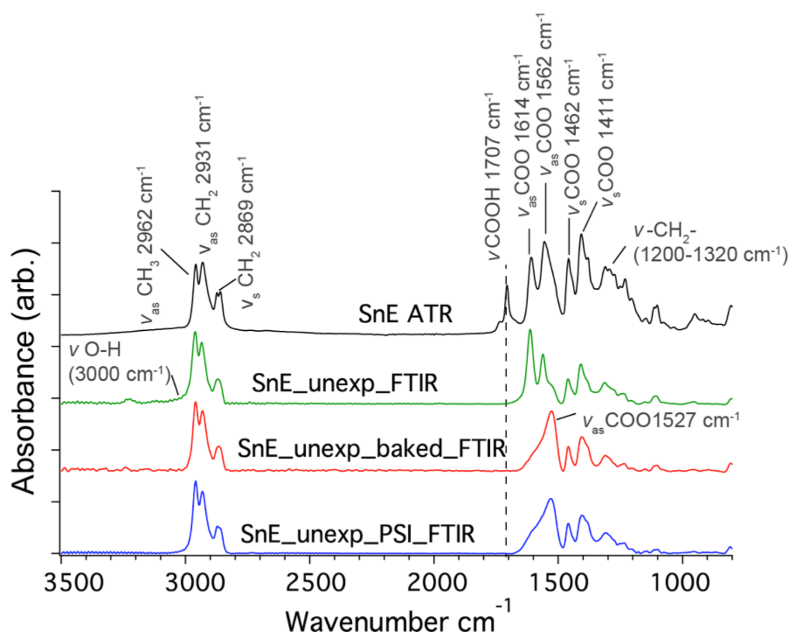

Figure 9.9. *IR spectra of SnE liquid measured using ATR (black), freshly prepared SnE unexposed thin film (green), (100°C 2 min) baked SnE unexposed thin film (red) and baked SnE unexposed thin film after one week of aging (blue), measured using FTIR.*

In order to follow the chemical changes of SnE under DUV/EUV exposure, FTIR spectra were measured of the DUV/EUV exposed thin films, as shown in Fig. 9.10 and 9.11. The spectra were normalized to the intensity of CH stretching. After DUV exposure, the COO stretching decreased significantly relative to the CH stretch, indicating that the decarboxylation reaction in the SnE dominated after DUV exposure. Although the carbon chain is connected with the carboxylate group, when the decarboxylate reaction happens, it generates a heptyl radical that could react with the tin atom or grape a hydrogen forming heptane remaining in the thin films. That could be the reason why the COO stretching is decreased the CH stretching.

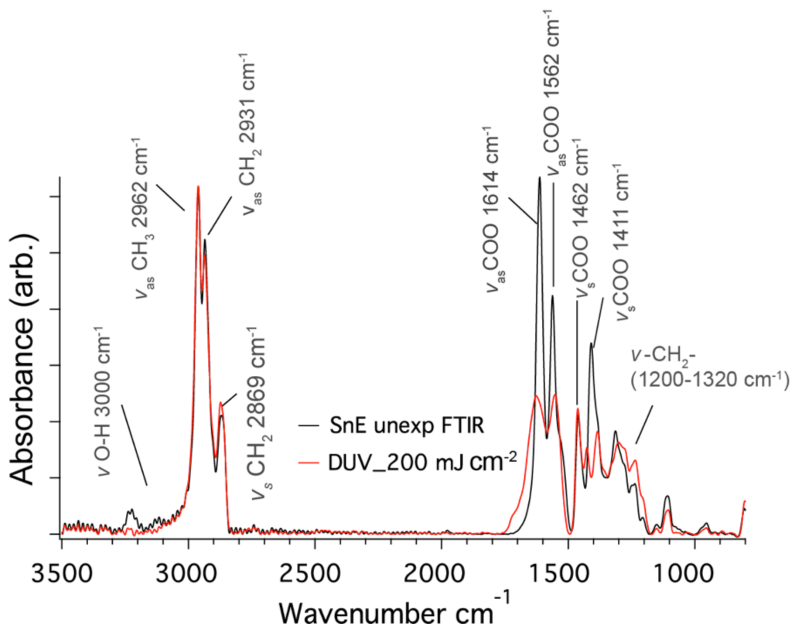

Figure 9.10. *IR spectroscopy of unexposed and 200 mJ/cm² DUV exposed SnE samples.*

The IR spectra of EUV exposed SnE samples are shown in Fig. 9.11. Since the EUV exposure was performed under vacuum, prebake is needed before the sample was introduced into the exposure chamber. The spectra from the exposed sample are compared with the spectrum from the unexposed-prebaked sample. Similarly, the spectra were normalized to CH stretching at 2962 cm^{-1}. The COO symmetric stretching decreased slightly with the exposure dose increasing, indicating that a small chemical change can already cause the solubility difference.

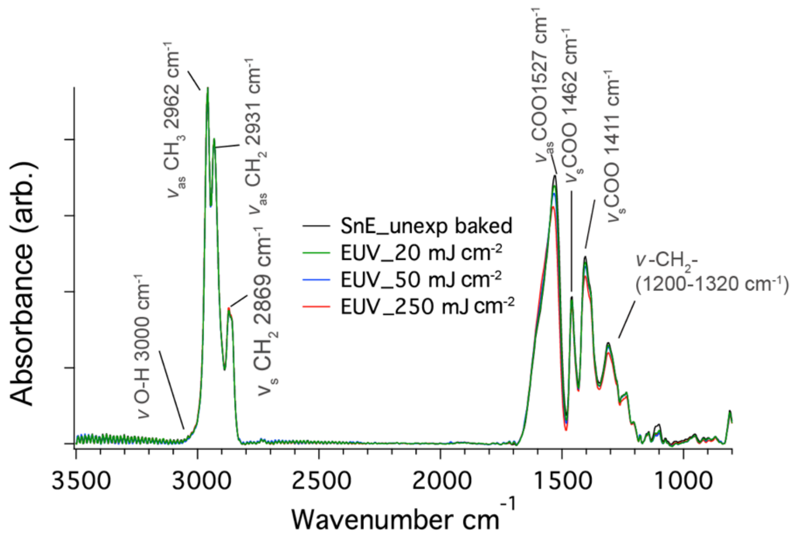

Figure 9.11. *IR spectroscopy of unexposed (100°C 2 min baked) and 20, 50, and 250 mJ cm^{-2} EUV exposed SnE samples.*

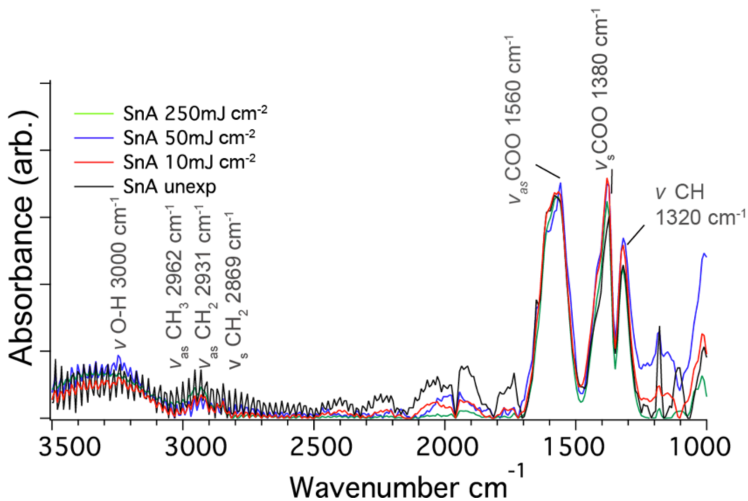

Figure 9.12. *IR spectra of SnA unexposed thin film (around 24 nm), and films exposed to DUV with doses 10, 50 and 250 mJ cm^{-2}.*

Comparing with SnE, the film of SnA is even thinner, namely 20 – 30 nm. Similarly, the IR spectra were recorded on different samples, but the signals from all the samples are quite weak as shown in Fig. 9.12. The spectra were presented as normalized to the COO antisymmetric stretching at 1560 cm^{-1}. As it shows in Fig. 9.12, with the DUV dose increasing, the COO symmetric stretching at 1380 cm^{-1} increased slightly, indicating that the carboxylate group could be reorganized in the samples.

9.3.3 X-ray Photoelectron Spectra of SnA and SnE

The SnA and SnE thin films prepared on conductive substrates (Au coated Si wafer) were characterized by means of XPS using the spectrometer (chapter 2) operating with a photon energy of 1.4 keV. For the SnE sample, the prebake effect and dose effect were investigated. Since the XPS measurement needs to be done under high vacuum, the freshly prepared SnE sample was kept under atmosphere for 24 h and it turned from viscous oil into solid before it was introduced into the XPS loadlock. This indicated chemical changes such as oxidation or hydrolysis happened in the thin film, which could form a mixture of SnO and SnE before the measurement. The overview spectra are shown in Fig. 9.13. All expected elements in the thin film are present as peaks in the spectra: O 1s at around 531 eV, Sn $3d_{5/2}$ and $3d_{3/2}$ at around 486 and 495 eV, and C 1s at around 285 eV.[11, 26] The small peaks at 84 eV are from the Au layer on the substrate. All spectra were normalized to the Sn 3d peak intensity. After normalizing, we did not see significant changes of the O 1s and C 1s peaks intensity in the exposed sample, but the O 1s and C 1s peaks are clearly decreased due to the pre-baking. The peak area ratio in the spectra corresponds to the element ratio listed in table 9.1.

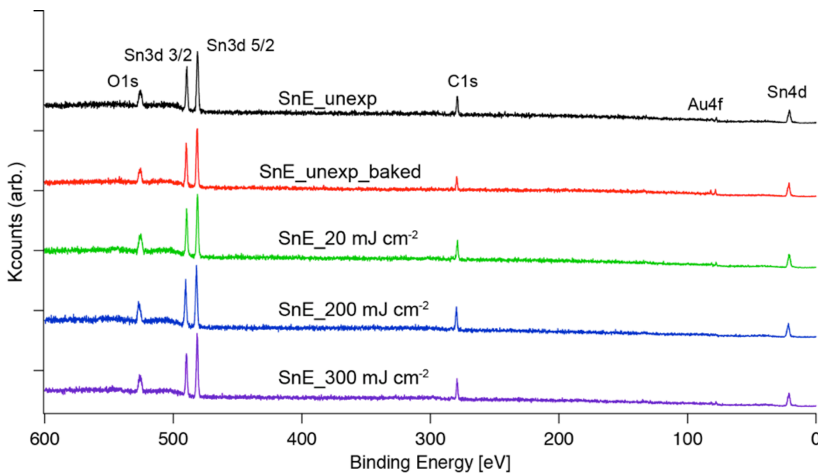

Figure 9.13. *Overview spectra of SnE unexposed, SnE baked (100°C 2 min) and no prebaked SnE exposed to 225 nm DUV with doses 20, 200, 300 mJ cm^{-2}.*

Comparing with the expected ratio, the ratio from the unexposed sample shows a significant difference. The oxygen atom signal is only 50% of what was expected, and the carbon content is even less than half of the expected stoichiometric ratio, presumably due to partial decomposition. The observed elemental ratio is consistent with a film composition of SnO : SnE $\approx$ 2 : 1, where the Sn: O: C ratio is 1: 2: 5.2. There is small decrease of the C 1s and O 1s ratio when we compare the ratio of the unexposed sample and the ratio from the prebaked sample. Based on reference[16],

when a photon was absorbed by the SnE molecule, a ligand to metal charge transfer transition would happen, where one electron could be transferred from the ethylhexanoate to the connected Sn^{2+} center into Sn^{+} and further into Sn atom, which is easy to be oxidized into SnO under air conditions. The electron loss in ethylhexanoate could induce decomposition of ethylhexanoate into CO_2 and heptyl radical. With DUV exposure, the oxygen and carbon ratios increased slightly, which is still hard to explain.

Table 9.1. *Sn, O and C atomic ratios from samples of SnE unexposed, SnE baked and 20, 200, 300 mJ cm^{-2} exposed to DUV.*

	Sn	O	C
SnE theoretical	1	4	16
SnE unexp	1	2.0 ± 0.1	5.6 ± 0.3
SnE unexp_baked	1	1.8 ± 0.2	5.0 ± 0.4
SnE 20 mJ cm^{-2}	1	2.0 ± 0.2	5.6 ± 0.4
SnE 200 mJ cm^{-2}	1	2.8 ± 0.3	6.3 ± 0.5
SnE 300 mJ cm^{-2}	1	2.6 ± 0.3	5.7 ± 0.4

Similarly, XPS was also performed on the unexposed, prebaked, 20, and 100 mJ cm^{-2} exposed SnA samples. The overview spectra of the samples were recorded as shown in Fig. 9.14. The Sn 3d, O 1s and C 1s peaks were clearly observed. To compare the intensity change, we assume that the Sn content does not change during the exposure and measurement. After normalizing the peak intensity to the Sn 3d peak, we can clearly observe that the C 1s peak intensity decreases in spectra from the prebaked and exposed samples, but the intensity of oxygen peak does not change. The peak ratios of all the spectra were calculated and are shown in table 9.2. When we compare the element ratio in the unexposed sample with the theoretical calculation, the oxygen and carbon ratios are lower than expected, as in the case of SnE. The observed elemental ratio is similar with a film composition of SnO : SnA ≈ 2 : 1, where the Sn: O: C ratio is 1: 2: 1.3. This indicates the chemical reaction already happened before the samples were introduced into the measurement. With a prebake step, carbon was lost, indicating that the heating promotes the reaction in the thin film. When the DUV exposed samples were checked, the higher the dose, the lower the carbon ratio was observed.

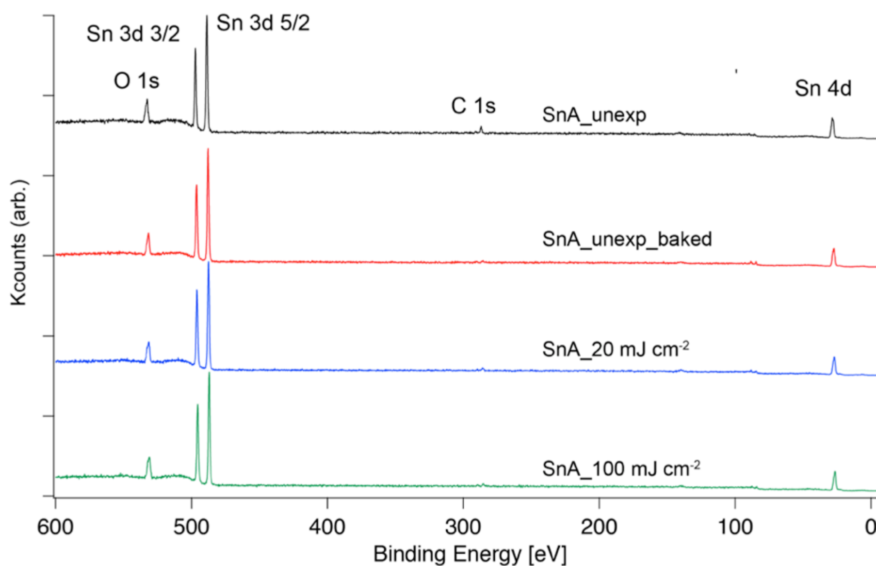

Figure 9.14. *Overview spectra of unexposed SnA, prebaked, 20, and 100 mJ cm^{-2} EUV exposed samples.*

Table 9.2. *Atomic ratios of Sn, O and C from unexposed SnA, prebaked, and EUV exposed samples.*

Atomic ratio	Sn	O	C
SnA theoretical	1	4	4
SnA unexposed	1	1.6 ± 0.1	1.3 ± 0.2
SnA unexposed baked	1	1.6 ± 0.1	1.0 ± 0.3
SnA 20 mJ cm^{-2}	1	1.6 ± 0.1	0.8 ± 0.3
SnA 100 mJ cm^{-2}	1	1.8 ± 0.2	0.4 ± 0.1

Above all, we confirmed that there were chemical changes in the SnA and SnE thin films upon prebake and exposure. The photolysis mechanism of SnE has been presented in the literature and is adapted here as Fig. 9.15a.[16] In reference 16, the photolysis products could be SnO, CO, CO_2 and hydrocarbon molecules. Additionally, the SnA and SnE could be hydrolyzed as proposed in Fig. 9.15b. The molecules have the opportunities to react with water and generate SnO or the intermediate HOSnCOOR, which could mix with the original molecules and lead to the difference between the measured and expected atomic ratio in XPS measurements. Since all the reactions in Fig. 9.15 are possible, the final remaining thin film could be a mixture of SnO, RCOOSnOH and $Sn(COOR)_2$, which is consistent with the XPS result that there is always carbon remaining after different processes.

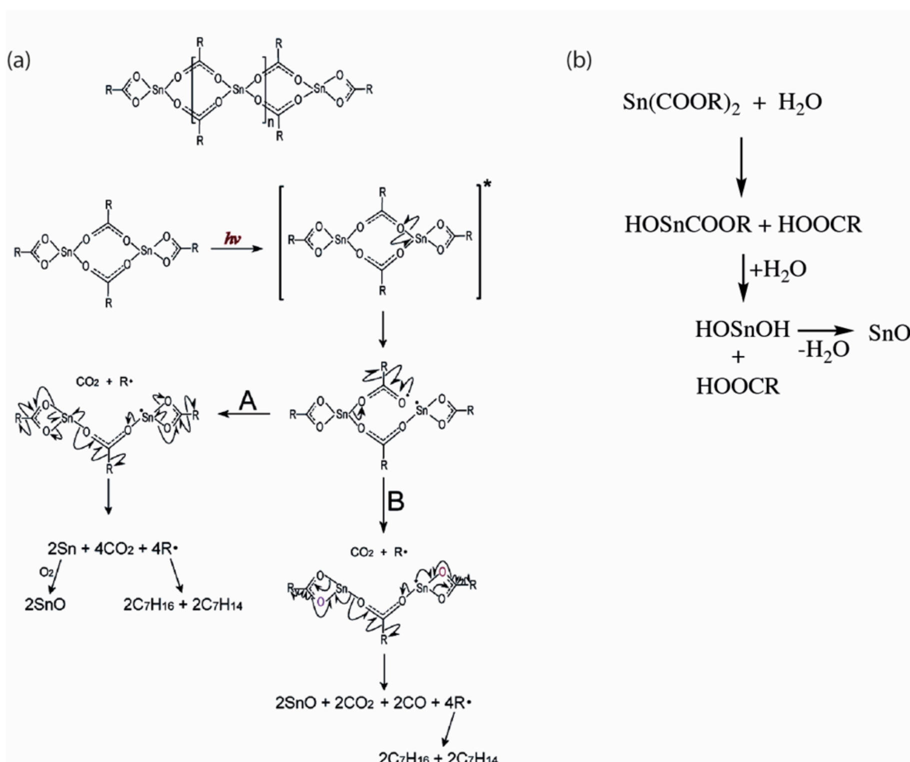

Figure 9.15. *(a) Proposed chemical reaction mechanism of SnA and SnE upon exposure, figure from reference 16. (b) hydrolysis of the tin(II)carboxylates.*

9.4 Conclusions

In this work, we investigated two small molecules SnE and SnA as EUV photoresists. We could demonstrate the sensitivity of the two materials under DUV and EUV exposure. We manage to develop the DUV/EUV exposed SnE and SnA samples by using either TMAH or KOH solution as developers. More efforts are needed to find better process conditions for high-resolution patterning. Evidence was found that chemical changes occurred when the compounds were deposited as thin films. Baking has a significant effect on the molecular composition. Based on the IR results, decarboxylation can happen in the SnE thin films upon bake and DUV exposure. To understand the chemical changes inside the thin film could help us get better understanding on the properties of the unexposed and exposed materials, which is important for developing proper process conditions.

9.5 References

1. B. L. Henke, E. M. Gullikson and J. C. Davis, "X-Ray Interactions: Photoabsorption, Scattering, Transmission, and Reflection at E = 50-30,000 eV, Z = 1-92", *Atomic Data and Nuclear Data Tables*, 1993, **54**, 181-342.

2. M. Trikeriotis, M. Krysak, Y. S. Chung, C. Ouyang, B. Cardineau, R. Brainard, C. K. Ober, E. P. Giannelis and K. Cho, "A new inorganic EUV resist with high-etch resistance", *Proc. SPIE*, 2012, **8322**, 83220U.
3. R. T. Frederick, S. Saha, J. Trey Diulus, F. Luo, J. M. Amador, M. Li, D.-H. Park, E. L. Garfunkel, D. A. Keszler and G. S. Herman, "Thermal and radiation chemistry of butyltin oxo hydroxo: A model inorganic photoresist", *Microelectron. Eng.*, 2019, **205**, 26-31.
4. R. Frederick, T. Diulus, D. Hutchison, M. Nyman and G. S. Herman, "Effect of Oxygen on Thermal and Radiation Induced Chemistries in a Model Organotin Photoresist", *ACS Appl. Mater. Interfaces*, 2019, DOI: 10.1021/acsami.8b16048.
5. R. Del Re, J. Passarelli, M. Sortland, B. Cardineau, Y. Ekinci, E. Buitrago, M. Neisser, D. A. Freedman and R. L. Brainard, "Low-line edge roughness extreme ultraviolet photoresists of organotin carboxylates", *J. Micro/Nanolitho. MEMS MOEMS*, 2015, **14**, 043506.
6. B. Cardineau, R. Del Re, M. Marnell, H. Al-Mashat, M. Vockenhuber, Y. Ekinci, C. Sarma, D. A. Freedman and R. L. Brainard, "Photolithographic properties of tin-oxo clusters using extreme ultraviolet light (13.5 nm)", *Microelectron. Eng.*, 2014, **127**, 44-50.
7. W. D. Hinsberg and S. Meyers, "A numeric model for the imaging mechanism of metal oxide EUV resists", *Proc. SPIE*, 2017, **10146**, 101460401-11.
8. S. T. Meyers, J. T. Anderson, J. B. Edson, K. Jiang, D. A. Keszler, M. K. Kocsis, A. J. Telecky and B. Cardineau, *US 9310684B2*, 2016.
9. S. T. Meyers, J. T. Anderson, J. B. Edson, K. Jiang, D. A. Keszler, M. K. Kocsis, A. J. Telecky and B. Cardineau, *US 2016/0116839 A1*, 2015.
10. J. Haitjema, L. Wu, A. Giuliani, L. Nahon, S. Castellanos and A. M. Brouwer, "Photo-induced Fragmentation of a Tin-oxo Cage Compound", *J. Photopolym. Sci. Technol.*, 2018, **31**, 243-247.
11. Y. Zhang, J. Haitjema, X. Liu, F. Johansson, A. Lindblad, S. Castellanos, N. Ottosson and A. M. Brouwer, "Photochemical conversion of tin-oxo cage compounds studied using hard x-ray photoelectron spectroscopy", *J. Micro/Nanolitho. MEMS MOEMS*, 2017, **16**, 023510.
12. R. Del Re, M. Sortland, J. Passarelli, B. Cardineau, Y. Ekinci, M. Vockenhuber, M. Neisser, D. A. Freedman and R. L. Brainard, "Low-LER tin carboxylate photoresists using EUV", *Proc. SPIE*, 2015, **9422**, 94222101-10.
13. J. Haitjema, Y. Zhang, M. Vockenhuber, D. Kazazis, Y. Ekinci and A. M. Brouwer, "Extreme ultraviolet patterning of tin-oxo cages", *J. Micro/Nanolitho. MEMS MOEMS*, 2017, **16**, 033510.
14. Y. Zhang, J. Haitjema, M. Baljozovic, M. Vockenhuber, D. Kazazis, T. A. Jung, Y. Ekinci and A. M. Brouwer, "Dual-tone Application of a Tin-Oxo Cage Photoresist Under E-beam and EUV Exposure", *J. Photopolym. Sci. Technol.*, 2018, **31**, 249-255.
15. Y. K. Lee, C.-S. Park and H.-H. Park, "One-step surface selective modification of UV-curable hard coatings with photochemical metal organics", *Appl. Surf. Sci.*, 2016, **389**, 882-888.

16. H. H. Park, W. L. Law, X. Zhang, S. Y. Hwang, S. H. Jung, H. B. Shin, H. K. Kang, H. H. Park, R. H. Hill and C. K. Ko, "Facile size-tunable fabrication of functional tin dioxide nanostructures by multiple size reduction lithography", *ACS Appl. Mater. Interfaces*, 2012, **4**, 2507-2514.
17. H.-H. Park, X. Zhang, S.-W. Lee, K.-d. Kim, D.-G. Choi, J.-H. Choi, J. Lee, E.-S. Lee, H.-H. Park, R. H. Hill and J.-H. Jeong, "Facile nanopatterning of zirconium dioxide films via direct ultraviolet-assisted nanoimprint lithography", *J. Mater. Chem.*, 2011, **21**, 657-662.
18. H.-H. Park, D.-G. Choi, X. Zhang, S. Jeon, S.-J. Park, S.-W. Lee, S. Kim, K.-d. Kim, J.-H. Choi, J. Lee, D. K. Yun, K. J. Lee, H.-H. Park, R. H. Hill and J.-H. Jeong, "Photo-induced hybrid nanopatterning of titanium dioxide via direct imprint lithography", *J. Mater. Chem.*, 2010, **20**, 1921-1926.
19. L. S. Andronic and R. H. Hill, "The mechanism of the photochemical metal organic deposition of lead oxide films from thin films of lead (II) 2-ethylhexanoate", *J. Photochem. Photobiol., A*, 2002, **152**, 259-265.
20. H. J. Zhu and R. H. Hill, "The photochemical metal organic deposition of manganese oxide films from films of manganese(II) 2-ethylhexanoate: a mechanistic study", *J. Non-Cryst. Solids*, 2002, **311**, 174-184.
21. G. Sun, S. Cho, C. Clark, S. V. Verkhoturov, M. J. Eller, A. Li, A. Pavia-Jimenez, E. A. Schweikert, J. W. Thackeray, P. Trefonas and K. L. Wooley, "Nanoscopic cylindrical dual concentric and lengthwise block brush terpolymers as covalent preassembled high-resolution and high-sensitivity negative-tone photoresist materials", *J. Am. Chem. Soc.*, 2013, **135**, 4203-4206.
22. S. Seki, T. Suzuki, T. Senda, T. Nishide and Y. Sawada, "Thermal change during formation process of indium-tin-oxide transparent conductive films", *Thermochim. Acta*, 2000, **352-353**, 75-79.
23. M. Toshiro and T. Kenji, "Indium-Tin Oxide Thin Films Prepared by Chemical Vapor Deposition from Metal Acetates", *Jpn. J. Appl. Phys.*, 1990, **29**, L355.
24. J. D. Donaldson, W. Moser and W. B. Simpson, "1147. Tin(II) acetates", *J. Chem. Soc.*, 1964, **0**, 5942-5947.
25. Y. Wang, X. Gao, Y. Xiao, Q. Zhao, J. Yang, Y. Yan and J. Huang, "Temperature dependent coordinating self-assembly", *Soft Matter*, 2015, **11**, 2806-2811.
26. M. Fondell, M. Gorgoi, M. Boman and A. Lindblad, "An HAXPES study of Sn, SnS, SnO and SnO_2", *J. Electron. Spectrosc. Relat. Phenom.*, 2014, **195**, 195-199.

Summary

Photoresists are photosensitive materials that are used to transfer patterns in photolithography. New types of photoresists are needed for the next generation of photolithography, which uses extreme ultraviolet radiation (EUV, wavelength 13.5 nm). Organotin materials have drawn great attention in the photoresist field, not only due to their potential in industrial application but also because of the interest from the fundamental point of view. This thesis focuses on two kinds of organotin materials as photoresists: the tin oxo cages and tin(II) carboxylates molecules. We study the interaction of EUV and short-wavelength (deep) UV (225 nm) photons with the two types of photoresist candidates.

Chapter 1 gives an overview of the subjects of photolithography and photoresists. The developments of photolithography and photoresists are briefly summarized. Some metal-containing photoresists and their proposed reaction mechanisms are discussed. The organotin type of photoresists is attractive for us as a prototype for the study of the chemical reactions on metal containing photoresists upon light exposure. This is important for understanding the principles of EUV-induced chemical reactions, and can form the scientific groundwork for the optimization of metal-containing photoresist performance in the next generation photolithography.

In Chapter 2, we introduce the experimental techniques we used throughout the thesis. Various X-ray photoelectron spectroscopy (XPS) techniques that we used receive special attention, because they uniquely enable the characterization of the chemical reaction in the photoresist thin films.

The DUV photon-induced chemical changes in tin oxo cages are studied in Chapters 3, 4 and 5 by using the HAXPES technique (Hard X-ray Photoelectron Spectroscopy). In Chapter 3, based on the HAXPES spectra from the tin oxo cages with hydroxide counterions (TinOH) upon DUV exposure, we find direct evidence indicating that the Sn-C bonds in the tin oxo cages are cleaved upon DUV exposure. By comparing the chemical reaction of the tin oxo cages under dry nitrogen (N_2) and air atmosphere, we find that the average photochemical reaction yield of TinOH at high conversion is higher under air than in an atmosphere of N_2, but rather low (~1 %) in both cases. A reaction mechanism of TinOH photoresist exposed to DUV is proposed.

In chapter 4 we show that not only photons introduce chemical changes in the photoresist. Thermal processes in air after exposure (baking processes) cause chemical reactions in the tin oxo cages which further reduce the solubility. These

reactions occur at temperatures where the intact non-exposed film is thermally stable, and can be used to enhance the sensitivity (see Chapter 6). The photochemical reactions under nitrogen probably lead to a partial reduction of the tin cage, while the baking processes lead to oxidation, and more cross-linking of the tin cages.

In Chapter 5, the relationship between the DUV photon absorption and chemical reaction yield in the photoresist is further investigated by comparing three types of tin oxo cages, which have the same cage structure but three different counterions (hydroxide (TinOH), acetate (TinA), trifluoroacetate (TinF)). The chemical reaction yields of the three cages were evaluated through XPS and UV-absorption spectra. The solubility changes in the resist layer were quantified by constructing dose-contrast curves. The sensitivities of TinOH and TinA are similar, and higher than that of TinF. This provides evidence that the anions must be involved in some stage of the chemical process that leads to solubility switching. Interestingly, the weaker basicity and hydrogen bonding ability of the trifluoroacetate anion compared to acetate and hydroxide is reflected in the Sn 3d XPS spectra.

The EUV patterning abilities of the tin oxo cages are investigated in Chapter 6 and Chapter 8. The tin oxo cages can generate negative tone patterns as discussed in Chapter 6. The pattern performances of the tin oxo cages with different counterions (TinA and TinOH) under EUV exposure are studied. The results indicate that the sensitivity and the quality of the patterns can be affected by the counterions (hydroxide (TinOH), acetate (TinA) and malonate (TinM)). A possible reason is their physical properties are modified by the counterion such as the solubility. The results of Chapter 5 (which were obtained after the results from Chapter 6 were published), however, show that there is an effect of the counterions on the chemical reactivity in the DUV photochemistry, and this difference may also affect the EUV-induced reactions. The sensitivity of the photoresist can be improved by optimizing the process conditions, such as film thickness, post-exposure baking (PEB) temperature and development conditions. The thermal stability of the TinOH powder is characterized by TGA measurement, and it is shown to be stable at least until 100 °C. By comparing the pattern performance under different PEB temperatures, 100 °C is chosen as the proper PEB temperature for the TinOH to generate negative tone patterns. We also observed that the sensitivity and pattern resolution of the TinOH photoresists are improved by adding a PEB step. After a partial optimization, we achieved a 22 nm half pitch pattern with 57 mJ cm^{-2} EUV dose by using TinOH as photoresist. A 30 nm half pitch pattern with 57 mJ cm^{-2} EUV dose is realized by using TinA as photoresist.

The EUV photon-induced chemical changes in the tin oxo cages are systematically investigated in Chapter 7. The reaction mechanism of the tin oxo cages under EUV

is compared with the mechanism under DUV exposure. Different forms of XPS combined with mass spectrometry are used to investigate the photon-induced chemistry in the photoresist films. The photoemission spectrum of TinOH with photon energies around 92 eV is reported for the first time, where we confirm that the core-level electrons from Sn 4d orbitals are an effective source of primary electrons under EUV exposure. The photolysis-outgassing products (gaseous compounds that are released from the film) under EUV exposure are characterized by an outgassing system in collaboration with IMEC. Butane, butene and butanal are generated if TinOH is exposed to EUV, which further confirms that the Sn-C bond can be cleaved upon EUV exposure, as deduced from our XPS analyses. The DUV/EUV exposed TinOH thin films were analyzed by means of XPS and mass spectrometry. The chemical reaction quantum yield was found to be higher with EUV exposure than with DUV exposure. A reaction mechanism of the tin oxo cages upon EUV exposure is proposed.

As an extension of the research of Chapter 6, we found that dual-tone patterns can be realized by using the tin oxo cages as photoresist under high PEB temperature (150 °C), and this phenomenon is further explored in Chapter 8. The normal (negative tone) pattern is observed for TinOH with PEB temperature below 150 °C as shown in Chapter 6. When the PEB temperature reaches 150 °C, however, varying the exposure dose can reverse the tone of the pattern. This dual tone phenomenon is observed with EUV and E-beam exposure. By analyzing the sample with TGA and XPS, we related this phenomenon to the water loss occurring on the unexposed TinOH at this temperature.

In Chapter 9, we study the possibility of using tin(II) carboxylate compounds as EUV photoresists. The patterning performance and the chemical reaction of tin(II) acetate and tin(II) ethylhexanoate thin films upon DUV/EUV irradiation are studied. The sensitivities of the two molecules under DUV/EUV exposure are demonstrated. Post application baking has significant effect on the molecular composition. Both of the two molecules show clear chemical changes upon light exposure. High quality pattern, however, could not (yet) be achieved by using these two materials as photoresist.

Samenvatting

Fotolakken zijn lichtgevoelige materialen die worden gebruikt om patronen over te brengen in de fotolithografie. Nieuwe typen van fotolakken zijn nodig voor de nieuwe generatie fotolithografie, waarbij gebruik wordt gemaakt van extreem ultraviolet licht (EUV, golflengte 13.5 nm). In het onderzoeksgebied van fotolakken is er veel interesse in organotin-verbindingen, niet alleen vanwege hun potentiële toepassing als fotolak, maar ook vanuit fundamenteel oogpunt. Dit proefschrift spitst zich toe op twee soorten organotin-verbindingen die gebruikt worden als fotolakken: de tin-oxo kooien en tin(II) carboxylaat-verbindingen. We bestuderen de interactie van EUV en kortgolvig diep UV (225 nm) met de twee soorten organotin-verbindingen.

Hoofdstuk 1 geeft een overzicht van de onderwerpen fotolithografie en fotolakken. De ontwikkelingen die hierin plaatsvinden worden kort samengevat. Enkele metaal-bevattende fotolakken en hun reactiemechanismen worden besproken. Organotin-verbindingen zijn voor ons interessant als prototype voor de bestudering van de chemische reacties tijdens belichting. Dit is belangrijk om de principes van EUV-geïnduceerde chemische reacties te kunnen begrijpen, en het kan de wetenschappelijke basis vormen voor het optimaliseren van metaal-bevattende fotolakken in de nieuwe generatie fotolithografie.

In Hoofdstuk 2 introduceren we de experimentele methodes die we door het proefschrift heen hebben gebruikt. Met name XPS (fotoelektronspectroscopie met röntgenstraling) krijgt speciale aandacht, omdat deze techniek de chemische reactie in de dunne lagen fotolak goed kan karakteriseren.

In Hoofdstuk 3, 4 en 5 worden de chemische veranderingen besproken die in tin-oxo kooimoleculen optreden ten gevolge van de interactie met DUV fotonen. Deze veranderingen zijn bestudeerd met HAXPES (fotoelektronen-spectroscopie met harde röntgenstraling). In Hoofdstuk 3 maken we gebruik van HAXPES spectra van tin-oxo kooien met hydroxide-tegenionen (TinOH) en we vinden direct bewijs dat Sn-C bindingen worden verbroken bij belichting met DUV. We hebben de chemische veranderingen van tin-oxo kooien bij belichting onder lucht en stikstof (N_2) atmosfeer met elkaar vergeleken, waaruit bleek dat de gemiddelde opbrengst van de fotochemische reactie hoger is onder lucht dan onder N_2, maar in beide gevallen vrij laag (~1%). Een mechanisme wordt voorgesteld voor de reactie onder DUV-belichting van TinOH.

In Hoofdstuk 4 laten we zien dat niet alleen fotonen chemische reacties in de fotolak kunnen veroorzaken. Ook temperatuur-geïnduceerde processen in de lucht na belichting (bakprocessen) veroorzaken chemische reacties die de oplosbaarheid van de tin-oxo kooien verder verminderen Deze reacties vinden plaats bij temperaturen waarbij het onbelichte deel van de fotolak stabiel is, en deze reacties kunnen gebruikt worden om de gevoeligheid van de fotolak te verhogen (zie Hoofdstuk 6). De fotochemische reacties onder stikstof leiden waarschijnlijk tot gedeeltelijke reductie van de tin-oxo kooi, terwijl bakken leidt tot oxidatie en het meer cross-linken van de tin-oxo kooien.

In Hoofdstuk 5 wordt de relatie tussen absorptie van DUV-fotonen en opbrengst van de chemische reactie verder onderzocht door drie soorten tin-oxo kooien te vergelijken, die dezelfde kooistructuur hebben maar drie verschillende tegenionen (hydroxide (TinOH), acetaat (TinA) en trifluoroacetaat (TinF)). De opbrengst van de chemische reacties zijn onderzocht door middel van XPS en UV-absorptiespectra. De veranderingen in oplosbaarheid van de fotolak-lagen zijn gekwantificeerd met behulp van contrast curves. De gevoeligheid van TinOH en TinA is vergelijkbaar, en hoger dan die van TinF. Dit bewijst dat de tegenionen een rol spelen in de stap van het chemische proces die leidt tot de omslag in oplosbaarheid. Interessant genoeg zijn effecten van de kleinere basiciteit en zwakkere vorming van waterstofbruggen terug te vinden in de Sn 3d XPS-spectra.

De mate van geschiktheid van tin-oxo kooien voor het schrijven van EUV-patronen wordt bestudeerd in Hoofdstuk 6 en in Hoofdstuk 8. In tin-oxo kooien kunnen negatieve patronen geschreven worden, zoals staat beschreven in Hoofdstuk 6. De geschiktheid van tin-oxo kooien met verschillende tegenionen (TinA en TinOH) voor het schrijven van patronen onder EUV-belichting wordt hierin onderzocht. De resultaten wijzen uit dat de gevoeligheid en de kwaliteit van de patronen wordt beïnvloed door de verschillende tegenionen (hydroxide (TinOH), acetaat (TinA) en malonaat (TinM)). Een mogelijke verklaring hiervoor is dat fysische eigenschappen, zoals oplosbaarheid, veranderd worden door het tegenion. De resultaten van Hoofdstuk 5 (die zijn verkregen nadat de resultaten uit Hoofdstuk 6 werden gepubliceerd) geven echter aan dat er een effect is van de tegenionen op de chemische reactiviteit in DUV fotochemie, en dit verschil kan ook invloed hebben op EUV-geïnduceerde reacties. De gevoeligheid van de tin-oxo kooi fotolak kan verbeterd worden door procescondities te optimaliseren, zoals laagdikte, “post-exposure bake” (PEB) temperatuur, en de omstandigheden waaronder de ontwikkelingsstap plaatsvindt. De thermische stabiliteit van TinOH-poeder is onderzocht met thermogravimetrische analyse (TGA), en er wordt aangetoond dat het poeder stabiel is tot minstens 100 °C. Door de patroongeschiktheid van TinOH te vergelijken bij verschillende baktemperaturen, is gevonden dat 100 °C de juiste

baktemperatuur is voor TinOH om negatieve patronen te schrijven. Ook hebben we gezien dat de gevoeligheid en patroonresolutie van TinOH beter wordt bij het toevoegen van een bakstap (PEB). Na een gedeeltelijke optimalisatie hebben we met TinOH als fotolak een patroon kunnen schrijven van 22 nm “half pitch” met een dosis van 57 mJ cm^{-2} EUV. Met TinA als fotolak werd, met een dosis van 57 mJ cm^{-2} aan EUV, een 30 nm half pitch patroon bereikt.

De chemische veranderingen in TinOH ten gevolge van EUV bestraling worden systematisch onderzocht in Hoofdstuk 7. Het reactiemechanisme van de tin-oxo kooien onder EUV-belichting wordt vergeleken met het mechanisme onder DUV-belichting. Verschillende vormen van XPS, gecombineerd met massaspectrometrie, worden gebruikt om fotochemie in de fotolaklagen te onderzoeken. Het fotoemissiespectrum van TinOH onder 92 eV belichting wordt voor het eerst beschreven, waarbij we bevestigen dat elektronen die zich bevinden in het Sn 4d orbitaal onder belichting van EUV een effectieve bron zijn van primaire elektronen. De afdampproducten, gasvormige producten die onder belichting van EUV vrijkomen, worden bestudeerd door een afdampanalysesysteem, in samenwerking met IMEC. Butaan, buteen en butanal komen vrij als TinOH wordt belicht met EUV, wat een verdere aanwijzing is dat de Sn-C binding verbroken kan worden onder EUV-belichting, zoals uit de XPS-analyses bleek. De DUV/EUV-belichte dunne TinOH-lagen werden geanalyseerd door middel van XPS en massaspectrometrie. Er werd gevonden dat de kwantumopbrengst van de chemische reactie voor EUV-belichting hoger is dan voor DUV-belichting. Een reactiemechanisme voor tin-oxo kooien die belicht worden door EUV wordt voorgesteld.

Als aanvulling op het onderzoek in Hoofdstuk 6 hebben we gevonden dat patronen kunnen worden gerealiseerd met positieve en negatieve toon door de tin-oxo kooien te gebruiken als fotolak bij hoge PEB-temperatuur. Dit fenomeen wordt verder onderzocht in Hoofdstuk 8. Het normale (negatieve) patroon zien we als we voor TinOH gebruik maken van PEB-temperaturen beneden 150 °C, zoals te zien in Hoofdstuk 6. Als de PEB-temperatuur echter 150 °C bereikt, kan er een positief patroon gemaakt worden. Dit ‘dual tone’-fenomeen wordt gezien bij zowel EUV als elektronen-belichting. Door de verbinding te analyseren met TGA en XPS hebben we dit fenomeen gerelateerd aan het verlies van water dat plaatsvindt in het onbelichte TinOH bij deze temperatuur.

In Hoofdstuk 9 onderzoeken we de mogelijkheid om tin(II) carboxylaat-verbindingen te gebruiken als EUV-fotolakken. De geschiktheid van de patronen en de chemische reactie van dunne films van tin(II) acetaat en tin(II) ethylhexanoaat, onder belichting van DUV/EUV, worden bestudeerd. De gevoeligheid van deze twee verbindingen voor DUV/EUV-belichting wordt besproken. ‘Post-application

baking', het toevoegen van een bakstap vlak na aanbrengen van de dunne laag, heeft een groot effect op de moleculaire samenstelling. Beide verbindingen laten een duidelijke chemische verandering zien onder belichting. Patronen van hoge kwaliteit konden (nog) niet worden bereikt door deze twee verbindingen als fotolak te gebruiken.

Publication list

This thesis is based on the following publications:

1. Y. Zhang, J. Haitjema, X. Liu, F. Johansson, A. Lindblad, S. Castellanos, N. Ottosson and A. M. Brouwer, "Photochemical conversion of tin-oxo cage compounds studied using hard x-ray photoelectron spectroscopy", *J. Micro/Nanolitho. MEMS MOEMS*, 2017, **16**, 023510. [Chapter 3]
2. Y. Zhang, J. Haitjema, X. Liu, F. Johansson, A. Lindblad, N. Ottosson, S. Castellanos, A. M. Brouwer, "Influence of thermal process on the chemical reaction and the reaction yield in a model organotin EUV photoresist", *Manuscript in preparation.* [Chapter 4]
3. Y. Zhang, J. Haitjema, X. Liu, F. Johansson, A. Lindblad, S. Castellanos, N. Ottosson, A. M. Brouwer, "The relationship between photon absorption of tin-nanocages and the efficiency of photochemical reaction", *Manuscript in preparation.* [Chapter 5]
4. J. Haitjema, Y. Zhang, M. Vockenhuber, D. Kazazis, Y. Ekinci and A. M. Brouwer, "Extreme ultraviolet patterning of tin-oxo cages", *J. Micro/Nanolitho. MEMS MOEMS*, 2017, **16**, 7. [Chapter 6]
5. Y. Zhang, J. Haitjema, M. Baljozovic, F. Johansson, N. Sadegh, M. Vockenhuber, D. Kazazis, I. Pollentier, J. D. Keelor, D. De Simone, A. Lindblad, T. A. Jung, Y. Ekinci, S. Castellanos, A. M. Brouwer, "The photoreaction mechanism of tin oxo cages under EUV exposure", *Manuscript in preparation.* [Chapter 7]
6. Y. Zhang, J. Haitjema, M. Baljozovic, M. Vockenhuber, D. Kazazis, T. A. Jung, Y. Ekinci and A. M. Brouwer, "Dual-tone Application of a Tin-Oxo Cage Photoresist Under E-beam and EUV Exposure", *J. Photopolym. Sci. Technol.*, 2018, **31**, 249-255. [Chapter 8]

Other publications:

- J. Haitjema, Y. Zhang, N. Ottosson and A. M. Brouwer, "Photoreactions of Tin Oxo Cages, Model EUV Photoresists", *J. Photopolym. Sci. Technol.*, 2017, **30**, 99-102.
- J. Haitjema, Thomas Schlathölter, Yu Zhang, Rebecka Lindblad, Martin Timm, Tobias Lau, Ronnie Hoekstra, Albert M. Brouwer, Soft X-ray Fragmentation of Tin-oxo Cage Ions, *submitted.*
- K. T. L. Trinh, Y. Zhang and N. Y. Lee, "One-step DNA purification and amplification on an integrated plastic microdevice for on-site identification of foodborne pathogens", *Anal. Chim. Acta*, 2018, **1040**, 63-73. (co-first author)
- M. L. Ha, Y. Zhang and N. Y. Lee, "A functionally integrated thermoplastic microdevice for one-step solid-phase-based nucleic acid purification and isothermal amplification for facile detection of foodborne pathogen", *Biotechnol. Bioeng.*, 2016, **113**, 2614-2623. (co-first author)

- W. Wu, K. T. L. Trinh, Y. Zhang and N. Yoon Lee, "Portable plastic syringe as a self-actuated pump for long-distance uniform delivery of liquid inside a microchannel and its application for flow-through polymerase chain reaction on chip", *RSC Advances*, 2015, **5**, 12071-12077.
- Y. Zhang, K. T. L. Trinh, I.-S. Yoo and N. Y. Lee, "One-step glass-like coating of polycarbonate for seamless DNA purification and amplification on an integrated monolithic microdevice", *Sens. Actuators B Chem.*, 2014, **202**, 1281-1289.
- Q. Sun, D. H. Kim, S. S. Park, N. Y. Lee, Y. Zhang, J. H. Lee, K. Cho and J. H. Cho, "Transparent, Low-Power Pressure Sensor Matrix Based on Coplanar-Gate Graphene Transistors", *Adv. Mater.*, 2014, **26**, 4735-4740.
- F. Xin, H. Zhang, B. Hao, T. Sun, L. Kong, Y. Li, Y. Hou, S. Li, Y. Zhang and A. Hao, "Controllable transformation from sensitive and reversible heat-set organogel to stable gel induced by sodium acetate", *Colloids Surf. A Physicochem. Eng. Asp.*, 2012, **410**, 18-22.
- M. Li, Y. Zhang, S. Zhang, T. Xia and A. Hao, "The Enrichment of Isoflavones in Belamcanda Chinensis Using Hydroxypropyl-β-cyclodextrins", *Chin. J. Appl. Chem.*, 2011, **29**, 730-732.

Acknowledgement

It has been more than 4 years since the first day I started my PhD in the Netherlands. Now it comes to the end with a mix of excitement and sadness. It's one of the most exiting and unforgettable moments in my life. Meanwhile, it comes with sadness. The sadness is because it's also the time to say goodbye to super you, my dear friends, colleagues and supervisors. You made my life in the Netherlands enjoyable and meaningful. I cannot finish my PhD without the guidance and assistance from many of you. For this, at the end of this thesis, I would like to express my gratitude to all the people I had pleasures to meet and to work with.

First of all, I would like to express my deepest gratitude to my supervisor Prof. Fred Brouwer for offering me the opportunity to pursue my PhD degree in the Nanophotochemistry group. I still remember on the first day of my PhD, you picked me up at Schiphol airport at 5 a.m. I have felt so lucky that I get the chance to work with such a nice supervisor since that moment. Every time I jumped into your office, you were always patient to answer all my questions. Whenever I met difficulties, you always encouraged me and gave me your brilliant advice to shape my way of thinking critically and analytically, which benefitted my research work in the past and will definitely benefit my rest of life. You helped me to identify my character strengths and weakness and to know myself better. Your guidance over the past four years indeed helped me to become a better person.

I would like to express my special thanks to Dr. Sonia. You are the strongest girl I have ever seen, both physically and mentally. Your valuable suggestions, comments and guidance encouraged me to learn more day by day. You can always find the interesting parts in your life and share them with us. You and your funny stories always inspired me at the hardest moment during the past four years (If you write a book on your funny stories, I definitely would like to buy one☺). It's my honor to work with you.

I would like to acknowledge the help provided by my co-promotor Prof. Paul Planken. I also wish to express my deepest gratitude to Prof. Bas de Bruin, Prof. Moniek Tromp, Dr. Stefania Grecea, Prof. Wybren Jan Buma, and Dr. Yasin Ekinci for reviewing my thesis and participating in the defense committee. Especially Dr. Yasin, without the support of your amazing and unique tool (EUV interference lithography), I cannot finish my PhD project.

I wish to thank all my colleagues at ARCNL. It has been so nice to join this big family. Marjan and Joost, thanks for your endless efforts to make every amazing

event possible in ARCNL. Whenever I need your help, you're always ready to solve any problem at the first time. I would like to thank Romy, Rosa and Cathelijne for all your kind help, your patience and strong support. I also give my special thanks to previous and current group members both from Nanophotochemistry and EUV photoresists group. Jarich, I appreciate your efforts involved in this project. You're a patient person and thank you for providing all kinds of our magic cages on time. I really enjoyed the four years' cooperation with you. Especially, thanks for your help with the Samenvating. Lianjia, my lovely sister, you always cook nice food, especially the green bean cake you made for me. I enjoyed all the free chats about science and life during our teatime and during all the beamtime trips in the past 2+ years. Olivier, you're always full of energy and ready to work with enthusiasm, which inspired me a lot. Neha, I enjoyed your milk tea so much. Najmeh, I'd like to thank you for your kind assistance with beamtime. Hero Ivan, I enjoyed the cooperation and all the discussion with you. Thank you for your patience and I'm happy that you enjoyed your trip to China. Robbert, I indeed like your cooking. The cake you baked and the professional Chinese hotpot you made were so delicious. Moreover, you're always there to help everyone. Aniket, everytime I came across a problem with AFM, you were the first one coming into my mind. Thank you for your kind help. Sander, you're always there, quiet and patient, being prepared for all the questions and for providing strong support for all the facilities in the lab. Maarten, Zhichao and Lotte, I'm not professional on supervising students, thank you for your patience, understanding and cooperation. It's my pleasure working with you, goodluck for your PhD programs. Bruno, you are my first friend in the Netherlands, without you I cannot adapt to the new environment so fast. Kevin, I really enjoyed the cooperation with you, and thanks for your contribution to this project, please help convey my gratitude to Qian, I enjoyed her cooking. Niklas, you showed me the way to work with XPS, I appreciate your kind help at the beginning of my PhD. I would like to thank Reinout, you are always patient to answer all of my questions and to solve all the problems on XPS, and it's so nice to work with you. I am also grateful to all my colleagues at ARCNL, Wenqian, Sandra, Daniel, Mees, Jeremy, Hans, Martijn, Eline, Kendra, Unnati, Luuk, Christian (AMOLF), Johannes (AMOLF), Pavel, Mengqi, Feng-Chun, Ruben, Victor, Peter, Stephen, Bo, Oscar, Thomas, Vanessa, Randy, Tiago, Hao, Renfeng, Jan, Cristina, and all my colleagues from support groups et al. for every wonderful moment during the past four years in my memory.

I'm glad to join Molecular photonics group at UvA. I would like to express my gratitude to all the group members. I would like to thank Prof. Wybren Jan Buma, Prof. Sander Woutersen, Dr. Rene Williams and Prof. Hong Zhang for your kind help, comments and advice on my project. I would like to express my special thanks to Michiel and Hans for your patience and strong technical support for all the

experimental facilities in the lab. And Michiel, I really enjoyed your paella. I would like to thank Mina, what you did made me feel so warm when I first came to the Netherlands. I would like to thank Dina, I enjoyed every chat with you. You're a patient person always with a smile on your face. I'm grateful to all the group members: Bert, Benjamin, Roberto, Mark, Floor, Steven, Tomislav, Tatu, Luuk, Maximilian, Hernan, Wim, Elena, Aylin, Marije, Yorrick, Janita, Marco, Celine, Ruben, Imme, Aishwarya, Thijs, David, Adriaan, Charlotte, Threes, Jeroen. On my first day in MP group, I was introduced to the "Chinese Mafia" leading by Hong with members Dongdong, Hung-Cheng, Fei, Yadan, Rafeal, and with new members Yansong, Jing Zuo, Yanni, Langping, Jiayun, Zhen Qu, Angela, Pengtao, Luting, Si Shen. I really appreciated your support both in scientific work and in daily life during the past years.

I also received significant support from other organizations. I would like to thank Bob, Dimitry, Andries and Hans from AMOLF/Amsterdam Nanocenter for your professional support with all the training and with problem solving of all the facilities; Michaela, Dimitrios and Roberto from Advanced Lithography and Metrology group at PSI for providing comprehensive support and for helping us get fruitful results; Milos, Mina and Thomas from Molecular Nanoscience group at PSI for providing assistance in XPS measurements; Fredrik and Andreas from Uppsala University, Ruslan and Erika from PM4 beamline, Roberto from HIKE endstation for the support during the beamtimes at BESSY; Danilo and Ivan from IMEC for the support with outgassing experiments and all the valuable advice for my project; Wim, Sander and Claire from ASML for all the nice advice, comments and discussion during the past years.

I wish to thank my master supervisor Prof. Nae Yoon Lee and Dr. Loan Trinh, who offered huge support during my application for the PhD program. Also my heartfelt thanks to many other friends in daily life: Yu Pan, Yuan Gao, Huaqian Leng, Feng Jiang, Lili Kong, Yao Li, Shan Zhu, Bin Sun, Shaotao, Mingchao Wang, Tingting Xia, Meihui Li, Yuliang Liu, Sen Zhang, Yiduo Wang, Xiangmeng Kong, Tiantian, Hainan Zhang, Honglin Chen, Mika et al. And I would like to thank all my friends in China.

I would also like to express my sincere gratitude to my all time friend Minmin, we have been together for more than seven years. Thank you for being there whenever I need you. We spent the most difficult time together in Korea and coincidently we moved to the Netherlands together. Over the past seven years, we have accumulated so many invaluable memories. I believe our friendship will last forever. With a coincidence that your wedding day is exactly the day that I submitted my thesis, we'll remember this special day together. I wish you all the best.

Last but not the least, I would like to thank my grandfather and grandmother, who have been so supportive all the time and always proud of me. Deep thanks to my parents, brother and all my relatives, without your endless love, I cannot finish my PhD. I would like to thank my husband Lingmin Sun for always standing by me. I'm the luckiest one to have such a special and wonderful man who always understands me. Without your motivation and understanding, I would never be the person that I am today. You encouraged and inspired me with your strength and wisdom. There are thousands of words in my heart that I want to say to you, all of which eventually converge into three words - thanks for everything. Finally, I'd like to thank my two lovely cats, Zhamao and Golden. You're so adorable that help me release a lot of pressure during the past four years.

张 宇

Yu Zhang

April 2019